

SANDIA REPORT

SAND2009-4795

Unlimited Release

Printed August 2009

Geomechanical Analyses to Investigate Wellbore/Mine Interactions in the Potash Enclave of Southeastern New Mexico

J. Guadalupe Argüello, James E. Bean, C. M. Stone, and Brian L. Ehgartner

Prepared by
Sandia National Laboratories
Albuquerque, New Mexico 87185 and Livermore, California 94550

Sandia is a multiprogram laboratory operated by Sandia Corporation, a Lockheed Martin Company, for the United States Department of Energy's National Nuclear Security Administration under Contract DE-AC04-94AL85000.

Approved for public release; further dissemination unlimited.



Sandia National Laboratories

Issued by Sandia National Laboratories, operated for the United States Department of Energy by Sandia Corporation.

NOTICE: This report was prepared as an account of work sponsored by an agency of the United States Government. Neither the United States Government, nor any agency thereof, nor any of their employees, nor any of their contractors, subcontractors, or their employees, make any warranty, express or implied, or assume any legal liability or responsibility for the accuracy, completeness, or usefulness of any information, apparatus, product, or process disclosed, or represent that its use would not infringe privately owned rights. Reference herein to any specific commercial product, process, or service by trade name, trademark, manufacturer, or otherwise, does not necessarily constitute or imply its endorsement, recommendation, or favoring by the United States Government, any agency thereof, or any of their contractors or subcontractors. The views and opinions expressed herein do not necessarily state or reflect those of the United States Government, any agency thereof, or any of their contractors.

Printed in the United States of America. This report has been reproduced directly from the best available copy.

Available to DOE and DOE contractors from
U.S. Department of Energy
Office of Scientific and Technical Information
P.O. Box 62
Oak Ridge, TN 37831

Telephone: (865) 576-8401
Facsimile: (865) 576-5728
E-Mail: reports@adonis.osti.gov
Online ordering: <http://www.osti.gov/bridge>

Available to the public from
U.S. Department of Commerce
National Technical Information Service
5285 Port Royal Rd.
Springfield, VA 22161

Telephone: (800) 553-6847
Facsimile: (703) 605-6900
E-Mail: orders@ntis.fedworld.gov
Online order: <http://www.ntis.gov/help/ordermethods.asp?loc=7-4-0#online>



SAND2009-4795
Unlimited Release
Printed April 2010

Geomechanical Analyses to Investigate Wellbore/Mine Interactions in the Potash Enclave of Southeastern New Mexico

J. Guadalupe Argüello
Strategic Initiatives Department

C. M. Stone
Strategic Initiatives Department

Brian L. Ehgartner
Geotechnology & Engineering Department

Sandia National Laboratories
P.O. Box 5800
Albuquerque, New Mexico 87185-0376

James E. Bean
Sandia Staffing Alliance, LLC
2500 Louisiana Blvd. NE Suite 325B
Albuquerque, New Mexico 87110

Abstract

Geomechanical analyses have been performed to investigate potential mine interactions with wellbores that could occur in the Potash Enclave of Southeastern New Mexico. Two basic models were used in the study; (1) a global model that simulates the mechanics associated with mining and subsidence and (2) a wellbore model that examines the resulting interaction impacts on the wellbore casing. The first model is a 2D approximation of a potash mine using a plane strain idealization for mine depths of 304.8 m (1000 ft) and 609.6 m (2000 ft). A 3D wellbore model then considers the impact of bedding plane slippage across single and double cased wells cemented through the Salado formation. The wellbore model establishes allowable slippage to prevent casing yield.

Acknowledgments

An oral presentation and review was conducted that addressed the analysis assumptions, approach and results; as well as interpretations and conclusions included in this report. The authors wish to thank John Holland, 1524; Dr. Joe Bishop, 1525; Dr. Charles Hickox, 6331; and Dr. Jim Redmond, 1525 who participated and provided helpful comments on the presentation.

In addition, we appreciate the efforts of Dr. Darrell Munson, 6312 (with Sandia Staffing Alliance) and Dr. Joe Bishop, 1525 who served as internal Sandia peer reviewers of this report. We also acknowledge and appreciate the time that Prof. Richard Regueiro of the Civil, Environmental, and Architectural Engineering Department at the University of Colorado took to provide a critical external review of the report

Contents

1. Introduction	11
1.1. History of Issue	11
1.2. Review of Previous Work to Resolve Issue	11
1.3. Sandia Analysis	12
1.4. JAS3D Analysis Code	12
2. Model Description	15
2.1. Global Mine Excavation Model	15
2.1.1. Assumptions	15
2.1.2. Idealization of the Enclave Stratigraphy	16
2.1.3. Plane Strain Model of a Mine	20
2.2. Wellbore Model	32
2.2.1. Assumptions	32
2.2.2. Idealization of the Wellbore Section	33
2.2.3. Three-Dimensional Computational Model of the Wellbore	36
3. Results	41
3.1. Global Mine Excavation Model Results	41
3.1.1. 1000 foot mine model	42
3.1.2. 2000 foot mine model	43
3.1.3. Sensitivity of Slip Results to Variations of Friction Coefficient and Interface Separation	44
3.1.4. Comparison with Field Observations	45
3.2. Wellbore Model Results	90
3.2.1. Single Casing	90
3.2.2. Double Casing	92
4. Summary & Conclusions	107
4.1. Global Mine Excavation Model	107
4.2. Wellbore Model	108
4.3. Combined Models	108
5. References	111
Appendix I: Analysis Plan for BLM Potash Gas Migration Study	113
Appendix II: Sandia Response to Stakeholder Comments on Analysis Plan	195

Figures

Figure 2.1.1. Stratigraphy Used in 304.8 m (1000 ft) Deep Mine	24
Figure 2.1.2. Stratigraphy Used in 609.6 m (2000 ft) Deep Mine	25
Figure 2.1.3. Location of Marker Beds in 304.8 m (1000 ft) Deep Mine	26
Figure 2.1.4. Location of Marker Beds in 609.6 m (2000 ft) Deep Mine	27
Figure 2.1.5. Volumetric Response to Compaction of Mine Excavation.....	28
Figure 2.1.6. FE Mesh Details for a Portion of the 304.8 m (1000 ft) Mine Model: 1 Mile Excavation Case	29
Figure 2.1.7. Kinematic Boundary Conditions Used in All Global Mine Excavation Models	30
Figure 2.1.8. FE Mesh Details for a Portion of the 609.6 m (2000 ft) Mine Model: 1 Mile Excavation Case	31
Figure 2.2.1. Schematic of Wellbore Model.	37
Figure 2.2.2. Idealized 3D Configuration for Single Casing Model.....	38
Figure 2.2.3. Idealized 3D Configuration for Double Casing Model	38
Figure 2.2.4. Computational Mesh and Boundary Conditions on Idealized 3D Configuration for Single Casing Model.....	39
Figure 2.2.5. Computational Mesh and Boundary Conditions on Idealized 3D Configuration for Double Casing Model	40
Figure 3.1.1. Mining Orientations Used in Global Model Calculations	50
Figure 3.1.2. 304.8 m (1000 ft) Mine Depth: Interface Slip Along MB 101 at Select Times	51
Figure 3.1.3. 304.8 m (1000 ft) Mine Depth: Maximum Interface Slip as a Function of Distance for MB 101 Over 25 year Time Period. (1.6 km, or 1 mile, Excavation at Rate of 1.6 km/year, or 1 mile/year)	52
Figure 3.1.4. 304.8 m (1000 ft) Mine Depth: Absolute Maximum Interface Slip as a Function of Distance for MB 101 Over 25 year Time Period. (1.6 km, or 1 mile, Excavation at Rate of 1.6 km/year, or 1 mile/year).....	53
Figure 3.1.5. 304.8 m (1000 ft) Mine Depth: Absolute Maximum Interface Slip as a Function of Distance for All Marker Beds Over 25 year Time Period (1.6 km, or 1 mile, Excavation at Rate of 1.6 km/year, or 1 mile/year).....	54
Figure 3.1.6. 304.8 m (1000 ft) Mine Depth: Absolute Maximum Interface Slip Envelope for the Mining Towards Well Scenario (1.6 km, or 1 mile, Excavation at Rate of 1.6 km/year, or 1 mile/year).....	55
Figure 3.1.7. 304.8 m (1000 ft) Mine Depth: Absolute Maximum Interface Slip Envelope for the Mining Away From Well Scenario (1.6 km, or 1 mile, Excavation at Rate of 1.6 km/year, or 1 mile/year)	56

Figure 3.1.8. 304.8 m (1000 ft) Mine Depth: Absolute Maximum Interface Slip Envelope for the Mining Towards Well Scenario (Varying Mine Excavation Sizes and Rates).....	57
Figure 3.1.9. 304.8 m (1000 ft) Mine Depth: Absolute Maximum Interface Slip Envelope for the Mining Away From Well Scenario (Varying Mine Excavation Sizes and Mining Rates)	58
Figure 3.1.10. 304.8 m (1000 ft) Mine Depth: Absolute Maximum Interface Slip Envelope (Envelope Over Mine Excavation Sizes and Mining Rates)	59
Figure 3.1.11. 609.6 m (2000 ft) Mine Depth: Interface Slip Along MB 101 at Select Times	60
Figure 3.1.12. 609.6 m (2000 ft) Mine Depth: Absolute Maximum Interface Slip as a Function of Distance for All Marker Beds Over 25 year Time Period (1.6 km, or 1 mile, Excavation at Rate of 1.6 km/year, or 1 mile/year)	61
Figure 3.1.13. 609.6 m (2000 ft) Mine Depth: Absolute Maximum Interface Slip Envelope for the Mining Towards Well Scenario (Varying Mine Excavation Sizes and Rates).....	62
Figure 3.1.14. 609.6m (2000 ft) Mine Depth: Absolute Maximum Interface Slip Envelope for the Mining Away From Well Scenario (Varying Mine Excavation Sizes and Rates).....	63
Figure 3.1.15. 609.6m (2000 ft) Mine Depth: Absolute Maximum Interface Slip Envelope	64
Figure 3.1.16. Comparison of Absolute Maximum Interface Slip Envelopes for 304.8 m (1000 ft) and 609.6 m (2000 ft) Mines	65
Figure 3.1.17. Close-Up View of Absolute Maximum Interface Slip Envelopes for 304.8 m (1000 ft) and 609.6 m (2000 ft) Mines	66
Figure 3.1.18. Effect of Friction Coefficient on Slip Envelope: Mining Away From Well	67
Figure 3.1.19. Effect of Friction Coefficient on Slip Envelope: Mining Towards Well	68
Figure 3.1.20. Effect of Interface Separation on Slip Envelope: Mining Towards Well	69
Figure 3.1.21. Effect of Interface Separation on Slip Envelope: Mining Away From Well	70
Figure 3.1.22. Illustration of Surface Measurement Quantities	71
Figure 3.1.23. Surface Layer Deformation at 25 years Magnified 100 Times	72
Figure 3.1.24. Surface Subsidence as a Fraction of Initial Mine Height.....	73
Figure 3.1.25. Effect of Mining Rate on Surface Subsidence at 25 years	74
Figure 3.1.26. Effect of Mining Rate on Surface Subsidence at 25 years	75
Figure 3.1.27. Surface Subsidence as a Fraction of Initial Mine Height.....	76
Figure 3.1.28. Effect of Mining Rate on Surface Subsidence at 25 years	77
Figure 3.1.29. Effect of Mining Rate on Surface Subsidence at 25 years	78
Figure 3.1.30. Effect of Mining Depth on Surface Subsidence at 25 years	79

Figure 3.1.31. Effect of Interface Properties on Surface Subsidence at 25 years	80
Figure 3.1.32. Ground Surface Strain at Select Times.....	81
Figure 3.1.33. Ground Surface Strain at Select Times.....	82
Figure 3.1.34. Ground Surface Strain for Mining Towards the Well Case.....	83
Figure 3.1.35. Ground Surface Strain for Mining Towards the Well Case.....	84
Figure 3.1.36. Comparison of Ground Surface Subsidence and Mine Roof Displacement	85
Figure 3.1.37. Comparison of Ground Surface Subsidence and Mine Roof Displacement	86
Figure 3.1.38. Comparison of Mine Closure Rates for 304.8 m (1000 ft) and 609.6 m (2000 ft) Mines	87
Figure 3.1.39. Comparison of Mine Closure Rates for 304.8 m (1000 ft) and 609.6 m (2000 ft) Mines	88
Figure 3.1.40. Effect of Interface Properties on Mine Closure for 304.8 m (1000 ft) Mine.....	89
Figure 3.2.1. Zoomed-In View of Deformed Configuration After 3/8 in. Relative Slip Along the Interbed.....	95
Figure 3.2.2. Zoomed-In View of Deformed Casing After 3/8 in. Relative Slip Along the Interbed in its Vicinity	95
Figure 3.2.3. Zoomed-In View Showing Plastic Strain in the Cement After ~3/80 & 3/8 in. Relative Slip of the Interbed (Upper Portion of Cement Removed For Clarity)	96
Figure 3.2.4. Zoomed-In View Showing Plastic Strain in the Casing After ~3/80 & 3/8 in. Relative Slip of the Interbed (Upper Portion of Casing Removed For Clarity)	97
Figure 3.2.5. Development of EQPS with Slip Along the Interbed for the Three Elements Through the Thickness at Location A in the Casing, For Interbed Slip of Up to 3/8 in.	98
Figure 3.2.6. Development of EQPS with Slip Along the Interbed for the Three Elements Through the Thickness at Location B in the Casing, For Interbed Slip of Up to 3/8 in.	98
Figure 3.2.7. Development of EQPS with Slip Along the Interbed for the Three Elements Through the Thickness at Location C in the Casing, For Interbed Slip of Up to 3/8 in.	99
Figure 3.2.8. Zoomed-In View of Deformed Double Casing Configuration After 3/8 in. Relative Slip Along the Interbed.....	100
Figure 3.2.9. Zoomed-In View of Deformed Casings in Double Casing Model After 3/8 in. Relative Slip Along the Interbed in its Vicinity.....	100
Figure 3.2.10. Zoomed-In View Showing Plastic Strain in the Two Cement Annuli After ~7/80 & 3/8 in. Relative Slip of the Interbed (Upper Portion of Cement Removed For Clarity).....	101

Figure 3.2.11. Zoomed-In View Showing Plastic Strain in the Two Casings After ~7/80 & 3/8 in. Relative Slip of the Interbed (Upper Portions of Casing Removed For Clarity) 102

Figure 3.2.12. Development of EQPS with Slip Along the Interbed for the Three Elements Through the Thickness at Location A in Each of the Two Casings, For Interbed Slip of Up to 3/8 in. 103

Figure 3.2.13. Development of EQPS with Slip Along the Interbed for the Three Elements Through the Thickness at Location A in Each of the Two Casings, For Interbed Slip of Up to ~1.0 in. 103

Figure 3.2.14. Development of EQPS with Slip Along the Interbed for the Three Elements Through the Thickness at Location B in Each of the Two Casings, For Interbed Slip of Up to 3/8 in. 104

Figure 3.2.15. Development of EQPS with Slip Along the Interbed for the Three Elements Through the Thickness at Location B in Each of the Two Casings, For Interbed Slip of Up to ~1.0 in. 104

Figure 3.2.16. Development of EQPS with Slip Along the Interbed for the Three Elements Through the Thickness at Location C in Each of the Two Casings, For Interbed Slip of Up to 3/8 in. 105

Figure 3.2.17. Development of EQPS with Slip Along the Interbed for the Three Elements Through the Thickness at Location C in Each of the Two Casings, For Interbed Slip of Up to ~1.0 in. 105

Figure 4.3.1. Slip Envelopes from the Global Mine Excavation Model versus Allowable Slip Prior to First Through-the-Thickness Yielding from the Wellbore Model. 109

Tables

Table 1. Material Layers specified in all Mining Simulations	17
Table 2. Non-Salt Properties used in Calculations.....	18
Table 3. Salt/Potash Properties used in Calculations	19
Table 4. Secondary Creep Properties used in Calculations.....	19
Table 5. Thermal Input used in Calculations.....	19
Table 6. Elastic-Plastic Material Model Parameters used for K55 Steel	34
Table 7. Sandia Geomodel Parameters used for Cement	35
Table 8. Calculated Angle of Break from Models	48

1. Introduction

1.1. History of Issue

The active potash mining area in SE New Mexico contains numerous existing and proposed oil and gas wells (see Figure 1 of Appendix I). This study will attempt to define acceptable standoff distances between the mining area and the oil and gas wells. Of concern is the potential loss of well integrity due to mine induced subsidence which could lead to damage of the wellbore casing and possibly permit oil and gas flow into the mine workings. The study will focus on mining/wellbore interaction conditions that can jeopardize well integrity. Analysis results will also examine the integrity of the intervening rocks separating the mines and wells.

For the purpose of protecting and conserving the potash deposits for future use, the Secretary of Interior withdrew 42,285 acres from oil and gas leasing in 1939. However, a number of wells had already been drilled and mining had commenced in the early 1930's. In 1951, the Secretary designated 298,345 acres as a "Potash Area" and revoked the ban on oil and gas leasing, thus providing for development and production of oil and gas and concurrent mining of potash deposits in the potash area. At that time, rules and guidelines were created to protect the mines and potash by requiring a salt protection string and cementing of the wellbore casing. Secretarial Orders in 1965 and 1975 expanded the potash area first to 420,212 and then to 491,916 acres. Expansions of the potash area encompassed wells that were completed under less stringent requirements. As a result, well completions within the potash area vary considerably. Technology, regulations, and practices have improved over time, and the arguments exerted today suggest that both industries can co-exist in a safe manner, yet some fundamental questions remain including an acceptable standoff distance between mining activities and proposed oil and gas wells.

1.2. Review of Previous Work to Resolve Issue

Determining what is acceptable practice has resulted in extensive litigation¹ over the past approximately 50 years, without resolution, as the views and opinions expressed by the potash and oil and gas industries are divergent. The intent of this study is to present an unbiased technical examination of this issue and apply our best technology to develop what we consider as reasonable guidelines to enable safe and efficient co-development of the natural resources. The responsibility for implementing the Secretarial Orders has resided with the Bureau of Land Management (BLM) since 1986 and they are the agency providing the impetus for this study.

¹ IBLA 2003-334, etc. constitutes 15,275 pages of testimony, 10,000 pages of administrative record, 1200 exhibits, and approximately 58,000 pages of documents (Yates Counsel, May 3, 2004; page 34,945 of IBLA 92-612, et al.).

The BLM compiled a list of stakeholders for the oil and gas industry and potash industry, including government agencies, and established a mechanism and protocol (non-disclosure agreement) whereby industry could share their information and data with the BLM and Sandia (Matis, BLM to stakeholders, 12/7/2007). Matis stated the desire to open a dialogue, create an information exchange, and gain access to scientific and engineering information having a bearing on the project. An approach was developed whereby Sandia would develop an analysis plan and request review from stakeholders (Matis, BLM to stakeholders, 3/13/2008). Information or suggestions were requested (Matis, BLM to stakeholders, 4/3/2008) relevant to well-mine interactions that would facilitate model development, such as rock mechanics properties, or a means to validate a model, including subsidence and convergence measurements. The volumes of testimony, exhibits, documents, and related studies as a result of past litigation and hearings were made available by the BLM. From this and other technical reports, primarily related to the Waste Isolation Pilot Plant (WIPP), a detailed analysis plan and the basis for the analyses were developed. The analysis plan contained in Appendix I of this report was released to stakeholders for review (Matis, BLM to stakeholders, 7/1/2008). Comments on that plan were received from the mining (Litt to Ehgartner, 9/26/2008) and the oil and gas (Bogle to Auby and Ehgartner, 9/26/2008) stakeholders. These comments were responded to in writing (Appendix II of this report) and in meetings with the stakeholders (12/9/08, 1/13/09) prior to completing the following analyses.

1.3. Sandia Analysis

As proposed in the analysis plan, two basic models were used in this study; a global model that simulates the mechanics associated with mining and subsidence (Section 2.1), and a wellbore model that examines the resulting impacts on wellbore casing (Section 2.2). The first model is a two-dimensional (2D) approximation of a potash mine using a plane strain idealization for mine depths of 304.8 and 609.6 m (1000 and 2000 ft). A 2D model is reasonable given the large areal extent of the mines relative to mine depth. The 3D wellbore model considers the impact of bedding plane slippage across single and double cased wells cemented through the Salado formation. The wellbore model establishes allowable slippage to prevent casing yield and failure. The predicted slippage across bedding planes in the global mine model (Section 3.1) are then compared to the allowable wellbore slippages (Section 3.2) to establish safe standoff distances between a mine and well. Summary and conclusions are presented in Section 4.

1.4. JAS3D Analysis Code

The finite element code used in these analyses was JAS3D. JAS3D is a three-dimensional iterative solid mechanics code developed at Sandia National Laboratories for analyzing the large deformation response of nonlinear materials subjected to a variety of loads. For quasistatic applications, as was the case here, this Lagrangian finite element program uses iterative algorithms to solve the equilibrium equations. A multi-level

solver provides effective treatment of severe nonlinearities and frictional contact response. Eight-node uniform strain hexahedral elements are used in the finite element formulation for the application describe here. Hourglass distortions can be effectively controlled without disturbing the finite element solution using the Flanagan-Belytschko hourglass control scheme, as was done here. All constitutive models in JAS3D are cast in an un-rotated configuration defined using the rotation determined from the polar decomposition of the deformation gradient. A robust contact algorithm allows for the interaction of deforming contact surfaces of quite general geometry (Blanford et al., 2001).

JAS3D is a mature production code. It represents approximately 30 plus years of R&D into explicit finite element code technology that has its genesis in the defense programs. Apart from its weapons usage, JAS3D has been used to support the WIPP (Waste Isolation Pilot Plant), YMP (Yucca Mountain Project), other commercial storage facilities, and various oil and gas applications. The technology embodied in JAS3D, through its predecessor codes Pronto (Taylor and Flanagan, 1989), JAC3D (Biffle, 1993), SANCHO (Stone et al., 1985), and SANTOS (Stone, 1997), has also been used for an even wider range of applications.

Since JAS3D has continually been modified and improved over its development lifetime, testing for “correctness” of results has been extremely important. A series of test problems (or regression suite) has been developed to this end and has been used by the code developers on a regular basis and before any new changes to the code were committed. It has been a JAS3D project requirement that the new versions of JAS3D be able to complete the regression suite with minimal differences from a set of archived results. The code is under configuration management and version control, being administered via a configuration management system repository. Version 2.3.A of the code was used for these analyses.

2. Model Description

2.1. Global Mine Excavation Model

2.1.1. Assumptions

In any numerical simulation of physical processes it is frequently necessary to invoke a number of assumptions which render the analysis tractable. Analyses involving geologic materials are well known to be very challenging due to the extreme variability of rock quality (e.g. degree of fracturing) and the inability to fully characterize the *in-situ* response of the rock when subjected to events such as mining. While laboratory tests can be performed under controlled conditions to give insight into the stress-strain behavior, there are always questions about the degree of sample disturbance caused during the retrieval of the sample from the ground or even the relevance of the tests since the lab samples do not usually incorporate features such as discontinuities.

For the computer simulations documented in this section it has been assumed that the mining process takes place over a sufficiently large areal region such that plane strain conditions can be reasonably assumed. Furthermore while room and pillar mining has not been explicitly considered, the effects of secondary mining, which reduces the pillar size, may be similar to those of long wall mining conditions once the secondary mining operation is initiated.

The finite element meshes developed for these analyses represent a region four miles in lateral dimension and extending vertically from the ground surface, considered to be the top of the Dewey Lake formation, down to the Salado-Castile boundary. In all cases the height of the mined region was assumed to be 3.048 m (10 ft). Modeling of simultaneous mining at multiple depths was initially considered but was not carried out in this work.

We have chosen a set of mining scenarios that illustrates the potentially important effect of slip at bedding interfaces. By varying the depth of the mine, the length of the mine, and the mine excavation rate, a range of typical mining conditions were examined. The two mine depths evaluated were 304.8 m (1000 ft) and 609.6 m (2000 ft). The mine excavation lengths and mining rates were chosen to be 0.8 km (0.5 mile) and 1.6 km (1 mile), and 0.48 km/year (0.3 mile/year) and 1.6 km/year (1.0 mile/year), respectively.

The various formations (Dewey Lake, Rustler, and Salado) generally contain a number of layers of rock of various type and thicknesses. These layers within the formations were not explicitly represented in the numerical model but were assigned properties representative of the specific formation rock. The individual potash ore zones, within the McNutt member of the Salado formation, were not included in the model but were assumed to behave similar in terms of their mechanical (elastic and creep) response to Salado salt. The lack of data on the creep characteristics of potash material, which likely depend on the mineral types and ore grades, made this choice necessary.

Within the Salado formation a number of marker beds (MB) exist. These marker beds were assumed to be the locations of potential relative displacement between the layers of salt. A total of eleven marker beds, represented as frictional planar interfaces, were included in these simulations as potential planes of slip. Of the eleven marker beds four were located in the upper Salado and seven were located in the McNutt Potash zone. One marker bed, MB 123, was located below the floor of the mine. By using frictional slip planes in the model it has been implicitly assumed that the tangential slip deformations will be localized to a very thin region. This assumption was chosen to be consistent with the noted presence of thin clay seams at the bottom of the marker beds. Furthermore, this assumption is consistent with the treatment of marker beds in the numerical models that were used for validation against experimental room data for the WIPP (Munson and DeVries, 1990; Munson et. al, 1990; Munson, 1997). For these analyses it was further assumed that the formations and marker beds were horizontally oriented.

2.1.2. Idealization of the Enclave Stratigraphy

In the next sections the depths and constitutive properties of the various formations and marker beds for the 304.8 m (1000 ft) and 609.6 m (2000 ft) deep mine are provided.

2.1.2.1. Material Layers

The potash zone where mining occurs can vary with depth from one location to another. In one location, it may be relatively shallow, but at a different location, it may be relatively deep. In the same way the thicknesses of the overburden layers, above the potash, may also vary. Table 1 and Figures 2.1.1 and 2.1.2 summarize the stratigraphy assumed for the numerical models used in the “shallow,” 304.8 m (1000 ft), and “deep,” 609.6 m (2000 ft), mine analyses. Note that the thickness of the McNutt Potash zone was identical in the two models; however, the Dewey Lake, Rustler, and the upper Salado and lower Salado have different thicknesses in the two models. In the 304.8 m (1000 ft) model the Dewey Lake was 61 m (200 ft) thick and in the 609.6 m (2000 ft) model it was 152.4 m (500 ft) thick. In the 304.8 m (1000 ft) model, the Rustler was 91.4 m (300 ft) and in the 609.6 m (2000 ft) model it was 152.4 m (500 ft) thick. The upper Salado was 76.2 m (250 ft) thick in the 304.8 m (1000 ft) mine model and 228.6 m (750 ft) thick in the 609.6 m (2000 ft) model while the lower Salado was 259.1 m (850 ft) thick in the 304.8 m (1000 ft) mine model and 396.2 m (1300 ft) thick in the 609.6 m (2000 ft) model.

In these figures the Salado formation appears to be divided into distinct regions, Upper Salado, McNutt Potash and Lower Salado. However, as previously noted, the material properties describing these regions were identical in the numerical model. The constitutive properties specified for all materials are discussed in Section 2.2.2.2.

Figures 2.1.3 and 2.1.4 illustrate the locations of the 11 marker beds in the upper Salado and McNutt Potash zone for the 304.8 m (1000 ft) and 609.6 m (2000 ft) deep mine models.

Table 1. Material Layers specified in all Mining Simulations

Formation / Member / marker bed	Distance from Ground Surface to bottom of bed ¹	
	1000 ft mine	2000 ft mine
Dewey Lake	61.0 m (200 ft)	152.4 m (500 ft)
Rustler =Top of Upper Salado	152.4 m (500ft)	304.8 m (1000 ft)
Upper Salado / MB 101	158.5 m (520 ft)	323.1 m (1060 ft)
Upper Salado / MB 102	169.2 m (555 ft)	356.6 m (1170 ft)
Upper Salado / MB 103	181.4 m (595 ft)	391.7 m (1285 ft)
Upper Salado / MB 109	201.3 m (660 ft)	452.6 m (1485 ft)
Bottom of Upper Salado = Top of McNutt Potash	228.6 m (750 ft)	533.4 m (1750 ft)
MB 117	249.9 m (820 ft)	554.7 m (1820 ft)
MB 118	259.1 m (850)	563.9 m (1850 ft)
MB 119	266.7 m (875 ft)	571.5 m (1875 ft)
MB 120	272.8 m (895 ft)	577.6 m (1895 ft)
MB 121	277.4 m (910 ft)	582.2 m (1910 ft)
MB 122	281.9 m (925 ft)	586.7 m (1925 ft)
Top of Mine (roof)	301.8 m (990 ft)	606.6 m (1990 ft)
Bottom of Mine (floor)	304.8 m (1000 ft)	609.6 m (2000 ft)
MB 123	317.0 m (1040 ft)	621.8 m (2040 ft)
Bottom of McNutt Potash = Top of Lower Salado	335.3 m (1100 ft)	640.1 m (2100 ft)
Bottom of Lower Salado = Top of Castile	594.4 m (1950 ft)	1036.3 m (3400 ft)

Note: ¹ The ground surface is considered to be the top of the Dewey Lake formation

2.1.2.2. Constitutive Models and Parameters

The non-salt materials located above the Salado formation (Dewey Lake and Rustler formations) were treated as isotropic linear elastic regions. The elastic constants, Young's Modulus and Poisson's ratio, and the mass density used in these regions are listed in Table 2.

Table 2. Non-Salt Properties used in Calculations

Material	Young's Modulus	Poisson's Ratio	Density
Dewey Lake	1.5 x 10 ¹⁰ Pa (2.18 x 10 ⁶ psi)	0.25	2160 kg/m ³ (135 lb/ft ³)
Rustler	2.0 x 10 ¹⁰ Pa (2.90 x 10 ⁶ psi)	0.30	2160 kg/m ³ (135 lb/ft ³)

The Salado formation, including the McNutt Potash zone, was modeled as rate-dependent material using a power law creep model. The components of the inelastic creep strain rate for the power law creep model can be described by the following equation.

$$\dot{\epsilon}_{ij}^c = \dot{\epsilon}_{eq}^c N_{ij}$$

where

$$\sigma_{eq} = \text{von Mises equivalent stress} = \sqrt{3J_2} = \sqrt{\frac{3}{2} S_{ij} S_{ij}}$$

$$S_{ij} = \text{components of the deviatoric stress tensor} = S_{ij} = \sigma_{ij} - \frac{1}{3} \sigma_{kk} \delta_{ij}$$

$$\dot{\epsilon}_{eq}^c = \text{equivalent creep strain rate} = A e^{-Q/RT} \sigma_{eq}^N$$

$$N_{ij} = \text{gradient of creep potential} = \frac{\partial \sigma_{eq}}{\partial \sigma_{ij}} = \frac{3S_{ij}}{2\sigma_{eq}}$$

$$\dot{\epsilon}_{ij}^c = \text{components of creep strain rate} = A e^{-Q/RT} \sigma_{eq}^N \frac{3S_{ij}}{2\sigma_{eq}}$$

The mechanical properties used for the salt (and potash) material are shown in Tables 3 and 4. The creep model representing the salt also incorporates a temperature effect

through the exponential term, $e^{-Q/RT}$. A linear thermal gradient of T_{grad} along with a reference temperature of T_{ref} and corresponding reference depth of y_{ref} was employed to specify the temperature profile in the Salado formation. The values of the thermal parameters are given in Table 5. The temperatures were treated as *time independent* variables in these analyses ($T = f(y)$).

Table 3. Salt/Potash Properties used in Calculations

Material	Young's Modulus	Poisson's Ratio	Density
Salt/Potash	3.1×10^{10} Pa (4.50×10^6 psi)	0.25	2160 kg/m ³ (135 lb/ft ³)

Table 4. Secondary Creep Properties used in Calculations

Material	Structure Factor (A)	Stress Exponent (N)
Salt/Potash	4.48×10^{-38} (Pa ^N ·sec) ⁻¹	5.0

Table 5. Thermal Input used in Calculations

Material	Reference Depth (y_{ref})	Reference Temperature (T_{ref})	Gradient (T_{grad})	Q/R
Salt/Potash	-650 m (-2132.6 ft)	300.15 K (27C)	0.01 K/ m	5033 K

Note: R is the universal gas constant = 1.987 cal/K-mole and Q is an experimental constant = 10000 cal/mole

2.1.2.3. Slip Interface Definitions and Parameters

It is important to define a few conventions used in the modeling activities. In these numerical models, the slip interfaces or contact surfaces are defined by an upper and lower surface. Slip is defined as the relative displacement between slave nodes on the lower surface relative to master nodes on the upper surface. The regions were discretized such that the master and slave nodes have the same coordinates at the beginning of the simulation. Positive slip occurs when a slave node on the lower surface moves to the right relative to the master node on the top surface. Negative slip occurs when a slave node on the lower surface moves to the left relative to the corresponding master node on the top surface. According to the Coulomb friction model used in these simulations, the

maximum allowable shear stress is linearly dependent on the normal stress acting at the point. Slip occurs when the shear stress on the interface equals the allowable shear stress. JAS3D uses an iterative procedure to ensure that all interface nodes satisfy the frictional constraints of the Coulomb model as well as satisfying the equilibrium conditions for the internal and external forces at the end of a load step. Since gravity stresses are included in these calculations the normal stresses acting on the interfaces are greater on the lower marker beds than the upper ones. Beyond the boundaries of the mined region the amount of slip that would be expected would be lower on the deeper marker beds because of the increased normal stresses at those locations.

Eleven slip interfaces, corresponding to the locations of the marker beds, were included in these analyses. All slip interfaces were modeled with a constant coefficient of friction of 0.2. This value of friction coefficient is, again, consistent with that used in the treatment of marker beds in the numerical models that were used for validation against experimental room data for the WIPP (Munson and DeVries, 1990; Munson et. al, 1990; Munson, 1997). The interfaces were not allowed to separate. The sensitivity of interface slip to different friction coefficients and the potential for separation and its effect on regional slip is evaluated in Section 3.1.3 for the 304.8 m (1000 ft) deep mine.

2.1.3. Plane Strain Model of a Mine

2.1.3.1. Simulation of Mining

In order to simulate the mining of potash, a numerical approach was employed in which the constitutive behavior of the element was modified when the element was identified as having been mined. By specifying the starting location of the mine and the rate of mining, each element centroid in the mine region was compared to the location of the advancing mining front. Thus an element in the mine region can be identified by its state: either pre-mined or mined. When the mining front reaches the mine element centroid the element was switched from state = pre-mined to state = mined.

Prior to the arrival of the mining front (state = pre-mined) the mine material was assumed to be elastic with material properties representative of salt (Table 3). However, once an element's state was changed to mined, the material behavior was changed to that of an inelastic material with a non-linear pressure-volume strain response. The deviatoric behavior in the inelastic model was assumed to be elastic/perfectly plastic with a low yield stress (~.1 MPa). The low yield strength in shear implies that the mined element will not sustain significant shear stress. The constitutive models for both states were assumed to be rate independent.

The pressure-volume strain curve used to describe the response of the material in the mined state was determined from a computational simulation of a hydrostatic test using a constitutive model for crushed salt. The constitutive model for crushed salt (Sjaardema and Krieg, 1987) was originally developed for analyzing the consolidation of backfilled shafts and drifts at the Waste Isolation Pilot Plant (WIPP). The crushed salt model used an assumed initial porosity (ϕ_0) and deforms toward a fully compact state (i.e. $\phi = 0$) under the action of a compressive confining stress. The pressure-volume strain curve

obtained from the crushed salt model simulation was then used to define the volumetric response of the elements in the mined state. This pressure-volume strain curve is shown in Figure 2.1.5 where pressure (P) and volume strain (ε_v) are defined by

$$P = -\frac{1}{3}(\sigma_{xx} + \sigma_{yy} + \sigma_{zz})$$

$$\varepsilon_v = \ln\left(\frac{\rho}{\rho_0}\right)$$

$\sigma_{xx}, \sigma_{yy}, \sigma_{zz}$ are the normal components of the true or Cauchy stress tensor and ρ and ρ_0 are the current and initial mass density of the mined elements. Using the intact density $\rho_{\text{int}} = 2160 \text{ kg} / \text{m}^3$ and the assumed initial porosity of $\phi_0 = 0.75$ yields the initial density $\rho_0 = (1 - \phi_0)\rho_{\text{int}} = (1 - .75)(2160 \text{ kg} / \text{m}^3) = 540 \text{ kg} / \text{m}^3$. The mined element will attain the intact density at a natural or logarithmic volume strain of 1.39.

2.1.3.2. 1000 Foot Mine Model

2.1.3.2.1. Finite Element (FE) Mesh

A Cartesian coordinate system was employed in these analyses oriented with the positive X axis pointing to the right and the positive Y axis pointed upward. The origin of the coordinate system was located at the top of the Dewey Lake formation halfway between the left and right mesh boundaries. The mesh was symmetric about the Y axis. The plane strain assumption was enforced in the 3D model by specifying the out of plane displacements (displacement components in Z direction) to be zero. The finite element discretization used in the 304.8 m (1000 ft) deep mine calculation consisted of 52668 eight-node uniform strain elements. There were a total of 396 elements in each row of the mesh and 133 rows. The elements corresponding to the region to be mined were 12.2 m (40 ft) in the X direction and 3.05 m (10 ft) in the Y direction for a total of 132 mine elements in the 1.6 km (1 mile) mine excavation model and 66 mine elements in the 0.8 km (0.5 mile) mine excavation model. Outside the mine region the vertical discretization was approximately 6.1 m (20 ft); however, all regions between potential sliding interfaces had at least 4 elements through the thickness in order to capture bending of the layers. Figure 2.1.6 illustrates a portion of the finite element mesh used in the 304.8 m (1000 ft) deep mine (1.6 km or 1 mile excavation case) calculations.

2.1.3.2.2. Boundary Conditions

The following kinematic (or displacement) boundary conditions were specified for nodes on the mesh boundaries

- 1) Left and right boundaries: no displacement in X direction
- 2) Bottom boundary: no displacement in Y direction.

- 3) Front and back boundaries: no displacement in Z direction.

These locations of the specified boundary conditions are shown in Figure 2.1.7.

2.1.3.2.3. Initial Stress and Temperature Conditions

Initial stress in the vertical or Y direction were assigned to the elements according to their distances (y) measured from the top of the Dewey Lake formation to the Y centroid of the element. The gravitation constant (g) with a value 9.8066 m/s^2 (32.2 ft/s^2) was used to assign the vertical stresses (σ_y) due to body forces. In accordance with the tension positive convention used in JAS3D, a negative sign indicates compressive stress. Since all materials were assumed to have a density of 2160 kg/m^3 (135 lb/ft^3), corresponding to a vertical stress gradient of 21263 Pa/m (0.94 psi/ft), the vertical stress at a location y meters from the top of the Dewey Lake is simply

$$\sigma_y = \rho gy = (2160 \text{ kg/m}^3)(9.8066 \text{ m/sec}^2)y$$

Using this relationship the vertical stress at the elevation of the mine ($y = -1000 \text{ ft} = -304.8 \text{ m}$) was

$$\sigma_y = (2160 \text{ kg/m}^3)(9.8066 \text{ m/sec}^2)(-304.8 \text{ m}) = -6.46 \times 10^6 \text{ Pa} \text{ (-937 psi)}$$

The lateral stresses in the non-salt upper regions (Dewey Lake and Rustler) were computed using the elastic uniaxial strain relationship $\sigma_x = \sigma_z = \frac{\nu}{1-\nu} \sigma_y$, where ν is Poisson's ratio. In the Salado formation (including the McNutt) the initial stresses were assumed to be isotropic and equal to the vertical stress.

The temperatures in the Salado formation increased linearly with depth according to the information given in Table 5. For the 304.8 m (1000 ft) mine the temperatures at the top and bottom of the Salado were 71.6 F (22.0 C) and 79.5 F (26.4 C), respectively.

2.1.3.3. 2000 foot mine model

2.1.3.3.1. Finite Element (FE) Mesh

The same Cartesian coordinate system described above was used in these analyses for the 609.6 m (2000 ft) mine. The finite element discretization used in the 609.6 m (2000 ft) deep mine calculation consisted of 49500 eight-node uniform strain elements. There were a total of 396 elements in each row of the mesh and 125 rows. The elements corresponding to the region to be mined were 12.2 m (40 ft) in the X direction and 3.05 m (10 ft) in the Y direction for a total of 132 mine elements in the 1.6 km (1 mile) mine excavation model and 66 mine elements in the 0.8 km (0.5 mile) mine excavation model. Outside the mine region the vertical discretization was approximately 12.2 m (40 ft) and as before, all regions between potential sliding interfaces had at least 4 elements through

the thickness in order to capture bending of the layers. Figure 2.1.8 illustrates a portion of the finite element mesh used in the 609.6 m (2000 ft) deep mine (1.6 km or 1 mile excavation case) calculations.

2.1.3.3.2. Boundary Conditions

The same kinematic boundary conditions described in Section 2.1.3.2.2 for the 304.8 m (1000 ft) mine and illustrated in Figure 2.1.7 were used in the 609.6 m (2000 ft) mine calculations.

2.1.3.3.3. Initial Stress and Temperature Conditions

The same methods of initial stress specification described in Section 2.1.3.2.3 were used in the 609.6 m (2000 ft) mine calculations. At the elevation of the mine ($y = -2000 \text{ ft} = -609.6 \text{ m}$), the initial vertical stress was $-12.9 \times 10^6 \text{ Pa}$ (-1871 psi).

For the 609.6 m (2000 ft) mine the temperatures at the top and bottom of the Salado were 74.3 F (23.5 C) and 87.6 F (30.9 C), respectively.

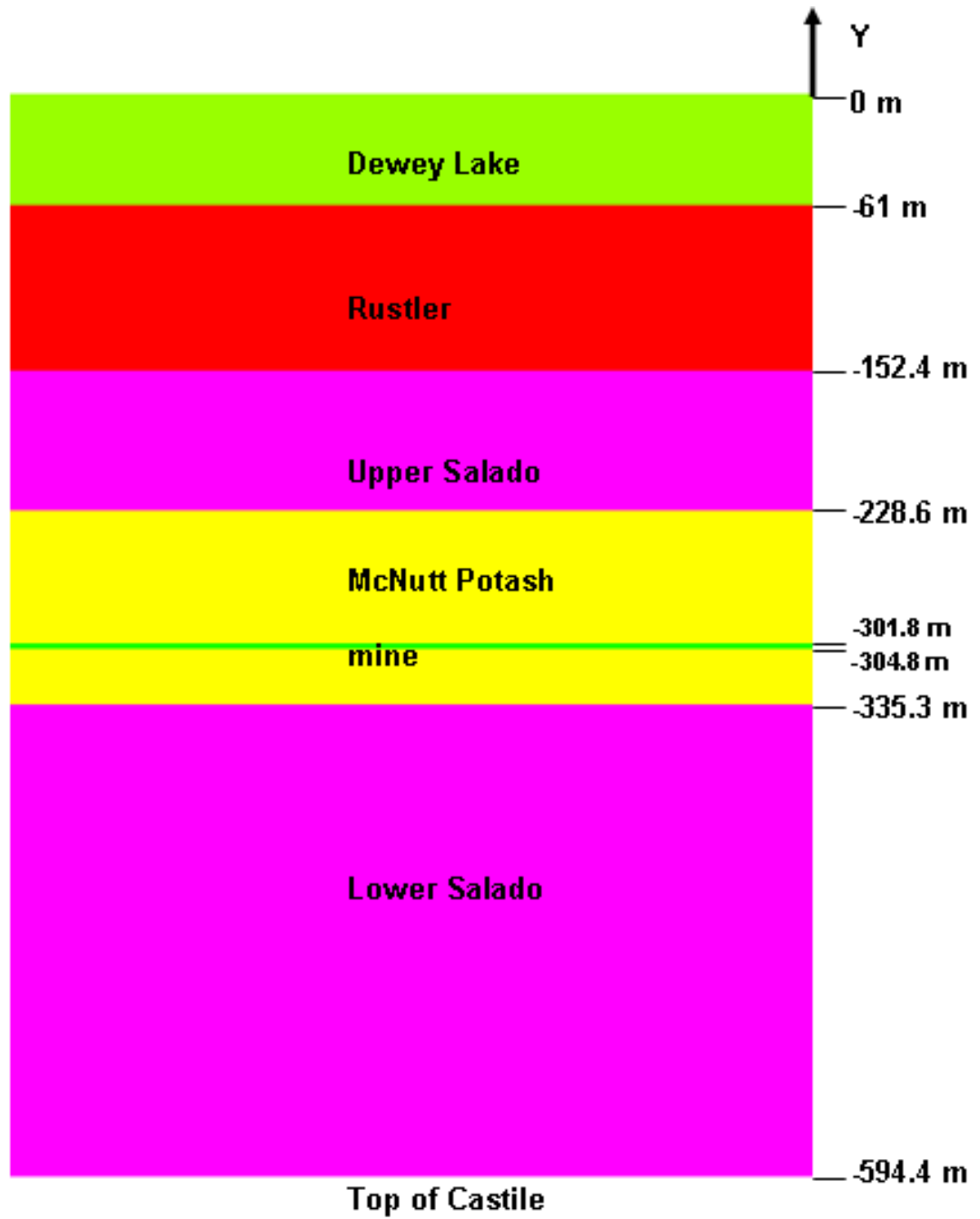


Figure 2.1.1. Stratigraphy Used in 304.8 m (1000 ft) Deep Mine

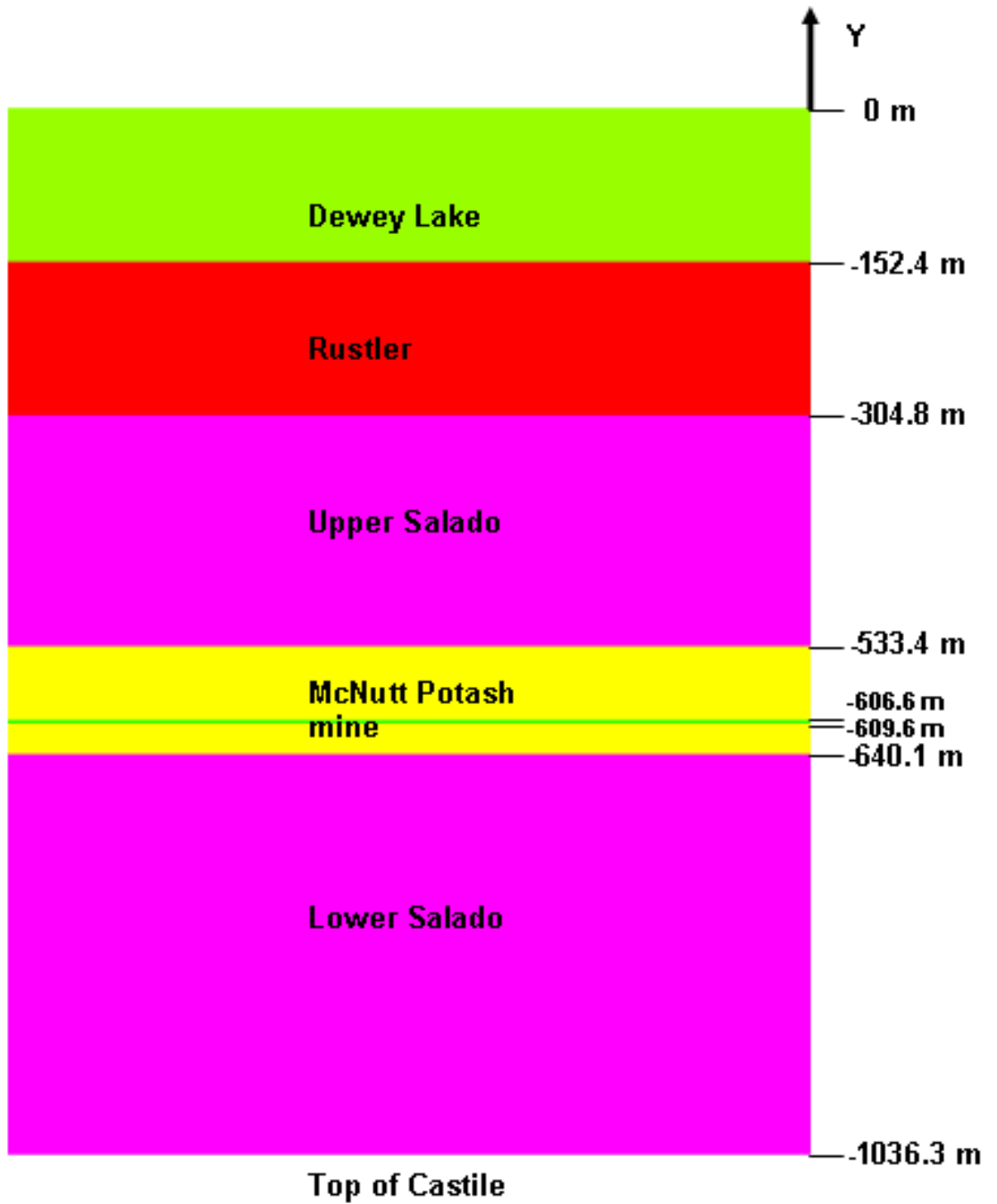
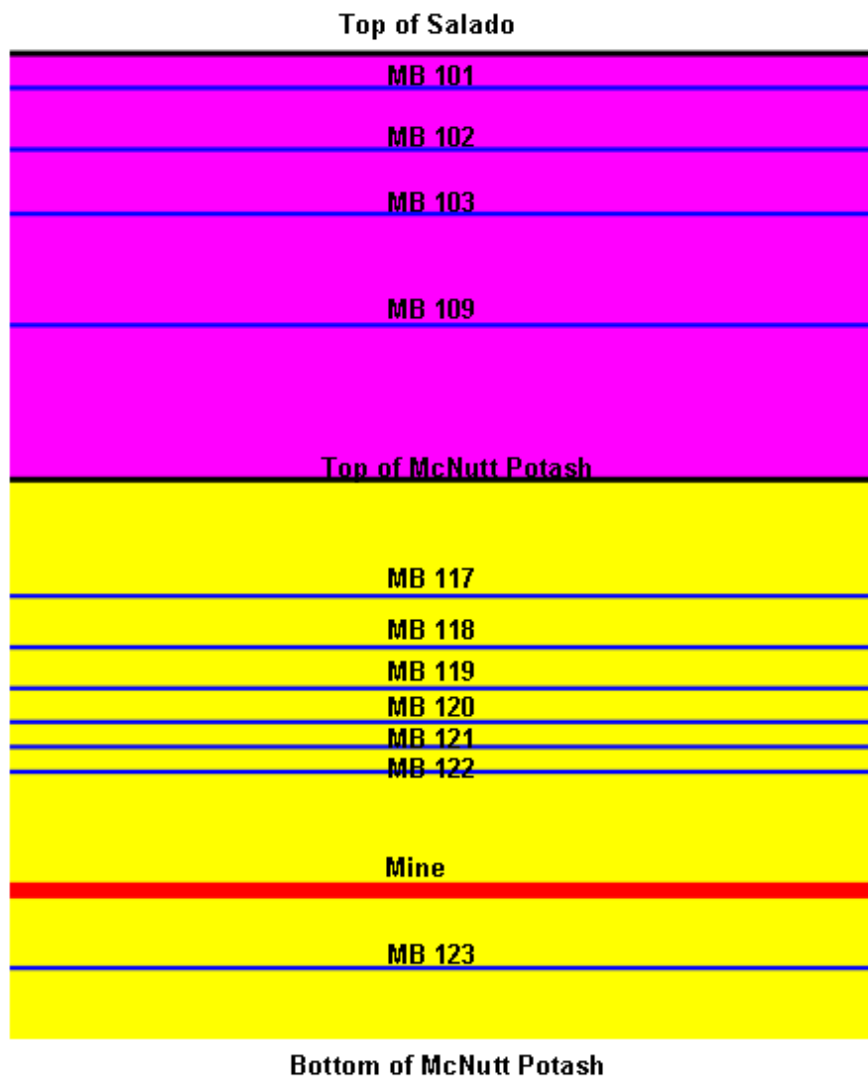
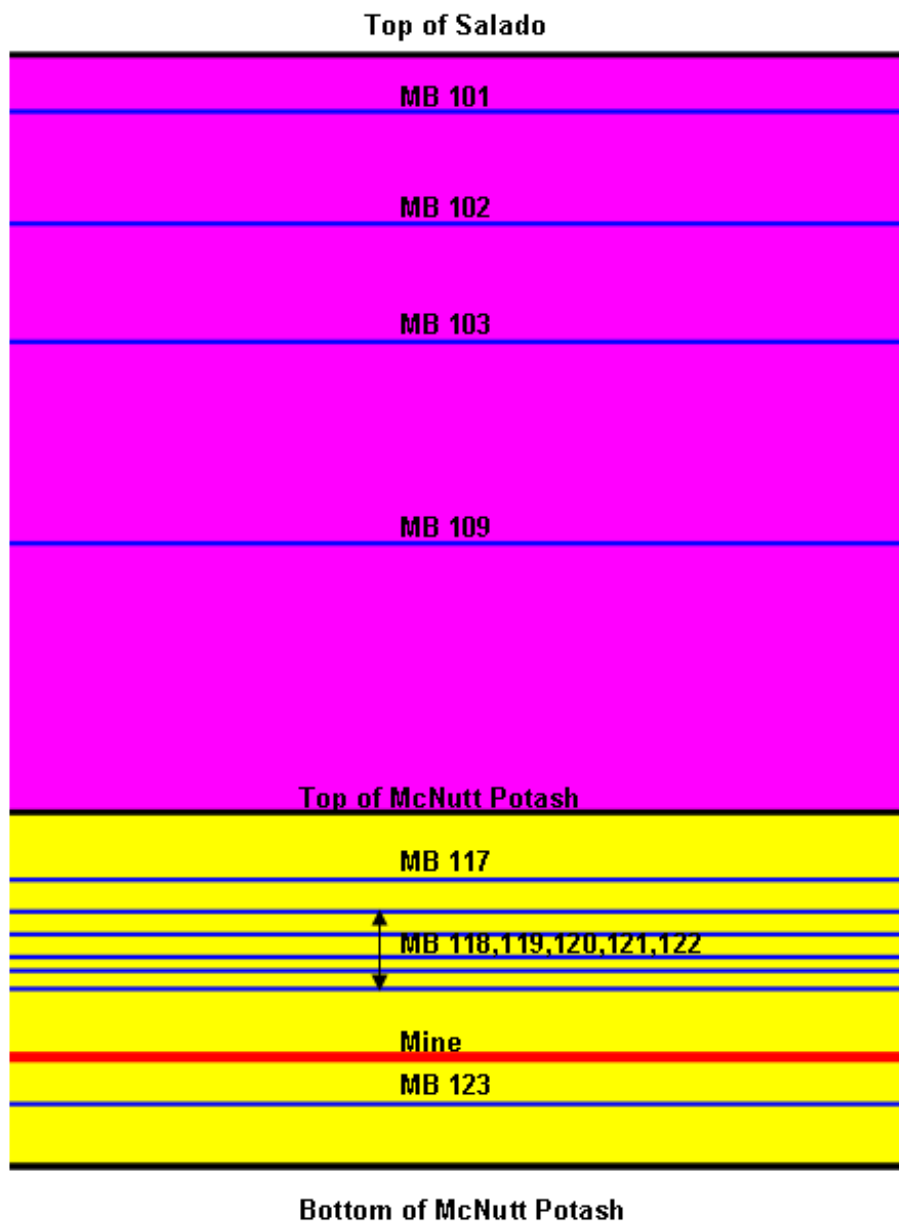


Figure 2.1.2. Stratigraphy Used in 609.6 m (2000 ft) Deep Mine



**Figure 2.1.3. Location of Marker Beds in 304.8 m (1000 ft) Deep Mine
(refer to Table 1 for elevations of marker beds)**



**Figure 2.1.4. Location of Marker Beds in 609.6 m (2000 ft) Deep Mine
(refer to Table 1 for elevations of marker beds)**

Crushed Salt Hydrostatic Test

Pressure vs Volume Strain

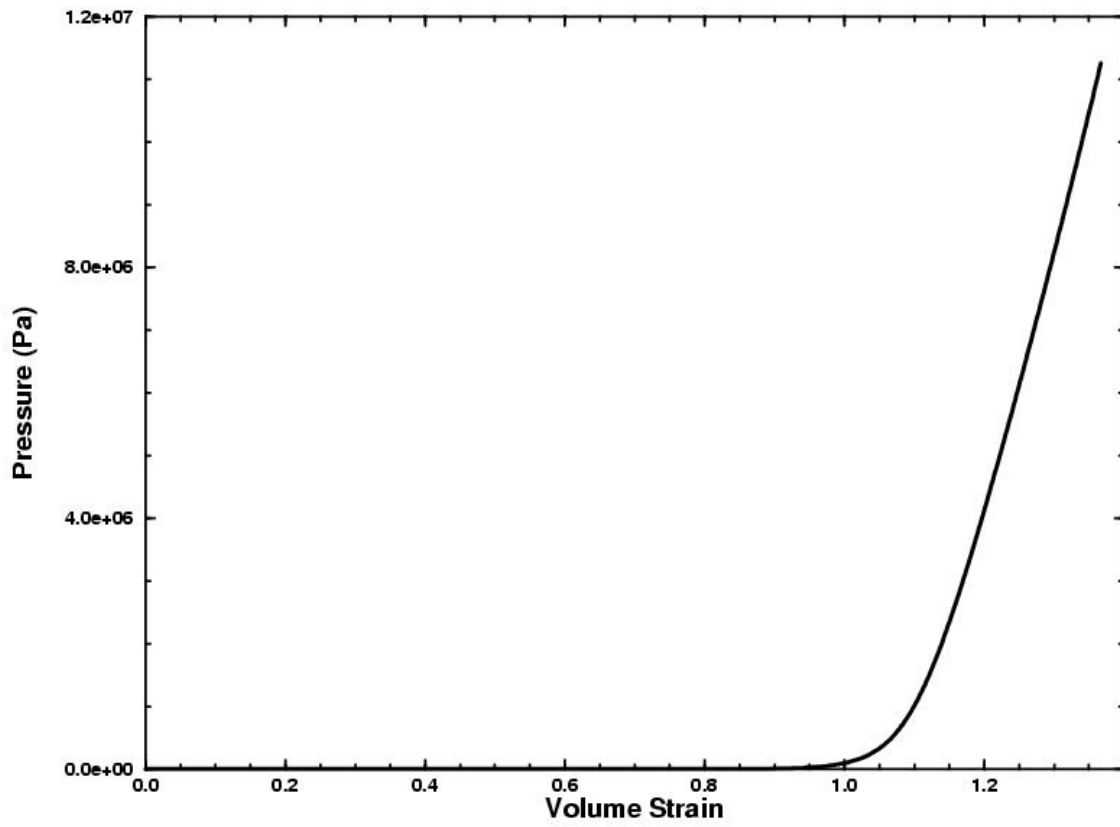


Figure 2.1.5. Volumetric Response to Compaction of Mine Excavation

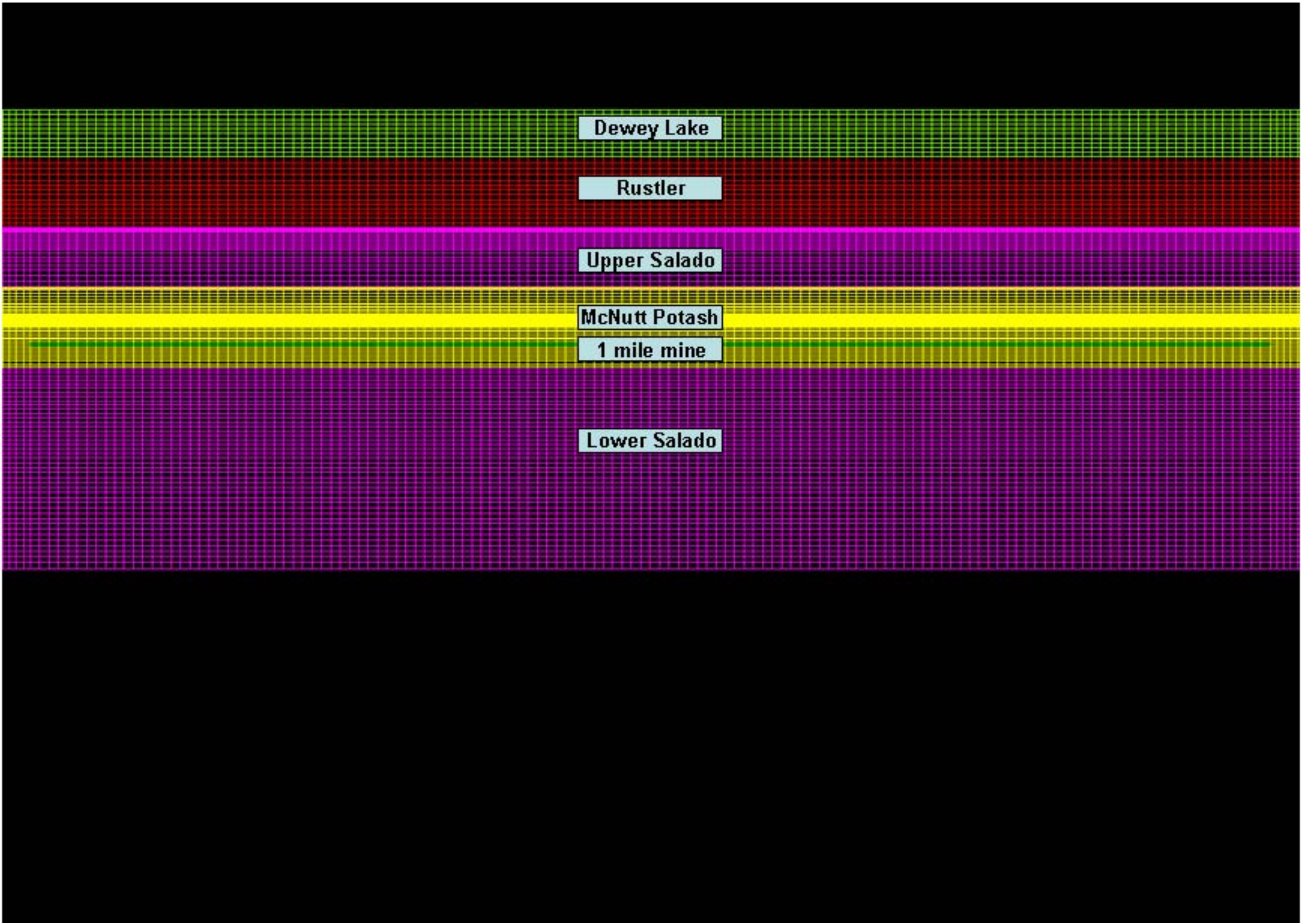


Figure 2.1.6. FE Mesh Details for a Portion of the 304.8 m (1000 ft) Mine Model: 1 Mile Excavation Case

No displacement in Z-direction for all nodes

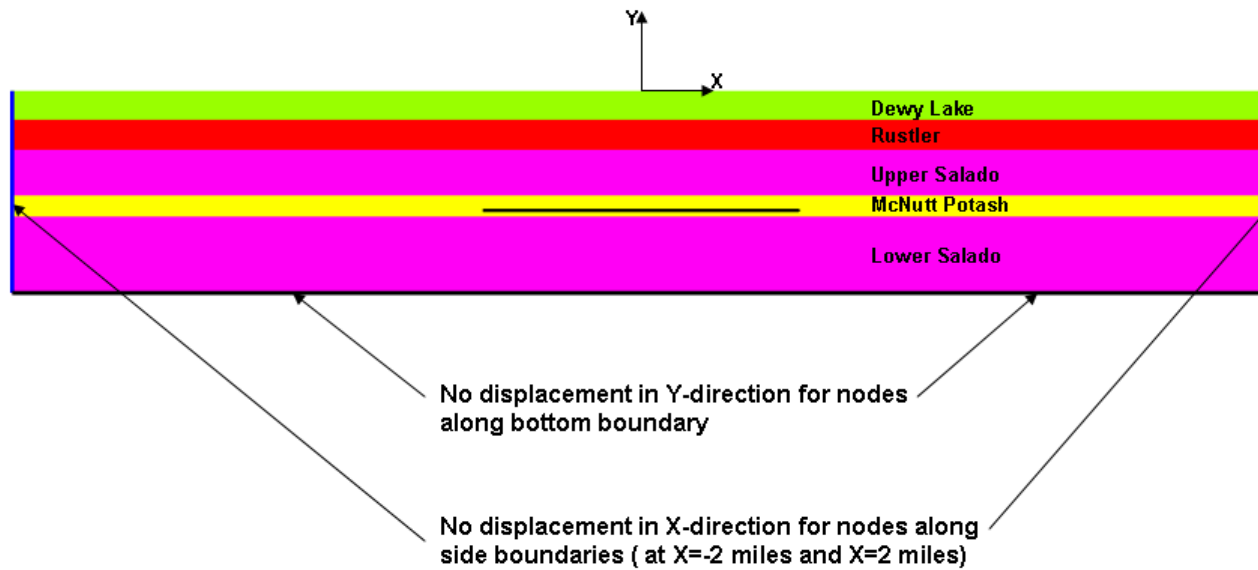


Figure 2.1.7. Kinematic Boundary Conditions Used in All Global Mine Excavation Models

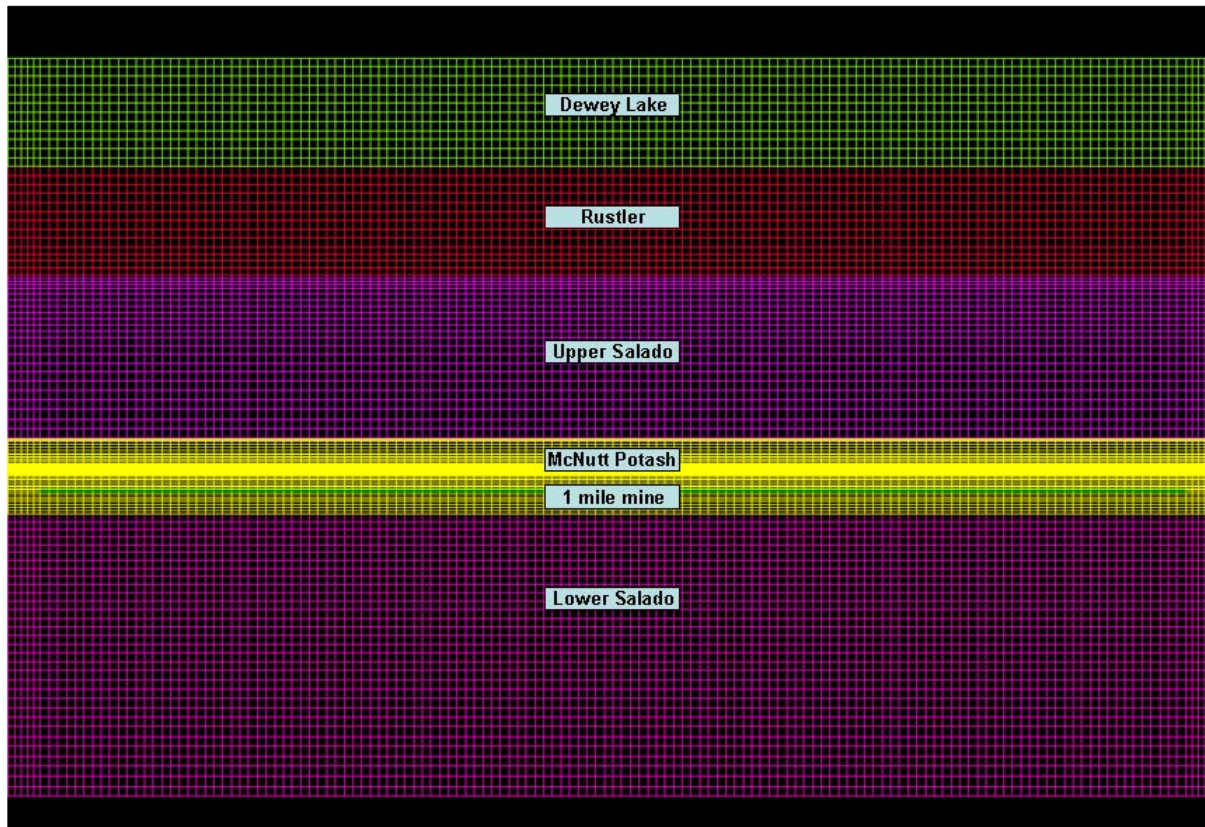


Figure 2.1.8. FE Mesh Details for a Portion of the 609.6 m (2000 ft) Mine Model: 1 Mile Excavation Case

2.2. Wellbore Model

A second model, the Wellbore Model, examines the resulting impacts from the Global Mine Excavation Model on a wellbore casing (or casings). A vertical slice through a representative wellbore is shown schematically in Figure 2.2.1. The model includes steel casing(s); cement surrounding the casing(s); and formation rock around everything. Displacement boundary conditions arising from slippage along the interbeds in the Global Mine Excavation Model are imposed on the boundaries of the Wellbore Model to simulate shearing and parting along a bedding plane cutting through the well axis. The bedding is treated as a “slip surface” at the top or bottom of a layer. The results of this model are used to evaluate the potential for casing and cement damage, and to assess the state of stress in the surrounding formation rock.

2.2.1. Assumptions

There were various assumptions made in developing this model that need to be highlighted:

- only two specific cases of what are understood to be generic, but typical, existing well completion scenarios (one single cased and one double cased) were examined;
- in these, the casing is assumed to be perfectly centered in the borehole and bonded to the cement (asymmetry of the casing within the borehole would result in a thinner cement annulus on one side relative to the other, with unknown but potentially debilitating effects on the overall strength of the composite, casing/cement, cross-section);
- the cement is assumed to be perfectly bonded to the surrounding rock formation;
- all materials are assumed to be homogeneous and isotropic,
- the cement can be adequately represented using “Conventional Strength Portland Concrete” properties, particularly for post-yield response (e.g., can carry compressive stresses but not tensile stresses, etc.);
- no account for hardening, post-yield, in the steel is considered (an elastic/perfectly-plastic material model is used);
- the bedding is treated as a planar “contact surface” which is consistent with in which these were modeled in validation against experimental room data for the WIPP (Munson and DeVries, 1990; Munson et. al, 1990; Munson, 1997); and

- loading from the slippage on the contact surface induced by the Global Mine Excavation Model and initial stresses in the configuration are the only loadings considered.

2.2.2. Idealization of the Wellbore Section

The 3D idealized wellbore configuration for the single casing simulations is shown in Figure 2.2.2. Overall the model extends 15 wellbore diameters (15 Φ) in the vertical and horizontal directions. Invoking symmetry, only half of the cylindrical configuration need be included.

For the single casing model, a single specific example has been analyzed for this study; a 35.7 kg/m (24 lb/ft) K55 casing in a 0.2794 m (11 in.) borehole. Thus, as shown in the zoomed portion of the figure (the upper materials have been removed for clarity), the wellbore diameter is assumed to be 0.2794 m (11 in.) and the casing has an outer diameter of 0.2191 m (8 5/8 in.). The wall thickness used for the casing was 6.71 mm (0.264 in.). From the wellbore and outer casing dimensions, the resulting cement thickness used was 30.2 mm (1 3/16 in.).

The 3D idealized wellbore configuration for the double casing simulations is shown in Figure 2.2.3. Once again, the overall model extends 15 wellbore diameters (15 Φ) in the vertical and horizontal directions. As was the case for the single casing model, a single specific example of a double casing situation has been analyzed for this study; a 35.7 kg/m (24 lb/ft) K55 casing, concentric within a 71.4 kg/m (48 lb/ft) K55 casing, within a 0.445 m (17 1/2 in.) borehole.

Thus, as shown in the zoomed portion of the figure (the upper materials have again been removed for clarity), the wellbore diameter for this case is assumed to be 0.4445 m (17 1/2 in.). The inner casing has an outer diameter of 0.2191 m (8 5/8 in.) and the outer casing having an outer diameter of 0.3397 m (13 3/8 in.). The wall thicknesses used for the two casings were 6.71 mm (0.264 in.) for the inner casing and 8.38 mm (0.33 in.) for the outer casing. From the wellbore and outer casing dimensions, the resulting cement thicknesses used were 52.39 mm (2 1/16 in.) for the outer ring of cement and 51.94 mm (2.045 in.) for the inner ring.

2.2.2.1. Materials

The three materials comprising the wellbore configuration, namely the steel, cement, and surrounding rock were modeled numerically using three different constitutive models. The K55 steel was modeled with an elastic-plastic constitutive model. The cement was modeled with the Sandia Geomodel, a generalized cap-plasticity model. The surrounding formation was modeled as an elastic material.

2.2.2.2. Constitutive Models/Parameters

The elastic-plastic model used here is based on a standard von Mises type yield condition and uses combined kinematic and isotropic hardening, in the most general case. This model is widely used in many finite element computer programs and the many details of its derivation and implementation are scattered throughout the literature (e.g., Krieg and Krieg, 1977 and Schreyer et. al, 1979). Flanagan and Taylor, 1989, provide details of the model, as implemented within the SNL codes. For purposes of the calculations herein, hardening was not allowed, thereby rendering the model to be elastic perfectly-plastic. Table 6 shows the K55 steel material parameters used in the calculations for the elastic-plastic model.

Table 6. Elastic-Plastic Material Model Parameters used for K55 Steel

Young's Modulus, E	Poisson's Ratio, ν	Yield Stress	β (Isotropic/Kinematic Hardening Parameter)	Hardening Modulus
1.999×10^{11} Pa (29.0×10^6 psi)	0.33	4.277×10^8 Pa (62,000 psi)	0.5	0.0

The overarching goal of the Sandia Geomodel developed by Fossum and Brannon is to provide a unified general-purpose constitutive model that can be used for any geological or rock-like material that is predictive over a wide range of porosities and strain rates. The details of the Sandia Geomodel, which is implemented in JAS3D, are provided in Fossum and Brannon, 2004. Being a unified theory, the Sandia Geomodel can simultaneously model multiple failure mechanisms or it can duplicate simpler idealized yield models such as classic Von Mises plasticity and Mohr-Coulomb failure (by using only a small subset of the available parameters). For natural geomaterials, as well as for some engineered materials (e.g., ceramics and concretes), common features are the presence of microscale flaws, such as porosity, and networks of microcracks. The former (microscale flaws) permit inelasticity even in purely hydrostatic loading. The latter (networks of microcracks) lead to low strength in the absence of confining pressure and to noticeable nonlinear elasticity, rate-sensitivity, and differences in material deformation under triaxial extension when compared to triaxial compression. Simpler models that do not include this phenomenology are incapable of accurately predicting the response of rock-like materials such as the cement.

Because of lack of actual data on Lite/Class C cement to generate the appropriate parameters for the Sandia Geomodel, the cement material response in the calculations was modeled using the parameters given in Fossum and Brannon, 2004, Appendix B for "Conventional Strength Portland Concrete." Table 7 shows the material parameters for the Sandia Geomodel used in the calculations to simulate the cement. The parameters B0 and G0 given in the table correspond to the elastic bulk and shear modulus, respectively. These values convert to a corresponding Young's modulus, E, of 18.405 GPa (2.67×10^6 psi) and Poisson's ratio, ν , of 0.22, which is on the order of the elastic properties for a Lite/Class C cement ($E=3.8 \times 10^6$ psi and $\nu=0.19$). While it is recognized that the simulant

contains aggregate and is a different material than Lite/Class C cement, from a purely elastic response point-of-view, the Sandia Geomodel and parameters used should adequately simulate the cement. The post-yield response of this representation for the cement is dictated by the remaining parameters below as determined for a Conventional Strength Portland Concrete with an initial porosity of ~6.5%. The unconfined compressive strength for this concrete is 27.6 MPa (4,000 psi).

Table 7. Sandia Geomodel Parameters used for Cement

Parameter	Value	Parameter	Value	Parameter	Value
B0	1.0954×10^{10} Pa (1.59×10^6 psi)	A1	4.26455×10^8 Pa (61,900 psi)	CTPS	1.0×10^6 Pa (145 psi)
B1	0.0 Pa	A2	7.51×10^{-10} Pa ⁻¹ (5.18×10^{-6} psi ⁻¹)	T1	0.0 s
B2	0.0 Pa	A3	4.19116×10^8 Pa (60,800 psi)	T2	0.0 s ⁻¹
B3	0.0 Pa	A4	1.0×10^{-10} Radians	T3	0.0
B4	0.0	P0	-1.95520×10^8 Pa (-28,400 psi)	T4	0.0 s ⁻¹
G0	7.5434×10^9 Pa (1.09×10^6 psi)	P1	1.2354×10^{-9} Pa ⁻¹ (8.52×10^{-6} psi ⁻¹)	T5	0.0 Pa
G1	0.0	P2	0.0 Pa ⁻²	T6	0.0 s
G2	0.0 Pa ⁻¹	P3	0.065714	T7	0.0 Pa ⁻¹
G3	0.0 Pa	CR	12.0	J3TYPE	3
G4	0.0	RK	1.0	A2PF	0.0 Pa ⁻¹
RJS	0.0 m	RN	0.0 Pa	A4PF	0.0 Radians
RKS	0.0 Pa/m	HC	0.0 Pa	CRPF	0.0
RKN	0.0 Pa/m	CTI1	3.0×10^6 Pa (435 psi)	RKPF	0.0
				SUBX	0.0

The surrounding material was assumed to be within the Salado Formation; hence the material was modeled as salt. Because the slippage at the interbeds in the Global Mine Excavation Model occurs over a relatively short time-frame (less than a year), the material was modeled as a time-independent elastic material. The elastic parameters used

for the salt were $E=31.0$ GPa (4.495×10^6 psi) and $\nu=0.25$, as recommended in Krieg, 1984.

2.2.2.3. Contact Surface Parameters

A contact surface was used to model the interbed in the surrounding rock; the cement and casing were continuous as they pass through the interbed. As was the case with the contact surfaces used in the Global Mine Excavation Model, this contact surface is modeled such that if $\tau < \mu|\sigma|$ then no slip occurs and if $\tau = \mu|\sigma|$ then slip takes place and τ is limited to this value ($\mu|\sigma|$). In the foregoing, τ is the shear stress acting across the interbed, σ is the stress normal to the interbed, and μ is the coefficient of friction in the interbed. The friction coefficient used on the contact surface was a value of 0.2, which is consistent with the baseline value used in the Global Mine Excavation Model. Furthermore, it should be noted that this value of friction coefficient is also consistent with that used for model validation of the WIPP experimental rooms (Munson and DeVries, 1990; Munson et. al, 1990; Munson, 1997).

2.2.3. Three-Dimensional Computational Model of the Wellbore

2.2.3.1. Approaches Considered in Modeling

In the process of developing the Wellbore Model, several approaches were assessed for viability in performing the numerical simulations. These differed mainly in how initial and boundary conditions on the idealized configuration should be incorporated and what types of loading were meaningful and appropriate. For example, should the top of the model have an applied normal traction or should it be prevented from displacing in the normal direction; should initial stresses in the surrounding formation be included; should the marker beds have a finite thickness versus how they have been typically modeled for WIPP applications (e.g. Munson and DeVries, 1990; Munson et. al, 1990; Munson, 1997), as infinitely thin; etc.? Ultimately, the models described in the subsections below were adopted and used to model the single and double casing situations.

2.2.3.2. Single Casing

The 3D computational mesh of the idealized wellbore configuration for the single casing simulations is shown in Figure 2.2.4. The boundary conditions used in the simulations are also shown. Essentially, the perimeter of the surrounding formation below the interbed was fixed against displacing in a direction normal to it. The perimeter of the surrounding formation above the interbed was prescribed to move in the X-direction, only, as a function of time (as indicated by the arrow) to simulate the interbed slippage. The displacement in the X-direction was linearly increased from zero to a value of 25 mm (~1.0 in) over the simulation period. In addition, for this upper portion, no Z-displacement was allowed along the side and no Y-displacement was allowed on top.

In addition to the imposed interbed slippage, the surrounding formation and the cement were assumed to have an initial stress equal to the lithostatic stress at a depth of 160 m (486.4 ft). This is consistent with the nominal depth of Marker Bed 101 in the 304.8m (1000 ft) deep mine. The maximum slip occurs at this depth per the Global Mine Excavation Model (Section 3.1). Thus the vertical stress was computed by using the weight of the overburden at this depth, assuming a nominal value of 22,620 Pa/m (1 psi/ft), and the horizontal stresses were also set equal to the same value. The computational finite element mesh contained ~612,000 elements and ~636,000 nodes.

2.2.3.2. Double Casing

The 3D computational mesh of the idealized wellbore configuration for the double casing simulations is shown in Figure 2.2.5. The boundary conditions used in the simulations are also shown, and are identical to the ones used for the single casing simulations described above. Similarly, the same initial stresses as described above for the single casing model were used for the double casing model. For the double casing model, the computational finite element mesh contained ~791,000 elements and ~818,000 nodes.

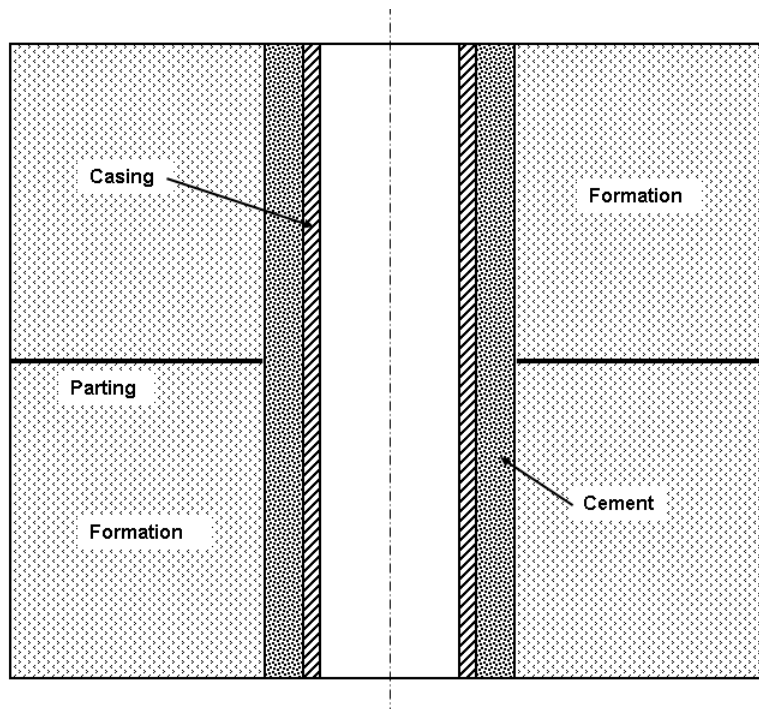


Figure 2.2.1. Schematic of Wellbore Model.

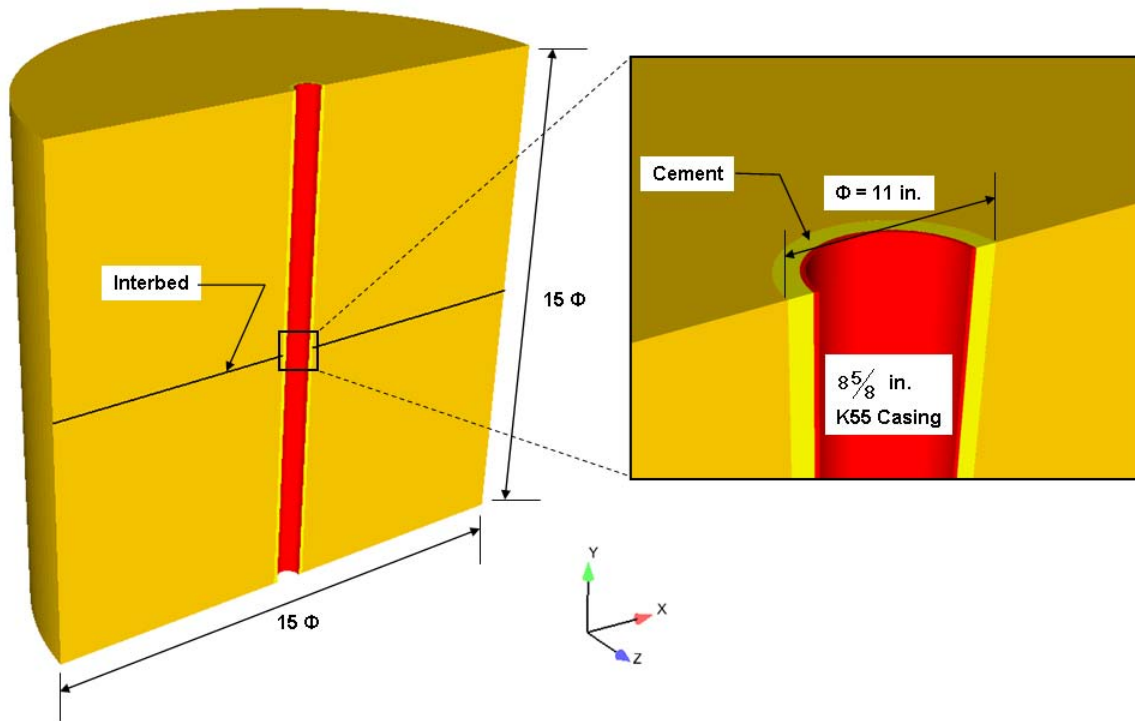


Figure 2.2.2. Idealized 3D Configuration for Single Casing Model

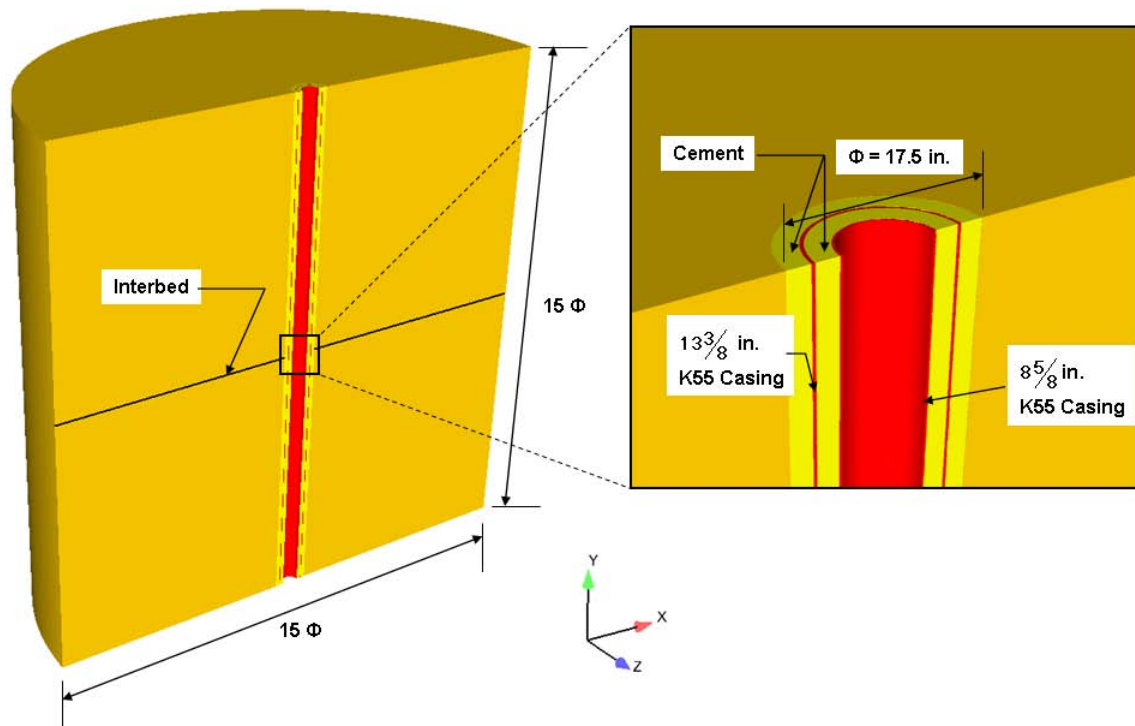


Figure 2.2.3. Idealized 3D Configuration for Double Casing Model

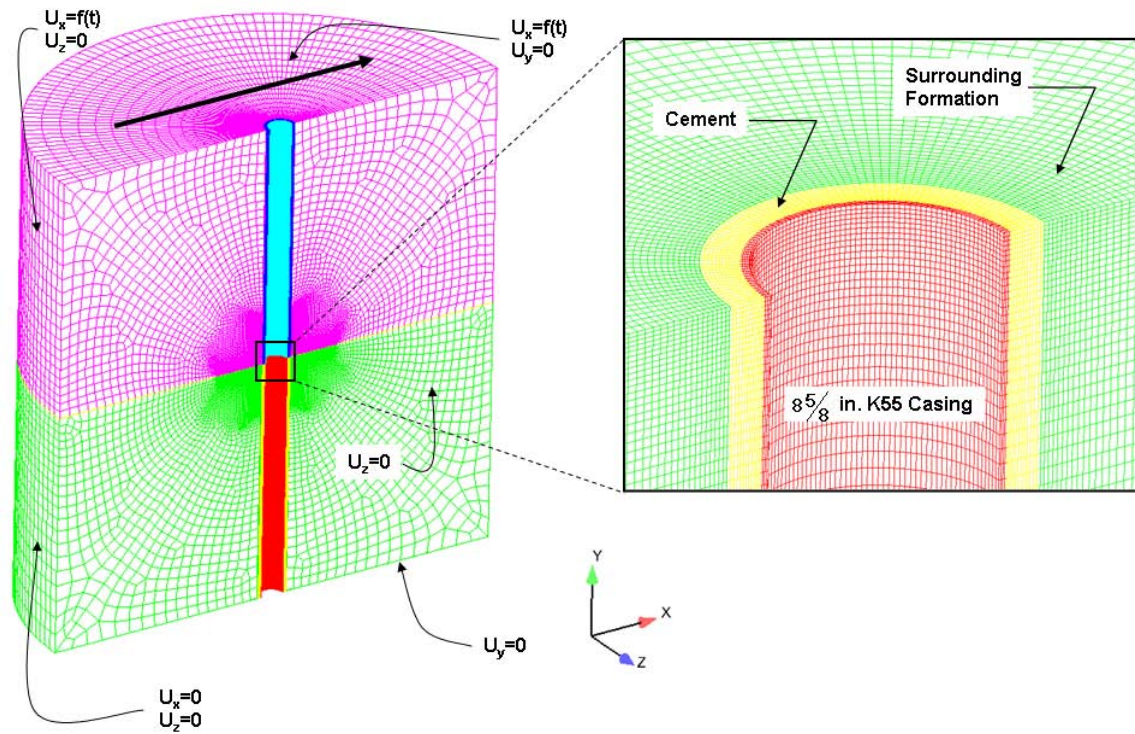


Figure 2.2.4. Computational Mesh and Boundary Conditions on Idealized 3D Configuration for Single Casing Model

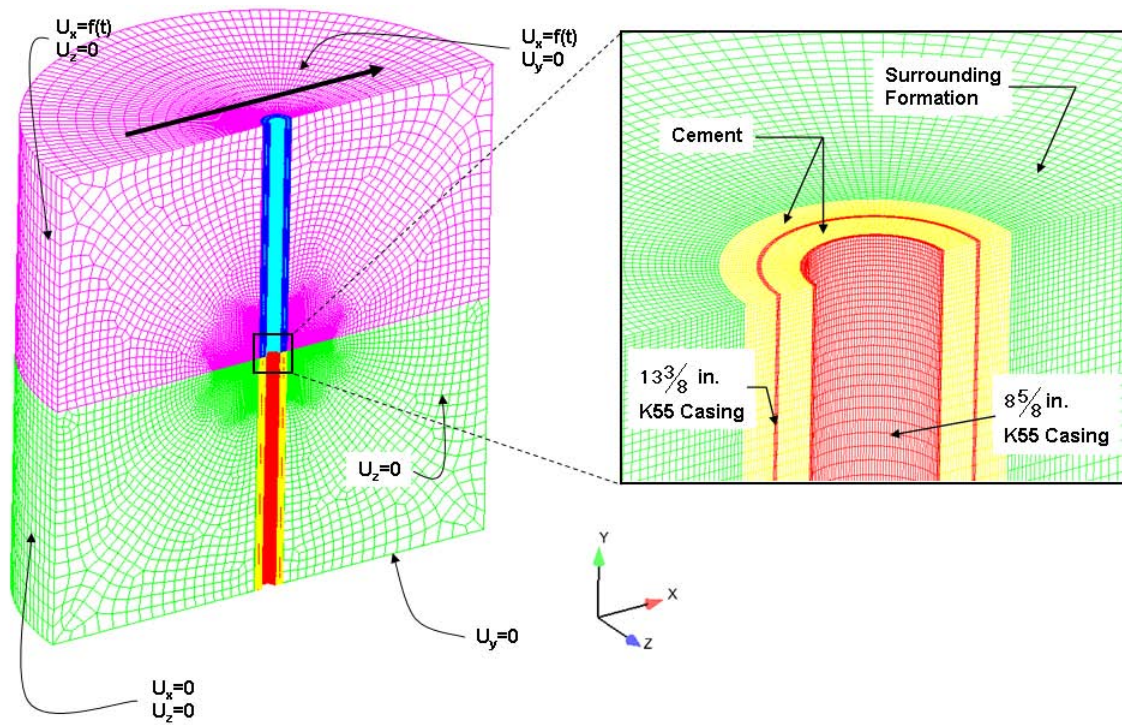


Figure 2.2.5. Computational Mesh and Boundary Conditions on Idealized 3D Configuration for Double Casing Model

3. Results

3.1. Global Mine Excavation Model Results

The results presented in this section provide estimates of the magnitude of slip, as a function of distance from the mine edges. The plane strain model is representative of the case where the mine is large in the out-of-plane direction (Z). The plane strain configuration used in these analyses would be expected to provide greater slip magnitudes when compared to general three dimensional simulations provided all other model attributes (e.g. mine length and constitutive properties) are the same.

These results in conjunction with the analysis of wellbore response described in Section 3.2 will be used to provide information on standoff distances between potash mines and oil and gas wells.

For each of the mine depths (304.8 m or 1000ft and 609.6 m or 2000 ft), the mining rate and length of mine excavation were varied to see what effect these variables have on the slip magnitude. Each calculation simulated a time period of 25 years from the start of mining. The 25 year time period was sufficient to capture all significant mining and subsidence related deformation.

In these simulations, mining occurs from left to right so interface slip at points located to the left of the mine excavation are those presented in the **mining away from well scenario** and those to the right of the mine edge are presented in the **mining towards the well scenario**. These concepts are illustrated in Figure 3.1.1.

The data processing steps used to produce the magnitude of slip versus distance are the same for each of the mine models. First, the slip at each interface node is recorded over the 25 year simulation time. Since the direction of slip, as indicated by the sign (positive or negative), may vary with position and time it is necessary to choose the absolute maximum slip at each node location. This is carried out in the following sequence of steps. From these results a maximum slip envelope can be determined.

Step 1) For each node on a marker bed interface, store the maximum (S_{\max}) and the minimum (S_{\min}) values of slip during the 25 year simulation time period.

Step 2) For each node on marker bed interface, calculate the absolute maximum slip, $\max(|S_{\max}|, |S_{\min}|)$. Note that in this step the direction of the maximum slip is disregarded because the result is always non-negative.

Step 3) For each mine excavation length and excavation rate, calculate the absolute maximum slip versus distance from the edges of the excavation over all marker beds.

Step 4) Calculate the absolute maximum slip over all combinations of mine excavation lengths and excavation rates. This is the maximum slip envelope that will be used to determine the standoff distances between mine and wells.

3.1.1. 1000 foot mine model

The results shown in Figures 3.1.2 through 3.1.7 are based on the case of a 1.6 km (1 mile) mine excavation with excavation rate of 1.6 km/year (1 mile/year). Figure 3.1.2 illustrates the interface slip calculated for MB 101, the uppermost marker bed included in the models. The individual curves represent the slip on this marker bed at times equal to 0.25, 0.5, 0.75, 1.0, 2.0, 5.0, and 25 years. It is clear that slip continues at some locations near the edge of the mined region even after the end of mining due to the creep of the Salado salt formation; however, the rate of slip is decreasing. The locations approximately 300 m (984 ft) beyond the edge of the mine boundaries do not slip after the excavation is complete at 1 year.

Figure 3.1.3 shows the maximum slip calculated for MB 101 (step 1 above) as a function of distance from the left boundary of the mesh ($X = -3.2 \text{ km} = -2 \text{ miles}$). This figure illustrates the regions where the maximum slip is positive and negative. For this marker bed the predicted maximum slip occurs near the start and end of the excavation though the simulations also predict that there is significant slip over a large region directly above the mined area for this marker bed. There are two locations at which the maximum slip shows a large jump. The first occurs approximately 2800 m (9186 ft) and the second occurs at 4100 m (13451 ft) from the left mesh boundary. These locations correspond to points where the slip changes direction or sign and indicates a location where the maximum slip is effectively zero.

Figure 3.1.4 shows the absolute maximum slip calculated for MB 101 (step 2 above). All the slip magnitudes in this figure are now positive and the direction of slip recorded in Figure 3.1.3 has been effectively removed from the figure. The direction of slip is not important to the well casing analysis as only the magnitude of slip is needed. For this marker bed the maximum calculated slip in the region over the excavation varies between 0.14 m (0.46 ft) and 0.55 m (1.8 ft).

Figure 3.1.5 shows the absolute maximum slip on all the marker beds for the 1.6 km (1 mile) mine excavation with excavation rate of 1.6 km/year (1 mile/year). It is clear from Figure 3.1.5 that the slip at nearly every location on MB 101 is greater than the slip at any corresponding location for the other marker beds.

Figure 3.1.6 is the maximum slip envelope (step 3 above) for the mining towards the well scenario and Figure 3.1.7 is the maximum slip envelope for the mining away from the well case for the case of a 1.6 km (1 mile) mine excavation with excavation rate of 1.6 km/year (1 mile/year).

It is now possible to examine the effect of mine excavation length and mining rate on the maximum slip envelope for the mining towards and mining away from the well scenarios. These comparisons are provided in Figures 3.1.8 and 3.1.9. These figures show that

close to the mine face the 0.8 km (0.5 mile) mine excavation cases give larger slip while further away the 1.6 km (1 mile) mine excavation provides larger slip magnitudes. For the mining towards the well scenario (Figure 3.1.8), the slower mining rate (0.48 km/year or 0.3 miles/year) simulations produce greater slip close to the mine face but beyond 400 m (1312 ft) the differences do not appear to be significant. For the mining away from the well scenario (Figure 3.1.9) the higher mining rate simulations produce greater slip close to the mine face but little difference beyond 400 m (1312 ft). In general, at distances greater than about 300 m (984 ft) from the mine face the larger mine excavations produce the greater slip.

Finally, the maximum slip envelope can be determined by taking the maximum slip over the four mining length and mining rate scenarios. These results are presented in Figure 3.1.10 for the cases of mining towards and mining away from the well. From the edge of the mine to about 140 m (459 ft) there is not much difference when comparing the mining away and mining towards the well cases. Beyond 140 m (459 ft) greater slip is calculated for the mining towards the well case.

While this study has primarily focused on slip occurring away from the mined area it must be noted that there is substantial slip predicted in the area directly over the excavation. This poses questions about the impact of interface slip on the existing wells in regions where mining has already occurred.

3.1.2. 2000 foot mine model

These results shown in Figures 3.1.11 and 3.1.12 are based on the case of a 1.6 km (1 mile) long 609.6 m (2000 ft) deep mine with excavation rate of 1.6 km/year (1 mile/year). Figure 3.1.11 illustrates the interface slip calculated for MB 101. As was the case in the 304.8 m (1000 ft) deep mine simulation, the predicted maximum slip on this marker bed occurs near the start and end of the excavation. There are some notable differences in the predicted slip along MB 101 when comparing the mines at the two depths (compare with Figures 3.1.2 for the 304.8 m, or 1000 ft, deep mine case). For example, for locations to the left of the left most edge of mine, the 304.8 m (1000 ft) deep mine shows a definite transition point separating positive and negative slip magnitudes, corresponding to different slip directions, while the 609.6 m (2000 ft) mine model predicts only negative slip approaching the edge of the mine. At the other edge of the mine there is a transition point between positive and negative slip for both 304.8 m (1000 ft) and 609.6 m (2000 ft) deep mine cases though the absolute magnitude of slip is reduced in the 609.6 m (2000 ft) deep mine case. Another difference that can be observed is that directly over the 609.6 m (2000 ft) deep mine the maximum positive slip on MB 101 increases with time while in the 304.8 m (1000 ft) deep mine the maximum positive slip decreases between 0.25 and 1 year but increases after 1 year.

Figure 3.1.12 shows the absolute maximum slip on all of the marker beds. Figure 3.1.12 shows that the slip on MB 101 at nearly every location outside the mine boundaries is greater than the slip at any corresponding location for the other marker beds. This result is similar to that seen in Figure 3.1.5 for the 304.8 m (1000 ft) deep mine. Above the mine excavation a maximum slip of approximately 1.4 m (4.6 ft) occurs on MB 109 in a

region near the center of the mine while in the 304.8 m (1000 ft) deep mine the maximum slip was approximately 0.55 m (1.8 ft) on MB 101 and occurred near the edges of the mine.

Figure 3.1.13 is the maximum slip envelope (step 3 above) for the mining towards the well scenario. This figure illustrates the effect of mine length and mining rate for the 609.6 m (2000 ft) deep mine case. The lower excavation rates (0.48 km/year, or 0.3 miles/year) for both the 0.8 km (0.5 mile) and 1.6 km (1 mile) mines produce greater slip out to about 550 m (1804 ft) from the mine edge than the higher 1.6 km/year (1 mile/year) excavation rate. Beyond about 550 m (1804 ft) the 1.6 km (1 mile) long mine excavated at a rate of 1.6 km/year (1 mile/year) produces the most slip.

Figure 3.1.14 is the maximum slip envelope for the mining away from the well scenario. For this scenario, the larger mine length and excavation rates produce the greatest slip magnitudes for all distances.

Figures 3.1.15 combines the results for the various cases shown in Figures 3.1.13 and 3.1.14 to two maximum slip envelopes, one for the mining towards well case and one for the mining away from the well case, for the 609.6 m (2000 ft) deep mine case. For all distances the mining towards the well case produces greater slip.

Figures 3.1.16 and 3.1.17 illustrate the comparison of the 304.8 m (1000 ft) and 609.6 m (2000 ft) cases. Figure 3.1.16 shows that within 450 m (1476 ft) from the mine boundaries the 609.6 m (2000 ft) mine model produces greater slip magnitudes for both the mining towards and mining away from the well scenarios compared to the 304.8 m (1000 ft) mine model. Figure 3.1.17 is a view of the results for distances between 500 m (1640 ft) and 1200 m (3937 ft) from the mine boundaries. The 609.6 m (2000 ft) deep mine model, mining towards well scenario, produces the greatest distance from the mine boundary before no slip is calculated. The slope discontinuity for the 609.6 m (2000 ft) deep mine, mining towards the well case, occurring at approximately 550 m (1804 ft) is due to a transition from the 0.48 km/year (0.3 mile/year) excavation rate case being the dominant one to the 1.6 km/year (1 mile/year) case being the dominant slip predictor both being for the 1.6 km (1 mile) long mine excavation cases.

3.1.3. Sensitivity of Slip Results to Variations of Friction Coefficient and Interface Separation

All of the results shown in the Sections 3.1.1 and 3.1.2 were obtained using a coefficient of friction equal to 0.2. In addition, in all of these calculations the marker bed interfaces were not allowed to separate. In this section we examine separately the impact of selecting higher values of the friction coefficient and allowing interface surface separation and the resulting impact these choices have on the interface slip envelope. For these comparisons the 1.6 km (1 mile) long mine located 304.8 m (1000 ft) below the surface and excavated in 1 year has been taken as the base case to which the slip results from these parameter variation calculations will be compared.

3.1.3.1. Coefficient of Friction

Additional simulations using constant coefficient of friction values of 0.4, 0.6, and 0.8 were performed. Interface separation was not allowed in these calculations. The slip envelopes for the mining away and towards the well cases are shown in Figures 3.1.18 and 3.1.19 respectively. From the results shown in these figures it can be concluded that when the friction coefficient is increased, less slip is predicted and the distance to the location of no slip is reduced. These results agree with our expectation that increased frictional resistance would reduce the amount of slip.

3.1.3.2. Interface Separation

In this calculation the friction coefficient was set to the baseline value of 0.2 but no tension was allowed to develop on the marker bed thus allowing the marker beds to separate. Figures 3.1.20 (mining towards the well) and 3.1.21 (mining away from the well) compare the slip envelope computed when interface separation was allowed to the case where separation was not allowed. Allowing interface separation is seen to reduce the amount of slip calculated and the reduction is more significant in the mining towards the well case.

3.1.4. Comparison with Field Observations

Currently there are no reported field measurements of interface slip from the potash mine area that can be used to validate these model results. However, it may be useful to compare the numerical predictions with typical observations of field behavior to provide some confidence that the global behavior of the model is similar to that observed in the typical potash mine region. Figure 3.1.22 illustrates some of the measurable quantities that have been reported in the literature. These include ground surface strains, subsidence profile, and the angles of break and draw.

3.1.4.1. Ground Surface Subsidence and Angle of Draw

Ground surface subsidence occurs over large mined areas. Over regions where pillars remain and the material extraction ratio is low the observed subsidence is small, typically a few inches. However, over areas that have been retreat mined, with extraction ratios frequently over 75 percent, the subsidence can be greater than two thirds of the mine height. Ground surface subsidence typically continues for 1 to 3 years after mining has completed with the rate of subsidence decreasing after mining ceases.

Figure 3.1.23 illustrates the shape of the calculated subsidence trough after 25 years for the 1.6 km (1 mile) long, 304.8 m (1000 ft) deep mine excavated in 1 year. This figure only shows the Dewey Lake formation and the displacements have been magnified by a factor of 100. The locations of the mine boundary and the areas of tensile (positive values) and compressive (negative values) horizontal normal stress have been identified. The regions of maximum tensile stresses, shown with red contours, occur at the surface just outside the mine boundaries. These are the regions where surface cracks would be expected to be seen. The characteristic tensile and compressive regions are similar for all

mine lengths and mining rate combinations; however, the specific magnitudes of the stresses are different for each case.

Figure 3.1.24 shows the evolution of subsidence for the 304.8 m (1000 ft) deep, 1.6 km (1 mile) long mine excavated in 1 year, expressed as a percentage of the initial mine height (3.05 m, or 10 ft). Figures 3.1.25 and 3.1.26 show the influence of mining rate on the subsidence at 25 years for the 0.8 km (0.5 mile) and 1.6 km (1 mile) long mine excavations. The 0.8 km (0.5 mile) mine does not show the region of near constant subsidence exhibited by the longer mine and the maximum subsidence is somewhat smaller. In general the impact of mining rate on the subsidence predicted at 25 years by the calculations appears small.

Figure 3.1.27 shows the calculated evolution of subsidence for the 609.6 m (2000 ft) deep, 1.6 km (1 mile) long mine while Figures 3.1.28 and 3.1.29 show the influence of mining rate on the subsidence for the 0.8 km (0.5 mile) and 1.6 km (1 mile) long mine 609.6 m (2000 ft) deep cases. For all cases subsidence is essentially complete within a few years of the end of mining. This is consistent with field experience.

Figure 3.1.30 compares the subsidence for the 304.8 m (1000 ft) and 609.6 m (2000 ft) mine cases for the 1.6 km (1 mile) long mine excavated at a rate of 1.6 km/year (1 mile/year) at 25 years. A portion of the ground surface outside the mine boundaries is predicted to rise up (indicated by positive values of subsidence) in the 304.8 m (1000 ft) mine case. This feature is not observed in the 609.6 m (2000 ft) mine results. The subsidence trough for the 609.6 m (2000 ft) deep mine case is larger in lateral extent than that of the shallower 304.8 m (1000 ft) deep mine. The maximum subsidence is a little greater for the 609.6 m (2000 ft) deep mine, 2.5 m (8.2 ft), versus 2.35 m (7.7 ft) in the 304.8 m (1000 ft) mine. In both cases the rate of subsidence decreases after the end of the one year mining phase in agreement with observations. For the 609.6 m (2000 ft) deep mine, these results suggest that the excavation would have to be greater than 1.6 km (1 mile) in length for the subsidence trough to have a similar region of near constant subsidence seen in the 304.8 m (1000 ft) mine case.

It is reasonable to ask what effect the choice of friction coefficient has on surface subsidence and this result is illustrated in Figure 3.1.31. In this figure a comparison is made for the 1.6 km (1 mile) long, 304.8 m (1000 ft) deep mine excavated in 1 year using the friction factors 0.2, 0.4, 0.6, 0.8. Also included in this figure are the results from the calculation where interface separation was allowed in conjunction with the coefficient of friction of 0.2 and another calculation where the interfaces were not allowed to slip or separate. From this figure it may be concluded that the choice of friction coefficient or interface treatment has only a minor effect on the calculated surface subsidence trough.

As shown in Figure 3.1.22 the angle of draw is the angle measured from the vertical line at the edge of the mine excavation to the point on the ground surface at which the subsidence is essentially zero (from a practicality standpoint, *zero* is 0.01 ft \approx 3 mm). From field measurements the angle of draw ranges from about 30 to 55 degrees. Examination of Figures 3.1.25 and 3.1.26 for the 304.8 m (1000 ft) deep mine cases and Figures 3.1.28 and 3.1.29 for the 609.6 m (2000 ft) deep mine cases show that the angle

of draw from the model is somewhat closer to 63 degrees than 55 degrees. This estimate was based on visual estimation from the figures. The difference between the model results and angles computed from field measurements is probably due to the use of an elastic constitutive model for the upper non salt materials. This is discussed further in Section 3.1.4.2.

Through the use of the mining model described in Section 2.2.3.1, subsidence magnitudes produced by the model are consistent with field observations of subsidence. If the excavated region had been treated as an empty cavity, the roof of the mine, in the 1.6 km (1 mile) excavations, would have come into contact with the floor and the maximum surface subsidence would have been approximately 3.05 m (10 ft). While restricting the mine closure to approximately 75% of the initial mine height is consistent with typical subsidence observed above mines it also likely reduces the maximum calculated slip on the interfaces had the full 3.05 m (10 ft) of subsidence been allowed.

3.1.4.2. Ground Surface Strain and Angle of Break

Ground surface strain may be determined by establishing survey markers and measuring the change in horizontal distance between the markers as mining proceeds. Figures 3.1.34 and 3.1.35 show the surface strains computed for the 304.8 m (1000 ft) and 609.6 m (2000 ft) deep mine cases. Both of these figures are for 1.6 km (1 mile) long mines excavated in 1 year. The strain profiles show the progression of a tensile region (positive strain) ahead of the mined region and thus the potential for surface cracks to appear as the mine excavation proceeds to the right. Within the boundaries of the excavation the surface strains are generally compressive.

Tensile strains and stresses occur past the boundaries of the excavation as a result of bending of the surface layer as it subsides. For simulation times after 1 year, when the excavation is complete, the maximum tensile strain decreases due to creep of the salt formation. Figures 3.1.34 and 3.1.35 provide a close up view showing the surface strain variation for the mining towards the well surface locations. Comparing these two figures it is seen that the maximum ground surface tensile strains are slightly greater in the 304.8 m (1000 ft) deep mine case. From the previous examination of surface subsidence we noted that the 304.8 m (1000 ft) deep mine calculation predicted a local region of positive displacement not seen in the 609.6 m (2000 ft) deep mine. This deformation pattern increases the magnitude of the tensile strains near the edge of the excavation in the 304.8 m (1000 ft) deep mine. Since the subsidence trough is larger in the deeper mine case the extent of tensile surface strains is also greater in the 609.6 m (2000 ft) deep mine model.

Field observations have shown that the maximum tensile strain typically varies from 0.04% to 0.09% per foot of subsidence. For a surface subsidence of 2.35 m (7.7 ft) computed in the 304.8 m (1000 ft) deep mine cases the tensile strain range would be 0.003 to 0.0069. The model predictions are 0.0018 and 0.0012 for the 304.8 m (1000 ft) and 609.6 m (2000 ft) deep mines, respectively. The consistent under-prediction of the maximum tensile strain by the numerical model is likely the result of using an elastic constitutive model for the Dewey Lake and Rustler formations. Discrete surface cracks typically observed in the field cannot be replicated with an elastic constitutive law and a

more sophisticated model capable of treating failure or cracking when a principal stress exceeds the tensile strength of the material would be needed.

Field observations have shown that the maximum compressive strain at the surface varies over a range of 0.01% to 0.13% per foot of subsidence over mined area. From Figures 3.1.32 and 3.1.33 it can be seen that the computed surface strains over the mined area are primarily compressive with some tensile strains existing for a short distance within the mined area boundaries. Based on the 2.35 m (7.7 ft) subsidence value computed in the 304.8 m (1000 ft) deep mine case the maximum compressive strain range would be 0.00077 to 0.01. Assuming the survey markers were 12.2 m (40 ft) apart these maximum strains would result from a relative displacement of 0.8 mm (0.03 in.) to 10.2 mm (0.4 in.). At the end of the 1 year excavation phase, the maximum compressive strain was approximately 0.0013 for both the 304.8 m (1000 ft) and 609.6 m (2000 ft) cases. For times greater than 1 year, the maximum compressive strain decreases due to creep relaxation of the salt.

While the model is not capable of accurately predicting maximum tensile surface strain it may be worthwhile to examine the location of the maximum tensile strain. The angle of break (see Figure 3.1.22) is obtained by locating the point where the surface strain is maximized (tensile) after mining is complete. This corresponds to a location where ground surface cracks would be most evident. The angle of break determined from field surveys typically varies between -10 and +20 degrees. A negative value of angle of break would mean the maximum surface strain would occur over the mined region and a positive value means that it would occur outside the mine boundaries. As shown previously in Figures 3.1.32 through 3.1.35, the location of maximum tensile strain varies with time due to the creep of the salt material and in all cases occurs outside the boundary of the mine in these calculations. The predicted angles of break for the two cases described are tabulated in Table 8. The angle of break predicted by the simulations is in general agreement with the stated field observations. Therefore, although the maximum surface strains predicted by the model are low relative to field observations, the locations at which they occur are within the ground surface bounds of the -10 to 20 degrees particularly at the earlier times.

Table 8. Calculated Angle of Break from Models

Time (years)	Angle of Break (degrees)	
	1000 ft deep mine	2000 ft deep mine
1	5	14
2	13	21
5	18	23
25	22	27

Note: These angle of break values were computed for the case of a 1 mile mine excavated in 1 year.

3.1.4.3. Mine Closure

Another feature for comparison is the time it takes for the mine to close following excavation. In this study the mine closure time is calculated as the time for the mine height to reach a state where it is not changing significantly. The mine height varies with lateral (X) position and time and was calculated by computing the vertical distance between points on the roof and floor. Floor heave and roof sag are implicitly accounted for in the mine height calculations.

Field observations indicate that the time required for a mine excavation to close is between 30 and 150 days with the shorter time being attributed to poor ground conditions (see Appendix I section on “Field Measurements and Observations”). The constitutive model for salt creep used in all of these simulations includes only secondary creep effects. It would be expected that including primary creep effects would increase the closure rate and thus decrease the time for mine closure.

Figures 3.1.36 and 3.1.37 compare the ground surface subsidence and mine roof vertical displacement predicted for the 304.8 m (1000 ft) and 609.6 m (2000 ft) cases. In the 304.8 m (1000 ft) deep mine case the roof displacement shows a flat region of near constant displacement near the center of the excavation similar to that calculated for the surface subsidence. In both cases, within the mine boundaries and slightly away from the pillars the roof displacement exceeds the surface displacement except at the center region of the mine.

Figure 3.1.38 shows the mine height as a function of time at three locations for the 304.8 m (1000 ft) and 609.6 m (2000 ft) deep mines. These locations correspond to the quarter point (0.4 km, or 0.25 mile), the center (0.8 km, or 0.5 mile), and three quarter points (1.2 km, or 0.75 mile) for the 1.6 km (1 mile) mine excavated in 1 year. The final mine heights are a little smaller for the deeper mine but there is little difference in the time to closure (100 to 130 days) in terms of location and mine depth.

Figure 3.1.39 shows the mine height as function of time for the 1.6 km (1 mile) long 304.8 m (1000 ft) and 609.6 m (2000 ft) deep mines excavated at the slower rate of 0.48 km/year (0.3 miles/year). These results show that the time for the mine to close is directly related to the mining rate. The lower excavation rate cases take approximately 3.3 times longer to close because the mining rate is 3.3 times smaller. This means that the apparent rate dependence is artificial, and is really just the rate of mine face advance.

Figure 3.1.40 shows the influence of interface properties on the mine closure. These results are for the 1.2 km (0.75 mile) point in the 1.6 km (1 mile) long 304.8 m (1000 ft) deep mine excavated at the rate of 1.6 km/year (1 mile/year). The larger friction coefficient cases reduce the initial closure rate but in general the times to final closure are pretty similar for all cases. The case where interface separation is allowed produces the earliest closure time. The result for the case of no slip provides the upper limit of infinite friction coefficient and produces the longest time to closure. This suggests that the rate of closure is controlled primarily by the structural (bending) response of the material layers above the mine excavation rather than the frictional behavior of the interfaces.

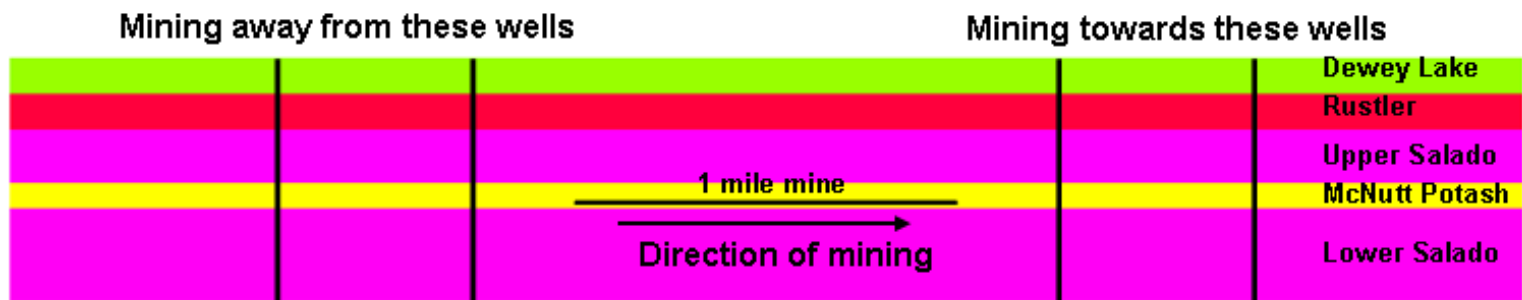
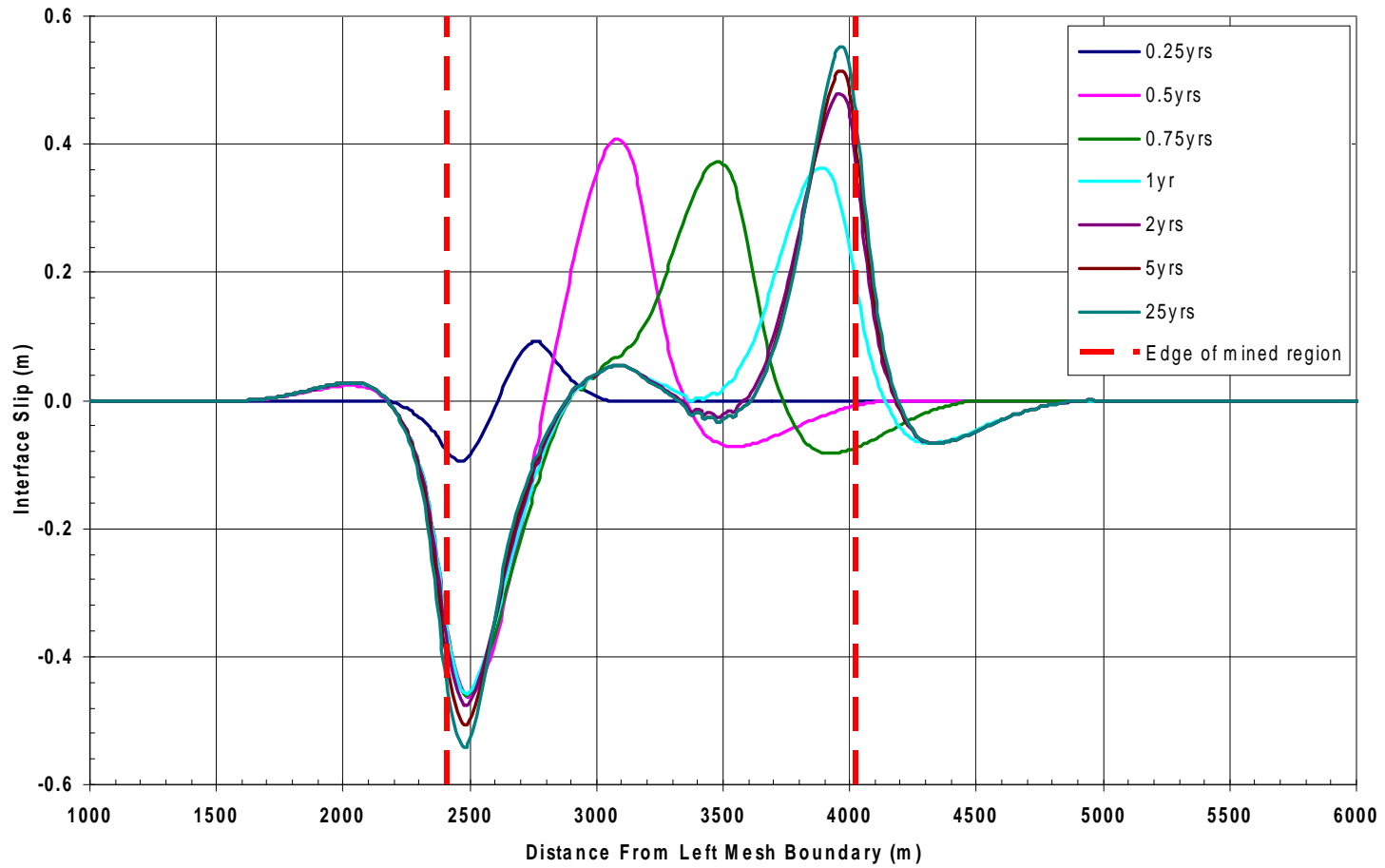


Figure 3.1.1. Mining Orientations Used in Global Model Calculations



**Figure 3.1.2. 304.8 m (1000 ft) Mine Depth: Interface Slip Along MB 101 at Select Times
1.6 km (1 mile) Excavation at Rate of 1.6 km/year (1 mile/year)**

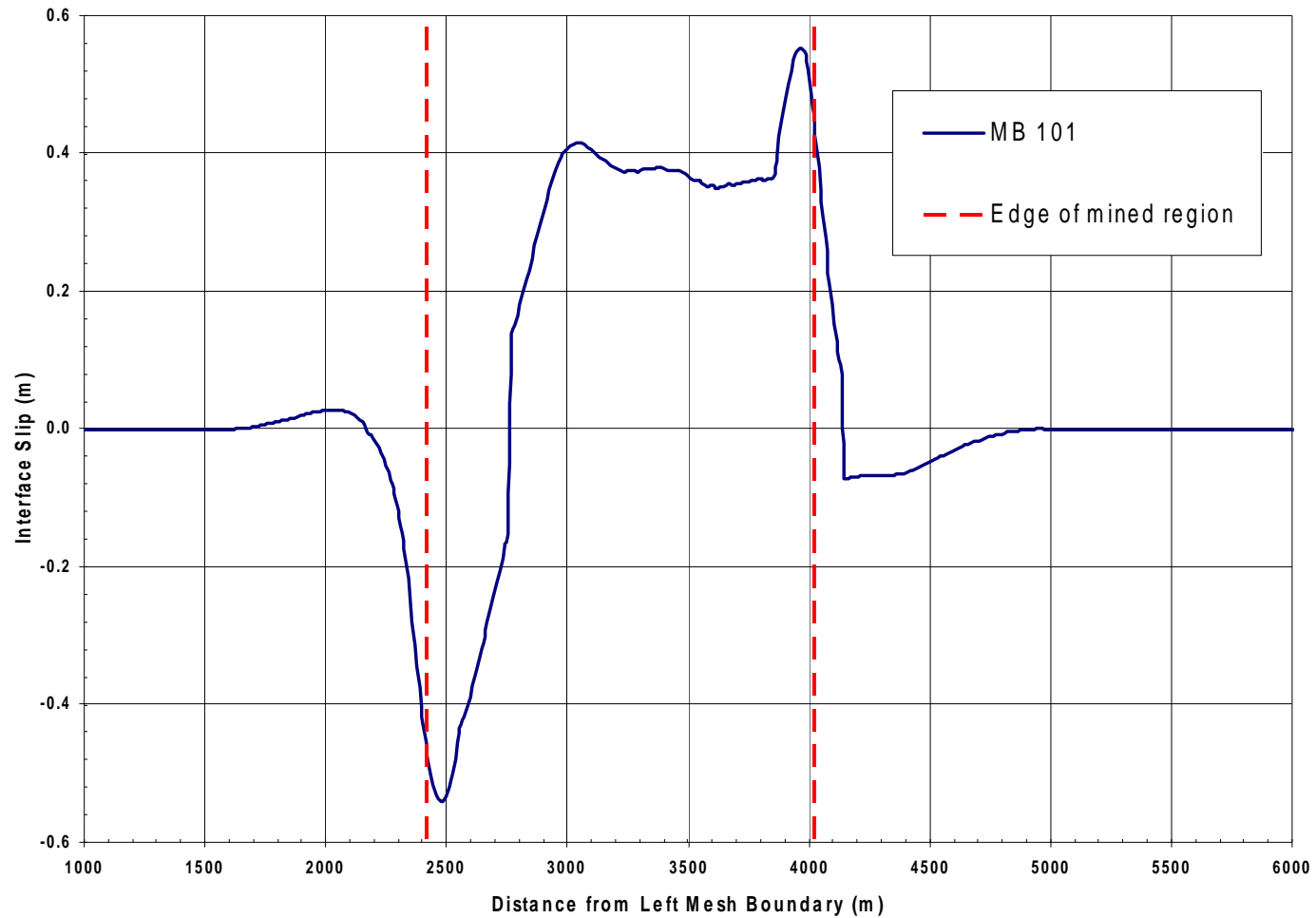


Figure 3.1.3. 304.8 m (1000 ft) Mine Depth: Maximum Interface Slip as a Function of Distance for MB 101 Over 25 year Time Period. (1.6 km, or 1 mile, Excavation at Rate of 1.6 km/year, or 1 mile/year)

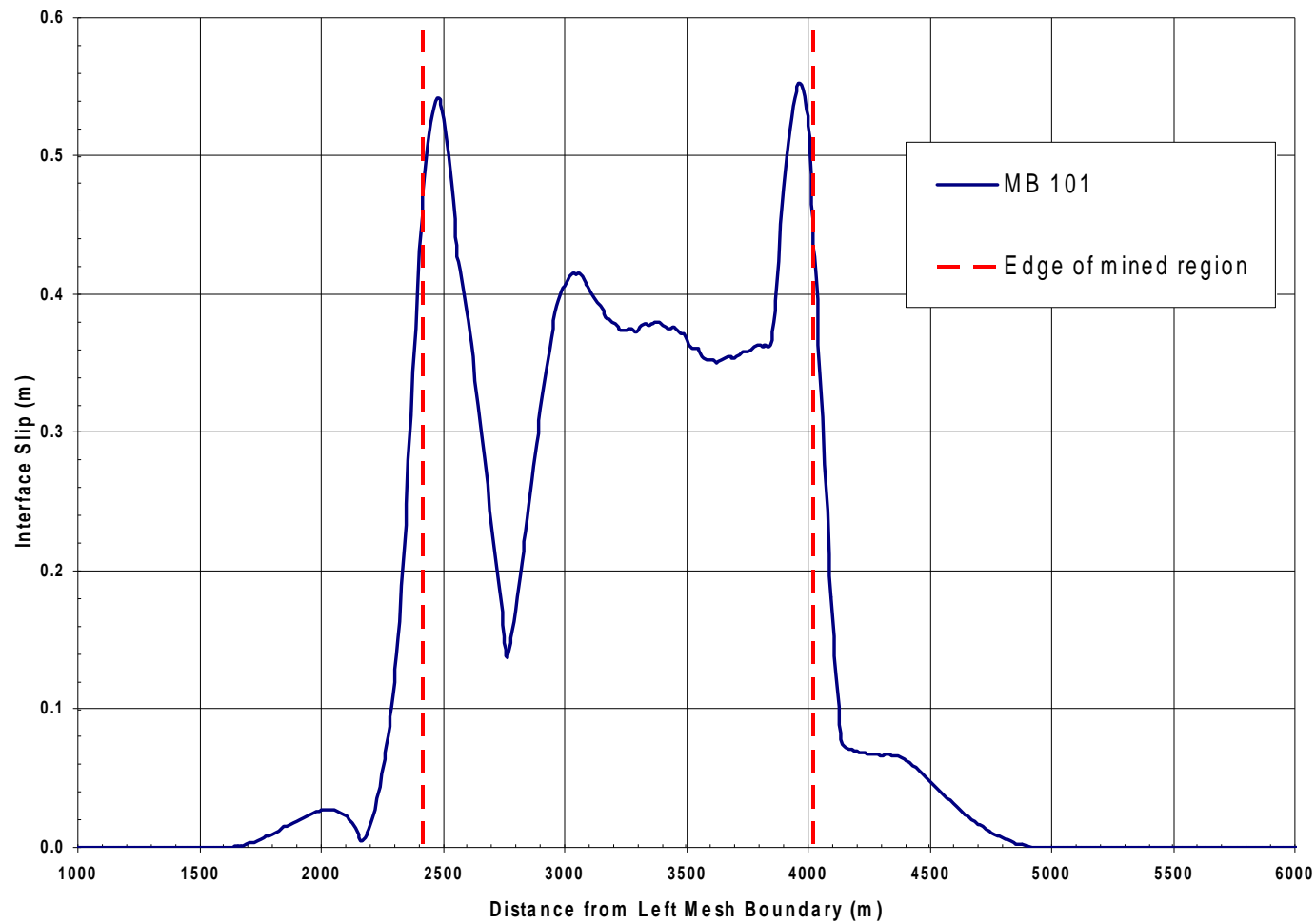


Figure 3.1.4. 304.8 m (1000 ft) Mine Depth: Absolute Maximum Interface Slip as a Function of Distance for MB 101 Over 25 year Time Period. (1.6 km, or 1 mile, Excavation at Rate of 1.6 km/year, or 1 mile/year)

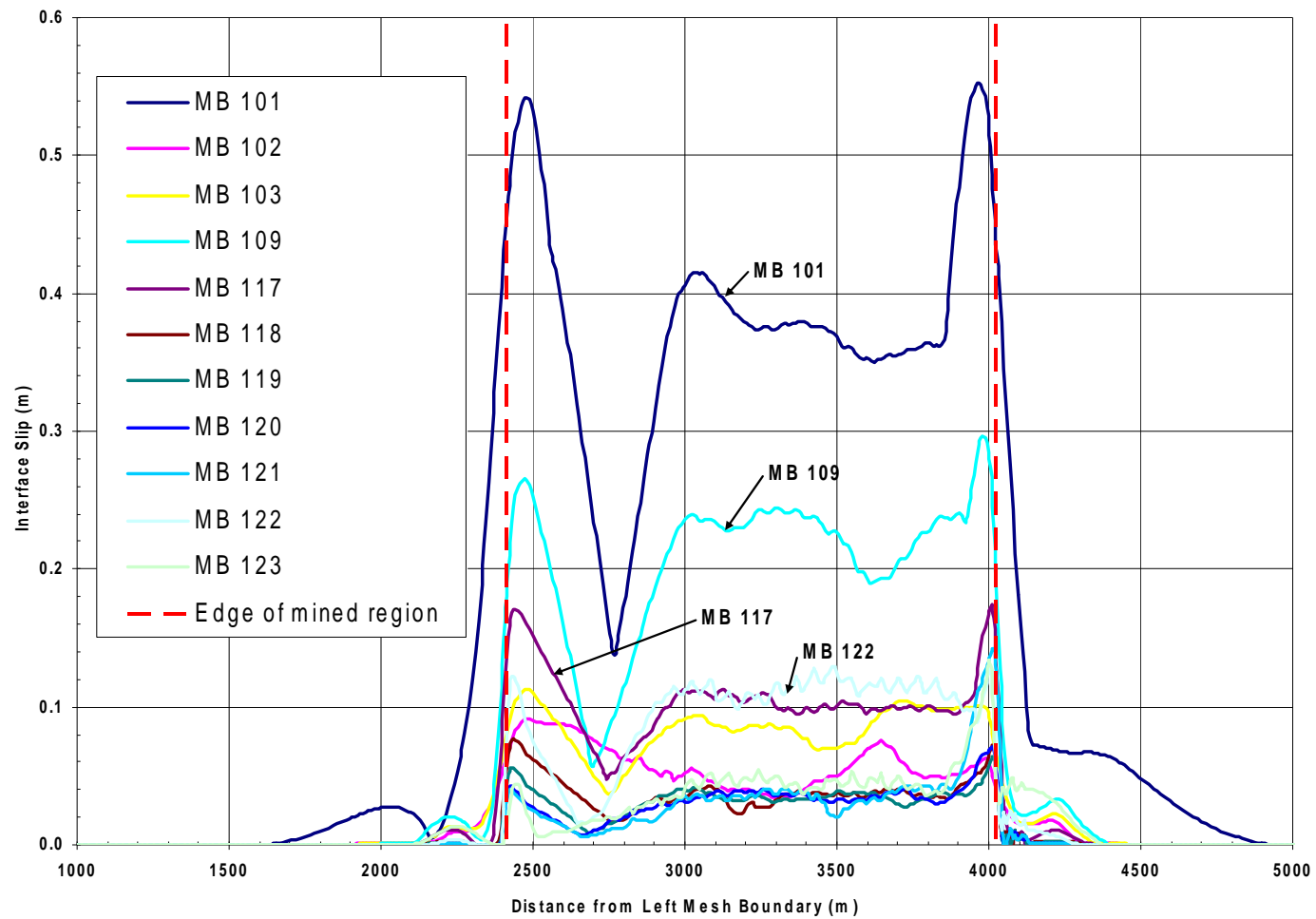


Figure 3.1.5. 304.8 m (1000 ft) Mine Depth: Absolute Maximum Interface Slip as a Function of Distance for All Marker Beds Over 25 year Time Period (1.6 km, or 1 mile, Excavation at Rate of 1.6 km/year, or 1 mile/year)

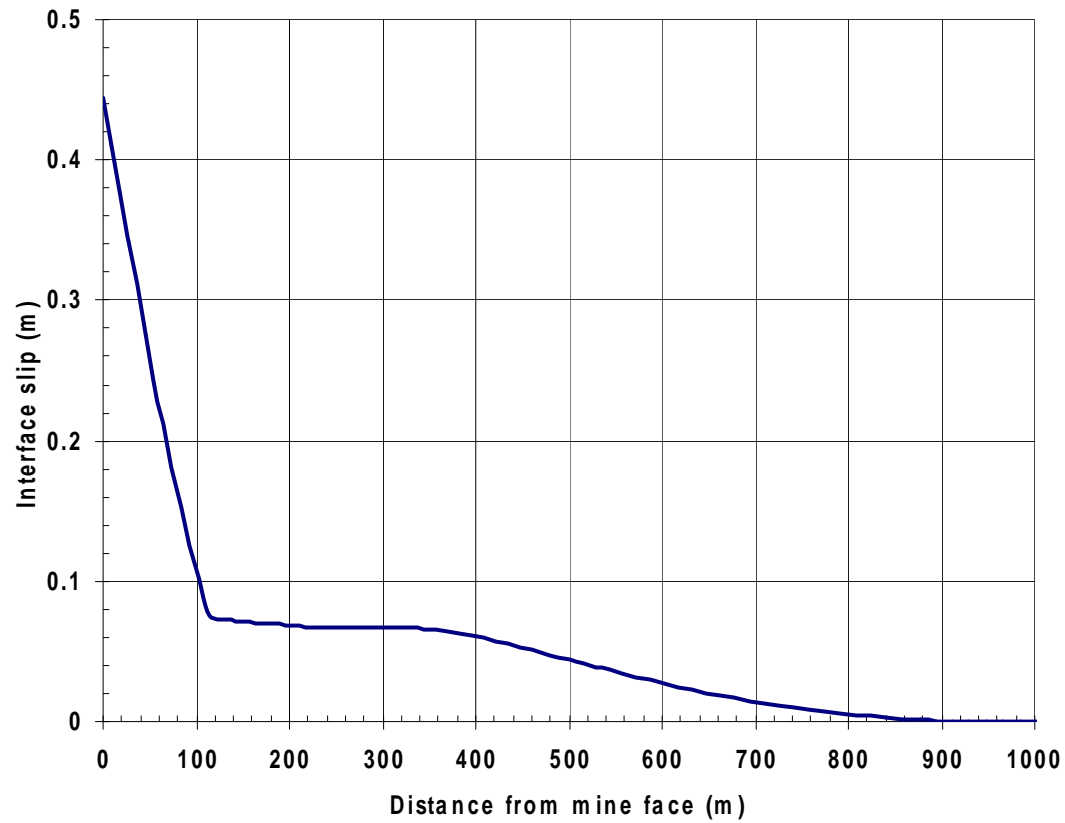


Figure 3.1.6. 304.8 m (1000 ft) Mine Depth: Absolute Maximum Interface Slip Envelope for the Mining Towards Well Scenario (1.6 km, or 1 mile, Excavation at Rate of 1.6 km/year, or 1 mile/year)

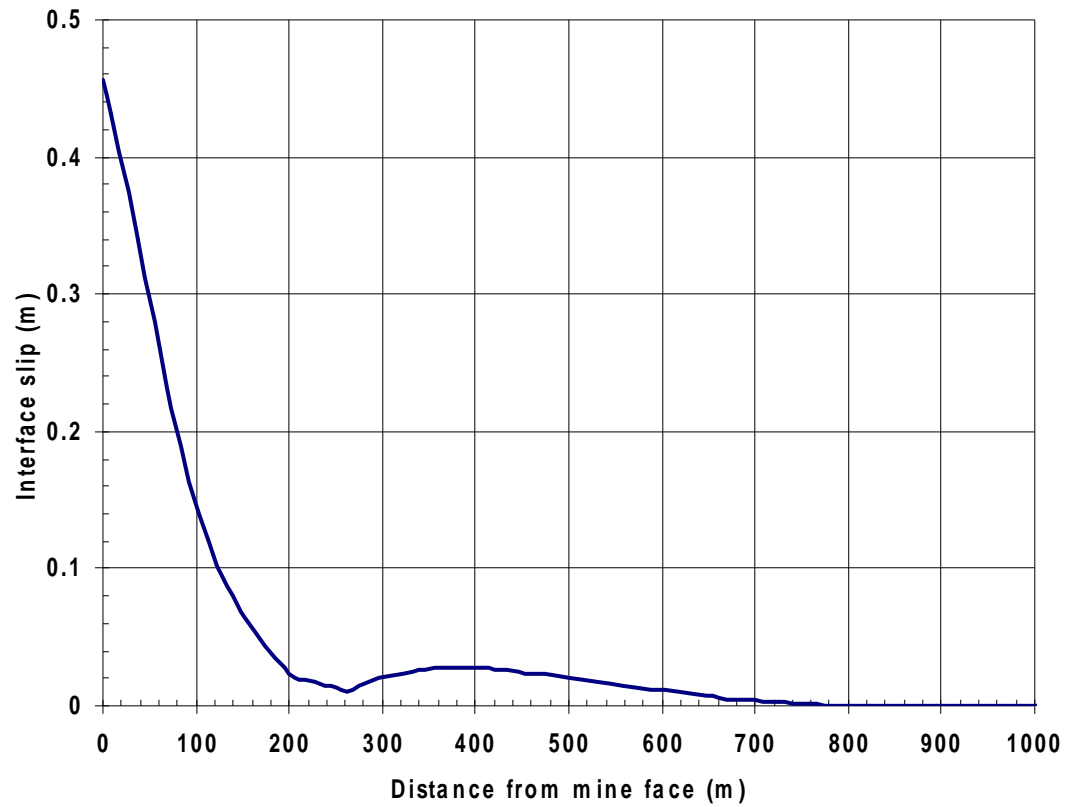


Figure 3.1.7. 304.8 m (1000 ft) Mine Depth: Absolute Maximum Interface Slip Envelope for the Mining Away From Well Scenario (1.6 km, or 1 mile, Excavation at Rate of 1.6 km/year, or 1 mile/year)

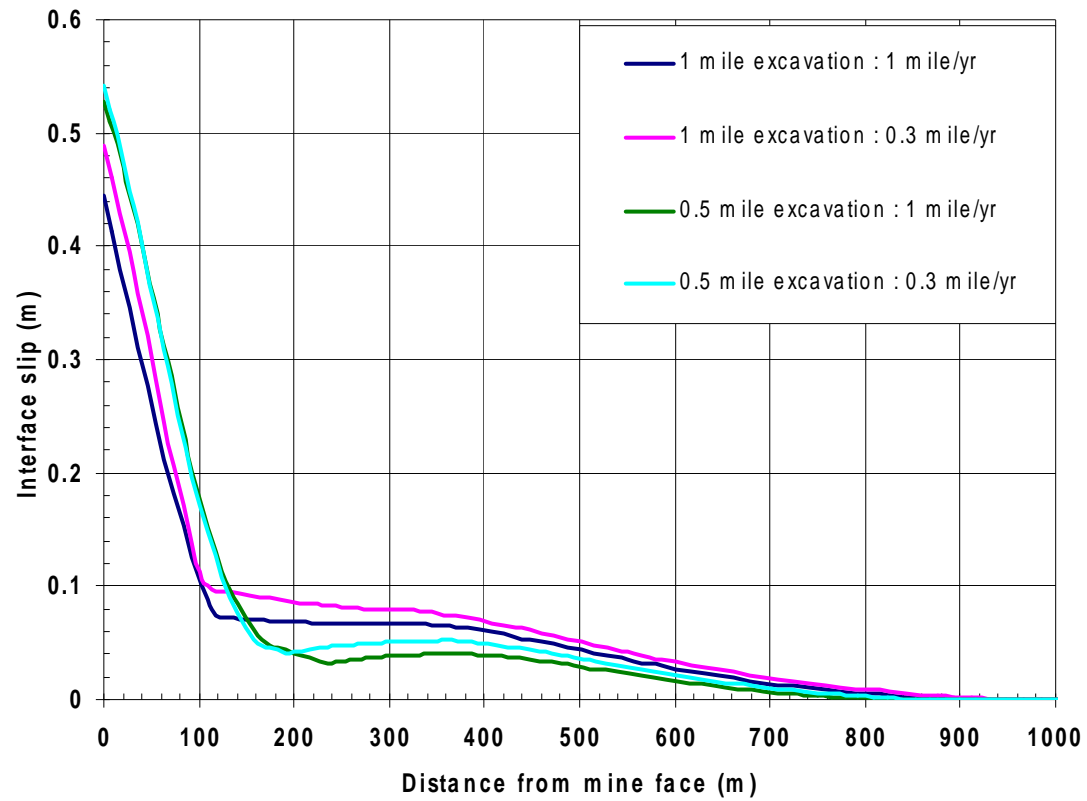


Figure 3.1.8. 304.8 m (1000 ft) Mine Depth: Absolute Maximum Interface Slip Envelope for the Mining Towards Well Scenario (Varying Mine Excavation Sizes and Rates)

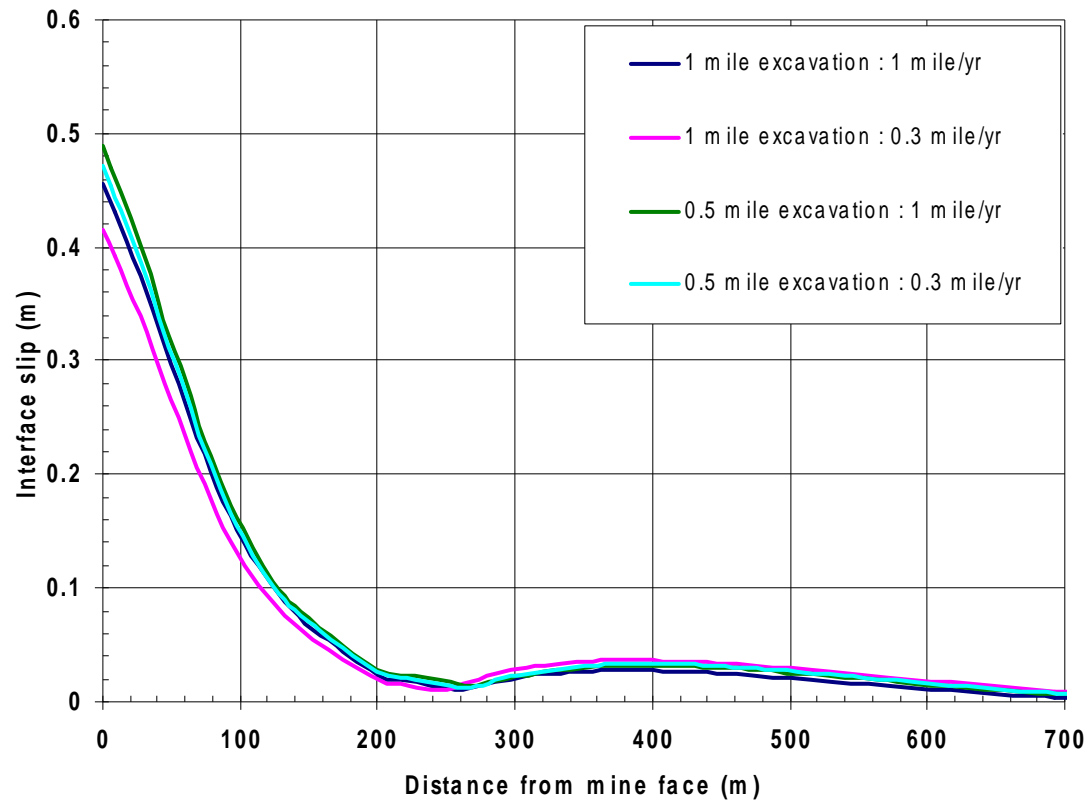


Figure 3.1.9. 304.8 m (1000 ft) Mine Depth: Absolute Maximum Interface Slip Envelope for the Mining Away From Well Scenario (Varying Mine Excavation Sizes and Mining Rates)

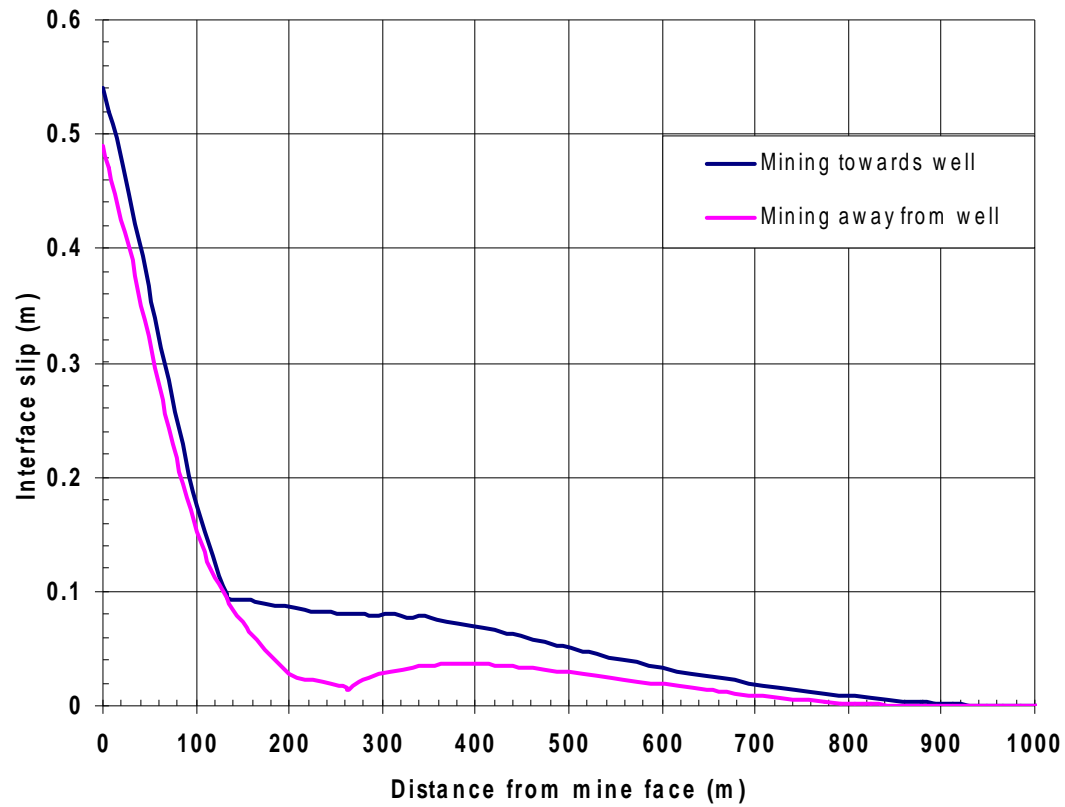
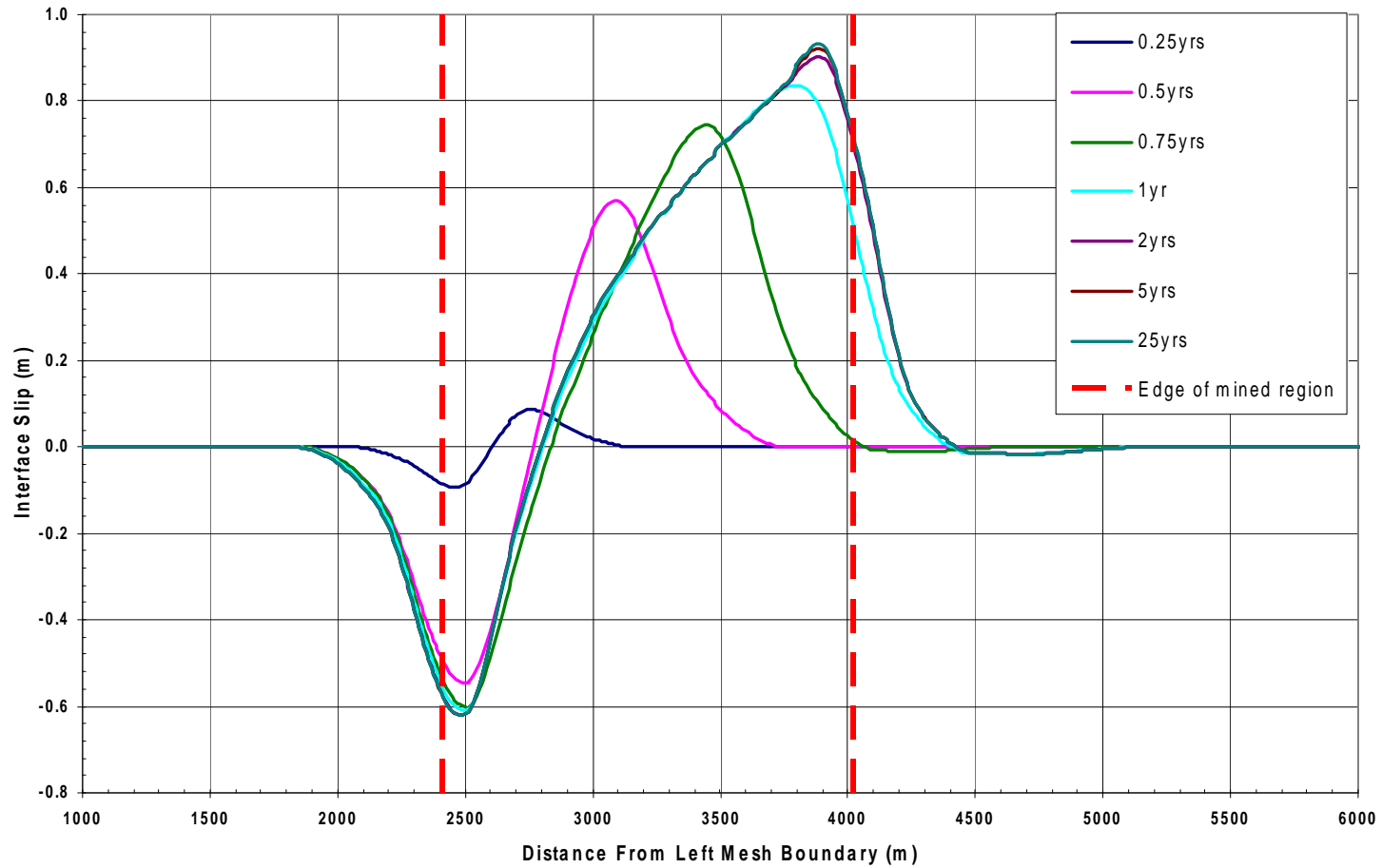


Figure 3.1.10. 304.8 m (1000 ft) Mine Depth: Absolute Maximum Interface Slip Envelope (Envelope Over Mine Excavation Sizes and Mining Rates)



**Figure 3.1.11. 609.6 m (2000 ft) Mine Depth: Interface Slip Along MB 101 at Select Times
1.6 km (1 mile) Excavation at Rate of 1.6 km/year (1 mile/year)**

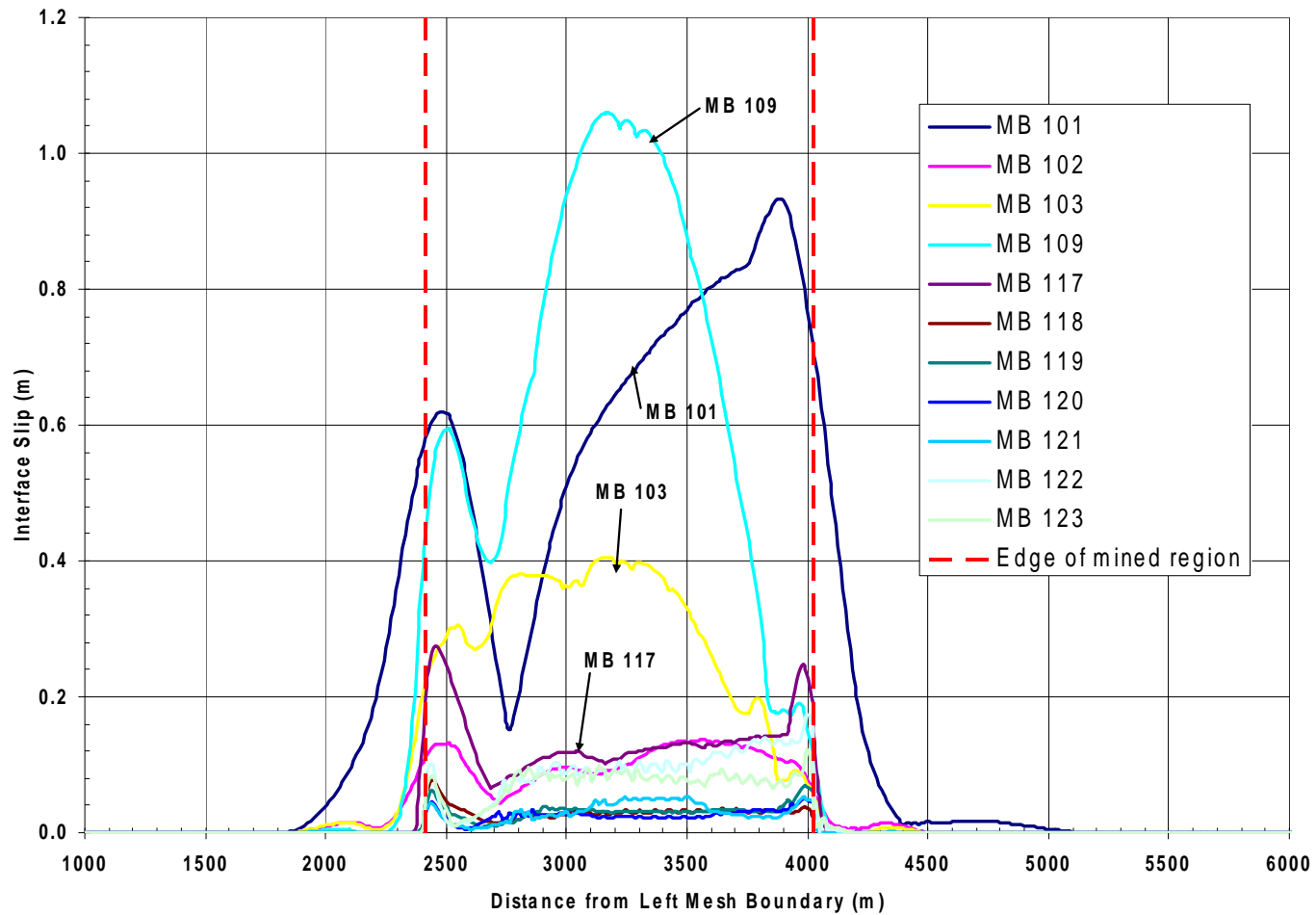


Figure 3.1.12. 609.6 m (2000 ft) Mine Depth: Absolute Maximum Interface Slip as a Function of Distance for All Marker Beds Over 25 year Time Period (1.6 km, or 1 mile, Excavation at Rate of 1.6 km/year, or 1 mile/year)

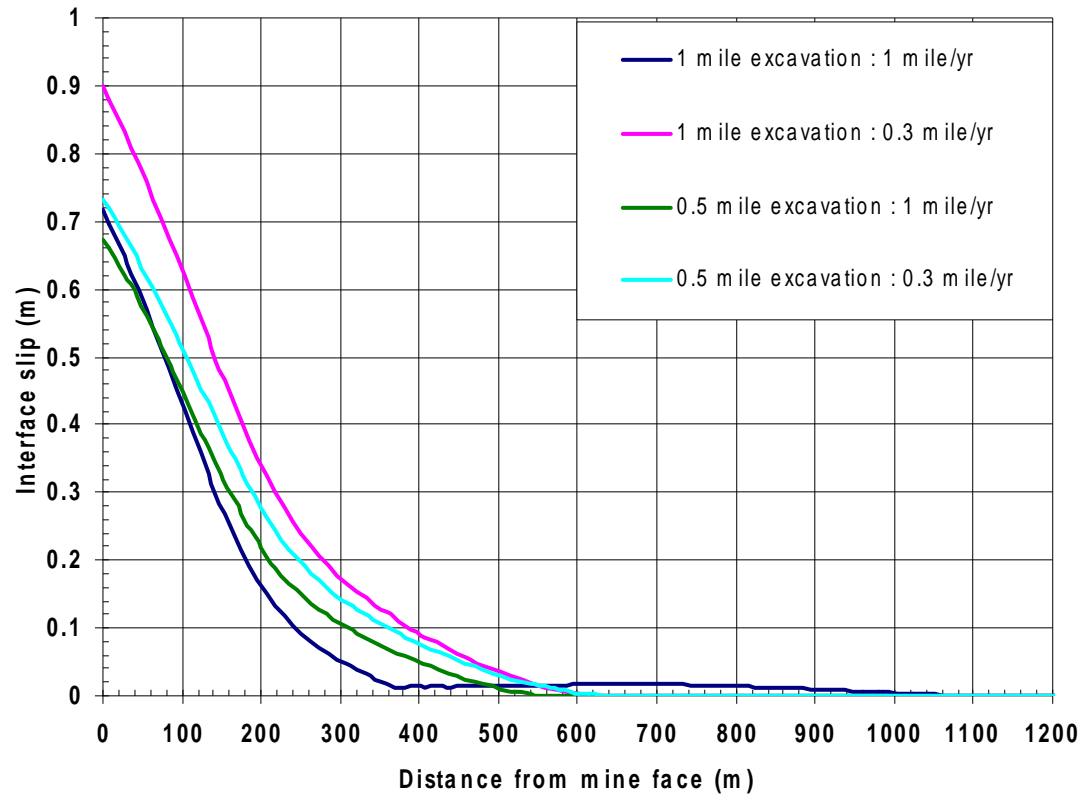


Figure 3.1.13. 609.6 m (2000 ft) Mine Depth: Absolute Maximum Interface Slip Envelope for the Mining Towards Well Scenario (Varying Mine Excavation Sizes and Rates)

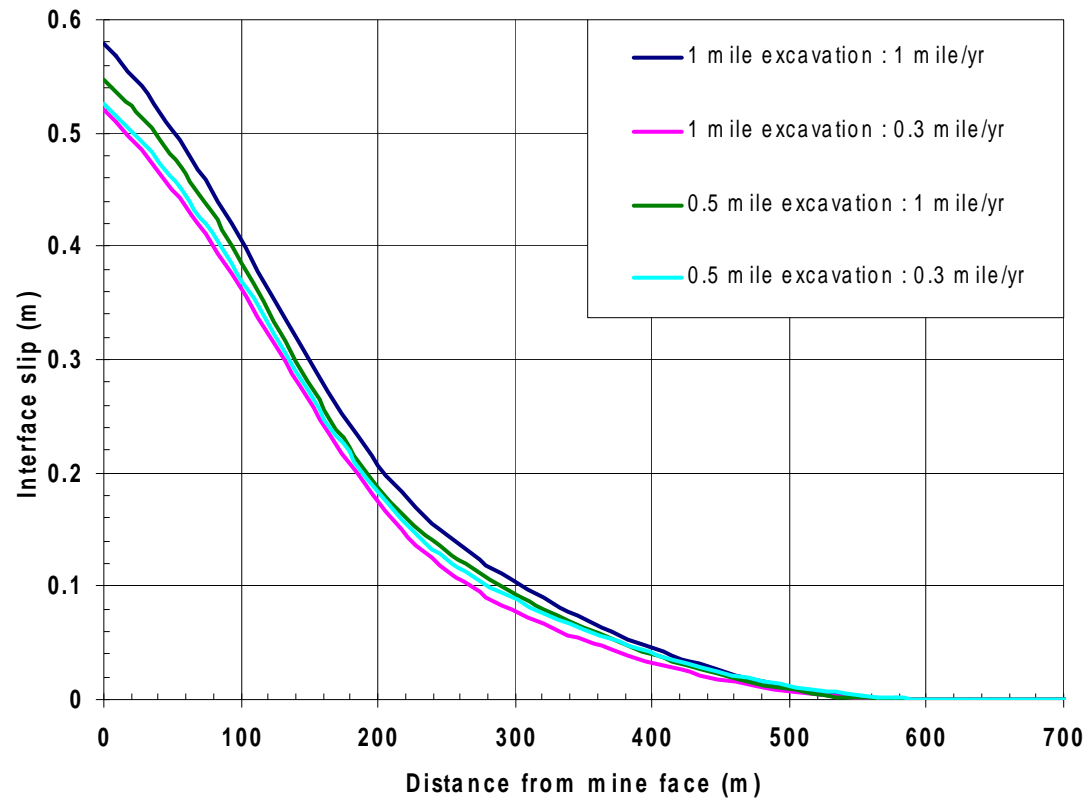
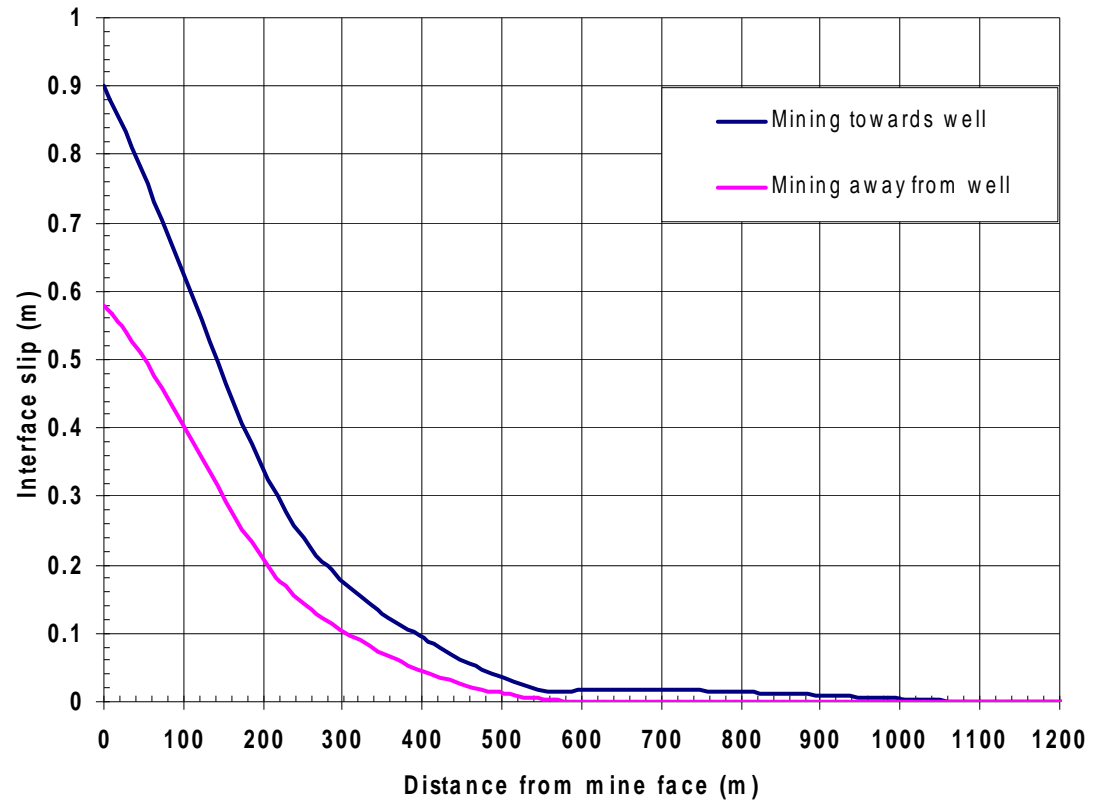


Figure 3.1.14. 609.6m (2000 ft) Mine Depth: Absolute Maximum Interface Slip Envelope for the Mining Away From Well Scenario (Varying Mine Excavation Sizes and Rates)



**Figure 3.1.15. 609.6m (2000 ft) Mine Depth: Absolute Maximum Interface Slip Envelope
(Envelopes Over Mine Excavation Sizes and Mining Rates)**

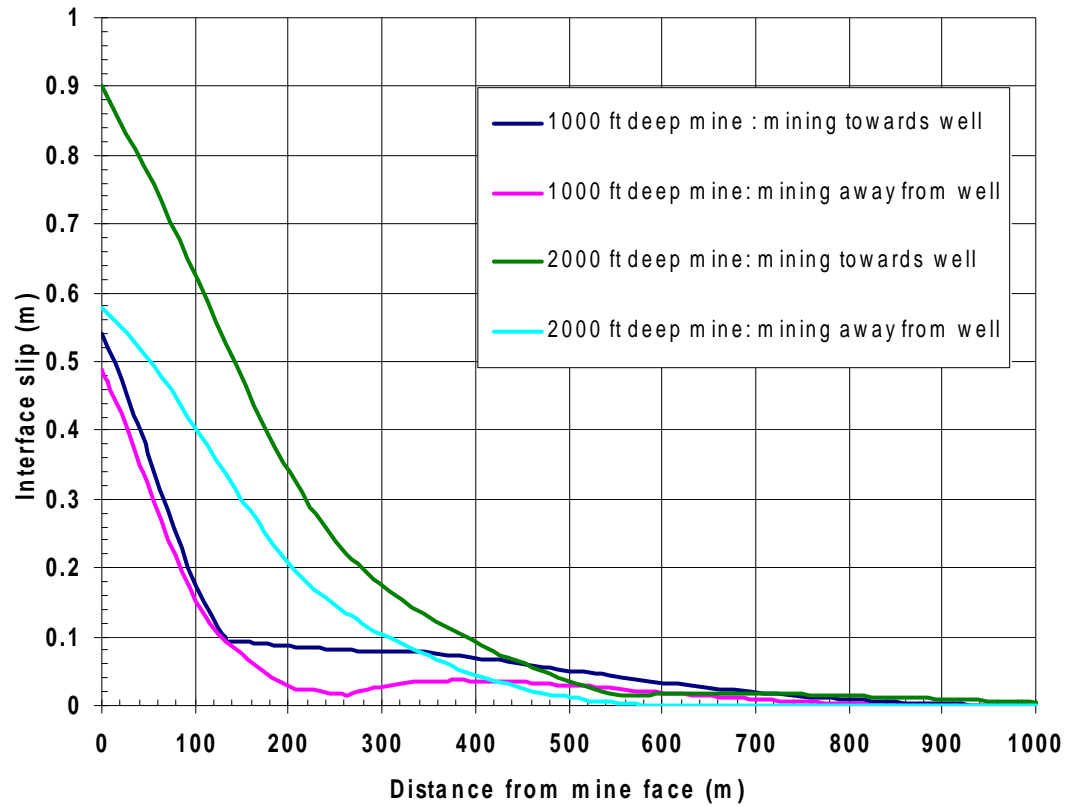


Figure 3.1.16. Comparison of Absolute Maximum Interface Slip Envelopes for 304.8 m (1000 ft) and 609.6 m (2000 ft) Mines

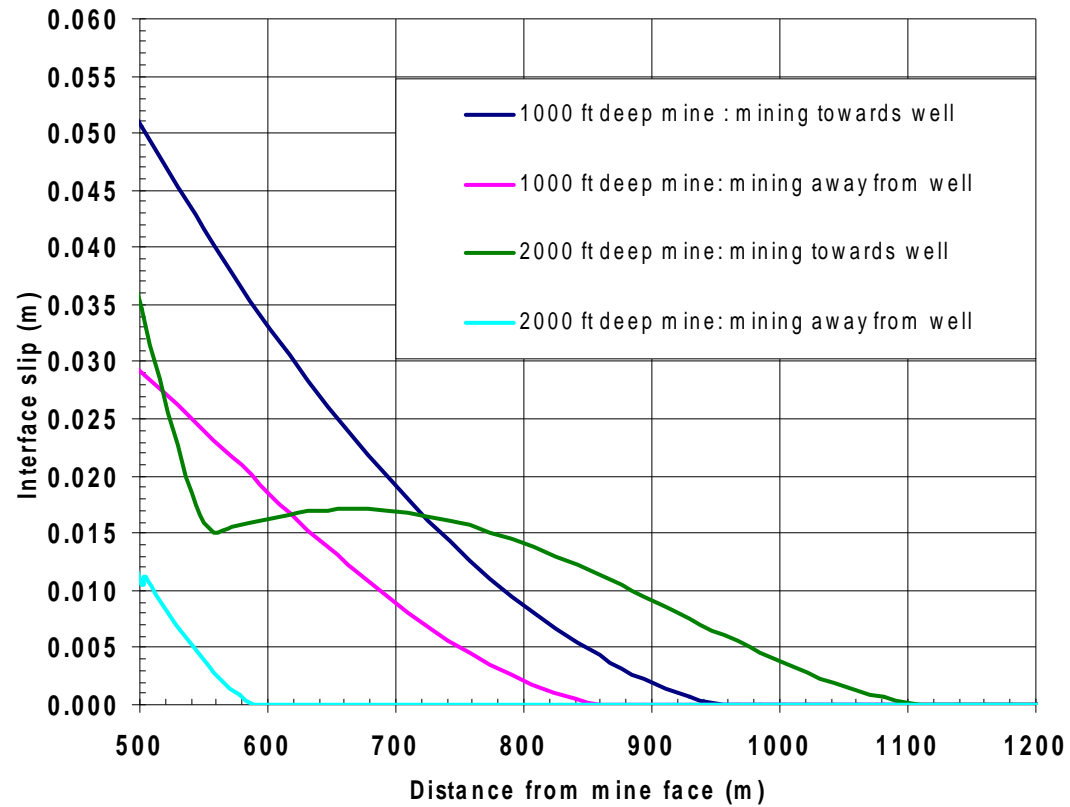
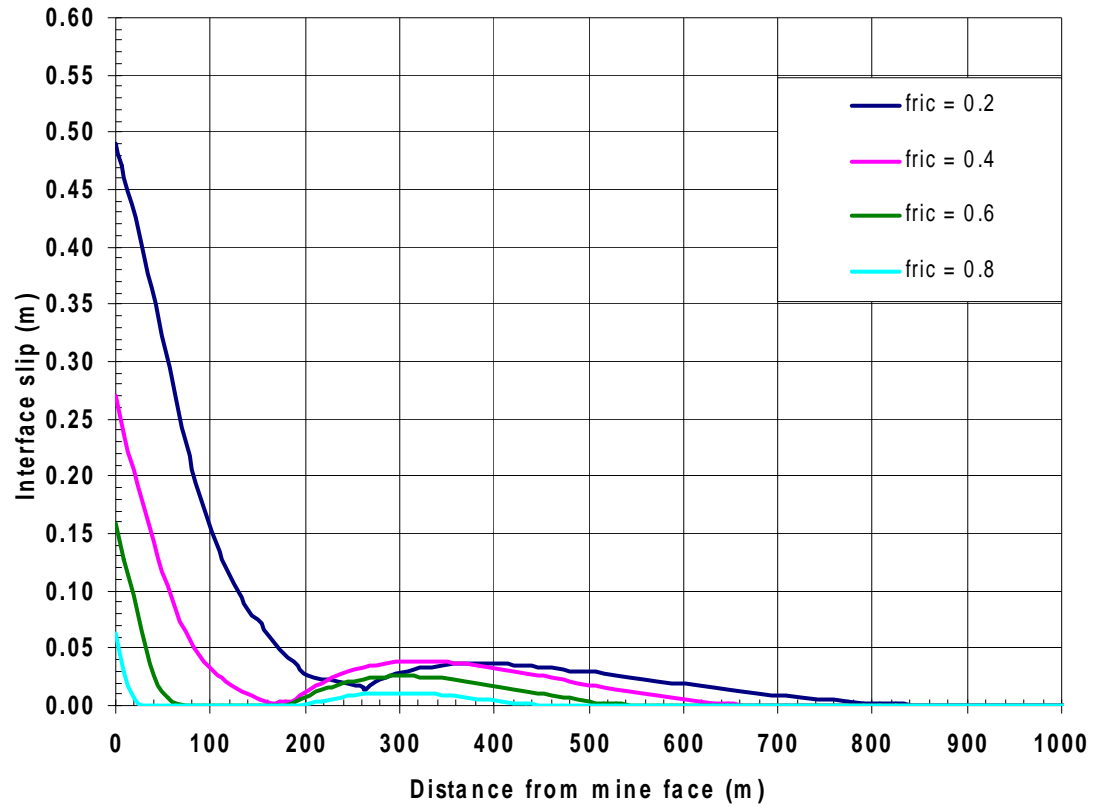
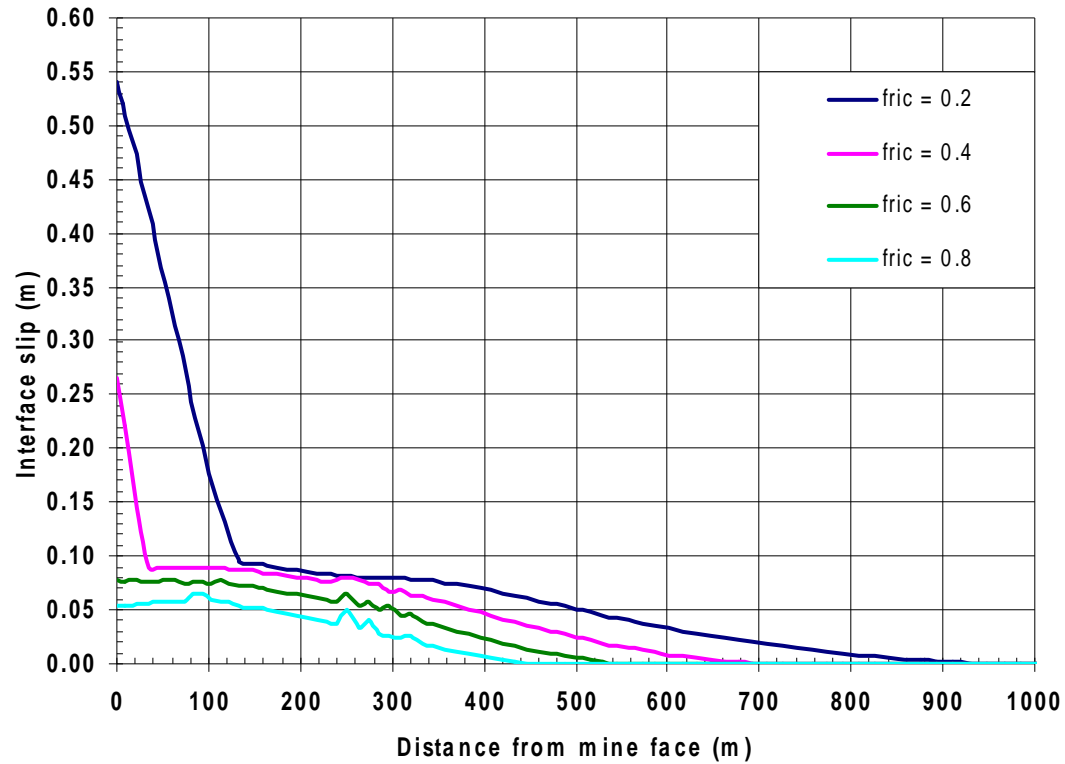


Figure 3.1.17. Close-Up View of Absolute Maximum Interface Slip Envelopes for 304.8 m (1000 ft) and 609.6 m (2000 ft) Mines



**Figure 3.1.18. Effect of Friction Coefficient on Slip Envelope: Mining Away From Well
(304.8m, or 1000 ft, Deep Mine; 1.6 km, or 1 mile, Excavation; 1.6 km/year, or 1 mile/year, Excavation Rate)**



**Figure 3.1.19. Effect of Friction Coefficient on Slip Envelope: Mining Towards Well
(304.8m, or 1000 ft, Deep Mine; 1.6 km, or 1 mile, Excavation; 1.6 km/year, or 1 mile/year, Excavation Rate)**

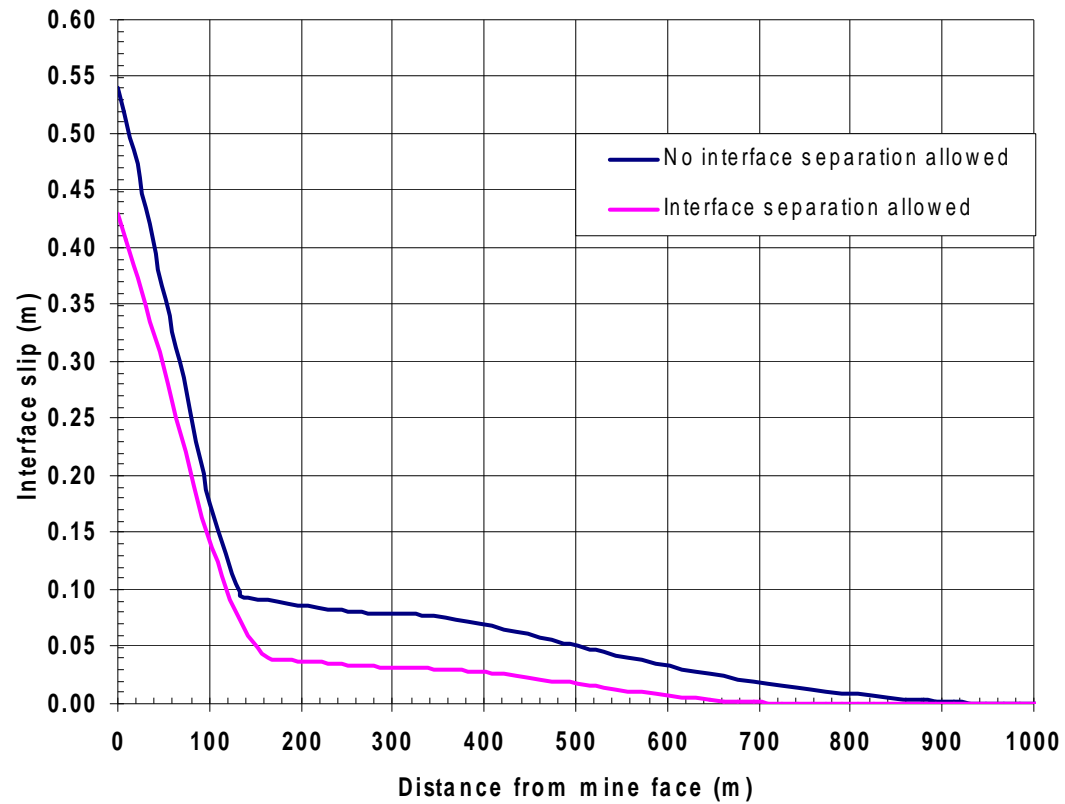
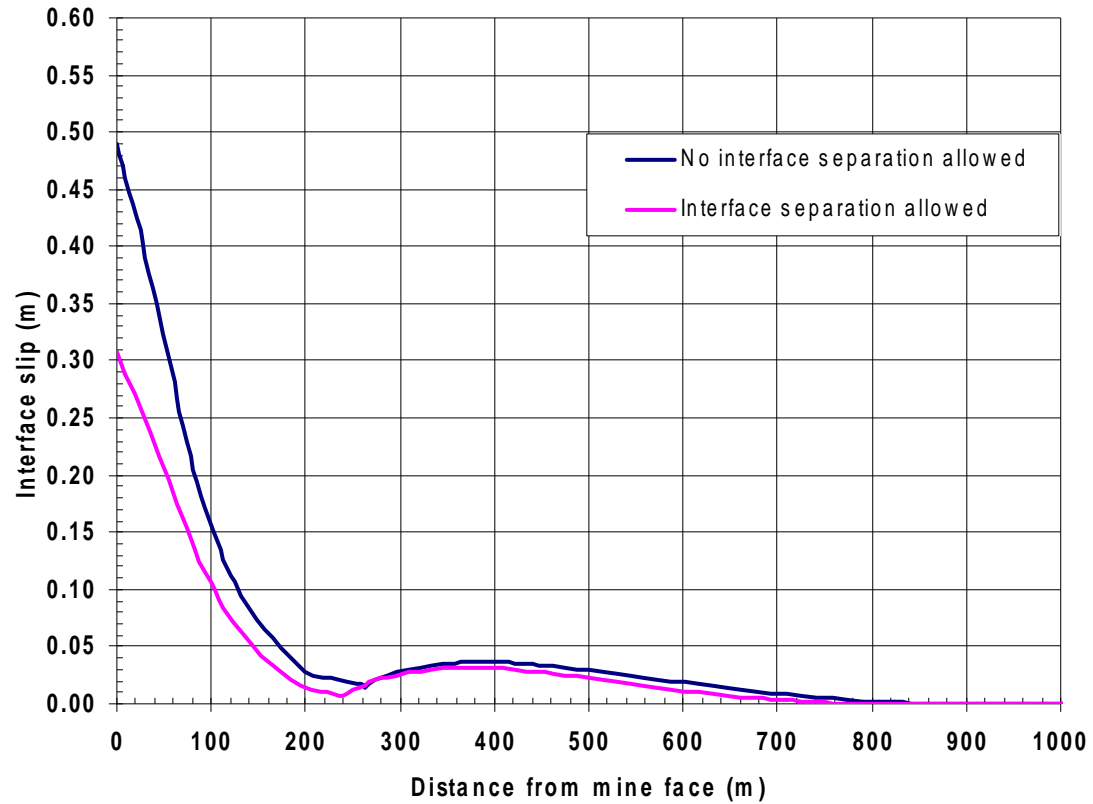


Figure 3.1.20. Effect of Interface Separation on Slip Envelope: Mining Towards Well
(304.8 m, or 1000 ft, Deep Mine; 1.6 km, or 1 mile, Excavation; 1.6 km/year, or 1 mile/year, Excavation Rate)



**Figure 3.1.21. Effect of Interface Separation on Slip Envelope: Mining Away From Well
(304.8 m, or 1000 ft, Deep Mine; 1.6 km, or 1 mile, Excavation; 1.6 km/year, or 1 mile/year, Excavation Rate)**

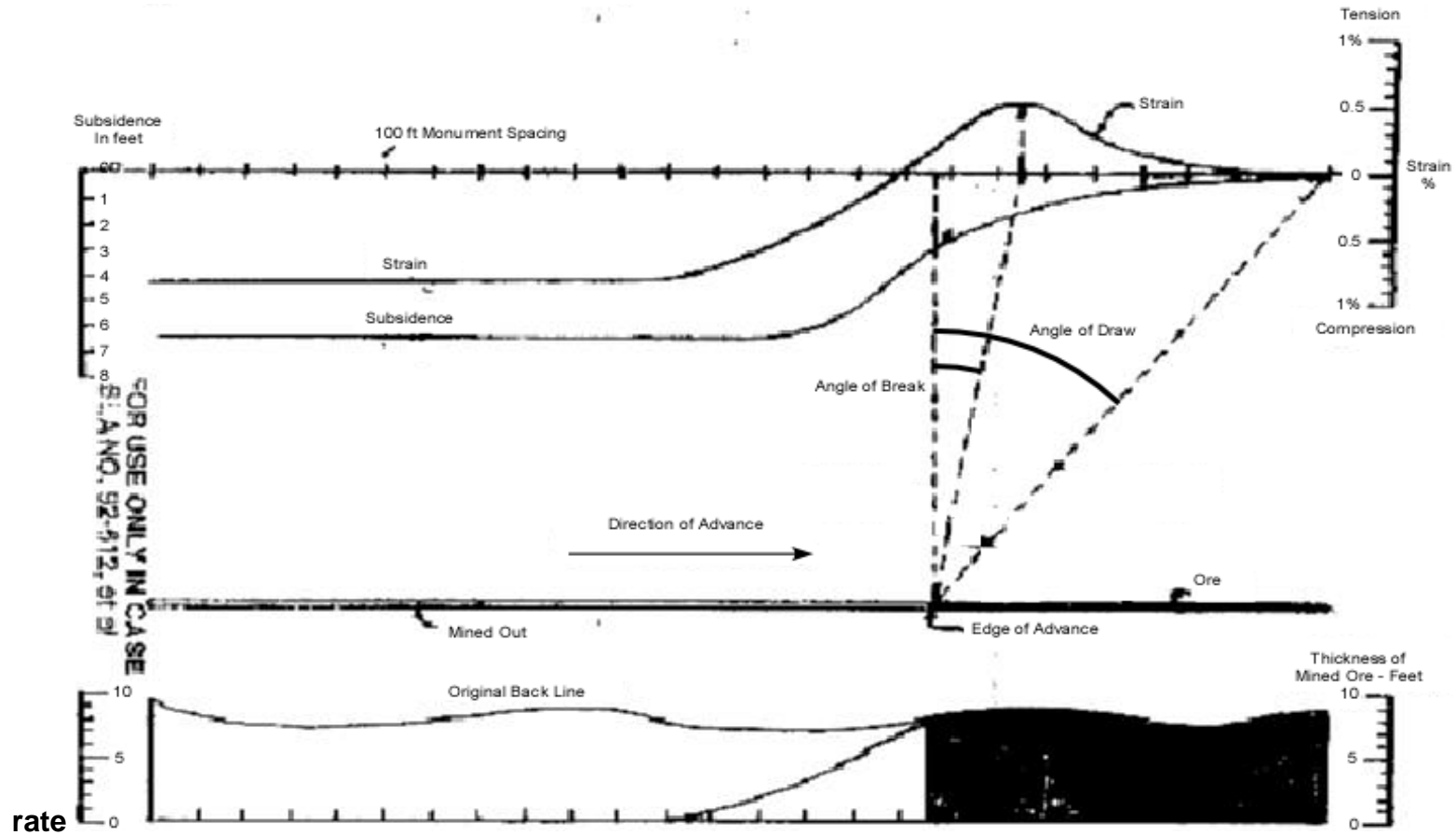


Figure 3.1.22. Illustration of Surface Measurement Quantities

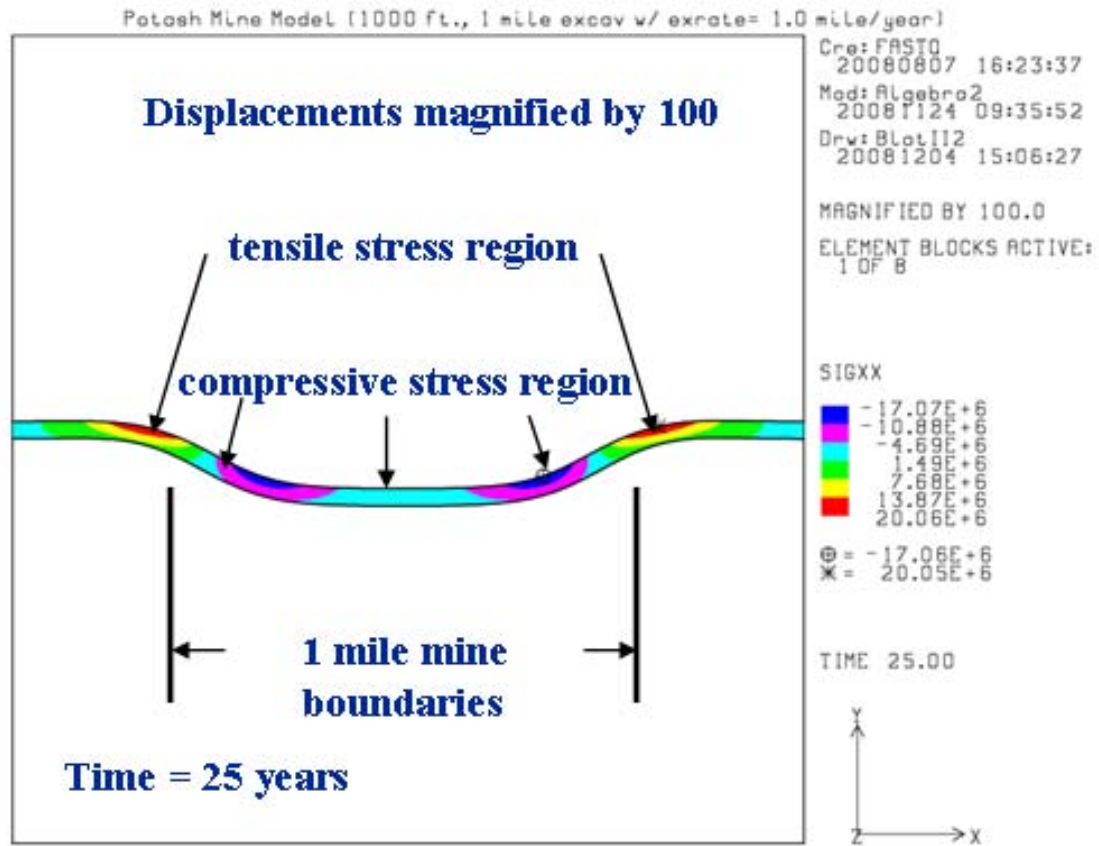


Figure 3.1.23. Surface Layer Deformation at 25 years Magnified 100 Times

(304.8 m, or 1000 ft, Deep Mine; 1.6 km, or 1 mile, Long; 1.6 km/year, or 1 mile/year, Excavation Rate)

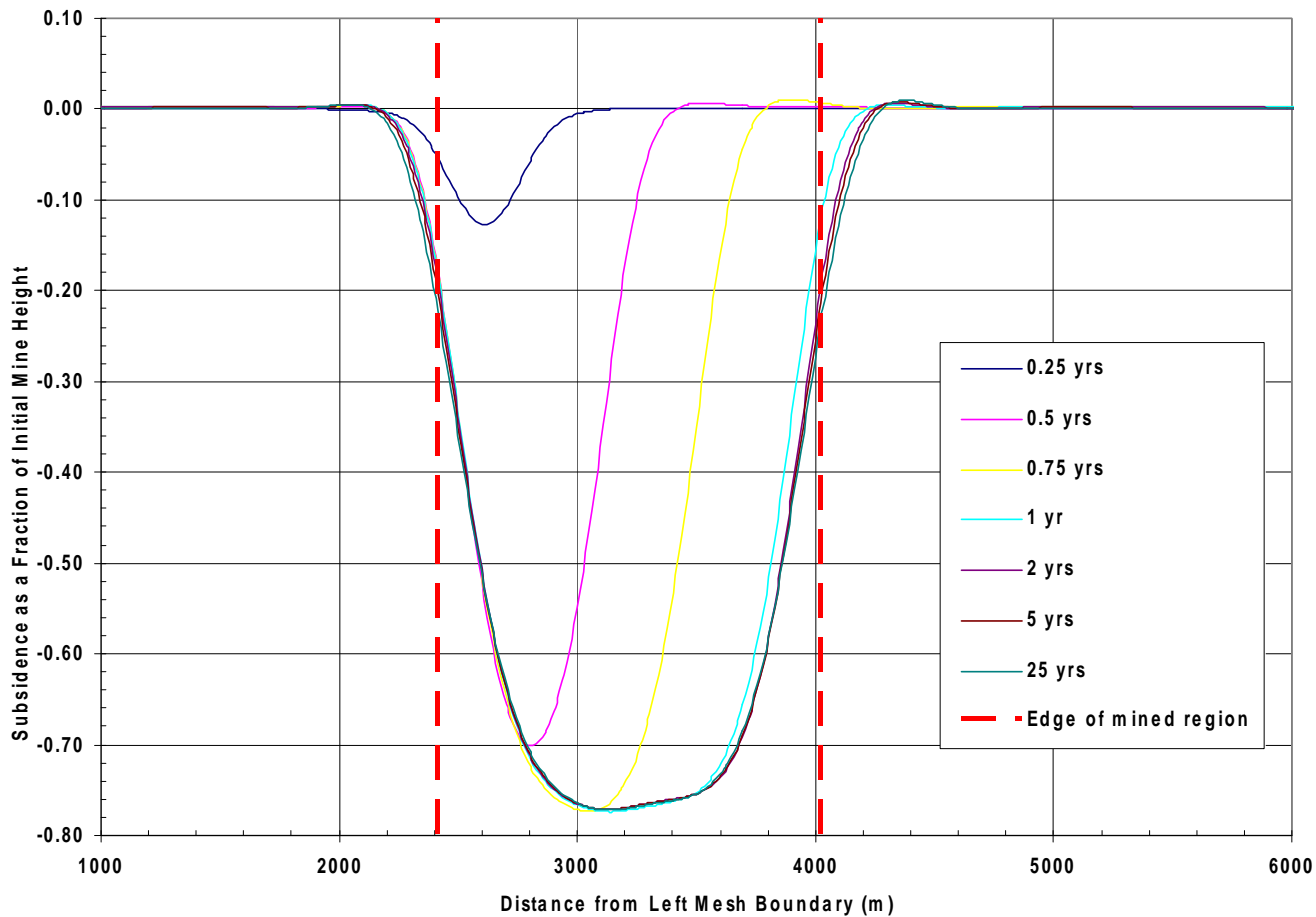
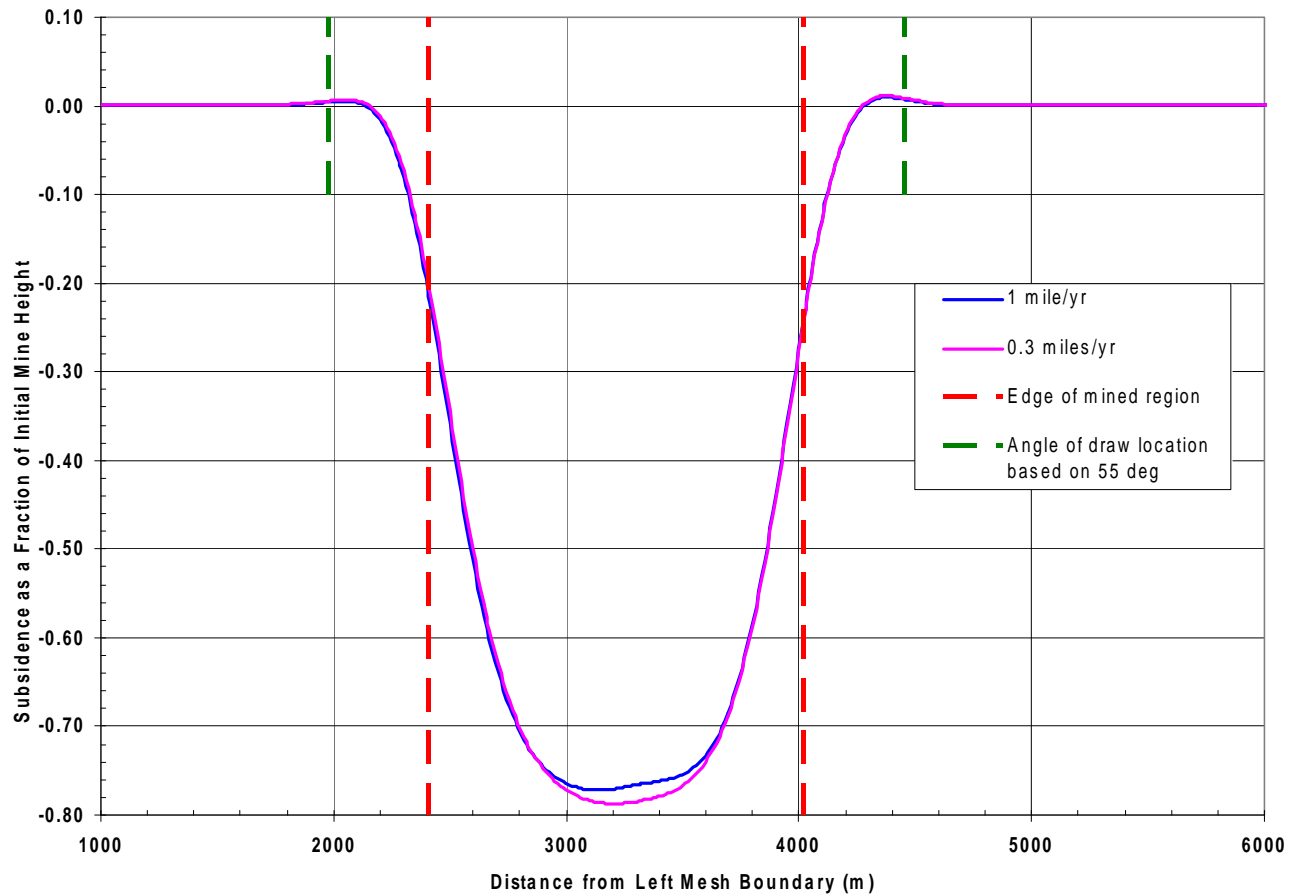
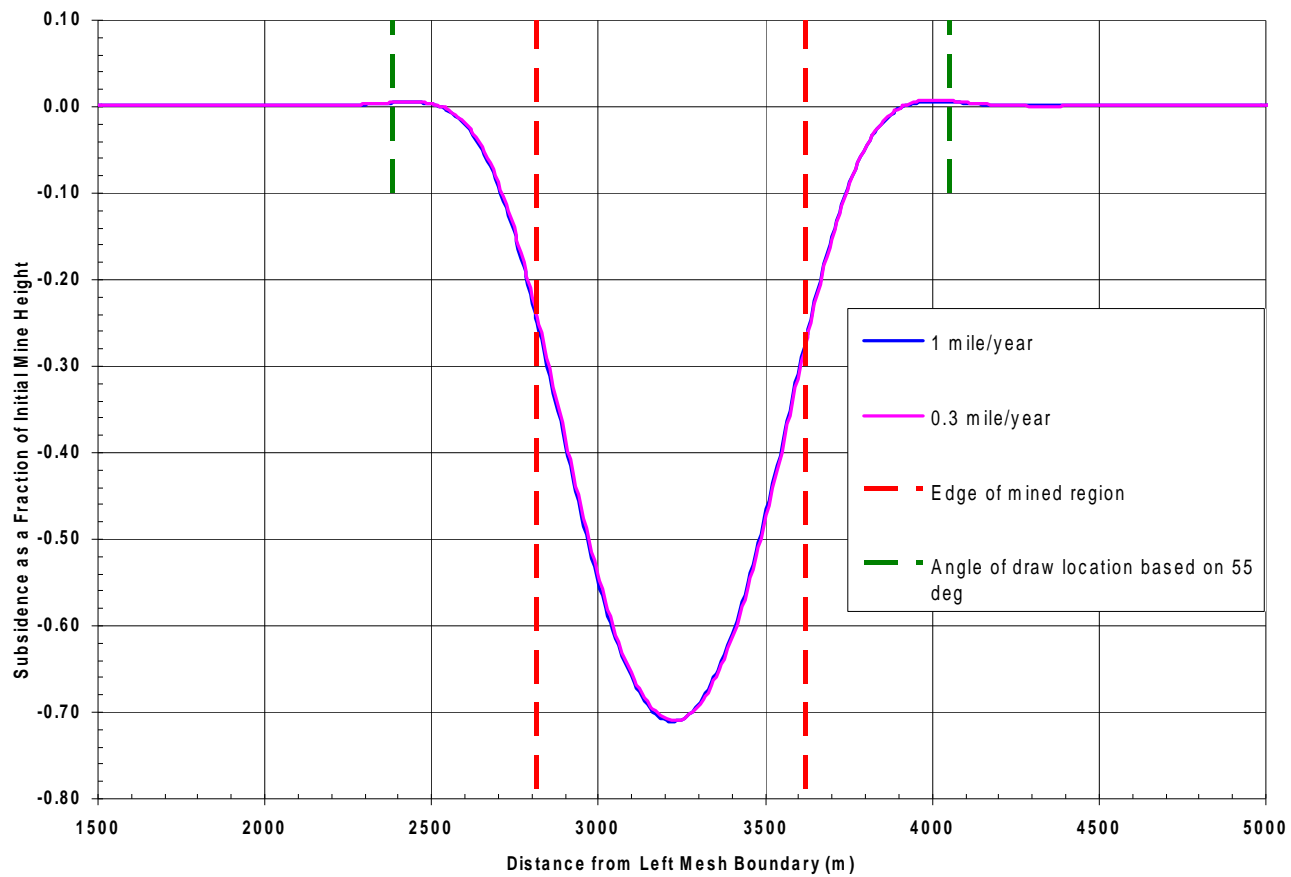


Figure 3.1.24. Surface Subsidence as a Fraction of Initial Mine Height

(304.8 m, or 1000 ft, Deep Mine; 1.6 km, or 1 mile, Long; 1.6 km/year, or 1 mile/year, Excavation Rate)



**Figure 3.1.25. Effect of Mining Rate on Surface Subsidence at 25 years
(304.8 m, or 1000 ft, Deep Mine; 1.6 km, or 1 mile, Long)**



**Figure 3.1.26. Effect of Mining Rate on Surface Subsidence at 25 years
(304.8 m, or 1000 ft, Deep Mine; 0.8 km, or 0.5 mile, Long)**

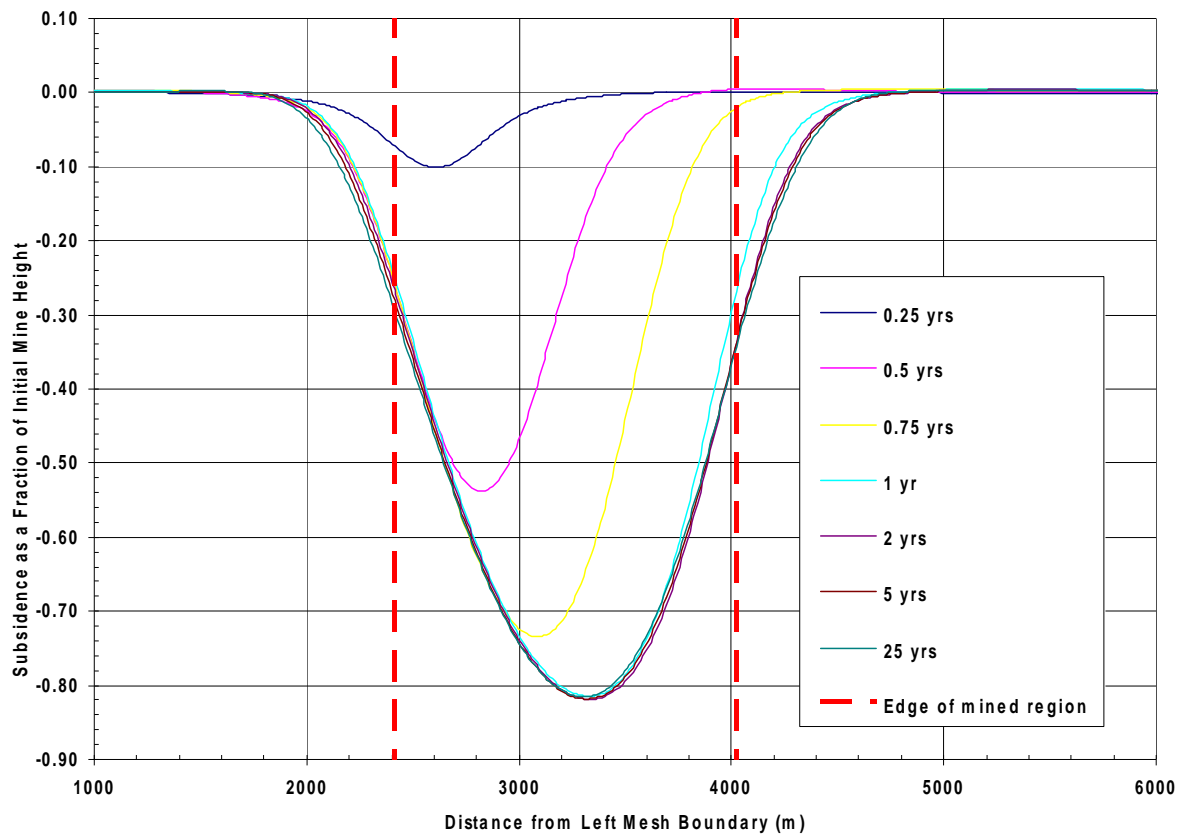
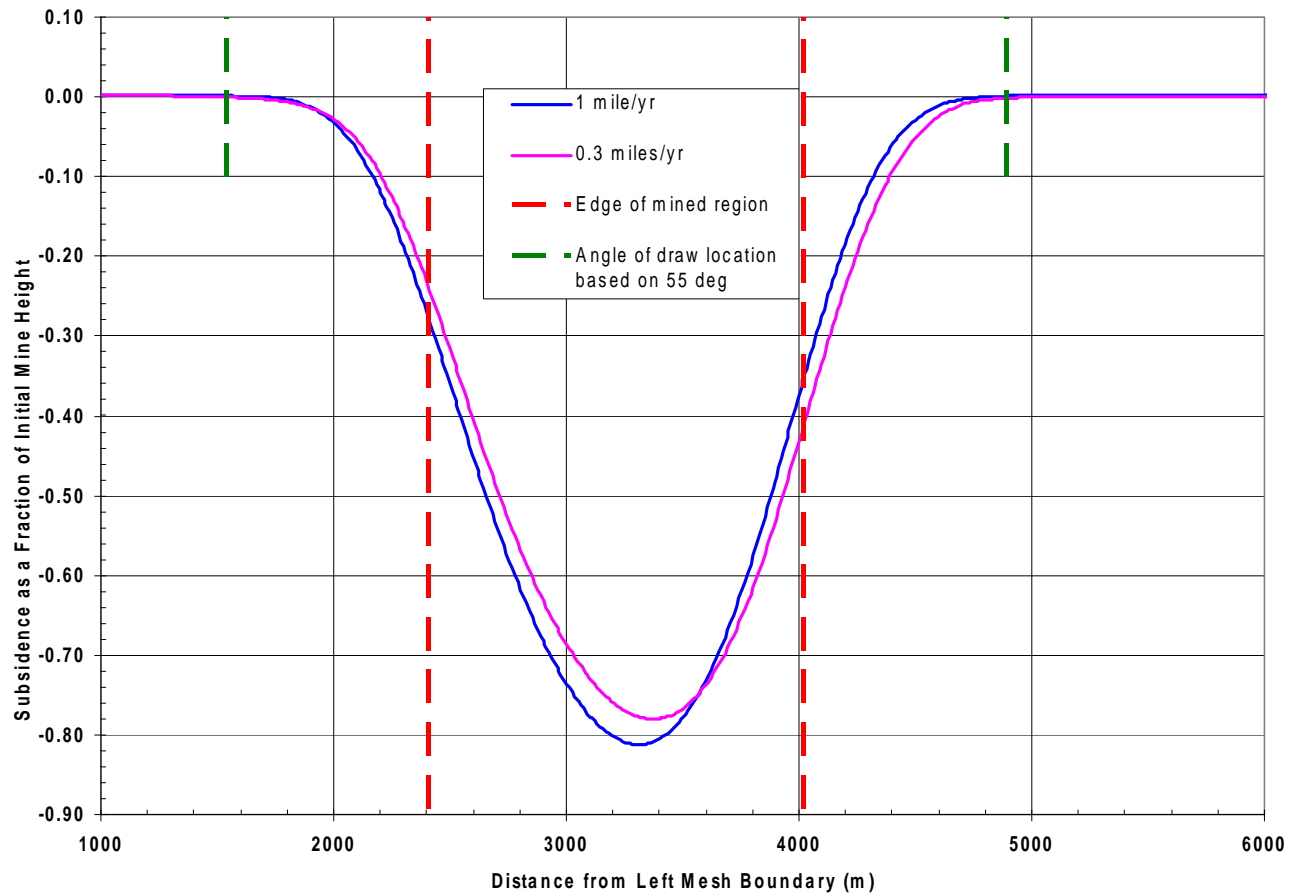
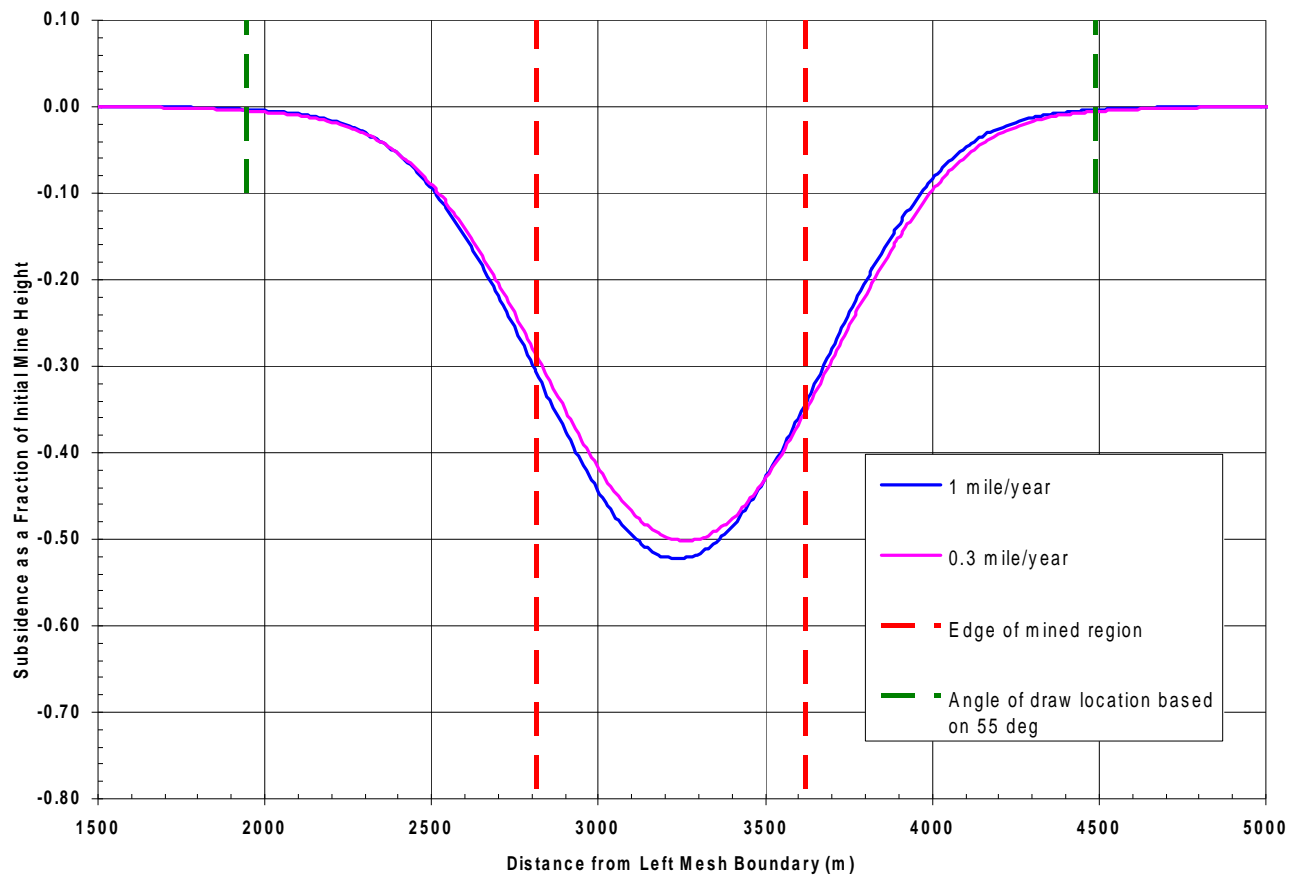


Figure 3.1.27. Surface Subsidence as a Fraction of Initial Mine Height

(609.6 m, or 2000 ft, Deep Mine; 1.6 km, or 1 mile, Long; 1.6 km/year, or 1 mile/year, Excavation Rate)



**Figure 3.1.28. Effect of Mining Rate on Surface Subsidence at 25 years
(609.6 m, or 2000 ft, Deep Mine; 1.6 km, or 1 mile, Long)**



**Figure 3.1.29. Effect of Mining Rate on Surface Subsidence at 25 years
(609.6 m, or 2000 ft, Deep Mine; 0.8 km, or 0.5 mile, Long)**

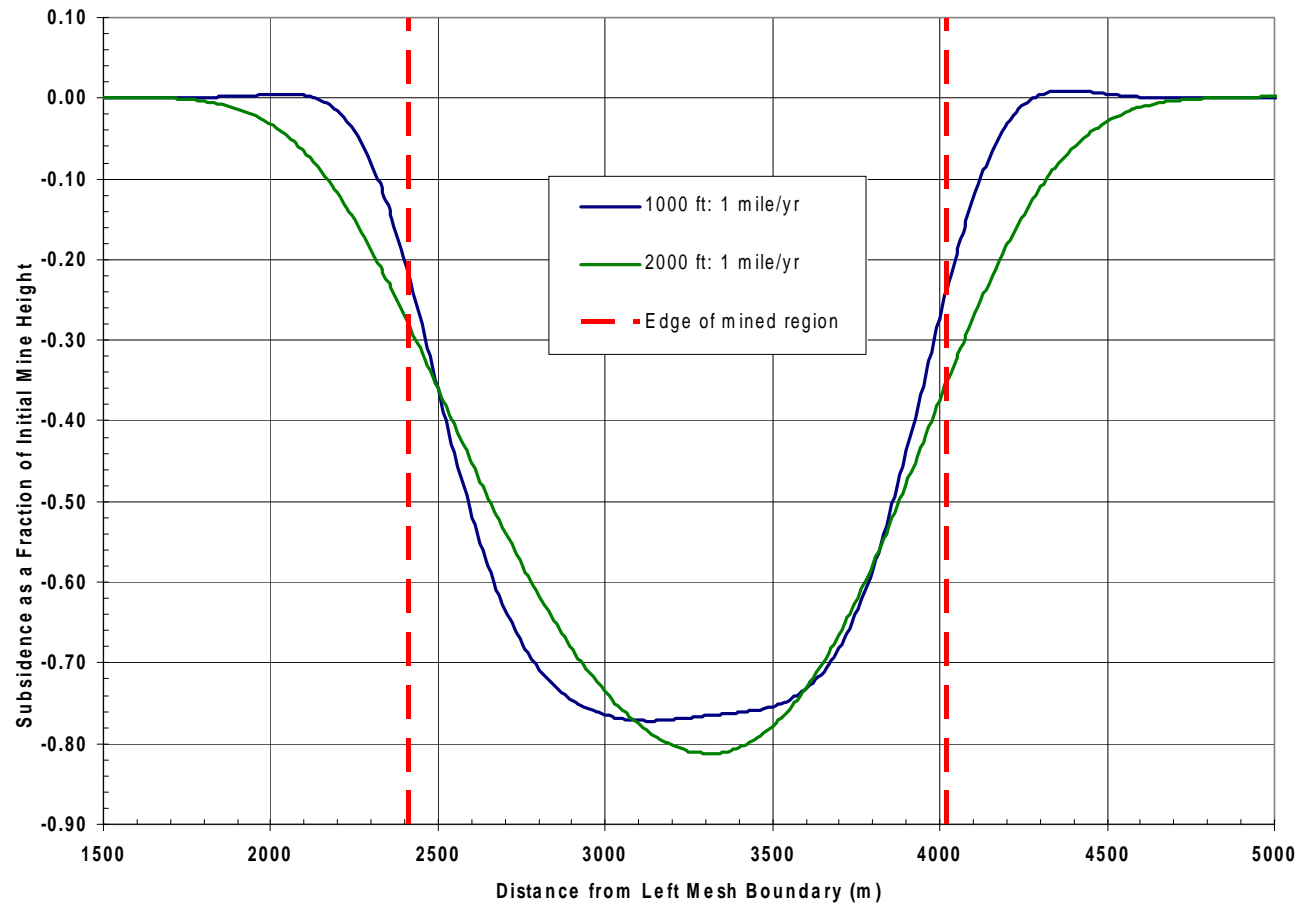


**Figure 3.1.30. Effect of Mining Depth on Surface Subsidence at 25 years
(1.6 km, or 1 mile, Long; 1.6 km/year, or 1 mile/year, Excavation Rate)**

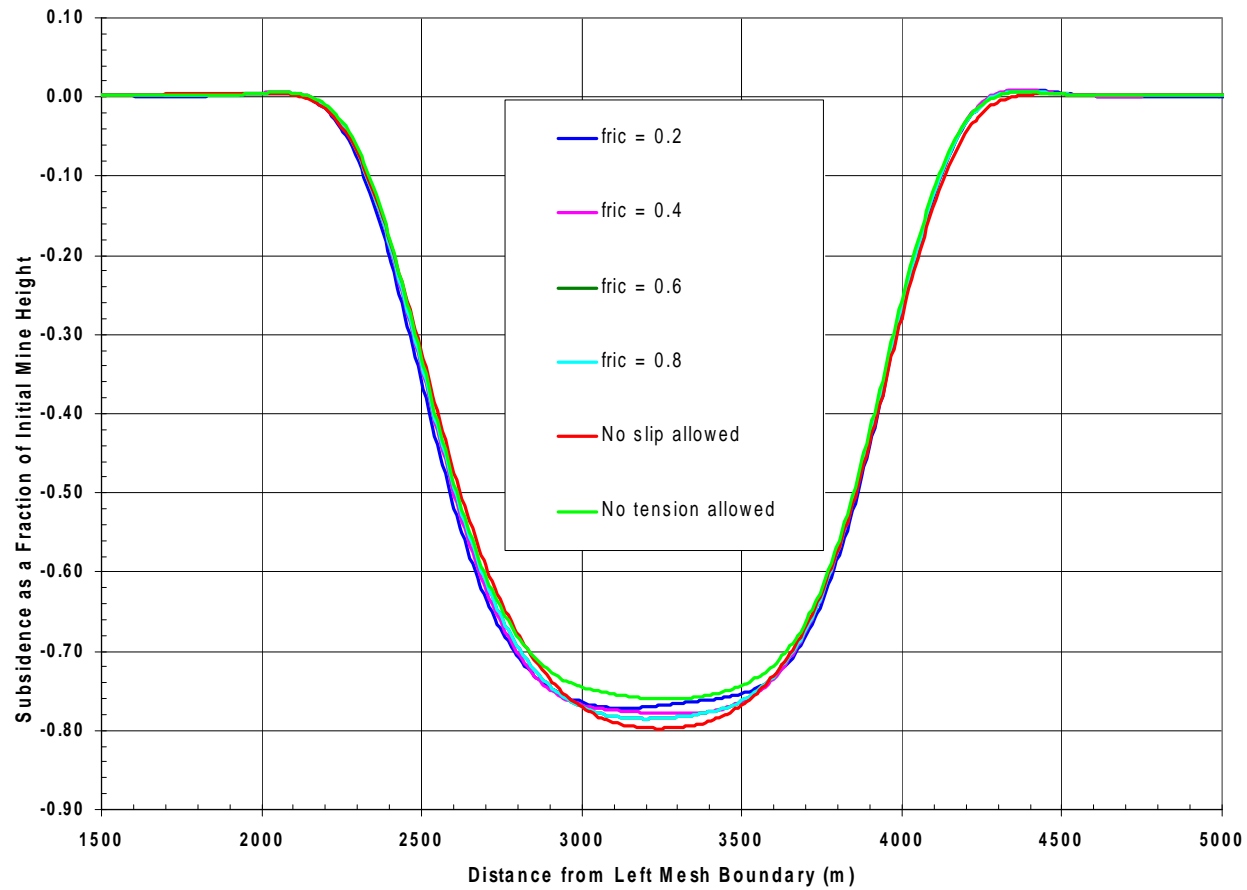


Figure 3.1.31. Effect of Interface Properties on Surface Subsidence at 25 years

(304.8 m, or 1000 ft, Deep Mine; 1.6 km, or 1 mile, Long; 1.6 km/year, or 1 mile/year, Excavation Rate)

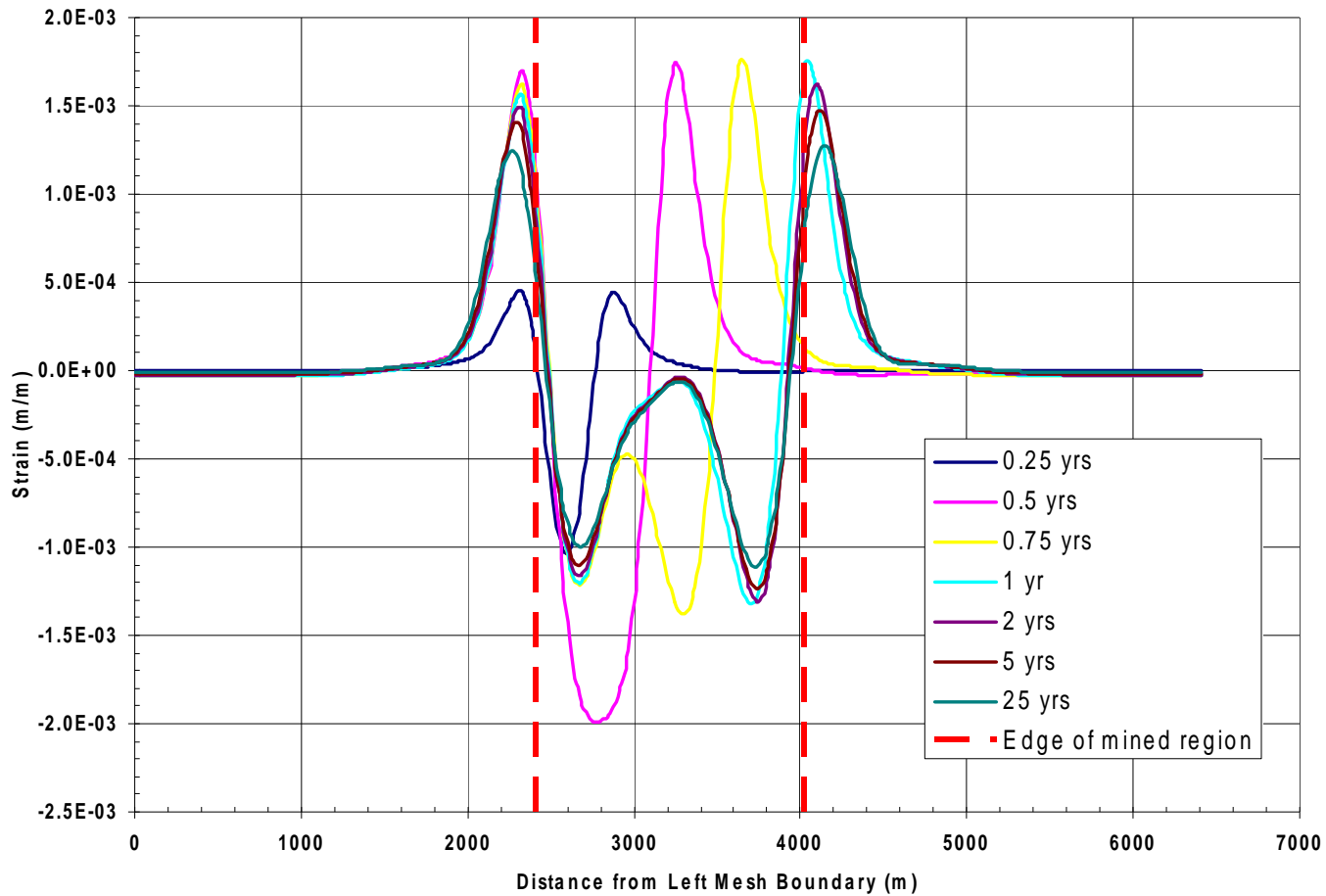


Figure 3.1.32. Ground Surface Strain at Select Times

(304.8 m, or 1000 ft, Deep Mine; 1.6 km, or 1 mile, Long; 1.6 km/year, or 1 mile/year, Excavation Rate)

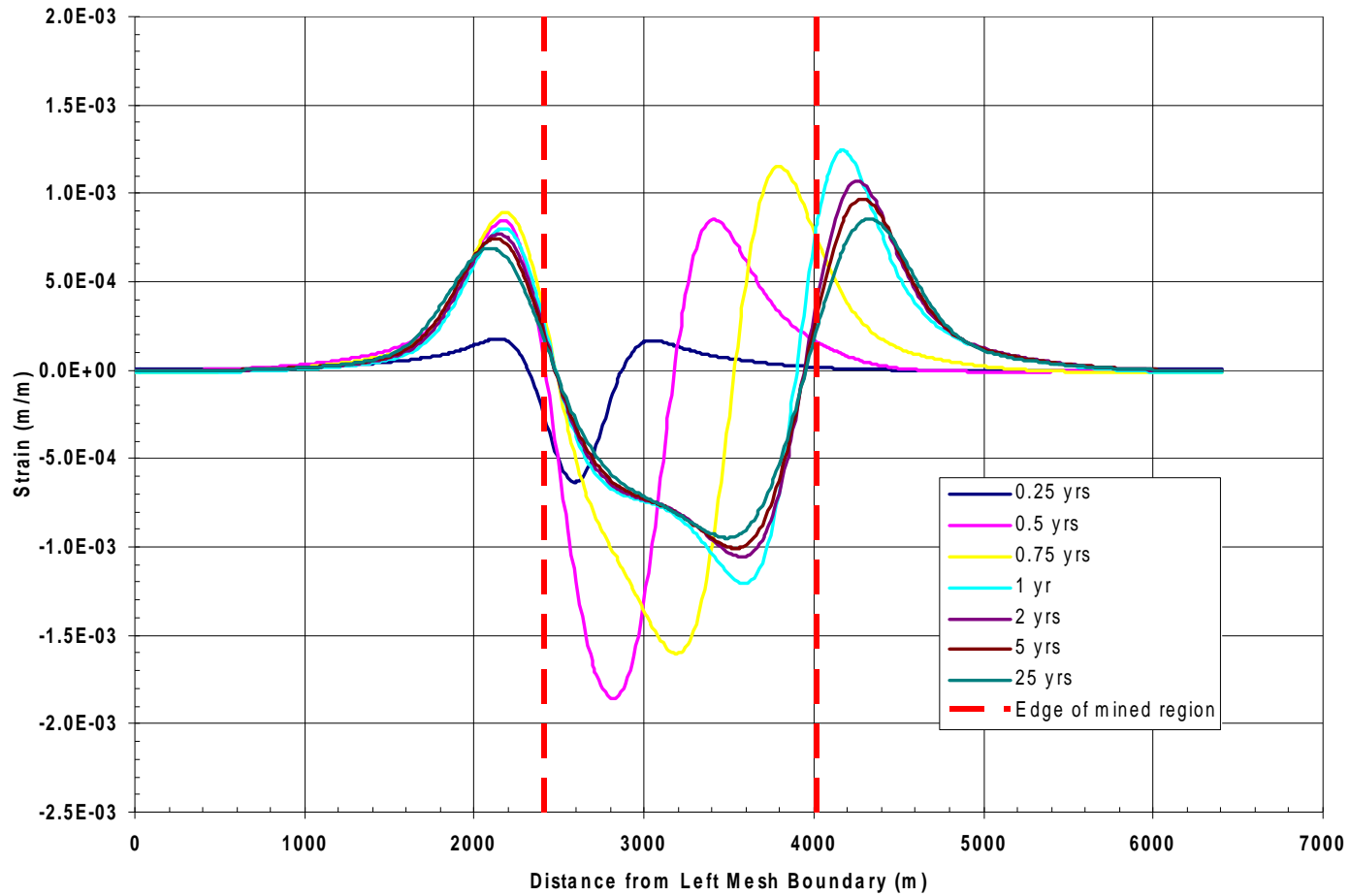


Figure 3.1.33. Ground Surface Strain at Select Times

(609.6 m, or 2000 ft, Deep Mine; 1.6 km, or 1 mile, Long; 1.6 km/year, or 1 mile/year, Excavation Rate)

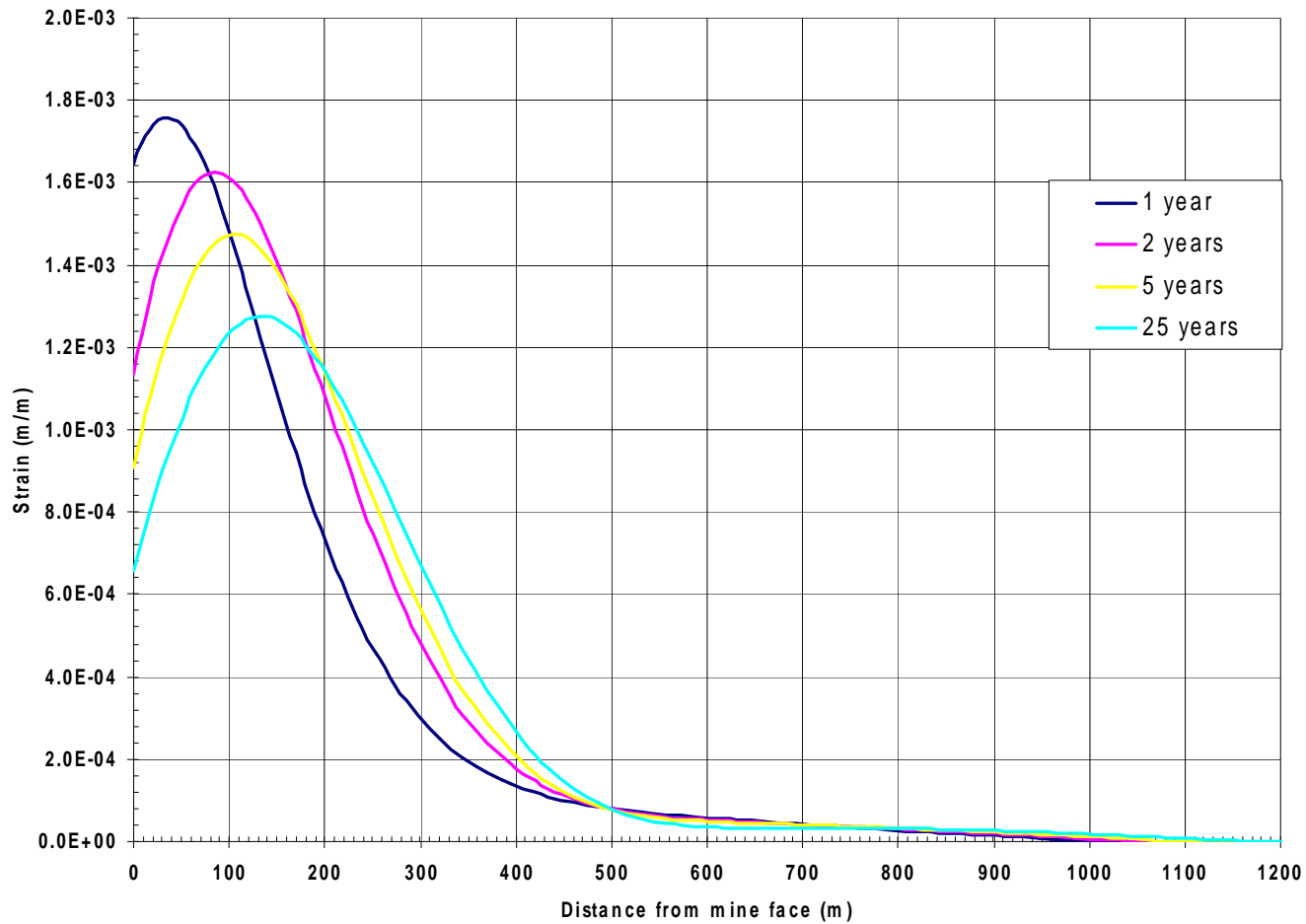


Figure 3.1.34. Ground Surface Strain for Mining Towards the Well Case

(304.8 m, or 1000 ft, Deep Mine; 1.6 km, or 1 mile, Long; 1.6 km/year, or 1 mile/year, Excavation Rate)

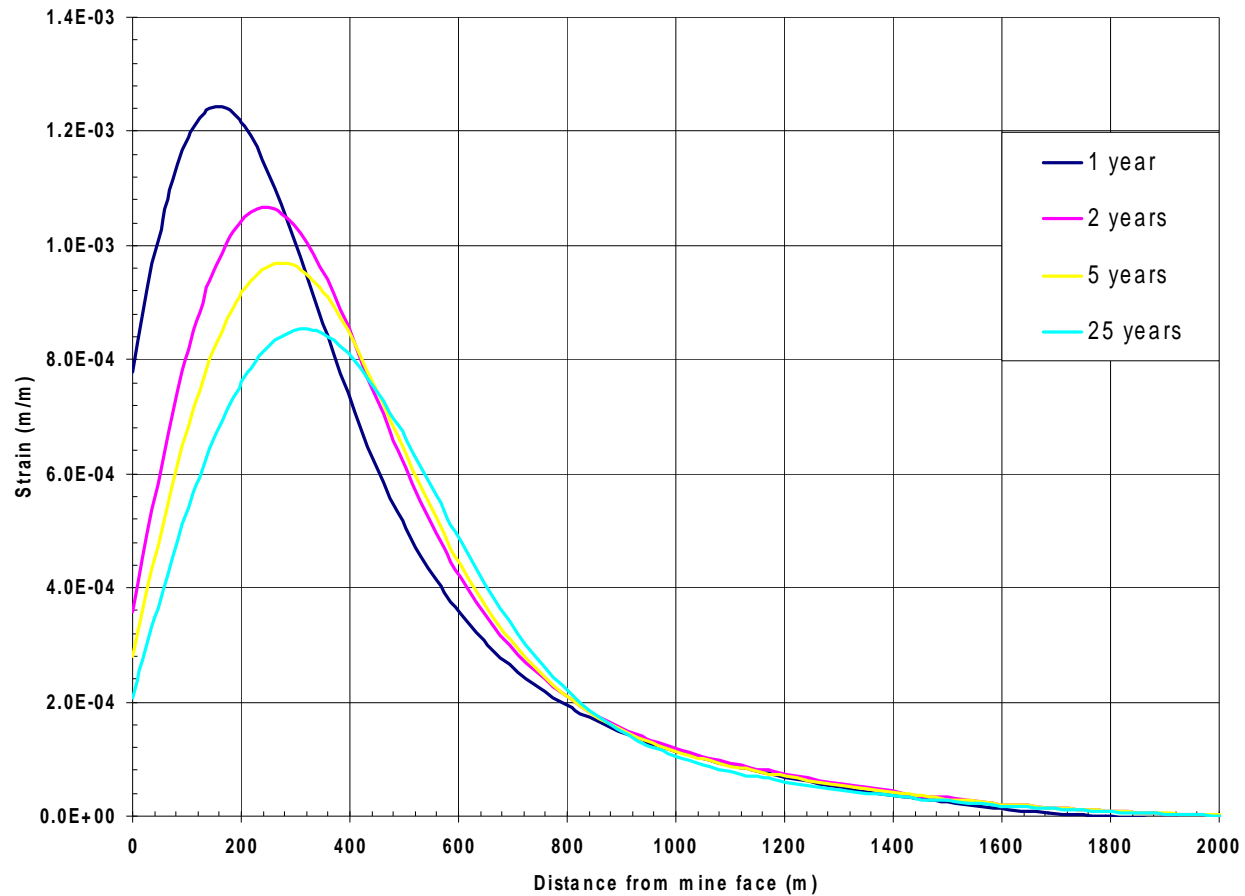


Figure 3.1.35. Ground Surface Strain for Mining Towards the Well Case

(609.6 m, or 2000 ft, Deep Mine; 1.6 km, or 1 mile, Long; 1.6 km/year, or 1 mile/year, Excavation Rate)

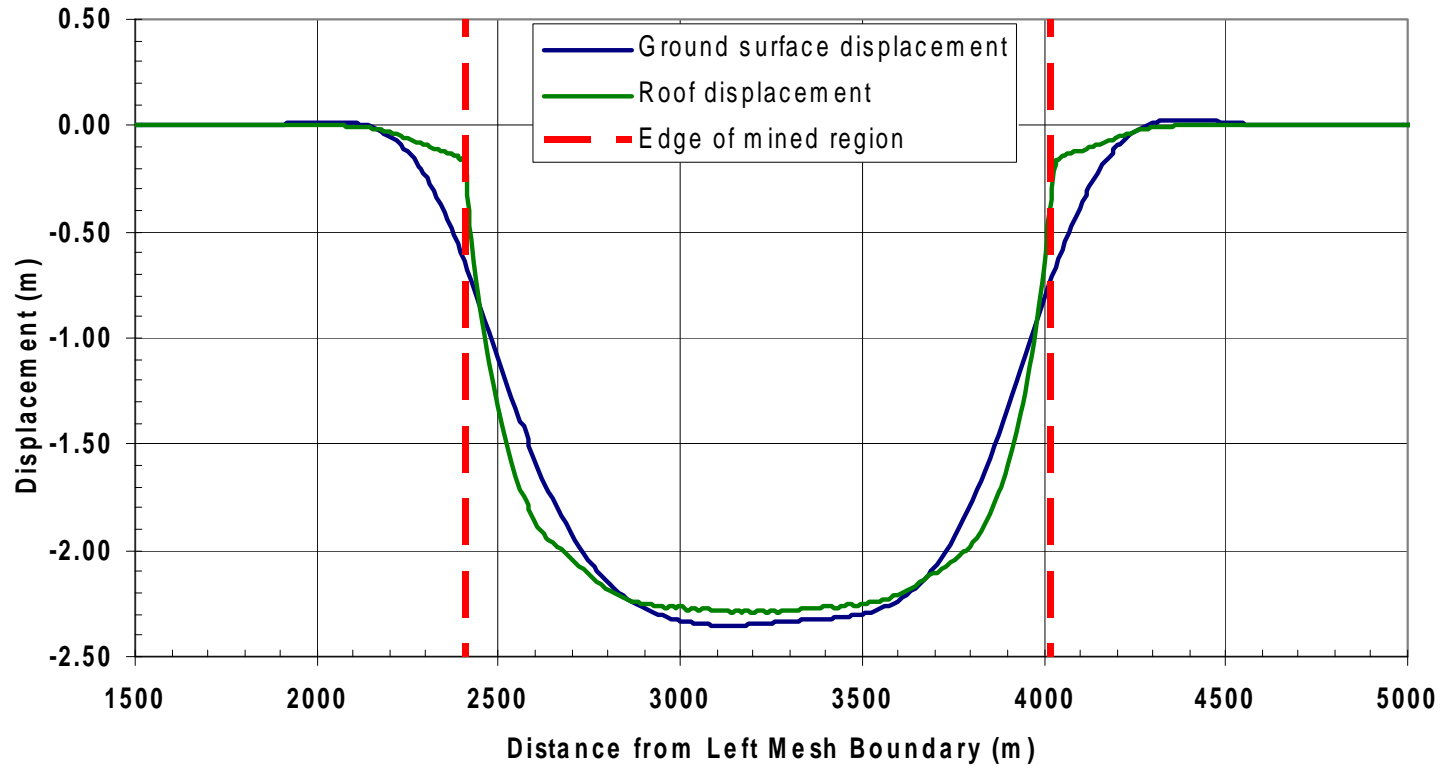


Figure 3.1.36. Comparison of Ground Surface Subsidence and Mine Roof Displacement (304.8 m, or 1000 ft, Deep Mine; 1.6 km, or 1 mile, Long; 1.6 km/year, or 1 mile/year, Excavation Rate)

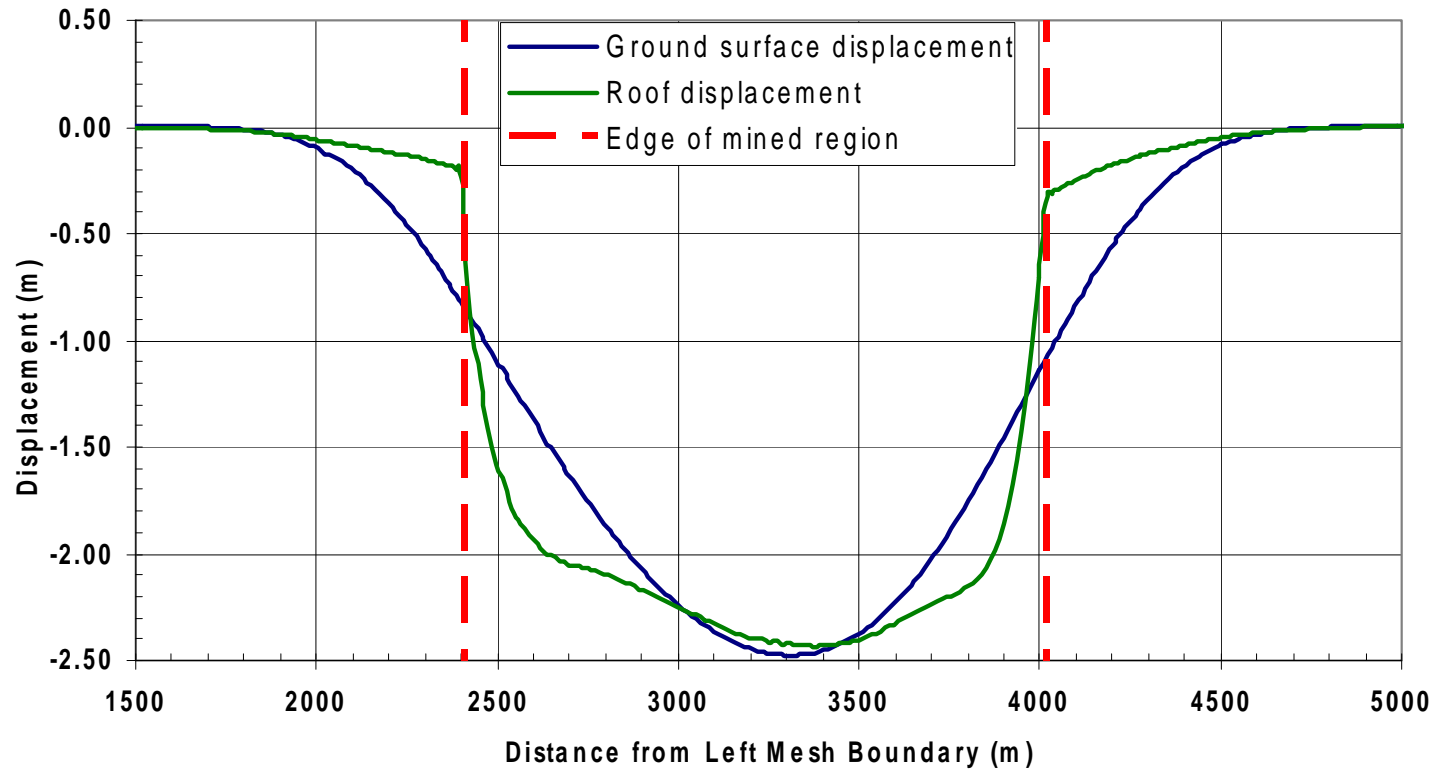


Figure 3.1.37. Comparison of Ground Surface Subsidence and Mine Roof Displacement (609.6m, or 2000 ft, Deep Mine; 1.6 km, or 1 mile, Long; 1.6 km/year, or 1 mile/year, Excavation Rate)

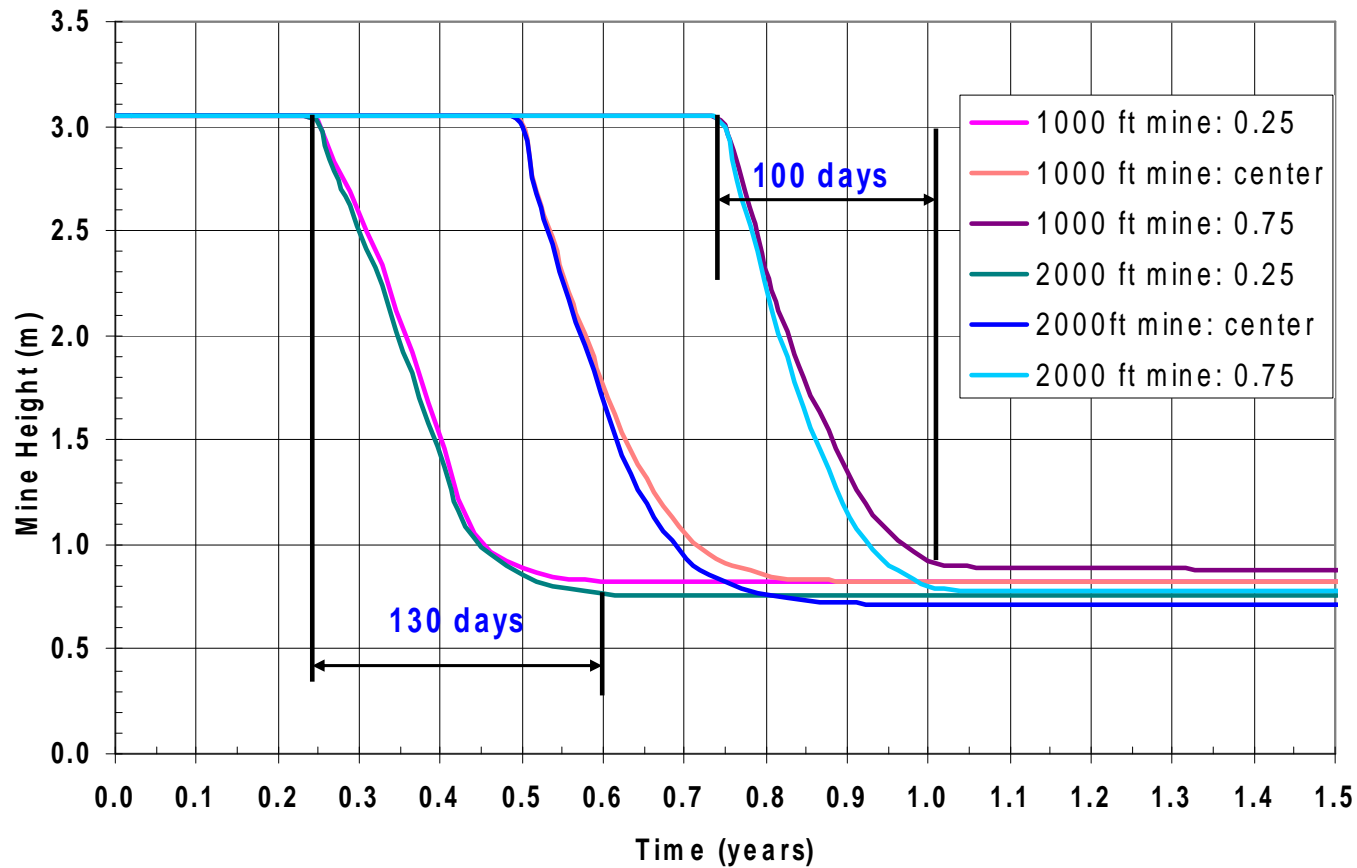


Figure 3.1.38. Comparison of Mine Closure Rates for 304.8 m (1000 ft) and 609.6 m (2000 ft) Mines (1.6 km, or 1 mile, Long; 1.6 km/year, or 1 mile/year, Excavation Rate)

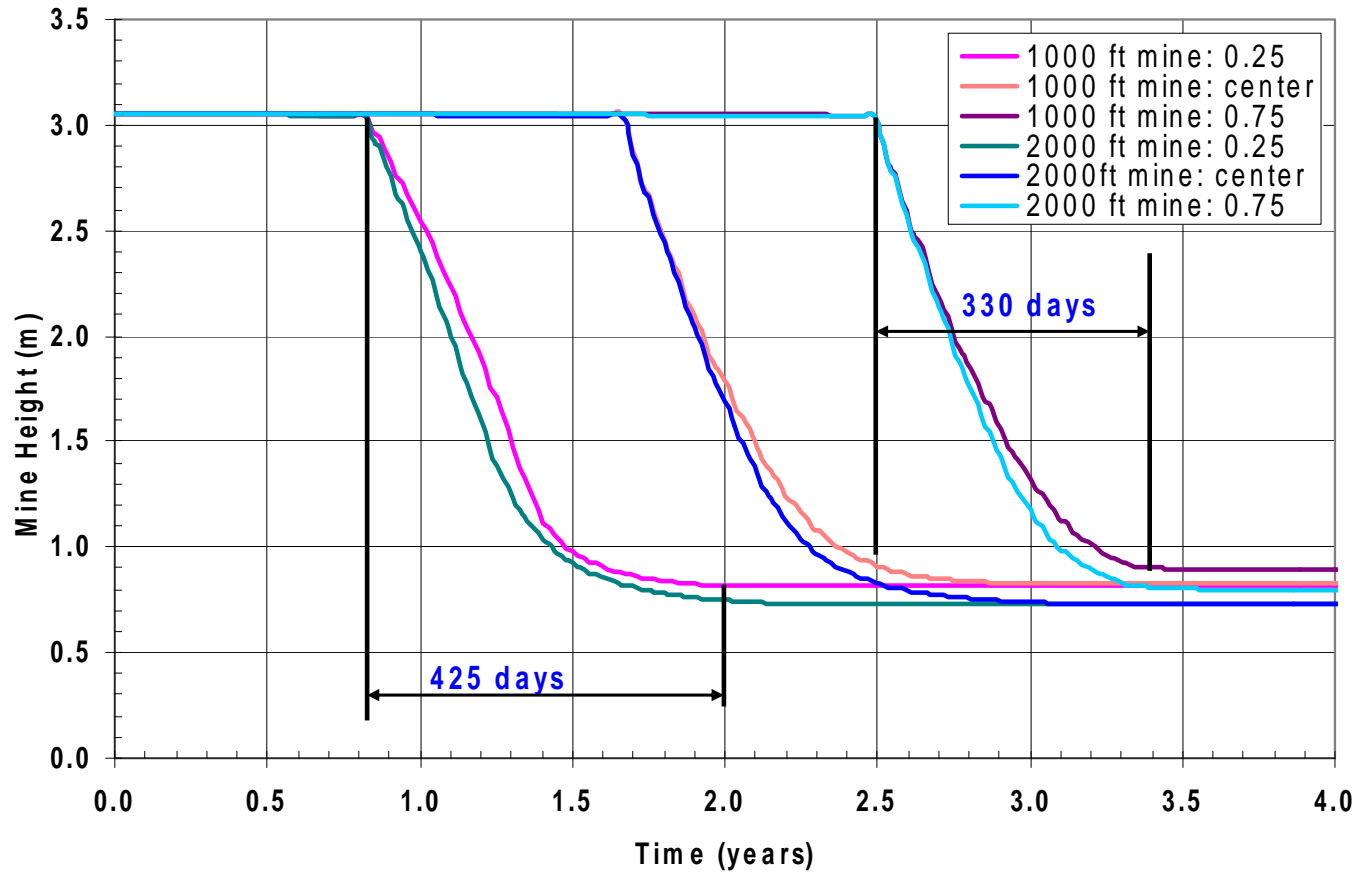


Figure 3.1.39. Comparison of Mine Closure Rates for 304.8 m (1000 ft) and 609.6 m (2000 ft) Mines (1.6 km, or 1 mile, Long; 0.48 km/year, or 0.3 mile/year, Excavation Rate)

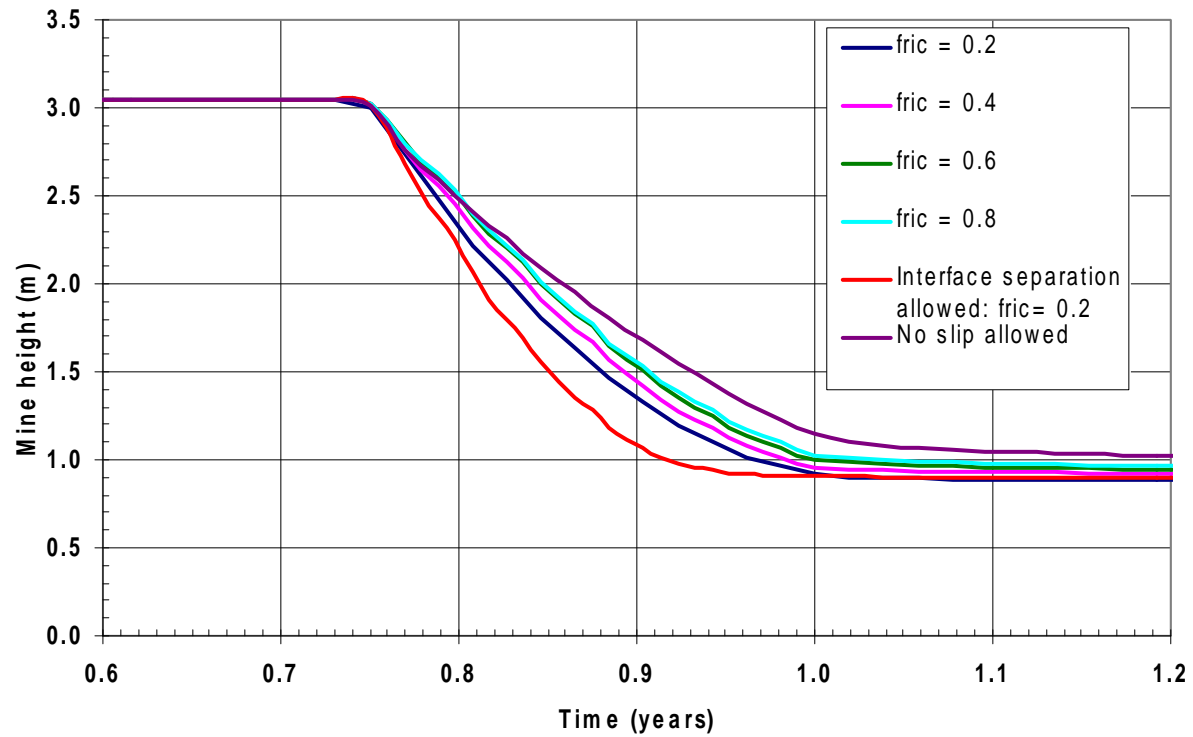


Figure 3.1.40. Effect of Interface Properties on Mine Closure for 304.8 m (1000 ft) Mine (1.2 km, or 3/4 mile, Point; 1.6 km, or 1 mile, Long; 1.6 km/year, or 1 mile/year, Excavation Rate)

3.2. Wellbore Model Results

Results from the simulations using the Wellbore Model for both the single and double casing situations are presented in this section. The primary quantity of interest from a results perspective is the condition of the casing(s) after slippage of an interbed. In particular, what sort of straining does the casing undergo? Does it initially remain elastic and for how much interbed movement does it remain elastic? Given sufficient interbed slip, does it eventually yield and start accumulating plastic strain and how much?

3.2.1. Single Casing

Figure 3.2.1 shows a zoomed-in view of the deformed shape of the configuration after a relative slip of 9.525 mm (3/8 in.) along the interbed between the top and bottom portions of the Wellbore Model. The upper materials have been “lightened” in the visualization so that the interface is visible. In this figure, the movement of the top is toward the right relative to the bottom. The upper left and the lower right portions of the surrounding formation adjacent to the cement/casing undergo an increase in compressive stress over the initial value, while the upper right and the lower left portions of the surrounding formation adjacent to the cement/casing undergo a decrease in compressive stress below the initial value. As a consequence, these changes in stress result in the deformation of the cement and casing in the vicinity of the interface, as seen in the figure.

Figure 3.2.2 shows the deformed shape of the casing (isolated from the cement and surrounding formation) due to this 9.525 mm (3/8 in.) slip along the interbed. The results show that there is a visible permanent offset between the upper and lower portions of the casing.

To understand how the load is transmitted from the relative movement of the surrounding formation along the interbed into the casing, it is instructive to see what happens to the cement. Figure 3.2.3 shows a zoomed-in view of the cement isolated from the rest of the materials at two levels of slip along the interbed. The upper figure shows the fringes of equivalent plastic strain (EQPS) in the cement at approximately 0.95 mm (~3/80 in.) of interbed slip, and the lower figure shows fringes of EQPS in the cement at 9.525 mm (3/8 in.) of interbed slip. The presence of plastic strains indicates that the cement has been stressed beyond its elastic range and is behaving inelastically. Notice that the scales on the two fringe plots are different, the one in the upper figure has a maximum range of 3.8% EQPS while the one in the lower figure has a maximum range of 65.0% EQPS. Thus, the upper figure indicates that even at the relatively small value of approximately 0.95 mm (~3/80 in.) of interbed slip, there is already a nontrivial amount of plastic strain that has accumulated in the cement along a significant portion of its circumference. The lower figure shows that by the time the interbed slip has reached 9.525 mm (3/8 in.), the cement has undergone quite large strains in the inelastic regime, with much of the circumference at more than 30% plastic strain and a smaller amount reaching plastic strains as high as 65%. This large amount of plastic straining indicates that the cement is quite damaged and incapable of resisting further movement, but instead is moving along with the surrounding formation and transmitting the load into the casing.

The deformation of the casing in Figure 3.2.2 is an indirect indicator of the state of the casing, in terms of whether it has yielded or not. Figure 3.2.4 shows fringe plots of the equivalent plastic strain (EQPS) at two levels of slip of the interbed (note that again the upper portion of the casing has been removed for clarity). EQPS begins to register as non-zero only after there has been yielding of the casing. The upper plot in the figure shows color fringes of EQPS in the casing after ~0.95 mm (~3/80 in.) of slip along the interbed. It is at this level of interbed slip that the casing first yields all the way through its thickness in the area denoted by red in the upper plot of the figure. Note by the scale on this upper plot, that the maximum EQPS is relatively small, at this level of interbed slip (~3/80 in.), on the order of 0.2% plastic strain.

The lower plot in Figure 3.2.4 is a fringe plot of EQPS in the casing after 9.525 mm (3/8 in.) of slip along the interbed. Note the different scale of this fringe plot from the one above it. As indicated by this scale, at this level of interbed slip (3/8 in.), the maximum EQPS has reached 12.5% along a large section of the circumference of the casing (as indicated in red). A plastic strain in the range of ~12% corresponds to the strain at the ultimate strength of the material in a tensile test specimen of the K55 material (e.g., Matthiasson and Ingason, 2007). Plastic strains on the order of those seen for the maximum in this lower plot could lead to initiation of tearing of the material in that region.

To further quantify the development of the plastic strain with slip along the interbed, Figures 3.2.5–3.2.7 show the plastic strain as a function of slip along the interbed at three locations along the circumference, as indicated by the Locations A, B, and C in Figure 3.2.4 above. Each of the figures shows the development of the plastic strain in three elements through the thickness of the casing. Shown are EQPS for the elements at the inner and outer surfaces of the casing and a third element in the interior; the last one to yield and begin accumulating plastic strain.

Figure 3.2.5 shows that the outer surface element at “Location A” is the first to yield, at that location, when the interbed slip reaches a value of approximately 2.6 mm (~0.10 in.). At “Location A,” that element also undergoes the largest plastic strain accumulation, reaching a value of approximately 1.15% by the time the interbed has slipped 9.525 mm (3/8 in.). At “Location A,” the last element through the casing thickness that yields does so at an interbed slip of approximately 8.4 mm (~0.33 in.) and goes on to accumulate approximately 0.08% plastic strain.

Figure 3.2.6 shows that all three elements through the casing thickness at “Location B” yield almost simultaneously at that location when the interbed slip reaches a value of approximately 0.80 mm (~0.03 in.). *Hence, it should be noted that the casing first yields through its thickness in this general location and does so at an interbed slip of approximately 0.80 mm (~0.03 in.).* Thereafter, all three elements accumulate plastic strain that reaches a value of approximately 12.5% by the time the interbed has slipped 9.525 mm (3/8 in.).

Figure 3.2.7 shows that the outer surface element at “Location C” is again the first to yield, at that location, when the interbed slip reaches a value of approximately 2.6 mm

(~0.10 in.). At “Location C,” that element also undergoes the largest plastic strain accumulation, reaching a value of approximately 1.07% by the time the interbed has slipped 9.525 mm (3/8 in.). At “Location C,” the last element through the casing thickness that yields does so at an interbed slip of approximately 8.1 mm (~0.32 in.) and goes on to accumulate approximately 0.09% plastic strain.

The fact that the casing has yielded through the thickness at all three locations at an interbed slip of 8.4 mm (~0.33 in.) indicates that the entire circumference of the casing has yielded at this value of interbed slip. By the time interbed slip reaches a value of 9.525 mm (3/8 in.), the upper half of the wellbore model is moving relative to the lower half without further resistance from the casing. Any further interbed slip, beyond 9.525 mm (3/8 in.) will only result in further accumulation of plastic strain until the entire cross-section tears.

3.2.2. Double Casing

Figure 3.2.8 shows a zoomed-in view of the deformed shape of the doubly cased configuration after a relative slip of 9.525 mm (3/8 in.) along the interbed between the top and bottom portions of the Wellbore Model, similar to Figure 3.2.1 for the singly cased model. Once again, the upper materials have been “lightened” in the visualization so that the interface is visible. As was the case for the previous single casing model, the movement of the top is toward the right relative to the bottom. The upper left and the lower right portions of the surrounding formation adjacent to the cement/casing undergo an increase in compressive stress over the initial value, while the upper right and the lower left portions of the surrounding formation adjacent to the cement/casing undergo a decrease in compressive stress below the initial value. As a consequence, these changes in stress result in the deformation of the two cement annuli and the two casings in the vicinity of the interface, as seen in the figure.

Figure 3.2.9 shows the deformed shape of the casings (isolated from the cement and surrounding formation) due to this 9.525 mm (3/8 in.) slip along the interbed. The results show that there is a visible permanent offset between the upper and lower portions of both of the casings.

To understand how the load is transmitted from the relative movement of the surrounding formation along the interbed into the two casings, it is instructive to see what happens to the cement. Figure 3.2.10 shows a zoomed-in view of the cement isolated from the rest of the materials at two levels of slip along the interbed. The upper figure shows the fringes of equivalent plastic strain (EQPS) in the cement at approximately 2.10 mm (~7/80 in.) of interbed slip, and the lower figure shows fringes of EQPS in the cement at 9.525 mm (3/8 in.) of interbed slip. The presence of plastic strains indicates that the cement has been stressed beyond its elastic range and is behaving inelastically. Notice that the scales on the two fringe plots are different, the one in the upper figure has a maximum range of 3.8% EQPS while the one in the lower figure has a maximum range of 65.0% EQPS. Thus, the upper figure indicates that even at the small value of approximately 2.10 mm (~7/80 in.) of interbed slip, there is already a nontrivial amount of plastic strain that has accumulated in the cement along a significant portion of its

circumference, for the outer cement ring. The lower figure shows that by the time the interbed slip has reached 9.525 mm (3/8 in.), this same outer cement ring has undergone quite large strains in the inelastic regime, with much of the circumference at more than 15% plastic strain and a smaller amount reaching plastic strains as high as 40%. This relatively large amount of plastic straining indicates that the cement is quite damaged and incapable of resisting further movement, but instead is moving along with the surrounding formation and transmitting the load into the casing, even at this value of interbed slip with two casings present.

The deformation of the two casings in Figure 3.2.9 above is an indirect indicator of the state of the casing, in terms of whether they have yielded or not. Figure 3.2.11 shows fringe plots of the equivalent plastic strain (EQPS) at two levels of slip of the interbed (note that again the upper portions of the casing have been removed for clarity). EQPS begins to register as non-zero only after there has been yielding of the casing. The upper plot in the figure shows color fringes of EQPS in the casing after ~2.10 mm (~7/80 in.) of slip along the interbed. It is at this level of interbed slip that the inner casing first yields all the way through its thickness in the area of the inner casing denoted by red in the upper plot of the figure. Note that the outer casing has also already yielded through its thickness in the same general vicinity. As denoted by the scale on this upper plot, the maximum EQPS is relatively small, at this level of interbed slip (~7/80 in.), on the order of 0.2% plastic strain.

The lower plot in Figure 3.2.11 is a fringe plot of EQPS in the casings after 9.525 mm (3/8 in.) of slip along the interbed. Note the different scale of this fringe plot from the one above it. As indicated by this scale, at this level of interbed slip (3/8 in.), the maximum EQPS has reached ~8.0% along a large section of the circumference of both the inner and outer casings (as indicated in green).

To further quantify the development of the plastic strain with slip along the interbed, Figures 3.2.12–3.2.17 show the plastic strain as a function of slip along the interbed at three locations along the circumference, as indicated by the Locations A, B, and C in Figure 3.2.11 referenced above. Each of the figures shows the development of the plastic strain in the three elements through the thickness of the casing, for an interbed slip of up to 9.525 mm (3/8 in.). Shown are EQPS for the elements at the inner and outer surfaces of the casing and a third element in the interior; the last one to yield and begin accumulating plastic strain.

Figure 3.2.12 shows that the inner surface element of the inner casing (IC) at “Location A” is the first to yield, at that location, when the interbed slip reaches a value of approximately 6.0 mm (~0.24 in.). At “Location A,” that element also undergoes the largest plastic strain accumulation, early on, reaching a value of approximately 0.2% by the time the interbed has slipped 9.525 mm (3/8 in.). At “Location A,” the last element through the inner casing thickness that yields does so at an interbed slip of approximately 8.6 mm (~0.34 in.) and goes on to accumulate approximately 0.04% plastic strain. The last element through the outer casing (OC) thickness that yields does so at an interbed slip greater than 9.525 mm (3/8 in.). To show this, Figure 3.2.13 is the same plot as Figure 3.2.12, but now extended to an interbed slip of approximately 25 mm (1.0 in.).

The last element in the outer casing to yield at “Location A” does so at an interbed slip of 12.0 mm (0.47 in.). The inner surface element of the outer casing accumulates the most plastic strain at this location, reaching a value of 2.5% plastic strain at an interbed slip of approximately 25 mm (1.0 in.).

Figure 3.2.14 shows that all three elements through the casing thickness at “Location B,” for both the inner and outer casings yield almost simultaneously at that location when the interbed slip reaches a value of approximately 1.6 mm (~0.06 in.). *Hence, it is in this general location that the inner casing first yields through its thickness and the value of interbed slip at which this happens is 1.6 mm (~0.06 in.).* Thereafter, all three elements in the outer casing accumulate plastic strain that reaches a value of approximately 8.2% and all three elements in the inner casing accumulate plastic strain that reaches a value of approximately 5.4% by the time the interbed has slipped 9.525 mm (3/8 in.). Figure 3.2.15 shows the same information but extended to an interbed slip of approximately 25 mm (1.0 in.). At this value of interbed slip and at this location, the figure shows that the outer casing has accumulated 22% plastic strain and the inner casing has accumulated 15% plastic strain and, at these levels of plastic strain, tearing is likely initiating or progressing in both.

Figure 3.2.16 shows that the inner surface element of the inner casing at “Location C” is again the first to yield, at that location, when the interbed slip reaches a value of approximately 5.8 mm (~0.23 in.). At “Location C,” that element also undergoes the largest plastic strain accumulation, initially, reaching a value of approximately 0.21% by the time the interbed has slipped 9.525 mm (3/8 in.). At “Location C,” the last element through the inner casing thickness that yields does so at an interbed slip of approximately 8.2 mm (~0.32 in.) and goes on to accumulate approximately 0.05% plastic strain at an interbed slip of 9.525 mm (3/8 in.). The outer casing remains elastic up to an interbed slip of 9.525 mm (3/8 in.), as seen in Figure 3.2.16, but eventually goes plastic. To show this, Figure 3.2.17 is the same plot as Figure 3.2.16, but now extended to an interbed slip of approximately 25 mm (1.0 in.). At “Location C,” the outer surface element is the first element in the outer casing to go plastic and does so at an interbed slip of approximately 10.0 mm (0.39 in.). It goes on to accumulate the most plastic strain at this location, reaching a value of slightly less than 2.0% plastic strain. The last element to go plastic in the outer casing, at this location, is an interior element and does so at an interbed slip of approximately 14.0 mm (0.55 in.).

Once again, the fact that both of the casings (inner and outer) have yielded through the thickness at all three locations at an interbed slip of approximately 14.0 mm (0.55 in.) indicates that the entire circumferences of both casings have yielded. Any further interbed slip, beyond 14.0 mm (0.55 in.) will only result in further accumulation of plastic strain until the entire cross-sections of both the inner and outer casings tear.

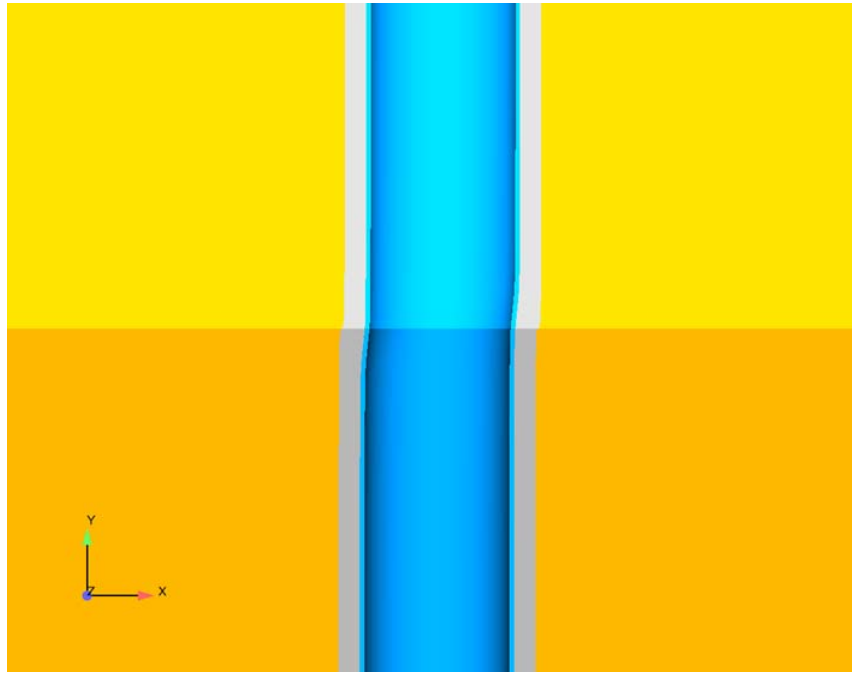


Figure 3.2.1. Zoomed-In View of Deformed Configuration After 3/8 in. Relative Slip Along the Interbed

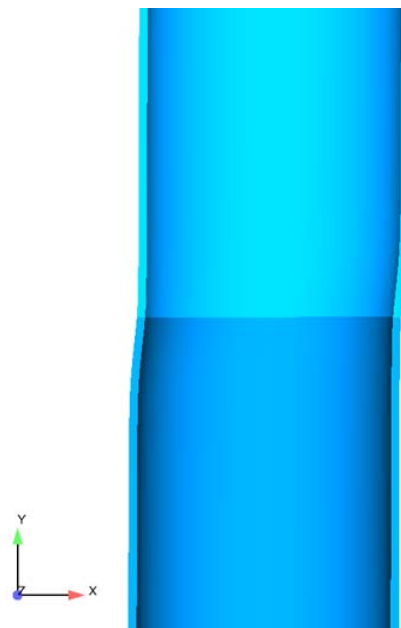


Figure 3.2.2. Zoomed-In View of Deformed Casing After 3/8 in. Relative Slip Along the Interbed in its Vicinity

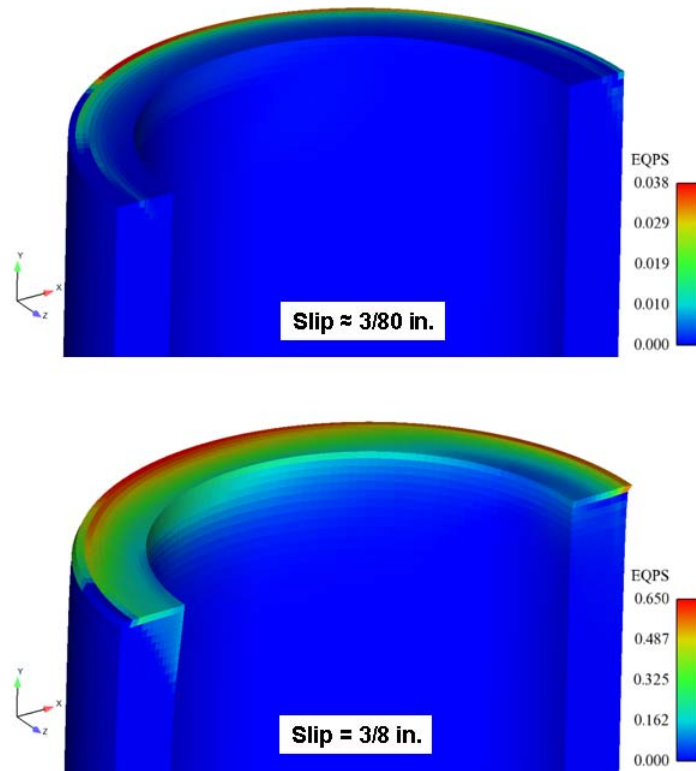


Figure 3.2.3. Zoomed-In View Showing Plastic Strain in the Cement After \sim 3/80 & 3/8 in. Relative Slip of the Interbed (Upper Portion of Cement Removed For Clarity)

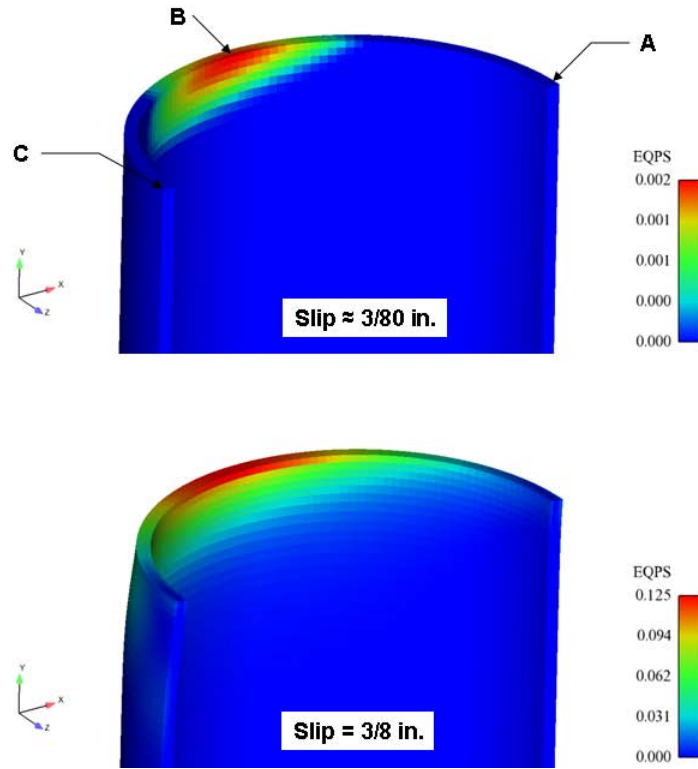


Figure 3.2.4. Zoomed-In View Showing Plastic Strain in the Casing After ~3/80 & 3/8 in. Relative Slip of the Interbed (Upper Portion of Casing Removed For Clarity)

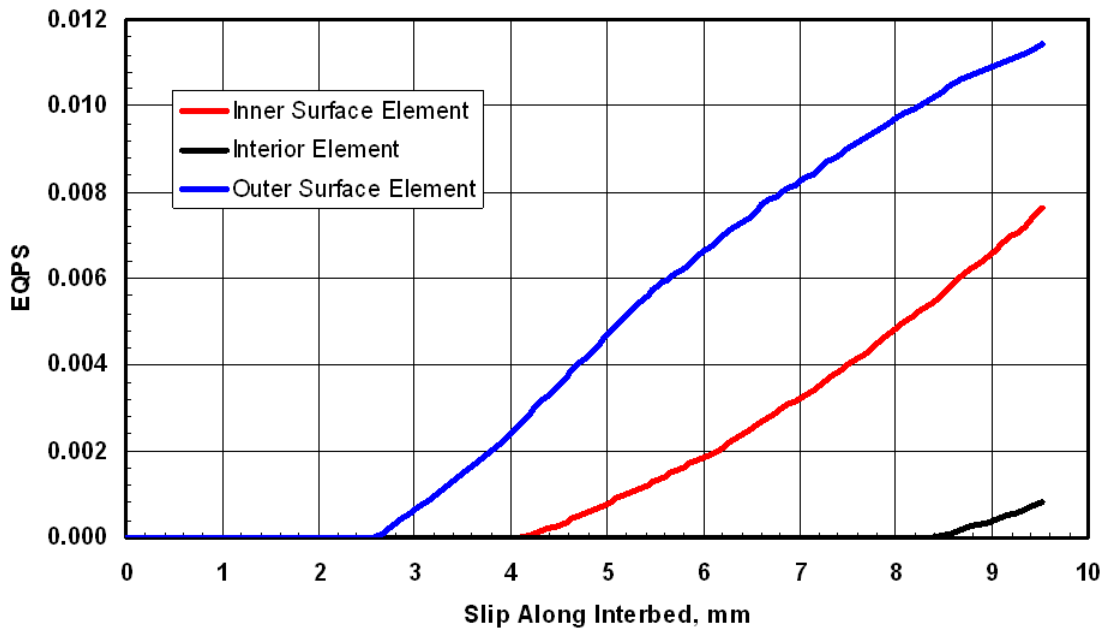


Figure 3.2.5. Development of EQPS with Slip Along the Interbed for the Three Elements Through the Thickness at Location A in the Casing, For Interbed Slip of Up to 3/8 in.

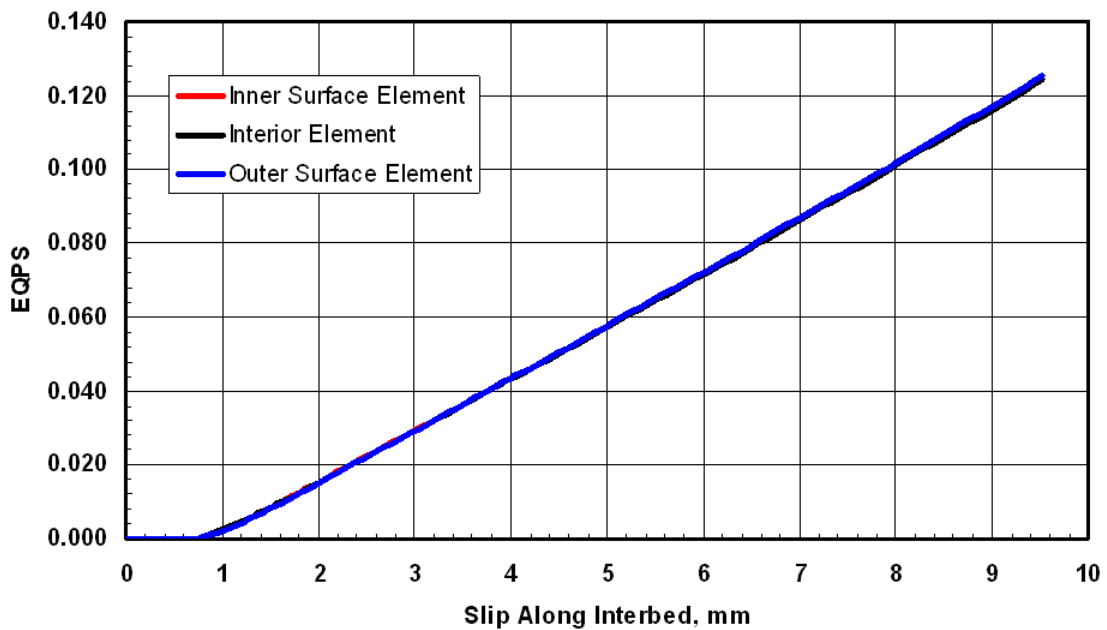


Figure 3.2.6. Development of EQPS with Slip Along the Interbed for the Three Elements Through the Thickness at Location B in the Casing, For Interbed Slip of Up to 3/8 in.

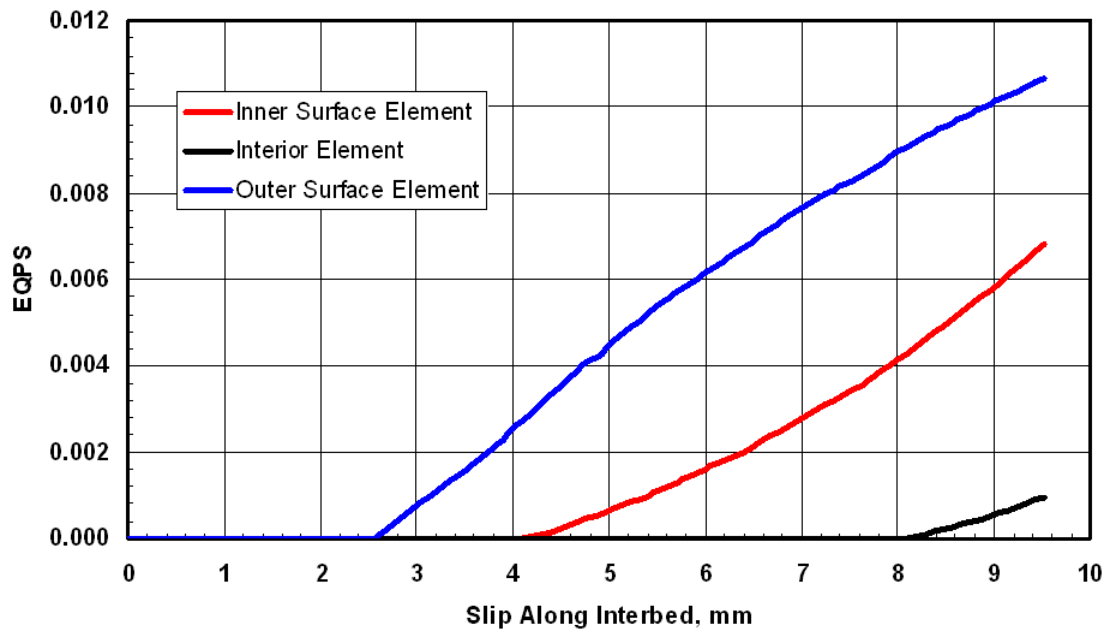


Figure 3.2.7. Development of EQPS with Slip Along the Interbed for the Three Elements Through the Thickness at Location C in the Casing, For Interbed Slip of Up to 3/8 in.

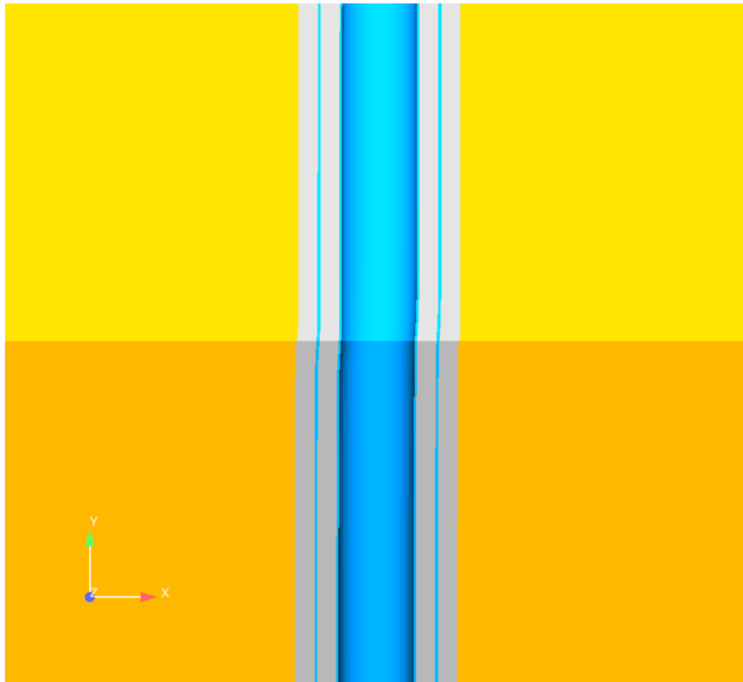


Figure 3.2.8. Zoomed-In View of Deformed Double Casing Configuration After 3/8 in. Relative Slip Along the Interbed

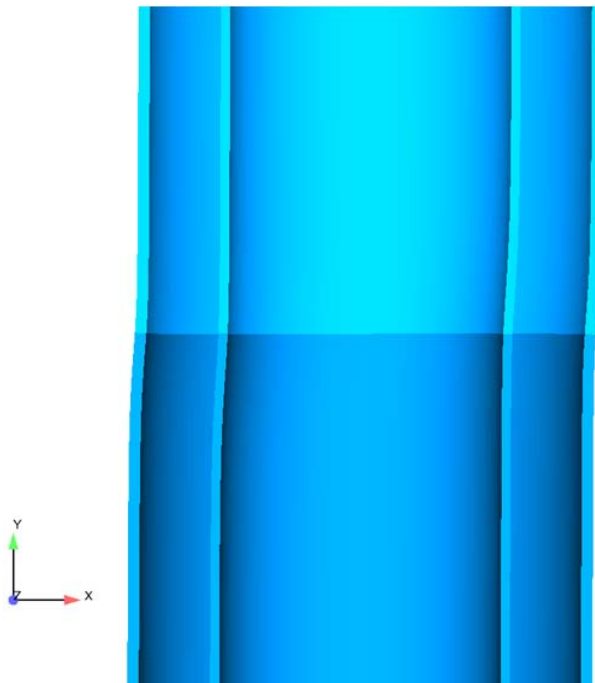


Figure 3.2.9. Zoomed-In View of Deformed Casings in Double Casing Model After 3/8 in. Relative Slip Along the Interbed in its Vicinity

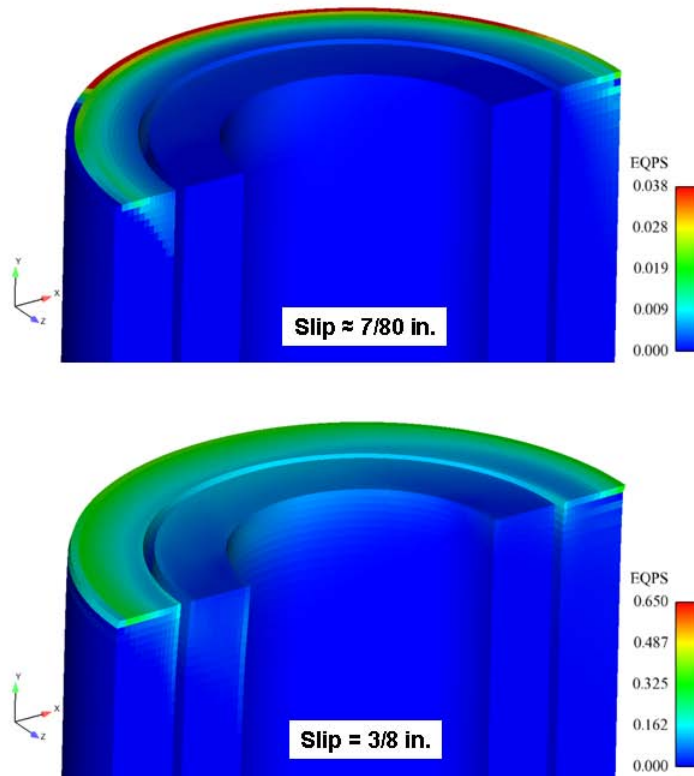


Figure 3.2.10. Zoomed-In View Showing Plastic Strain in the Two Cement Annuli After $\sim 7/80$ & $3/8$ in. Relative Slip of the Interbed (Upper Portion of Cement Removed For Clarity)

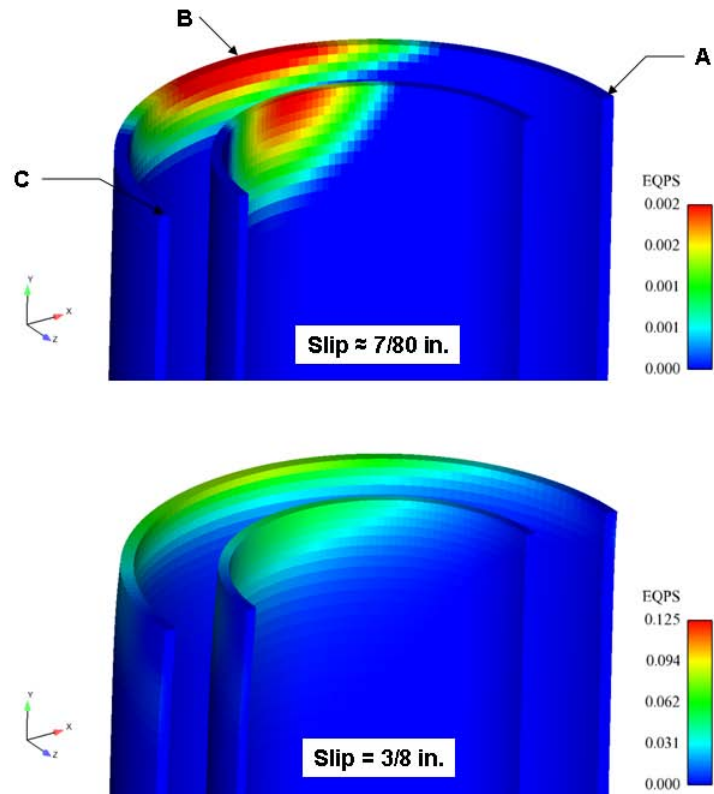


Figure 3.2.11. Zoomed-In View Showing Plastic Strain in the Two Casings After $\sim 7/80$ & $3/8$ in. Relative Slip of the Interbed (Upper Portions of Casing Removed For Clarity)

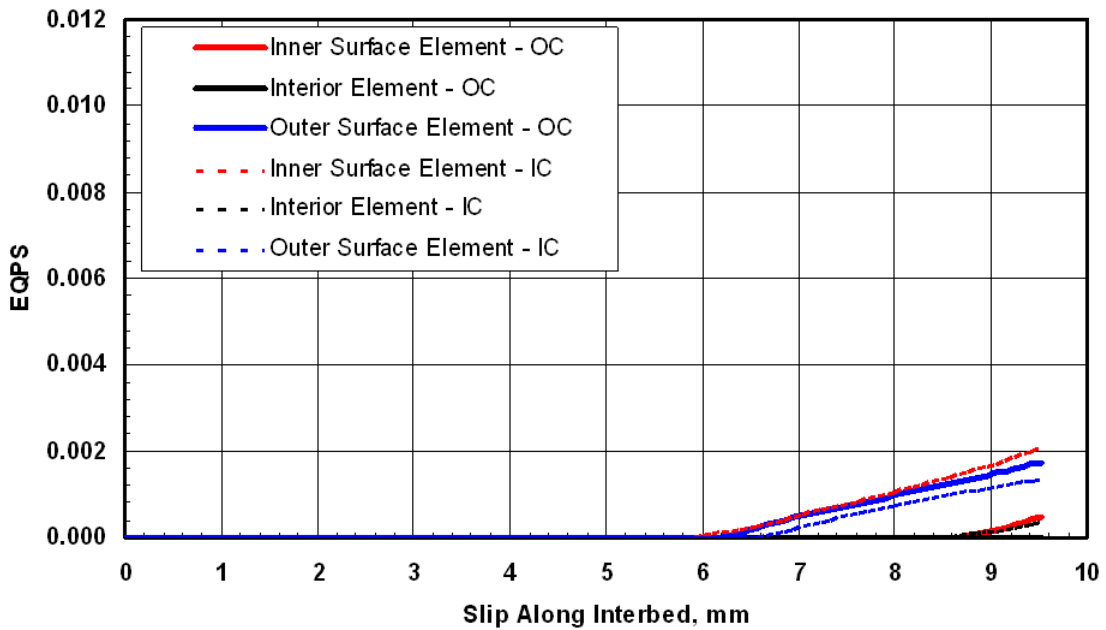


Figure 3.2.12. Development of EQPS with Slip Along the Interbed for the Three Elements Through the Thickness at Location A in Each of the Two Casings, For Interbed Slip of Up to 3/8 in.

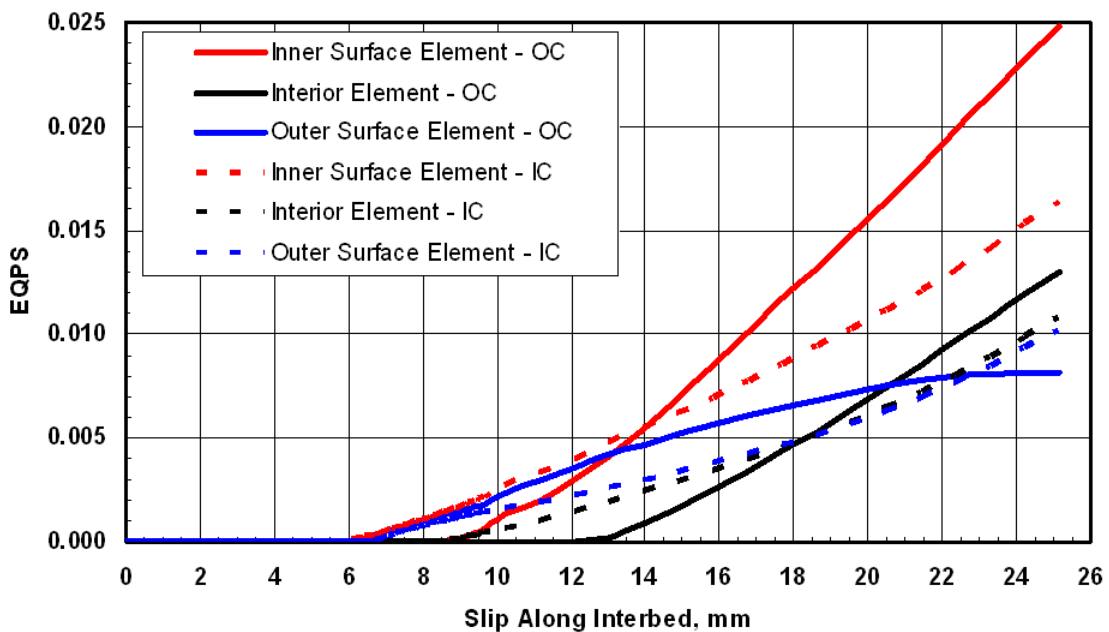


Figure 3.2.13. Development of EQPS with Slip Along the Interbed for the Three Elements Through the Thickness at Location A in Each of the Two Casings, For Interbed Slip of Up to ~1.0 in.

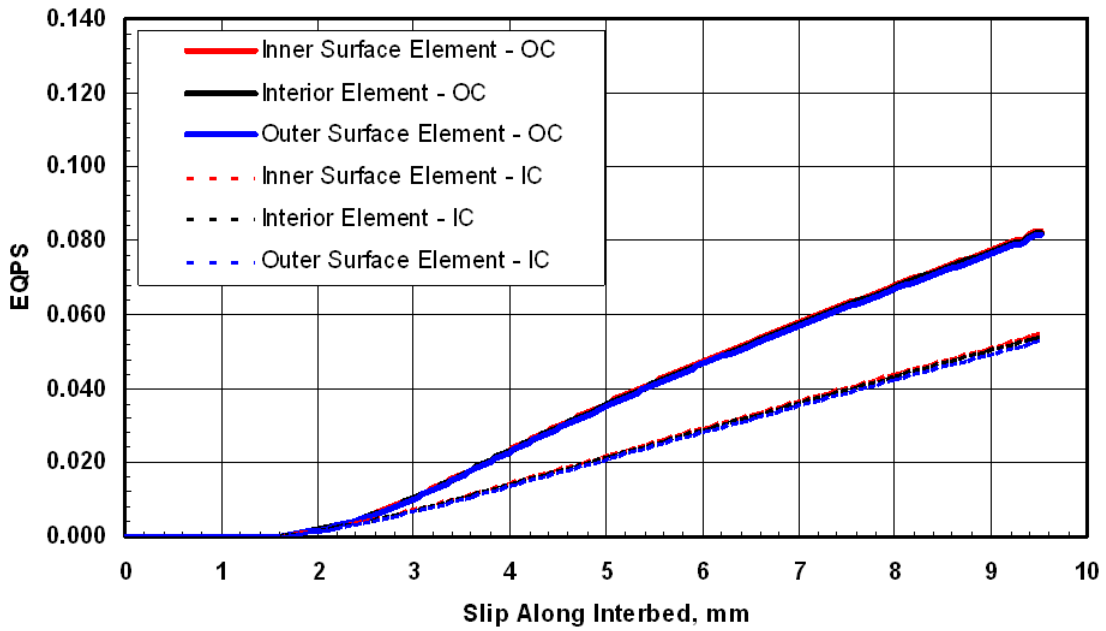


Figure 3.2.14. Development of EQPS with Slip Along the Interbed for the Three Elements Through the Thickness at Location B in Each of the Two Casings, For Interbed Slip of Up to 3/8 in.

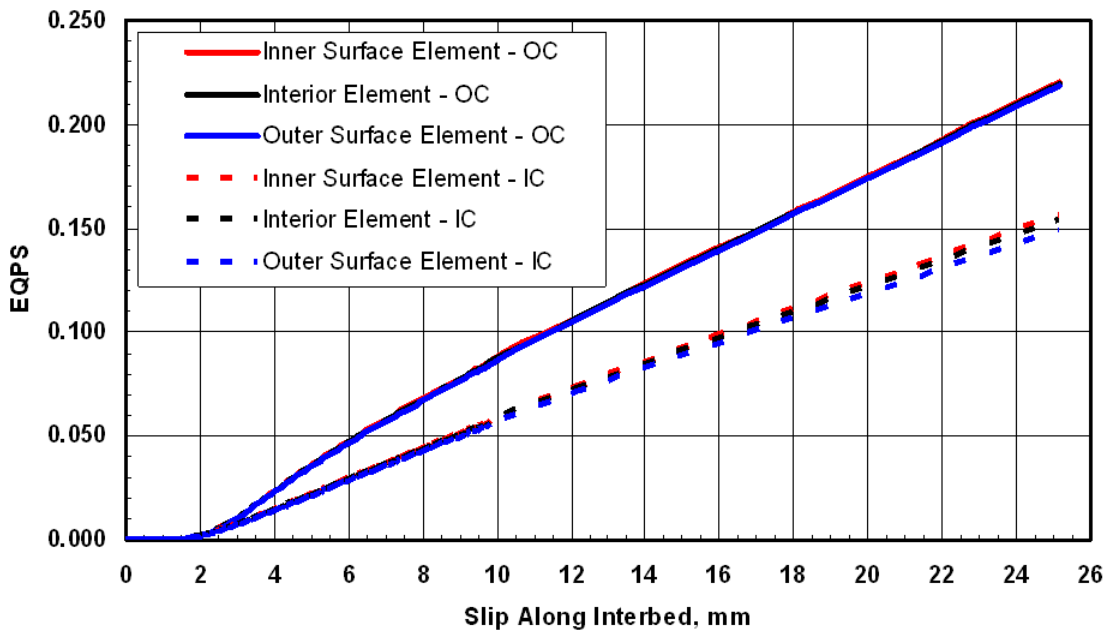


Figure 3.2.15. Development of EQPS with Slip Along the Interbed for the Three Elements Through the Thickness at Location B in Each of the Two Casings, For Interbed Slip of Up to ~1.0 in.

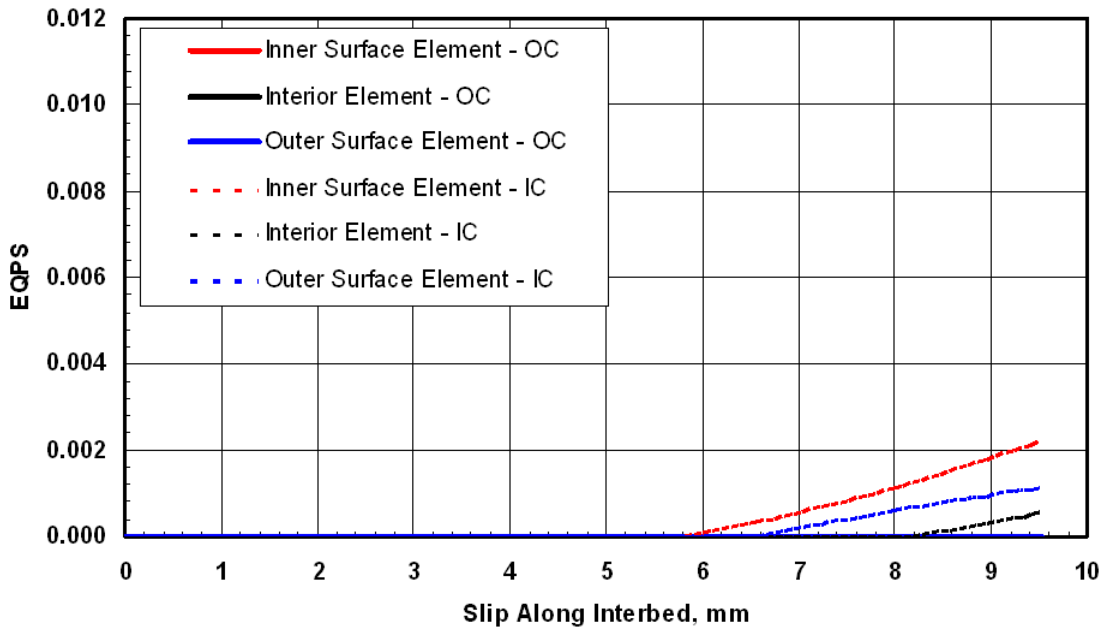


Figure 3.2.16. Development of EQPS with Slip Along the Interbed for the Three Elements Through the Thickness at Location C in Each of the Two Casings, For Interbed Slip of Up to 3/8 in.

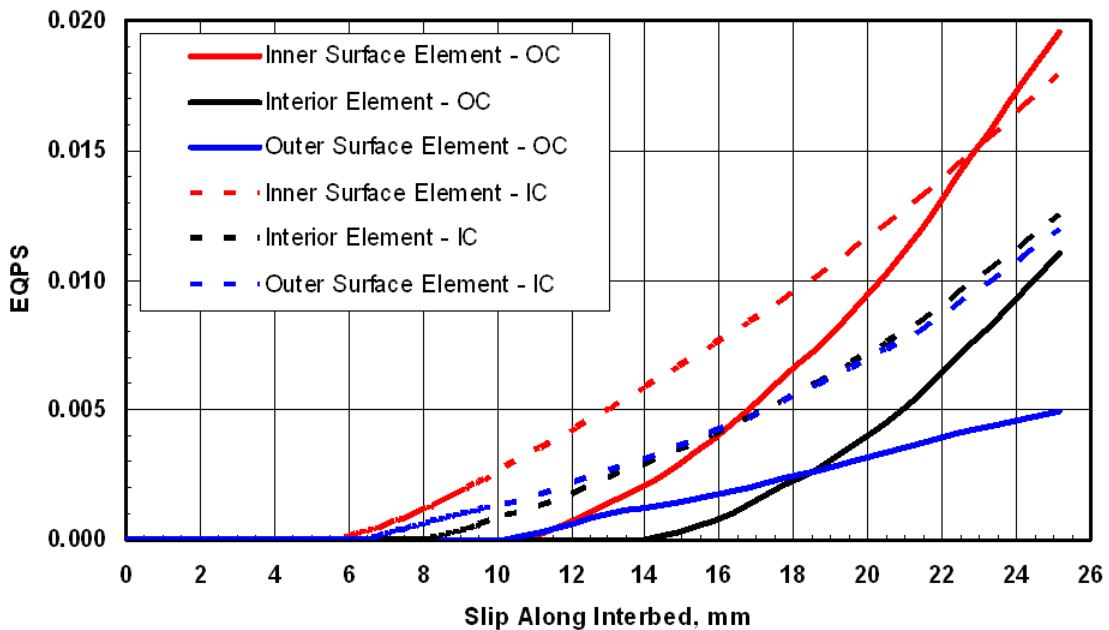


Figure 3.2.17. Development of EQPS with Slip Along the Interbed for the Three Elements Through the Thickness at Location C in Each of the Two Casings, For Interbed Slip of Up to ~1.0 in.

4. Summary & Conclusions

In summary, as proposed in the analysis plan, two basic models were used in this study; a Global Mine Excavation Model that simulates the mechanics associated with mining and subsidence, and a Wellbore Model that examines the resulting impacts on wellbore casing for two generic, but what are considered typical, casing situations. The Global Model is a 2D approximation of a potash mine using a plane strain idealization for a 3.048 m (10 ft) high mine at a depth of 304.8 m (304.8 m (1000 ft)) or a depth of 609.6 m (609.6 m (2000 ft)). It incorporates a number of bedding planes present in the subsurface, both above and below the mine. A 2D model is considered reasonable given the large areal extent of the mine relative to the mine depth. The 3D Wellbore Model considers the impact of bedding plane slippage across single and double cased wells cemented through the Salado formation, as is typical of contemporary completions. The Wellbore Model is used to determine allowable slippage to prevent casing through-the-thickness yield. The predicted slippage across bedding planes from the global mine model are then compared to the allowable wellbore slippages to establish safe standoff distances between a mine and well, for the casing designs considered in the study.

4.1. Global Mine Excavation Model

From the Global Mine Excavation Model, numerical predictions of interbed slip magnitude were presented as a function of distance for a 304.8 m (1000 ft) and 609.6m (2000 ft) deep mine. These simulations were used to examine the influence of mining direction, mine length, and mine excavation rates. Subject to the assumptions used in the analyses, the following observations and conclusions are provided:

- the slip magnitude was generally largest on the uppermost marker bed,
- depending on mine depth and mining direction, the distance from the mine boundaries to the points where no slip occurs is between 600 m (~1970 ft) and 1100 m (~3610 ft) from the edge of the mine excavation, and
- large interbed slip magnitudes (greater than 0.5 m or ~20 in.) were predicted to occur on some interfaces over the mine excavation and would be expected to impact wells that have been mined around.

Although this study has primarily focused on slip occurring away from the mined area it must be noted that there is substantial slip predicted in the area directly over the excavation. This poses questions about the impact of interface slip on the existing wells in regions where mining has already occurred.

There are several sources of uncertainty in these Global Mine Excavation Model analyses (e.g., differences in material properties from those assumed in the analyses; the existence of more/less marker beds than used in the analyses; differences in the vertical locations of the marker beds; etc.) that could influence the predicted results. As noted in the analysis plan of Appendix I (section on “Evaluation of Results”), the impact of these uncertainties on the results could be accounted for with the use of a safety factor.

4.2. Wellbore Model

From the Wellbore Model, subject to the assumptions used in the analyses, there are two major conclusions:

- for the single-casing situation, the casing first yields through its thickness with very little interbed slip, namely at 0.80 mm (~0.03 in.) of slip, and
- adding a second cemented casing around it only doubles the amount of interbed slip needed for the inner casing to yield through its thickness, namely to 1.6 mm (~0.06 in.) of slip.

Other noteworthy observations from the Wellbore Model are as follows:

- for the single-casing situation, the *entire* cross-section of the casing first yields when the interbed slip reaches a value of ~8.4 mm (0.33 in.) – at this value of interbed slip the largest plastic strain in the casing is approaching ~11.0% (close to the maximum uniform strain from uniaxial test data observed for this material); beyond this value of slip any additional interbed slip results in unimpeded movement of the top of the model relative to the bottom at the interbed, and
- for the double-casing situation, the *entire* cross-section of the inner casing first yields when the interbed slip reaches a value of ~8.6 mm (0.34 in.) – at this value of interbed slip the largest plastic strain in the inner casing is ~7.2%; similarly, the entire cross-section of the outer casing first yields when the interbed slip reaches a value of ~14.0 mm (0.55 in.) and beyond this value of slip any additional interbed slip results in unimpeded movement of the top of the model relative to the bottom at the interbed.

It should be noted that there are several sources of uncertainty in these analyses (e.g., potential differences in the steel properties from what was assumed, imperfect bonding between the various materials, formation strength differences, etc.) that could influence the predicted results. Again, as noted in the analysis plan (Appendix I, section “Evaluation of Results”), a safety factor could be used to account for this uncertainty.

4.3. Combined Models

Using the results from the Global Mine Excavation Model in combination with the results from the Wellbore Model, one can infer a standoff distance for the two wellbore designs considered in this study. Figure 4.3.1 shows the results from the Wellbore Model overlaid on top of the results from the Global Mine Excavation Model. It can be seen from this figure, for example, that for the 304.8 m (1000 ft) mine for the case of mining away from the well, a standoff distance of ~810 m (~2660 ft) would be required for a single-cased well. Similarly, a standoff distance of ~830 m (~2720 ft) would be required for a double-cased well. In both situations, these are the required standoff distances to prevent first yielding of the casing (or inner casing for the double-cased situation) through-its-thickness, i.e., the criteria put forth in the analysis plan of Appendix I.

In a similar fashion, the standoff distance for mining toward the well for the 304.8 m (1000 ft) mine can be estimated from Figure 4.3.1. Likewise, the standoff distance for both mining toward and away from the well for the 609.6 m (2000 ft) deep mine can also be estimated from the figure.

Using the general approach developed herein, it should be possible to evaluate other casing designs, beyond those considered in the Wellbore Model, which are more specific for a given site within the potash enclave of southeastern New Mexico, as long as the basic assumptions used to develop the Global Mine Excavation Model are properly considered.

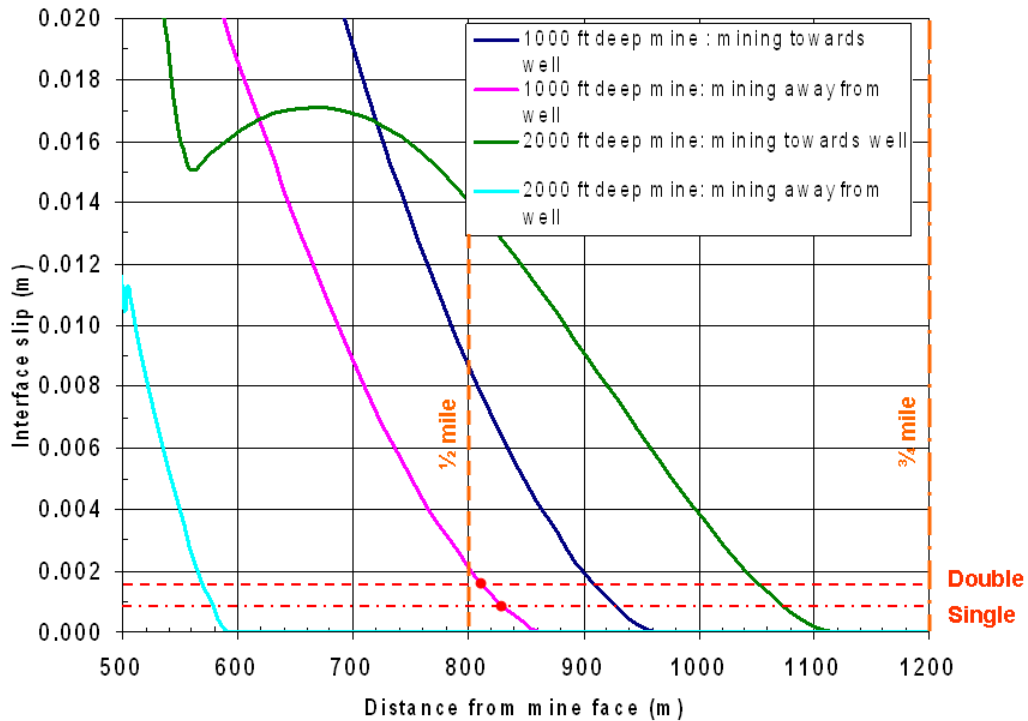


Figure 4.3.1. Slip Envelopes from the Global Mine Excavation Model versus Allowable Slip Prior to First Through-the-Thickness Yielding from the Wellbore Model.

5. References

Biffle, J. H., *JAC3D – A Three-Dimensional Finite Element Computer Program for the Nonlinear Quasi-Static Response of Solids with the Conjugate Gradient Method*, SAND87-1305, Sandia National Laboratories, Albuquerque, NM, 1993.

Blanford, M. L., Heinstein, M. W., and Key, S. W., *JAS3D A Multi-Strategy Iterative Code for Solid Mechanics Analysis User's Instructions, Release 2.0*, Draft SAND Report, Sandia National Laboratories, Albuquerque, NM, September 2001.

Fossum, A. F. and Brannon, R. M., *The Sandia Geomodel Theory and User's Guide*, SAND2004-3226, Sandia National Laboratories, Albuquerque, NM, 2004.

Krieg, R. D., *A Simple Constitutive Description for Cellular Concrete*, Sandia Report SC-DR-72-0883, Sandia National Laboratories, 1972.

Krieg, R. D. and Krieg, D. B., "Accuracies of Numerical Solution Methods for the Elastic-Perfectly Plastic Model," *ASME Journal of Pressure Vessel Technology*, vol. 99, pp. 510-515, 1977.

Krieg, R. D., *Reference Stratigraphy and Rock Properties for the Waste Isolation Pilot Plant (WIPP) Project*, SAND83-1908, Sandia National Laboratories, Albuquerque, NM, 1984.

Matthías Matthíasson and Kristinn Ingason, "Casing Design for Extreme Temperature," VGK Honnum, presented at a Workshop on Drilling Cost Effectiveness and Feasibility of High-Temperature Drilling, Reykjavik, Iceland, on July 3, 2007.
http://engine.brgm.fr/web-offlines/conference-Drilling_cost_effectiveness_and_feasibility_of_high-temperature_drilling_-_Reykjavik_Iceland_Workshop4/other_contributions/35-slides-0-15_KE-000-003a.pdf.
(last downloaded February 4, 2009).

Miller, E.M. and F.L. Pierson. *Underground Movement and Subsidence Over United States Potash Company Mine*. Society of Mining Engineers of A.I.M.E. Feb. 16-20, 1958.

Munson, D. E., "Constitutive Model of Creep of Rock Salt Applied to Underground Room Closure," *Int. J. Rock Mech. Min. Sci.*, Elsevier Science Ltd., Vol. 34, No. 2, pp. 233-247, 1997.

Munson, D.E. and DeVries, K. L., Progress in the Validation of Structural Codes for Radioactive Waste Repository Applications in Bedded Salt, *Proc. of GEOVAL-90*, OECD/NEA & SKI, Stockholm, Sweden, pp. 16-23, 1990.

Munson, D.E., DeVries, K.L. and Callahan, G.D, Comparison of Calculations and In Situ Results for a Large, Heated Test Room at the Waste Isolation Pilot Plant (WIPP), *Proc. 31st U.S. Symp. on Rock Mechanics*. AA. Balkerna, Brookfield, MA, pp 389-396, 1990.

Schreyer, H. L., Kulak, R. F., and Kramer, J. M., “Accurate Numerical Solutions for Elastic-Plastic Models,” *ASME Journal of Pressure Vessel Technology*, vol. 101, pp. 226-234, 1979.

Sjaardema, G. D. and R. D. Krieg. *A Constitutive Model for the Consolidation of WIPP Crushed Salt and Its Use in Analyses of Backfilled Shaft and Drift Configurations*”, SAND87-1977, Sandia National Laboratories, October, 1987.

Stone, C. M., Krieg, R. D., and Beisinger, Z. E., SANCHO – A Finite Element Computer Program for the Quasistatic, Large Deformation, Inelastic Response of Two-Dimensional Solids, SAND84-2618, Sandia National Laboratories, Albuquerque, NM, 1985.

Stone, C. M., SANTOS – A Two-Dimensional Finite Element Program for the Quasistatic, Large Deformation, Inelastic Response of Solids, SAND90-0543, Sandia National Laboratories, Albuquerque, NM, July 1997.

Taylor, L. M. and Flanagan, D. P., *PRONTO 3D A Three-Dimensional Transient Solid Dynamics Program*, SAND87-1912, Sandia National Laboratories, Albuquerque, NM, March 1989.

Van Sambeek, L.L., Ratigan, J.L., and Hansen, F.D., “Dilatancy of Rock Salt in Laboratory Tests,” *International Journal of Rock Mechanics and Mining Sciences and Geomechanics Abstracts*, Pergamon Press Ltd., Vol. 30, No. 7, pp. 735-738, 1993.

Appendix I: Analysis Plan for BLM Potash Gas Migration Study

(It should be noted that Appendix A contains several figures with “Confidential” and/or “For Case Use Only” markings. The markings should be considered obsolete artifacts, as these figures were declared public domain as part of the IBLA hearings.)

Analysis Plan for BLM Potash Gas Migration Study

Prepared by:

Sandia National Laboratories

P.O. Box 5800

Albuquerque, NM 87185-0706

Brian Ehgartner, blehgar@sandia.gov

Lupe Arguello

Jim Bean

Mike Stone

For:

US Dept of Interior

Bureau of Land Management

NM State Office

Santa Fe, NM 87502-0115

Bill Auby, bill_auby@blm.gov

John Matis, jmatis@blm.gov

Contract:

WFO 063070717

Potash Gas Migration Project

Version of Analysis Plan:

June 27, 2008

Draft for Stakeholder Review

Foreword

This version of the draft analysis plan was prepared for review by stakeholders. BLM has developed a list of stakeholders for both the oil and gas and potash industries along with state and federal government representatives, including WIPP. Comments on this plan are due back to Brian Ehgartner at Sandia within 60 days of delivery. At that time the comments will be incorporated into a final version of the plan and released at a date to be determined.

This plan was developed from litigation records provided by BLM and other sources of public information. While a non-disclosure agreement exists between Sandia and BLM, no proprietary or other company sensitive information (OUO) was transferred between the agencies for this project. BLM solicited industry stakeholders for technical information regarding the project but have not received anything as of the date of this writing. Perhaps enough has already been stated in the volumes of litigation, however the offer will remain open through the comment period for this draft plan as comments will need to be substantiated. As per earlier instructions to stakeholders, all information of a proprietary or confidential nature, including comments on this report, should be sent solely to Bill Auby at BLM for subsequent transmittal to Sandia.

After finalization of this plan, the analyses will be performed and a Sandia report will be prepared for BLM. That report will be reviewed both internally by Sandia and externally by competent, impartial, and unbiased reviewers. That will be the extent of Sandia's agreement with the BLM. Stakeholders should already have a copy of the Sandia_BLM work and non-disclosure agreements along with a list of the stakeholders. If not, please contact the BLM.

Please keep in mind that this is a draft plan. Your review is important to us, but your contributions are valued more so. Also it represents our current view of how we will proceed. This can change as we review your comments and contributions, and some changes may occur as we perform the analyses and better understand the mechanics associated with mine-well interactions. Our priority will be to best address the issue of gas migration. This plan does not constitute a contract.

Contents	pg
Foreword	2
Contents	3
List of Tables	4
List of Figures	5
Background	6
Regulations and Practice	6
Modeling Approach	7
Geology	13
Rock Properties	23
Mining Parameters	32
Field Measurements and Observations	33
Well Completions	50
Well Model and Properties	55
Model Variations	58
Evaluation of Results	61
Position on Gas Migration	62
Conclusion	63
References	64
APPENDIX A. Maps of Potash Area and Mines	69
APPENDIX B. Strength Data	79

List of Tables	pg
1. Model Variables	13
2. Description of Ochoan Rock	18
3. Stratigraphic Contacts for 1000 and 2000 ft Deep Mines	22
4. Reported Testing by CSM on MS Chemical Potash and Salt	25
5. Direct Shear Tests	25
6. Laboratory Determination of Elastic Properties of Potash	26
7. Comparison of Potash and Salt Strength	27
8. Elastic Properties	31
9. Reference Properties for WIPP Materials	31
10. Max Surface Strains and Subsidence at US Potash Mine	35
11. Angle of Draw and Break	40
12. Relationship between Subsidence and Closure at US Potash Mine	43
13. Mine Closure Data	47
14. Well Status in Mines	51
15. Typical Casing Specs.	52
16. Initial Pressure Gradients in Wells	55
17. Well Properties	55
18. Properties for Geomodel Cement	56
19. Well Model	57
20. Young's Moduli of Rocks from Handbooks	58
21. WIPP Crushed Salt Parameters	59
22. Drucker-Prager constants for anhydrite	60
23. Material properties of anhydrite	60

List of Figures	pg
1. Map of Potash Area	9
2. 2D Model Illustrations	10
3. 3D Model of Well	11
4. Inclusion of Stratigraphy into Models	12
5. North-South Cross-Section Across Potash Area	14
6. North-South Cross-Section showing location of Mines	15
7. Stratigraphic Column	16
8. Stratigraphic Column of the Ochoan	17
9. Upper Geologic Stratigraphy at WIPP	19
10. Lower Geologic Stratigraphy at WIPP	20
11. Stratigraphic Contact Depths	23
12. Potash Strength Testing	24
13. MS Chemical Data in Terms of Stress Invariants	27
14. New Mexico Potash Creep Tests	29
15. Steady-State Strain Rates Inferred from Testing Pillars in Laboratory	30
16. Location of Mines	32
17. Subsidence Measurements over US Potash Mine	35
18. Subsidence and Strain over the Modified Longwall Operation	36
19. Subsidence and Strain over the Longwall Operation	37
20. Subsidence and Strain over the Conventional Operation	38
21. Horizontal ground movement at US Potash Mine	39
22. Subsidence Profiles above US Potash Mine	41
23. Subsidence over the US Potash Mine	42
24. Subsidence and Closure at US Potash Mine	43
25. Subsidence Stations over Wills Weaver Mine	44
26. Subsidence Measurements over 1st North Panel	45
27. Subsidence Measurements over 2 nd North Panel	45
28. Subsidence Measurements over AMAX Mine	46
29. Location of Closure Measurements at Wills-Weaver	48
30. Measured Convergences in Wills Weaver Mine- 1 st North	49

31. Measured Convergences in Wills Weaver Mine- 2 nd North	49
32. Geologic Column Near WIPP showing Production Zones	53
33. Well Completions in Lower Brushy Canyon and Atoka and Morrow	54
34. Yield Surface of Geomodel Cement	57

Background

The potash area in SE New Mexico is currently being mined and contains numerous existing and proposed oil and gas wells. This study will attempt to define acceptable standoff distances between mining and oil and gas wells. Of concern is the potential loss of well integrity due to mine induced subsidence as oil and gas could flow into the mine workings. The study will focus on mining conditions that can jeopardize well integrity. Analysis results will also examine the integrity of the rocks and strata separating the mines and wells.

For the purpose of protecting and conserving the potash deposits, the Secretary of Interior withdrew 42,285 acres from oil and gas leasing in 1939. However, a number of wells had already been emplaced and mining had commenced in the early 1930's. In 1951, the Secretary defined 298,345 acres as a designated "Potash Area" and revoked the ban on oil and gas leasing, thus providing for concurrent development and production of oil and gas and potash deposits in the potash area. At that time, rules and guidelines were created to protect the mines and potash by requiring a salt protection string and cementing. Secretarial Orders in 1965 and 1975 expanded the potash area to 420,212 and 491,916 acres. Expansions of the potash area encompassed wells that were completed under less stringent requirements. As a result, well completions within the potash area vary considerably. Technology, regulations, and practices have improved over time, and the arguments exerted today suggest that both industries can co-exist in a safe manner, yet some fundamental questions remain including an acceptable standoff distance for a particular circumstance.

Determining what is acceptable has resulted in extensive litigation² over the past 50 or so years, without resolution, as the views and opinions expressed by the potash and oil and gas industries are divergent. The intent of this study is to present an unbiased technical examination of this issue and apply our best technology to develop what we consider as reasonable guidelines to enable safe and efficient co-development of the natural resources. The responsibility for implementing the Secretarial Orders has resided with the BLM since 1986 (BLM, 2005) and they are the impetus of this study.

Regulations and Practice

The current regulation for locating wells near mines in the potash area is based on R-111-P (OCD, 1988). The practice has been to approve applications to drill outside of Life of Mine Reserves (LMR) as indicated below; provided there is no protest from the potash leasee:

- (a) a shallow well shall be drilled no closer to the LMR than one-fourth (1/4) mile or 110% of the depth of the ore, whichever is greater

² IBLA 2003-334, etc. constitutes 15,275 pages of testimony, 10,000 pages of administrative record, 1200 exhibits, and approximately 58,000 pages of documents (Yates Counsel, May 3, 2004; page 34,945 of IBLA 92-612, et.al.).

(b) a deep well shall be drilled no closer than one-half (1/2) mile from the LMR.

Shallow and deep are delineated by 5000 ft or above the base of the Delaware Mountain Group, whichever is less and LMRs are areas reasonably believed to contain mineable grades and thicknesses of ore. As will be discussed later, the deep wells are more likely to produce gas.

While the regulations address new wells, there were 89 oil and gas wells within the mining operations area (Stoller, 1995) and numerous others just outside the mine boundaries. As a general practice, a 100 ft radius pillar is typically left around a well and secondary mining is generally prohibited within a horizontal distance equal to the depth of the ore (Traywick, 1963). This allows for primary mining at an extraction ratio of approximately 60% to occur within a seam depth without the full mine closures associated with secondary mining (extraction ratio of 90 to 95%). When the mines encounter abandoned wells, the area can be secondarily mined provided the wells have been adequately plugged (Griswold, 1984). Considerable variation to the above practices exist in the field, in some cases mining has occurred up to active wells albeit unintentionally (Stoller, 1995).

Modeling Approach

Two basic models will be used in this study; one that simulates the mechanics associated with a mine and subsidence, and another that examines the resulting impacts on a wellbore casing. The first model will be a 2D approximation of a potash mine using both plane strain and axi-symmetric idealizations. A 2D model is reasonable given the large areal extent of the mines relative to mine depth. The mined areas of the potash enclave are shown in Figure 1. Individual mine maps are provided in Appendix A.

A generic mine, well pillar, and surrounding mine geometry will be simulated. Depending on what is learned from the initial scoping calculations (which could limit or redirect the work effort listed below), the modeling may include:

1. a mine approaching a well location
2. a mine retreating from a well location
3. a mine that approaches and then retreats past the well location
4. a mine that surrounds the well- mining approaches the well location
5. a mine that surrounds the well- mining retreats from the well location

The first 3 cases are plane strain models and Cases 4 and 5 are axi-symmetric models. The plane strain models simulate an infinite mine dimension out of plane and are representative of long wall mining conditions. The axi-symmetric model simulates a mine that completely surrounds a well pillar. Figure 2 illustrates the individual model scenarios.

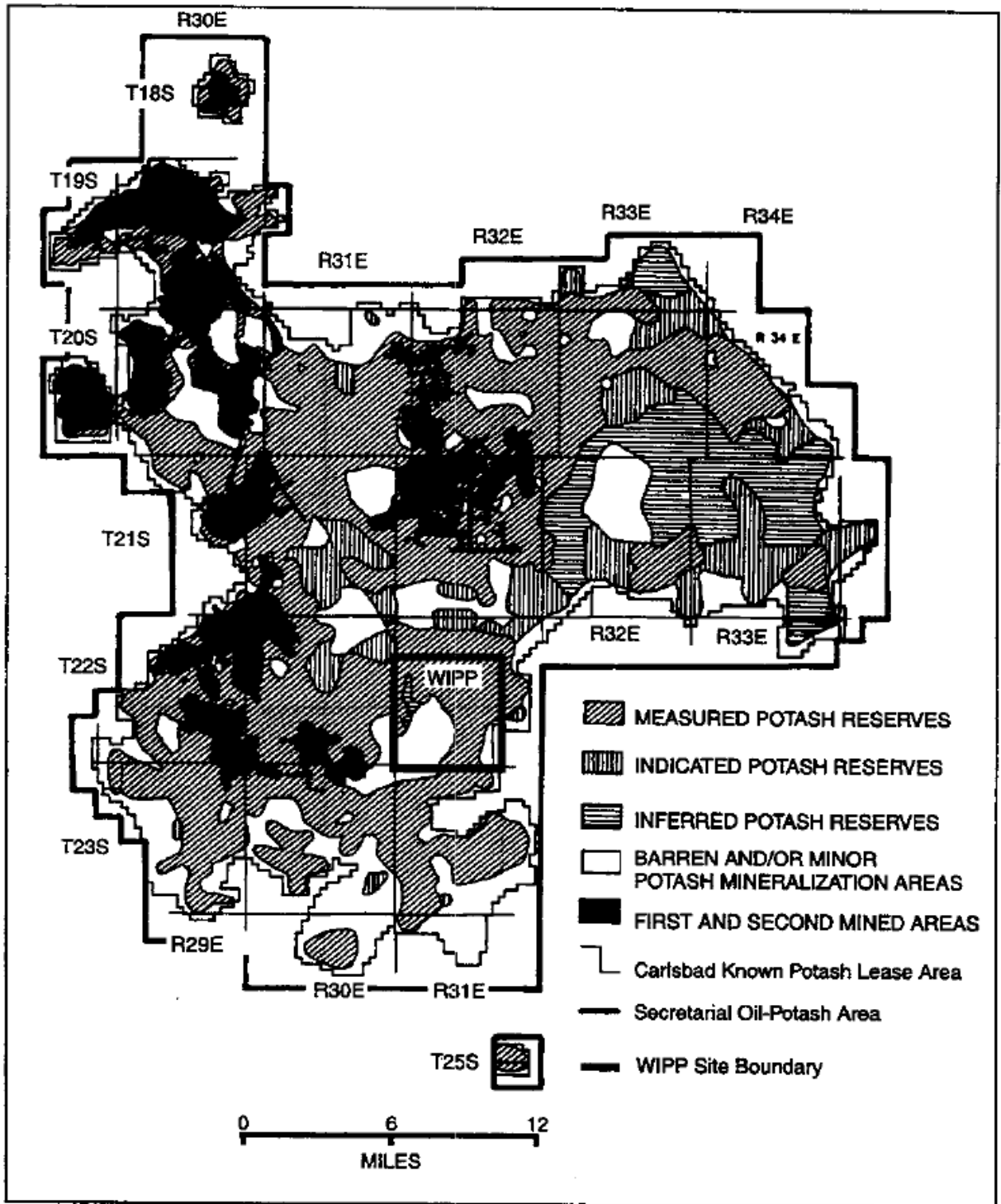


Figure 1. Map of Potash Area (Olsen, 1993)

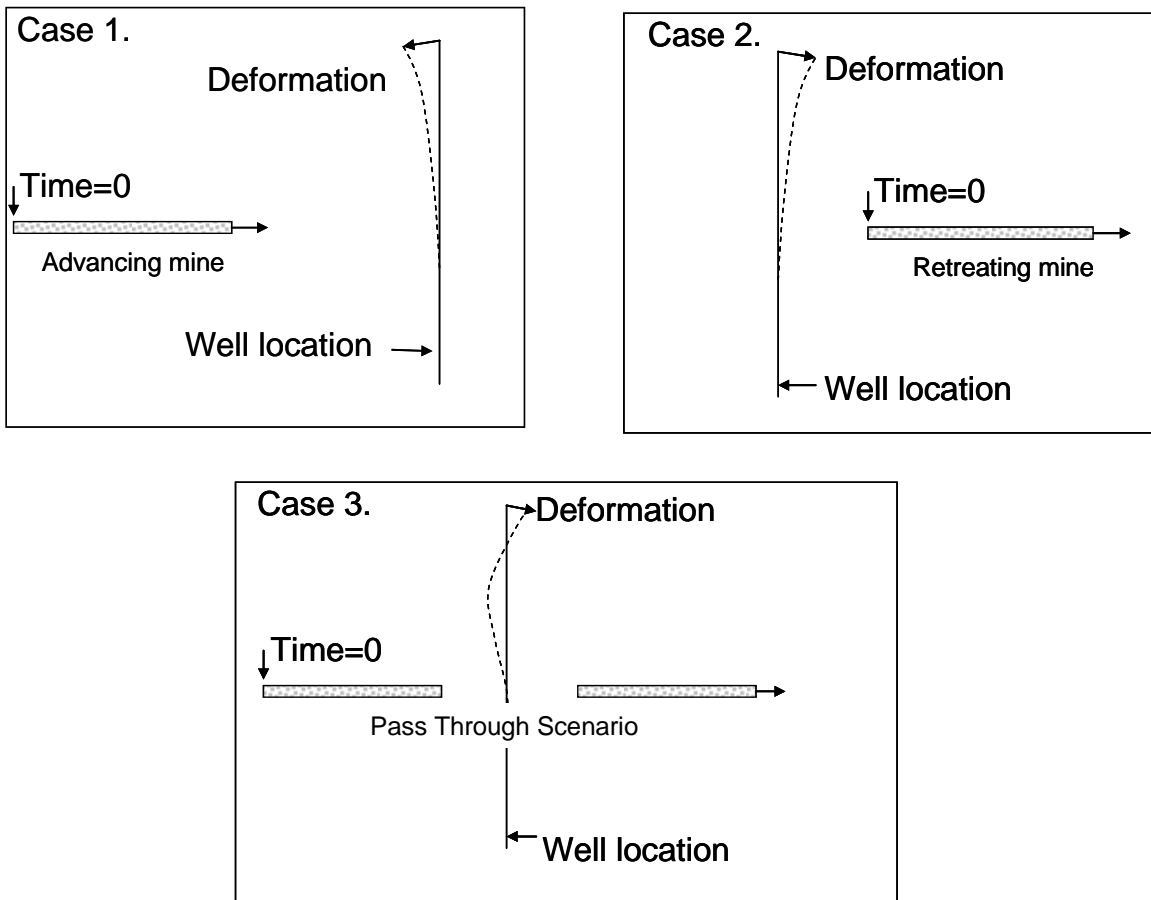


Figure 2. 2D Model Illustrations.

The plane strain models should capture axial, bending, and shear deformations in the vicinity of the well. The axi-symmetric models are limited to axial deformation due to symmetry, but the axial deformations may be greater than those predicted under plane strain conditions. The integrity of the well pillar and overlying strata will be evaluated. The 2D models³ will not include the actual well in the models. Predicted displacements

³ 3D codes may be used to model 2D problems.

at various well locations obtained from the 2D model will be imposed on the 3D wellbore model as boundary conditions.

The 3D wellbore model is illustrated in Figure 3. It includes a steel casing, cement sheath, and surrounding rock. Displacement boundary conditions from the 2D models will be imposed on the boundaries of the 3D model to simulate shearing and parting along a bedding plane through the well axis. The bedding will be treated as a “slip surface” at the top or bottom of the layer. The results of this model will be evaluated for casing, cement, and formation damage. Casing deformations will also be examined; as severe conditions can hinder the functionality of the well or its ability to have successful workovers (repairs, string removal, logging, etc.). Multiple casings may be used in this model consistent with well drilling practice.

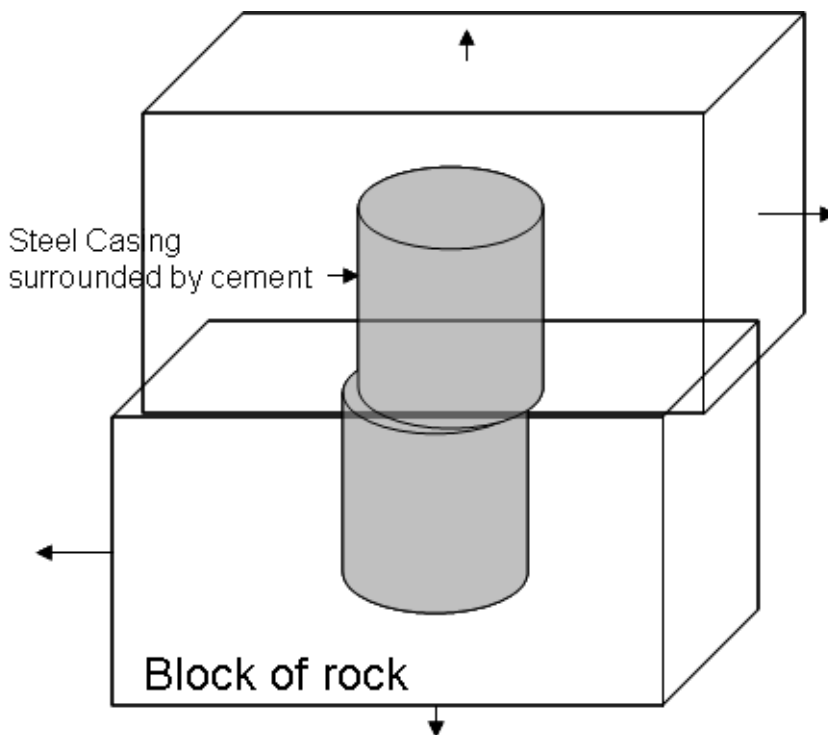


Figure 3. 3D Model of Well

A number of bedding planes will be included in the 2D models (depending on the geology and slippage predicted during preliminary scoping calculations). The selected bed displacements from the 2D models will be imposed on the 3D wellbore model. The

shearing and partings along the bedding planes can impact not only the deformation and integrity of the well casing and cement, but also can affect the migration of fluids or gases through the formation. A parted bedding plane is an obvious example. The inclusion of stratigraphy is illustrated in Figure 4.

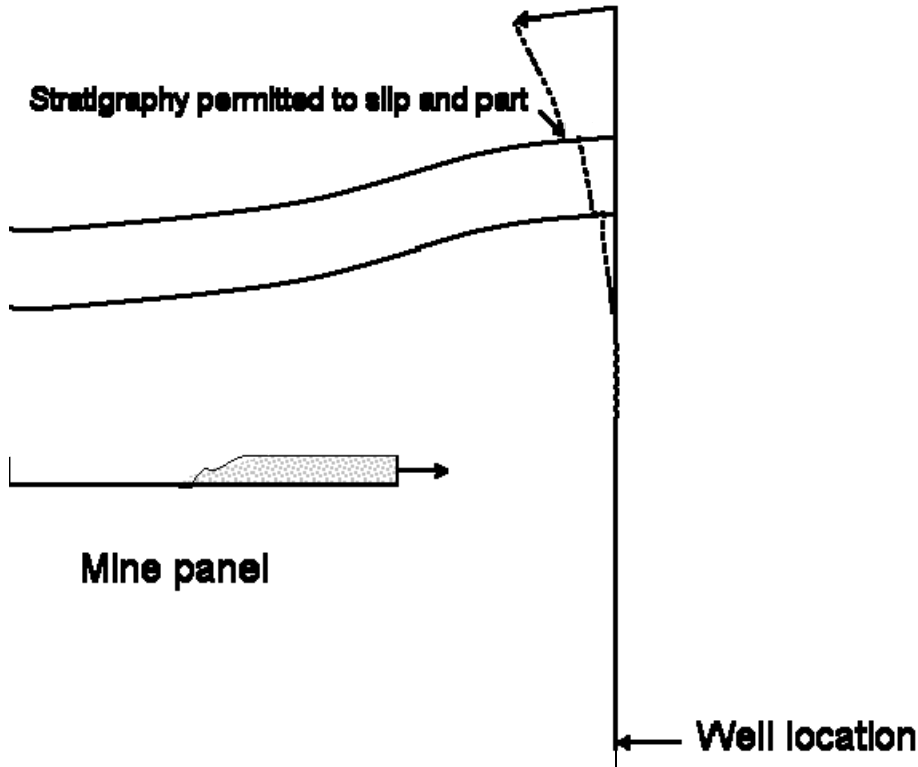


Figure 4. Inclusion of Stratigraphy into Models

There are a number of variables that may influence the modeling results. These are listed in Table 1 and actual field conditions will be discussed in subsequent sections of this report in order to define modeling parameters and limit the modeling to a reasonable number of analyses that capture the mechanics, bound the problem, and gain the most insight into developing acceptable standoff distances.

Table 1. Model Variables

Standoff distance to well
Mining rate
Extraction ratio
Height of panel
Depth of panel
Mining levels
Stratigraphy
Well diameter
Casing diameter
Casing thickness
Number of casings
Material properties -rocks, cement, steel, interfaces

Geology

The geology of the potash area is described by Griswold (1982) as located in a classical marine evaporite basin. The total thickness of the evaporites ranges from 1000 ft at the northern mines to as much as 3000 ft in the south. Two North-South cross-sections are provided in Figure 5 (Austin 1980/Jones 1972), showing the general basin geology, and Figure 6 (Griswold 1982), which provides correlation to mining operations. The potash deposits are restricted to thin lenses (generally 4 to 8 ft thick) within this thick sequence of salt and anhydrite beds. In addition to a general deepening of the potash as the beds enter into the Delaware basin, the potash zone dips about 90 ft per mile to the East. A geologic column adapted from USGS information (Jones, 1975) is presented in Figure 7 (Bureau of Mines, 1977).

Eleven ore zones have been identified in the McNutt formation (Figure 8). Ore zones are numbered starting at greatest depth, whereas Marker Beds are numbered from the surface. The terminology “Marker Beds” results from their great lateral continuity and use as geologic picks in the course of drilling throughout the basin. There are 43 Marker Beds in the Salado formation consisting of thin mudstones at the base with anhydrite above which can be replaced by polyhalite.

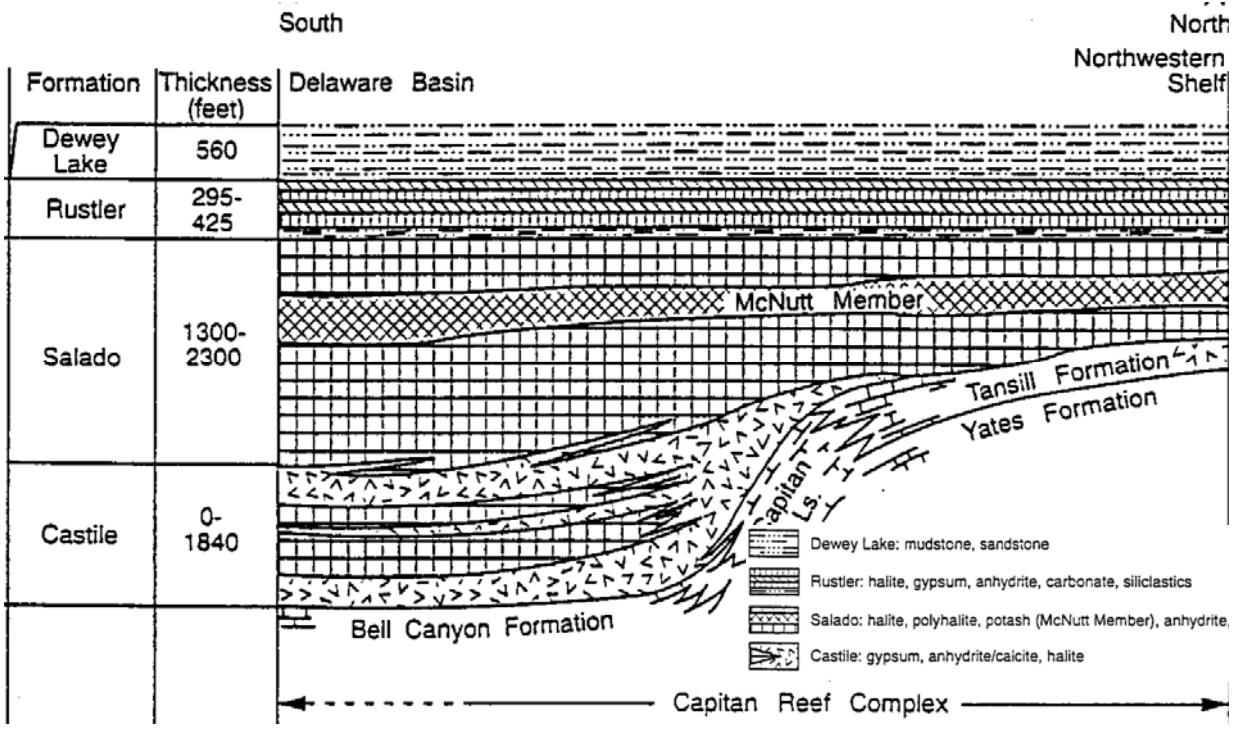
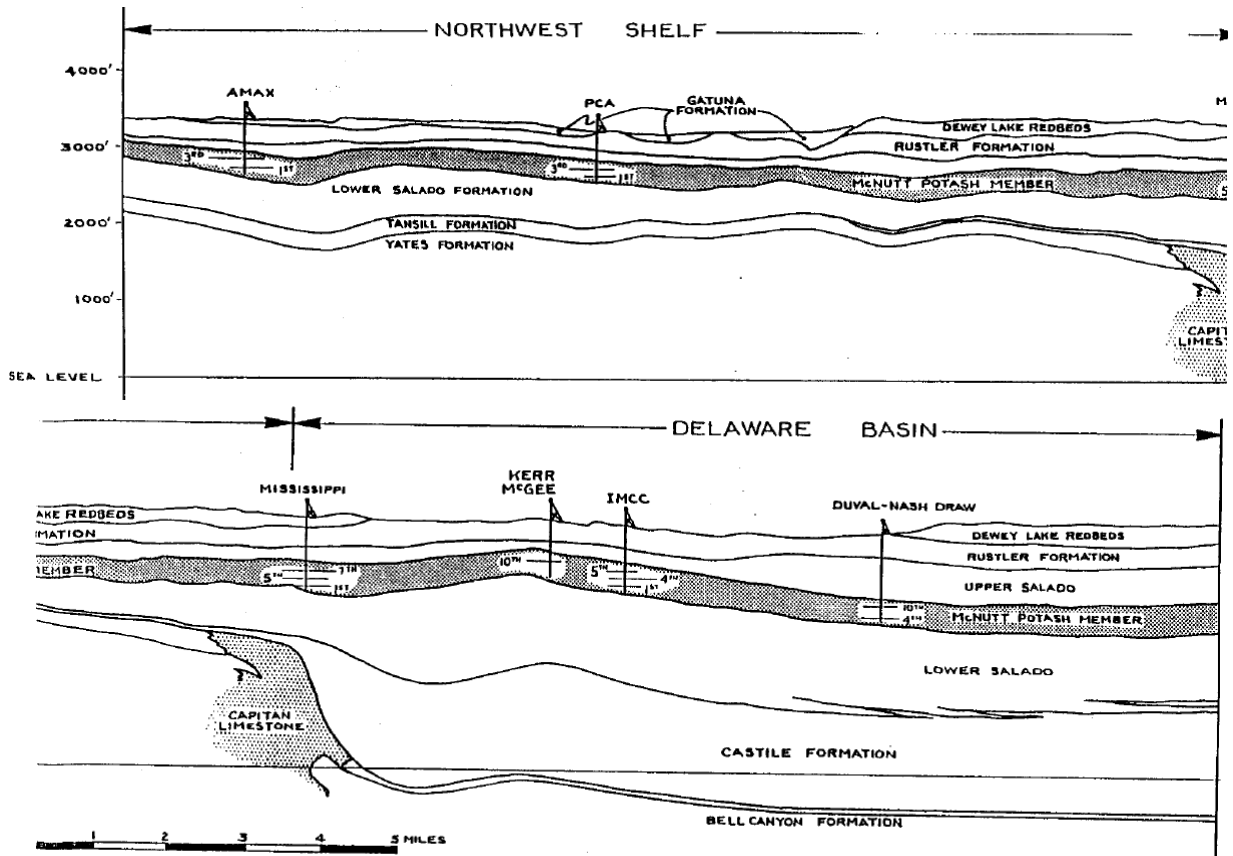


Figure 5. North-South Cross-Section Across Potash Area (Austin, 1980; Jones 1972).



STRUCTURE CROSS SECTION A-B

Figure 6. North-South Cross-Section showing location of Mines (Griswold, 1982).

The geologic sequence is called Ochoan and is comprised of the Dewey Lake, Rustler, Salado, and Castile Formations (Table 2). The formations were also characterized at the WIPP site, where the potash is deeper than typical mining depth. The WIPP is located in the lower portion of the Salado, below the potash horizon. Geologic columns for the upper and lower portions at WIPP are taken from Powers et al. (1979) in Figures 9 and 10.

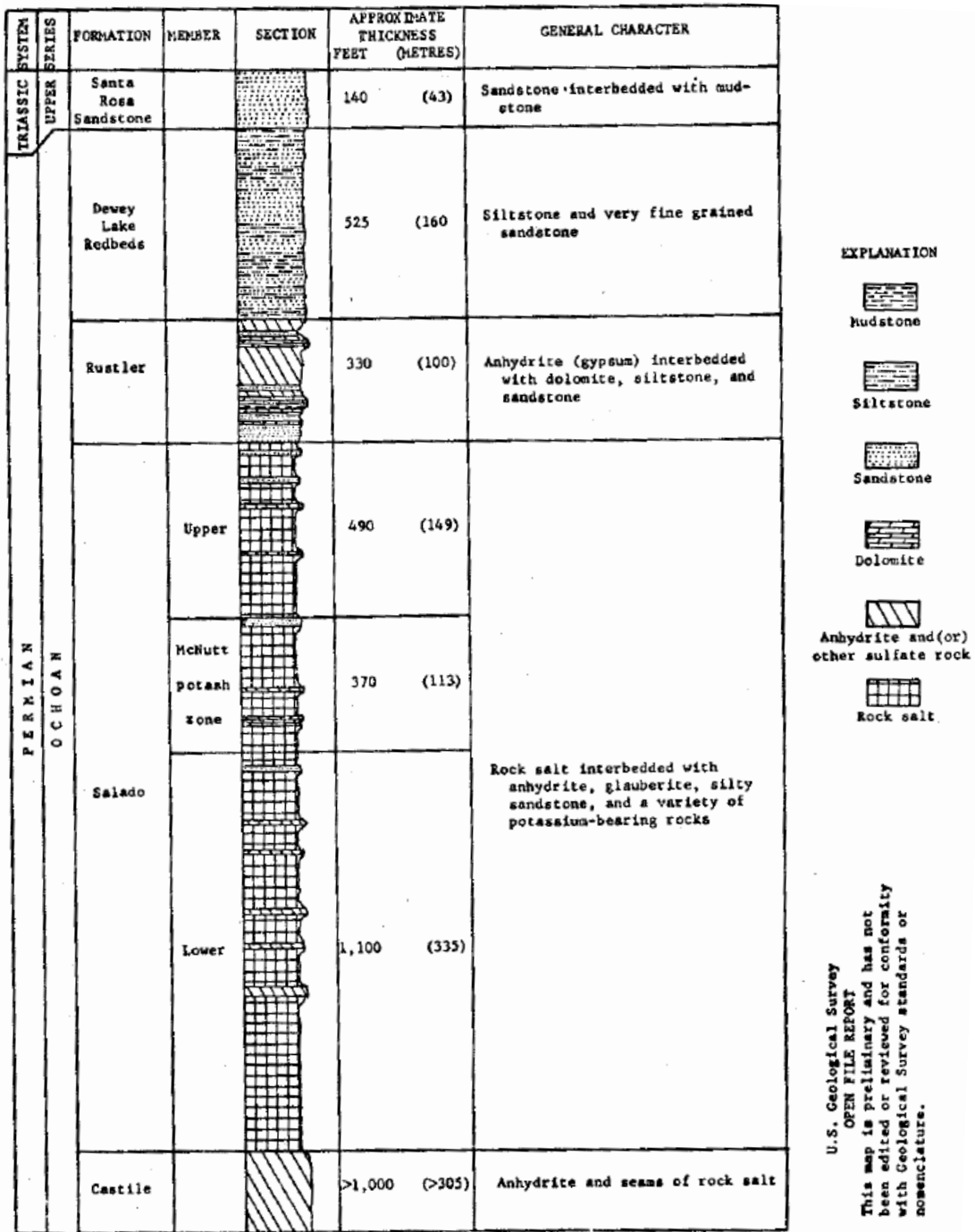


Figure 7. Stratigraphic Column by Bureau of Mines (1977) and Jones (1975).

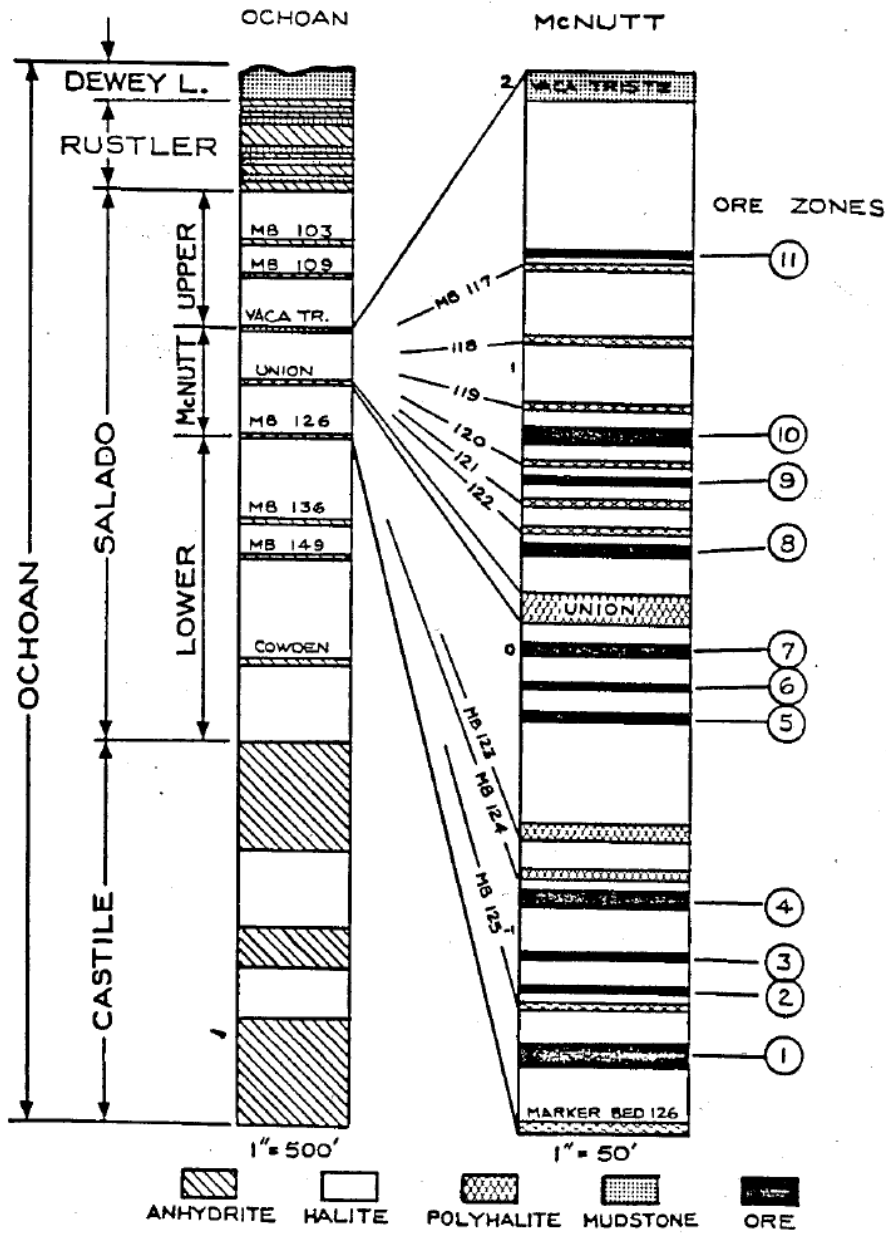


Figure 8. Stratigraphic Column of the Ochoan (Griswold, 1982)

Table 2. Description of Ochoan Rock

TRIASSIC		
Dewey Lake 200-300 ft.		Red siltstone, sandstone and mudstone. Thin lamination and small-scale cross lamination common.
Rustler 200-500 ft.		Mostly anhydrite with some salt. Contains two dolomite layers, a basal sandstone, and several thin layers of clastics. The two dolomite layers are normally aquifers in most of the eastern part of the district, and halite has been removed from the section and original anhydrite converted to gypsum.
	Upper 500 ft.	Halite with regular but thin beds of anhydrite and polyhalite. Clay seems common at the base of the anhydrite-polyhalite seams. Suberosion by groundwaters has removed much of this member in the eastern part of the district.
Salado	McNutt 300-500 ft.	The overall character is identical to the Upper and Lower Members. The important exception is that sylvite and Langbeinite occur as thin (1 to 10 feet) beds within this unit.
	Lower 400-1500 ft.	Identical in lithology to the Upper Member except that halite units are thicker and purer.
Castile	0-1500 ft.	This formation is present only in the Delaware Basin, i.e. south of the Capitan Reef. Near the reef the section is almost totally anhydrite. South of the reef it consists of equal portions of salt and anhydrite in thick beds. The halite is very pure. The anhydrite is "banded" with thin alternating layers of anhydrite and dolomite.

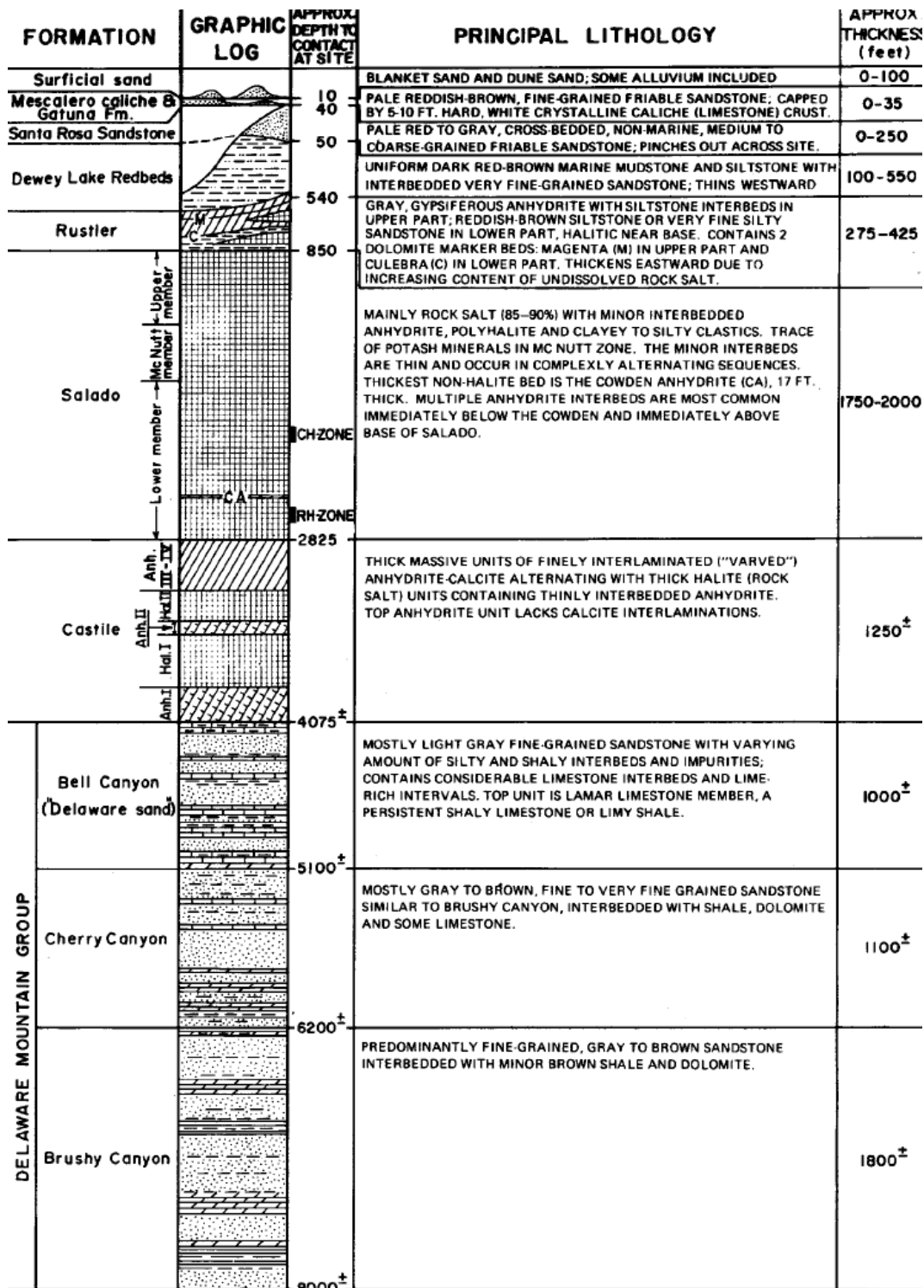


Figure 9. Upper Geologic Stratigraphy at WIPP (Powers, 1979).

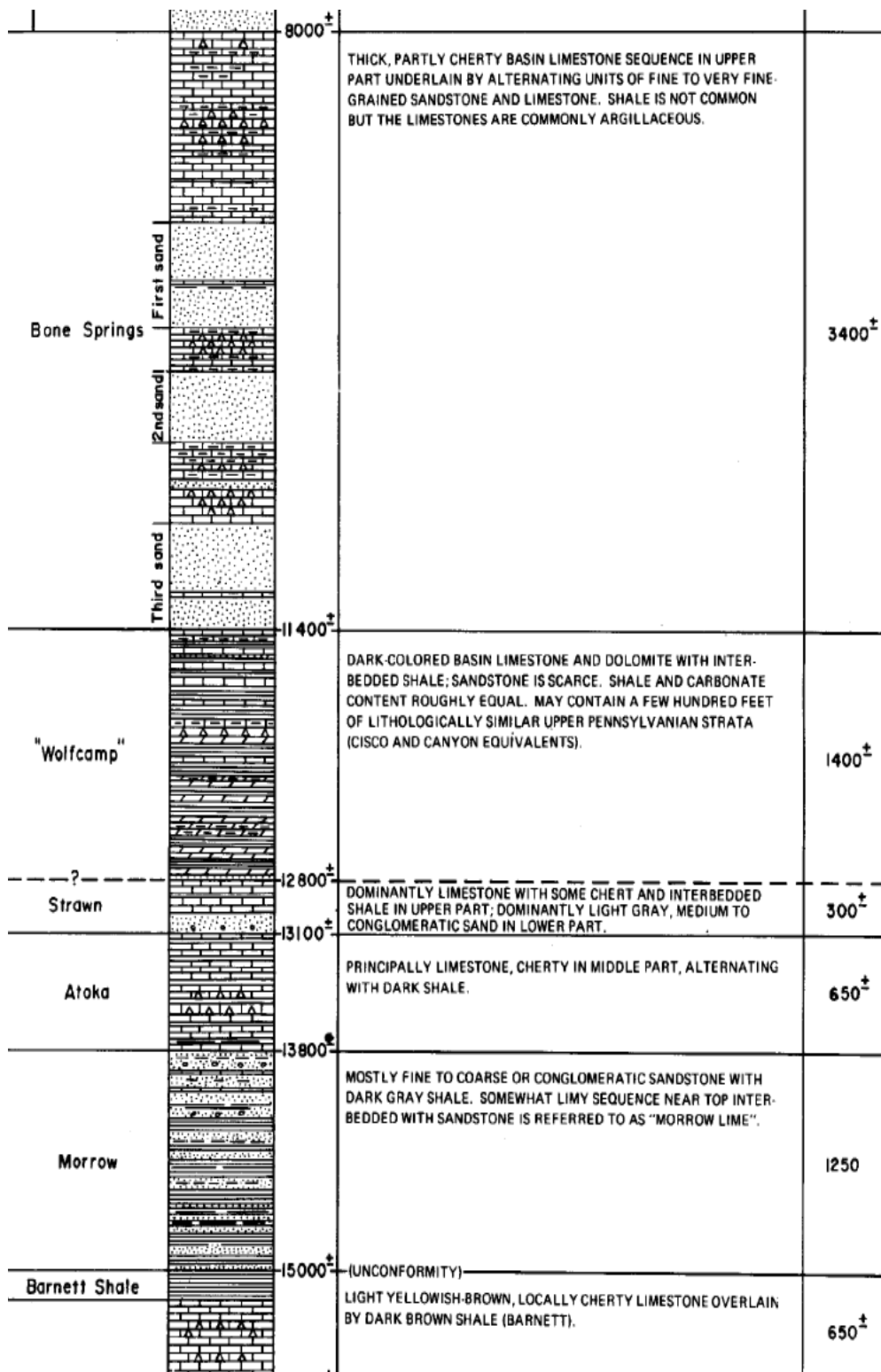


Figure 10. Lower Geologic Stratigraphy at WIPP (Powers, 1979).

Not all of the ore zones are being mined. Historically, the first zone was the major producing zone, followed by the tenth and third zones. The fourth zone is the principal source of langbeinite. Zones 5, 7, and 8 have moderate reserves and the others (2nd, 6th, 9th, and 11th) are not commercially produced (Griswold, 1982), at least at that time.

For purposes of the analyses, two mine depths and stratigraphies will be considered based on the above information. A 1000 ft deep mine will represent a typical mine depth, whereas a 2000 ft mine will represent deep mining conditions. Both mines will have a 10 ft seam. The marker beds and stratigraphic contacts will be simulated as frictional interfaces in the model. The locations of these interfaces are tabulated in Table 3 for both mine depths and graphically depicted in Figure 11. A number of interfaces will be initially simulated such that some may be eliminated from the model if they are found to be inconsequential, having limited or no slippage, or if their presence mitigates slippage on nearby interfaces. In the latter case, some of the contacts may be locked (not permitted to slip) in order to define the maximum lateral extent of slippage of other contacts. This would simulate conditions where some contacts in the field either do not participate in slip due to their geologic character, or in some regions, not exist.

Mud seams vary in thickness. They have been reported to range from a thin film up to 5 inches in thickness (Gunn and Hills, 1975). An earlier report (Rutledge, 1964) ranges the thickness from a few inches up to 5 ft thick. Significant slippage along these thin layers will result in localized casing shear. No thickness will be prescribed to the slippage layers in the models.

Mud seams are often associated with gas. Gas pressures across interfaces will reduce the slip resistance of the interbeds, however in-situ gas presence and associated pressures are difficult to estimate and will not be included in the models. In the mines, nitrogen and some methane gas has pressurized mud seams resulting in blowouts and deformed roof strata especially at intersections (Bur. of Mines, 1983). Pressures up to 60 psi were measured at the face of blow holes drilled into the roof. Insitu pressures (prior to mining, deformations, and any bleedoff) are likely higher than those measured. As a result of gas pressure and associated roof falls, it is a routine mining practice to drill relief holes.

The mud seams investigated by Rutledge (1964) revealed openings up to 2 inches and in some cases the presence of vugs (0.1 in diameter) that were connected by hairline cracks. Oil seeps observed in the mines are also associated with mud seams. Mud seams are believed to be the likely path of migration into the mines for any fluid leakage from wells. Deformation and shear across interfaces will likely alter the fluid flow potential of the seams. Flow through the Marker Bed interfaces will be addressed in a separate section of this report (see Position on Gas Migration).

Table 3. Stratigraphic Contacts for 1000 and 2000 ft Deep Mines

Mine Depth (ft)	1000	2000
Formation or Bed	Depth from surface to bottom of bed (ft)	
Dewey/Rustler	200	500
Magenta dolomite	300	665
Culebra dolomite	420	870
Rustler/Upper Salado	500	1000
MB 101	520	1060
MB102	555	1170
MB103	595	1285
MB109	660	1485
Upper Salado/McNutt	750	1750
Vaca Triste	765	1765
MB117	820	1820
MB 118	850	1850
MB119	875	1875
MB120	895	1895
MB 121	910	1910
MB 122	925	1925
Union	960	1960
Mine floor	1000	2000
MB 123	1040	2040
McNutt/Lower Salado	1100	2100
Lower Salado/Castile	1950	3400

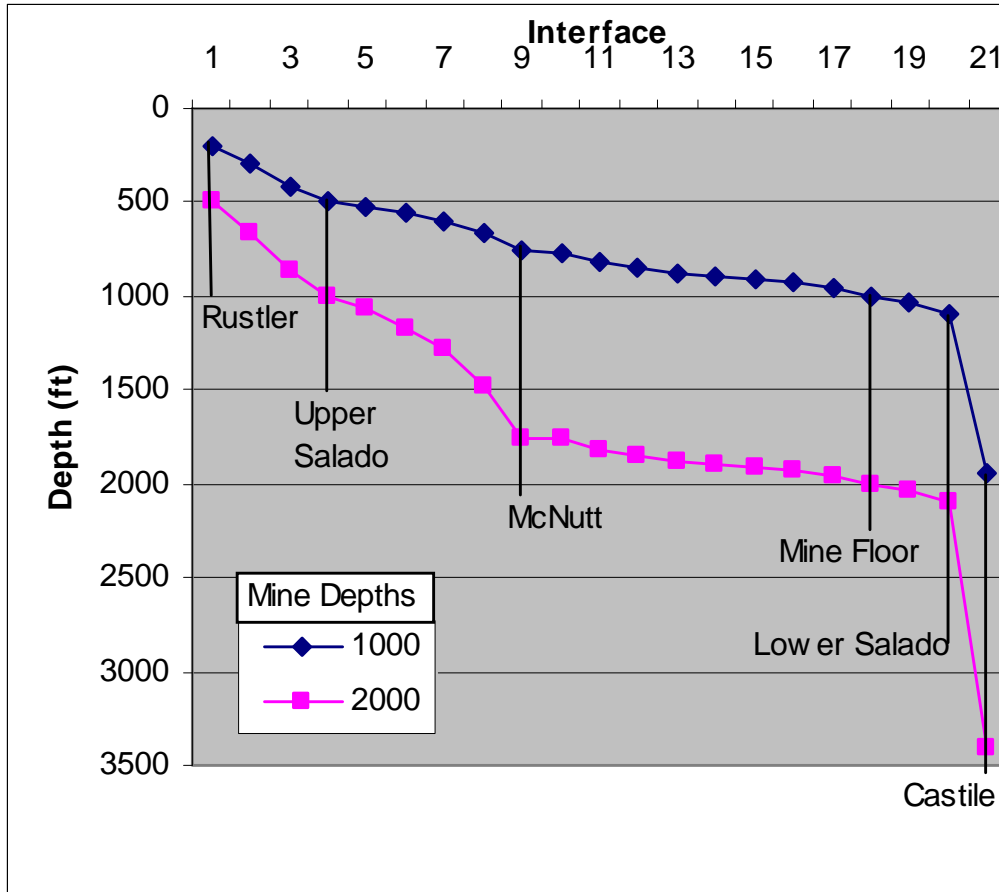


Figure 11. Stratigraphic Contact Depths.

Rock Properties

The failure strength of potash has been determined from core samples from the Mississippi Chemical mine by the Colorado School of Mines (CSM) in 1982. The results of those tests are presented in Figure 12. Considerable variation exists in the results. Variation and uncertainty in modeling parameters will be addressed through the use of a safety factor when interpreting results (see Section on Interpreting Results).

MISSISSIPPI CHEMICAL CORP

All data: Failure Strength (psi) = 3510 + 6.33 (Confining Pressure - psi)
 $r^2 = 0.061$; $S_{yx} = 1380$ psi
 $\phi = 46.6^\circ$; cohesion = 697 psi

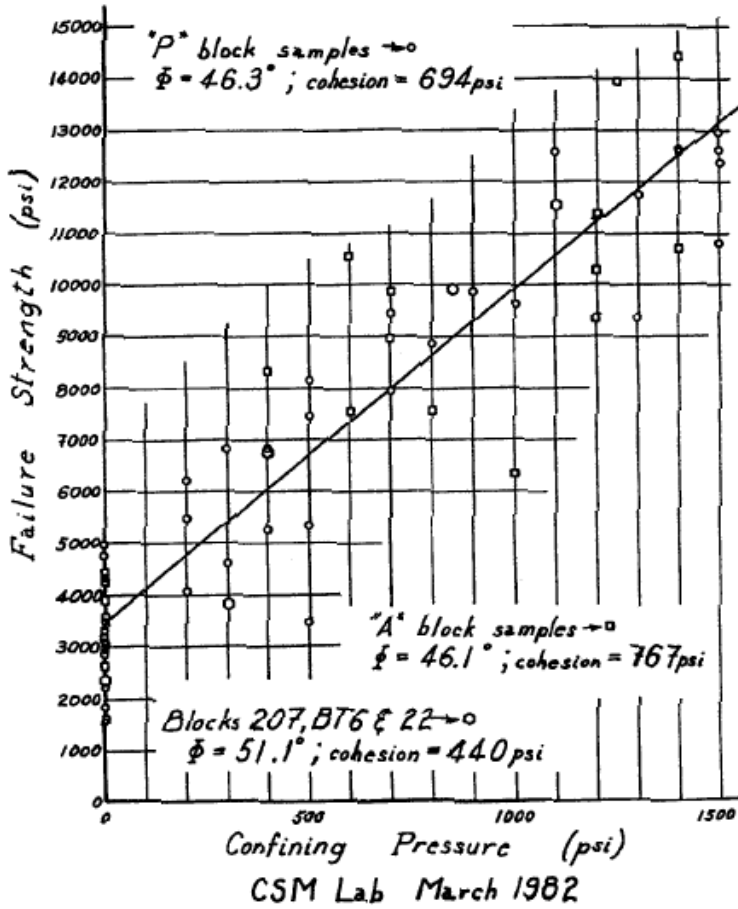


Figure 12. Potash Strength Testing

Additional strength testing from the MS Chemical mine is reported by Abel (1992) and is shown in Table 4.

Table 4. Reported Testing by CSM on MS Chemical Potash and Salt

	Internal Friction Angle (deg)	Cohesion (psi)	Confining Pressure (psi)	Number of Samples Tested
Cycle 7, Potash salt (1982)	46.6	700	0-1500	64
Cycle 5, Potash salt (1991)	36.9	720	0-1500	34
Cycle 5, Roof rock salt (1991)	39.3	750	0-2000	25
Cycle 5, Floor clayey rock salt (1992)	38.1	870	0-2000	20

Direct Shear Test results from CSM MN 321 Lab (1982) are reported in Table 5. Densities were also measured and found to have a specific gravity of approximately 2.15 for the roof and floor salts, and 2.08 for the potash ore.

Table 5. Direct Shear Tests CSM MN 321 Lab (April 1982 and June 1991).

	Cohesion (psi)	Friction Angle (deg)	Test Year
Block P-1	5.86	21.7	1982
Block P-2	2.55	17.6	1982
Block P-3	11.15	15.1	1982
Block P-4	0.48	20.5	1982
Block P-5	3.45	22.0	1982
Block 1-A	16.96	16.7	1982
Block 3-A	0	17.4	1982
Block 4-A	6.74	15.4	1982
Block 207	3.59	16.6	1982
Block BT6	0	23.2	1982
Lower Block- R1	0.91	15.6	1991
Upper Block- R21	1.20	11.5	1991

Tensile strengths were measured on 39 samples from the above blocks. The strengths ranged from 140 to 710 psi with an average strength of 460 psi in tension. The elastic modulus and Poisson's ratio were measured on 23 specimens from the above blocks and averaged 0.762 E6 psi and 0.328, respectively. Poisson's ratio is the measure of lateral to axial strain and is therefore a dimensionless quantity. The test results for the elastic

properties are provided in Table 6 where the units associated with Poisson's ratio are believed to be erroneous.

Table 6. Laboratory Determination of Elastic Properties of Potash

MN 321 Lab		April 1982		
- MISSISSIPPI CHEMICAL CORP.				
Elastic Properties Determinations, Cycle 7 Potash				
Specimen Ident.	Elastic Modulus (psi/ $\mu\epsilon$)	Stress Range (psi)	Poisson's Ratio (psi/ $\mu\epsilon$)	Stress Range (psi)
P-3 (NBI)	0.361 0.244	(880-1750) (1750-2240)	0.345	(450-1250)
2-A (SR)	0.440	(740-1420)	0.440	(380- 770)
4-A (AR)	1.59 0.331	(0- 330) (2170-3750)	0.213	(2170-3750)
4-A (SY)	0.968 0.284	(0-2240) (2240-4890)	0.451 0.256	(0-2240) (2240-4890)
P-5 (WA)	3.15 1.62	(970-1970) (3330-4950)	Irrational	
3-A (WR)	0.986	(320- 970)	Non-linear	
207 (RI)	0.812	(930-2350)	0.251	(930-2350)
P-3 (LO)	0.202 1.62	(0- 370) (850-2140)	0.375 0.431	(0- 370) (850-2140)
1-A (SP)	0.528	(1090-2120)	0.378	(1090-2120)
P-1 (BHH)	0.374	(620-1830)	0.395	(920-1570)
P-4 (DZ)	0.979 1.01	(150-1040) (1040-1860)	Irrational	
P-1 (SV)	0.343	(1540-2670)	0.446	(400-1700)
P-1 (BM)	0.367 0.185	(1460-2300) (2550-3530)	0.467	(2880-3200)
P-5 (HC)	0.140	(1970-3010)	0.438	(0-2220)
1-A (PG)	2.14 0.319	(0- 610) (1100-3100)	0.294	(0-2480)
P-2 (FMM)	2.07 0.188	(0- 640) (1640-2540)	0.377	(0-1640)
3-A (JR)	0.510	(70-1840)	0.256	(70-1840)
P-2 (MB)	0.767 0.090	(0- 120) (320- 620)	0.143 0.208	(0- 320) (320- 620)
P-3 (DG)	0.784 0.204	(350-1540) (1540-2220)	0.197	(350-1130)
3-A (JR)	1.56	(60-1840)	0.260	(60-1840)
P-4 (RJ)	0.733 0.367 0.411	(630-1540) (1540-2160) (2490-3180)	0.289	(0-1250)
P-3 (WD)	1.00 0.204	(350-1130) (1540-2220)	0.197	(350-1130)
P-4 (BD)	<u>0.227</u>	(1890-2820)	<u>0.411</u>	(1440-2230)
Wtd. Avg.	0.762 (Std. Dev.=0.655)		0.328 (Std. Dev.=0.090)	
	1st Linear Segment			
Wtd. Avg.	1.16 (Std. Dev.=0.808)		0.327 (Std. Dev.=0.087)	
	All Other Linear Segments			
Wtd. Avg.	0.603 (Std. Dev.=0.501)		0.329 (Std. Dev.=0.091)	

Typical yield and unconfined compressive strengths for potash and salt are reported by Boyd (1973) in Table 7. The amount of sylvinitic and clay influences the strength. The yield strength is approximately 60 percent of the compressive strength. A review of salt strengths (Tavares, 1994) also found that yield or damage occurs at about 60 percent of the ultimate compressive strength.

Table 7. Comparison of Potash and Salt Strength (Boyd, 1973)

psi	Potash Ore 15 to 20 % K ₂ O	Salt
Compressive Strength	3,300	4,400
Yield Strength	2,000	2,500

For purposes of the analyses, the CSM data (Appendix B) is recast in terms of stress invariants in Figure 13.

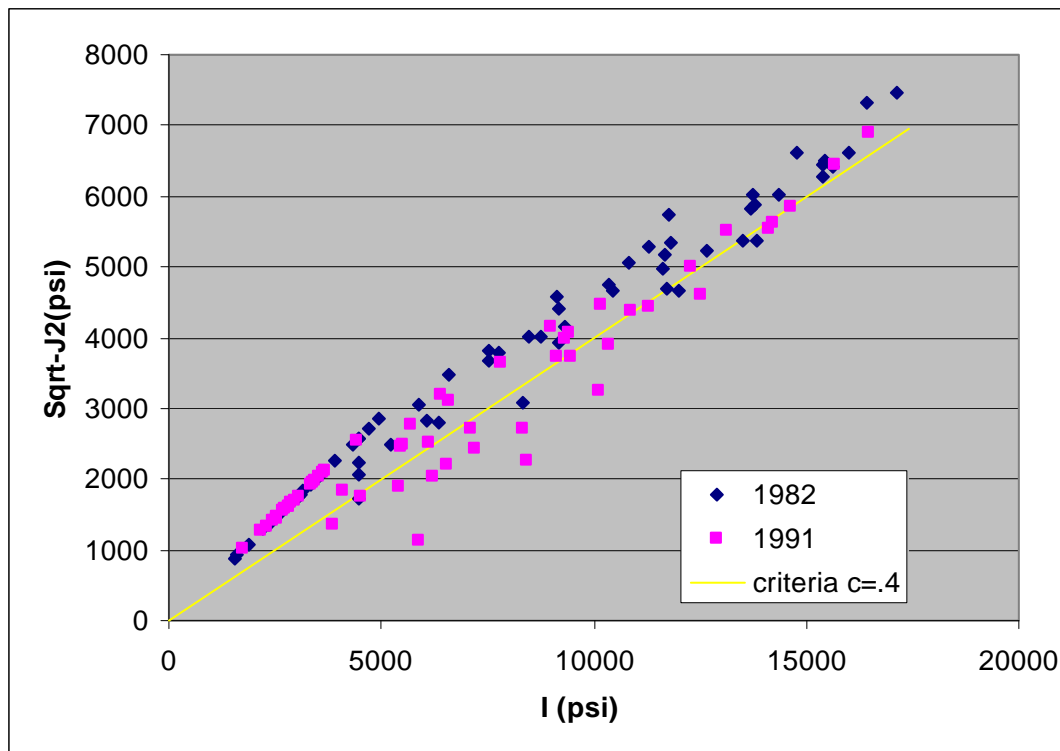


Figure 13. MS Chemical Data in Terms of Stress Invariants

A failure and damage criteria may be developed. A dilatant damage criterion is used to delineate potential zones of dilatancy in the salt formations surrounding the mine. Dilatancy is attributed to micro-fracturing or changes in the pore structure of the salt, resulting in an increase in permeability. The dilatancy and strength criterion can be expressed in terms of a safety factor as

$$SF = \frac{C \cdot I_1}{\sqrt{J_2}}$$

where, SF is the safety factor against damage or failure; $I_1 = \sigma_1 + \sigma_2 + \sigma_3 = 3\sigma_m$ is the first invariant of the stress tensor; $\sqrt{J_2} = \sqrt{\frac{(\sigma_1 - \sigma_2)^2 + (\sigma_2 - \sigma_3)^2 + (\sigma_3 - \sigma_1)^2}{6}}$ is the square root of

the second invariant of the deviatoric stress tensor; σ_1 , σ_2 , and σ_3 are the maximum, intermediate, and minimum principal stresses, respectively; σ_m is the mean stress. The constant C was determined to be 0.4 for failure and is taken as 0.25 for damage (60% of the failure strength). The resulting criteria is typical for salt and will also be used for anhydrite (Pfeifle and Hansen, 1998) and other formation rock other than the mudstone. For mudstone, slippage will be determined using an angle of friction of 11.3 degrees. This is consistent with the minimum measured shear slip (Table 5) and with that used for WIPP in simulating clay seams (Table 9).

When $SF < 1$, the shear stresses (J_2) are large compared to the mean stress (I_1) and dilatant or failure behavior is expected.

Laboratory creep testing on model pillars is reported by Golder (1979) for New Mexico potash ore. The tests by Obert (1965) simulated 4 inch diameter by 1 inch high pillars. Testing duration was 1000 hours at constant axial applied stresses ranging from 2,000 to 7,000 psi. Obert inferred from the results in Figure 14 that after an initial hardening phase, the strain rates were constant (steady-state).

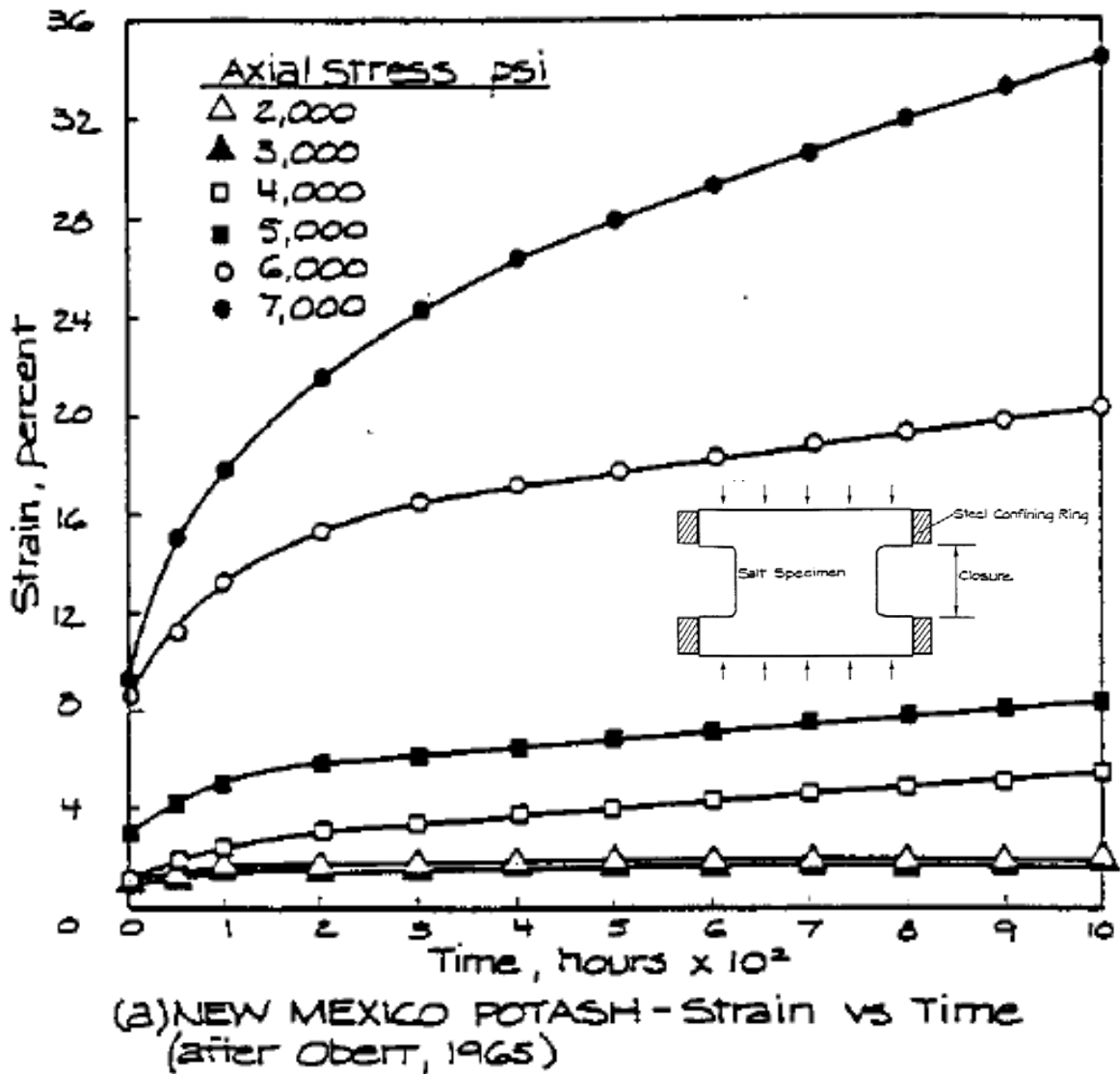


Figure 14. New Mexico Potash Creep Tests

Obert developed a relationship for steady-state creep (after 200 to about 400 hours) as

$$\dot{\epsilon} = K\sigma^{3.3}$$

Where $\dot{\epsilon}$ is the axial strain rate (1/hr), K is a constant (1.78E-17 psi^{-3.3}/hr), and σ is the applied vertical load (stress, psi). The steady-state "strain rates" are plotted in Figure 15 (in reality these "strains" are changes in height at a specific point on the test specimen, defined by the radial outer edges of the confining rings that are originally the same height as the pillar, divided by the original height of the pillar).

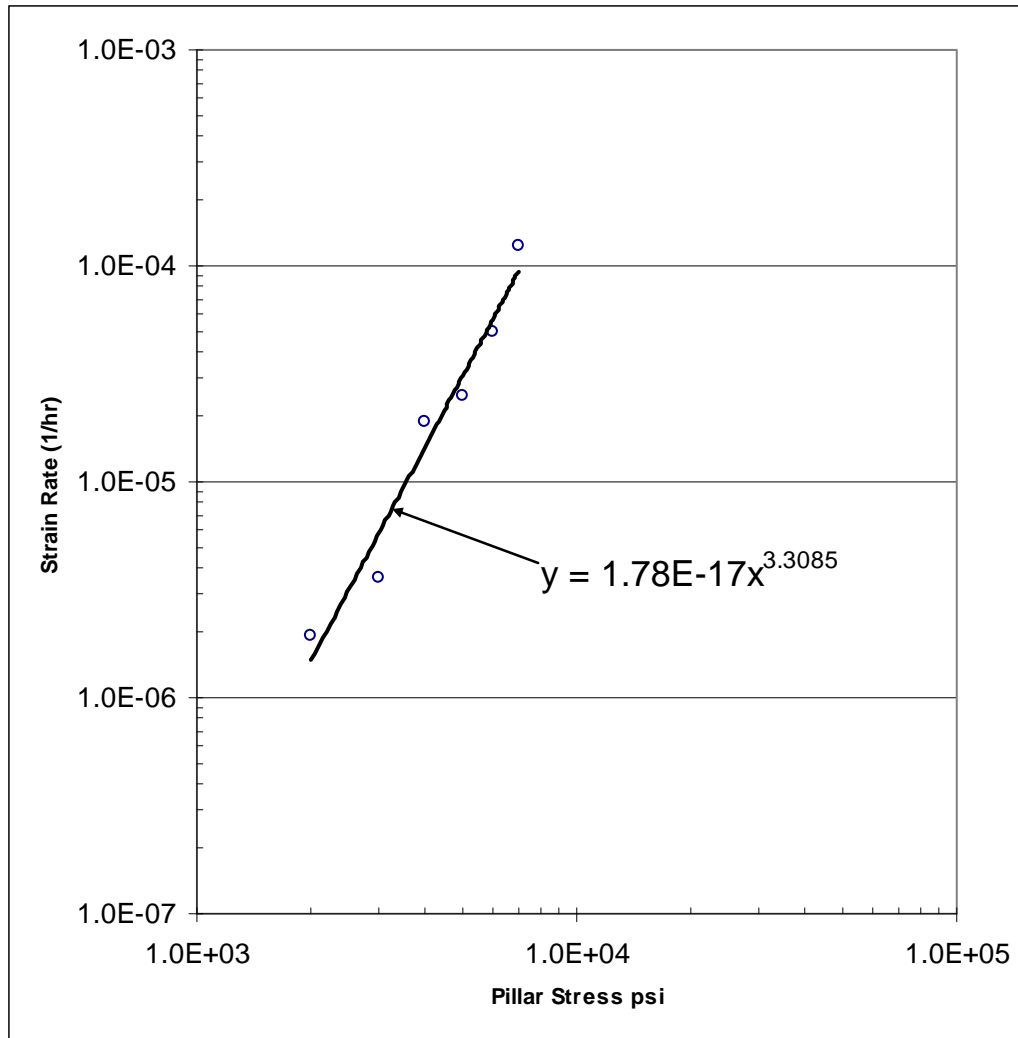


Figure 15. Steady-State Strain Rates Inferred from Testing Sample Pillars in Laboratory.

While the testing done by Obert shows that creep of potash is sensitive to stress, the testing results are difficult to interpret in terms of creep material properties and implement into a constitutive model. Creep rate is normally assumed to be a function of the deviatoric stress which is an unknown in the model pillar experiments. Modern typical laboratory tests control the deviatoric loading and develop relationships similar to that in Figure 15. However, the deviatoric stresses in the Obert pillar (not the “Pillar Stresses” shown in Figure 15) are uncontrolled and likely vary across the pillar width. If stress controlled creep testing has been performed on NM potash, the sharing of those results would contribute to this investigation (see Foreword).

In the absence of stress controlled creep testing, the above experiments will be simulated and a set of creep properties derived for potash. A comparison of the results with measurements will be provided along with the derived creep parameters. Creep testing has been performed for WIPP salt. Given the argillaceous nature of the salt in the upper

and mid-portions of the Salado, this type of salt may be assumed to represent non-potash salts near the mines.

Elastic parameters needed for the stratigraphy are provided in Tables 8 (Teufel, 1996). These parameters will be used as starting values in the calculations, but they may be varied to better represent field conditions (see Section on Model Variations). Table 9 (Munson, 1995) provides the elastic and creep parameters for argillaceous WIPP salt, as determined by modern material laboratory tests.

A power law creep model will be used for the salt creep constitutive model, which considers steady-state creep rate to be determined from the following law:

$$\dot{\epsilon} = A \left(\frac{\sigma}{\mu} \right)^n \exp\left(-\frac{Q}{RT} \right)$$

where, $\dot{\epsilon}$ = creep strain rate; σ = von Mises equivalent stress; μ = shear modulus = $E/2(1+\nu)$; T = absolute temperature; A = structure factor determined from fitting the model to creep data, n = stress exponent; Q = effective activation energy; and R = universal gas constant. A uniform salt temperature of 75 F will be assumed.

Table 8. Elastic Properties (Teufel, 1996)

Formation	Elastic Modulus (xE6 psi)	Poisson's Ratio
Dewey Lake Beds	2.175	.25
Rustler	2.9	.3
Castile	2.247	.25
Delaware	3.625	.2

Table 9. Reference Properties for WIPP Materials (Munson, 1995)

Material	Elastic Modulus (xE6 psi)	Poisson's Ratio
Anhydrite	10.89	.35
Polyhalite	8.02	.36
Halite	4.495	.25
Argillaceous Halite	4.495	.25
Clay Seam		
Friction Angle deg	11.31	
Argillaceous Salt Creep		
A 1/sec	1.314E13	
n	5.0	
Q Kcal/mol	10	

Mining Parameters

Potash was first discovered in the Carlsbad area in 1925 and the first mine production began in 1931. Since that time, seven companies have operated eleven mines producing potash from six different ore zones (Figure 16). The potash ore has been produced from depths ranging from 500 to 2400 ft below surface with mining heights of 4 to 15 ft. Currently there are two companies (Intrepid and Mosaic) operating three mines producing from four different ore zones (BLM, 2005).

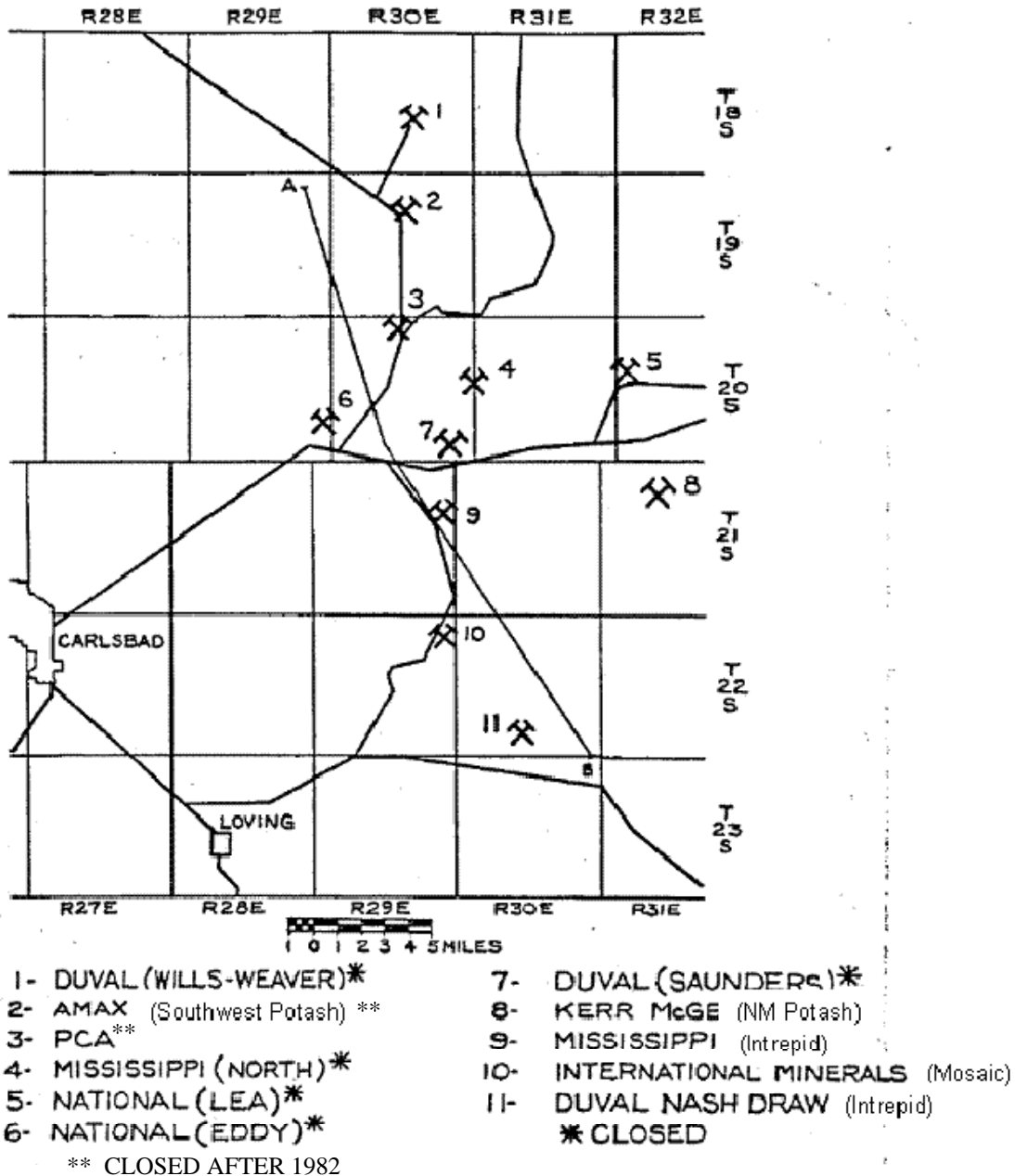


Figure 16. Location of Mines (Map from Griswold, 1982)

Mining typically proceeds by development of entries and panels at extraction ratios of 60 to 75%. Upon retreat mining, pillars are mined and the extraction ratio increases to 80 to 95%. Mining height varies (BLM, 2005) depending on the available ore. In the Intrepid mines, mining heights are 4 to 8 ft in the East Mine and 4 to 10 ft in the West Mine. The Mosaic Mine (former IMC mine) has a varied mining height from 4.5 to 15 ft. As mentioned earlier a 10 ft seam height will be used in the analyses. We are planning on normalizing analysis results to the mining height, if it is found reasonable to do so.

Multiple mine levels can exist and either the upper or lower levels can be mined first. For example, IMC mined the 1st, 4th, 5th, and 10th ore zones at the 900, 850, 800, and 700 ft levels, respectively. The mined areas do not necessarily overlap each other vertically. Historically when 2 levels have overlapped, the mine excavations have generally been separated by 35 to over 120 ft. Mining sequence may not be important if the lower seam is mined first. This has been evidenced in mining activity carried out in caved hangingwalls about 50 to 100 ft above earlier mining horizons. In these applications, the ore bed suffered no noticeable structural deformations other than elevation changes caused by subsidence (Golder, 1979). Mining the upper level first can result in roof problems in the lower level if the ores zones are too close. Simulating multiple levels will not be important to determining the standoff distance for a well, unless the distance is found to be on the same order as the separation of the ore zones. At this time, we do not plan to model multiple mining horizons.

The rate of mining was found to influence the rate of room closure and subsidence (Deere, 1957) and may therefore be an important modeling parameter. Upon reaching the outer limit of mining the economical ore in parts of the US Potash mine, final mining (robbing of pillars) was commenced at an average rate of about 12 to 13 ft per day (0.85 miles per year) in the 8 to 15 ft high seam. In their longwall operations, the average rate of retreat is approximately 200 ft per month or 0.45 miles per year (Pierson, 1965). A rate of advance of 0.5 miles per year was estimated for IMC (Traywick and Fulton, 1973) and later at 0.35 miles per year (BLM 1987). This is very consistent with a gross estimate that can be calculated knowing the total mining area and mine histories. In 1973, thirty thousand acres had been mined in 7 mines and the average mine age was 25 years (BLM, 1973). Assuming a square mining area, a gross mining rate of 0.5 miles per year is the result. Rates of advance are likely smaller than retreat rates as most of the potash is removed during advance. Retreat rates are dependent upon panel width. At the Wills-Weaver mine (Golder, 1979), retreat rates were about 1.5 miles per year in the 1st and 2nd north panels, however the panel widths were only approximately 1100 ft wide and maximum surface subsidence was not obtained over the panels. Subsidence was inhibited by the proximity of mine edges. For purposes of our analyses only retreat mining will be simulated at rates of 0.3 and 1 mile per year.

Field Measurements and Observations

Relatively little deformation is observed during initial or primary mining when extraction ratios are low compared to secondary mining. Deere (1957) believes that several inches may be associated with primary mining, but it has not been measured. However, upon retreat mining when pillars are split and extraction ratios become high, the remnant pillars are crushed and the salt roof bends down to meet a buckled floor. The presence of clay seams in the roof can cause the roof to slab off. A clay seam located in the floor can result in punching of the remnant pillars into the floor and produce floor heave. More globally, deformation of the roof is described as plastic and any minor fracturing that does develop may possibly heal when convergence is complete (Warnock, 1973). At least this is believed to be the condition by some as mine flooding has not occurred.

The mines are located below the water table (the Rustler Formation contains water bearing dolomites, e.g. Culebra). Unlike the plastic deformation and flow of the salt, the limestones, dolomites, and shales are observed to fracture above the Salado (Boyd, 1973) due to subsidence. Some brine inflow has been documented in large areas of secondary mining in the MS Chemical, Horizon, NM Potash, and Eddy mines by Stoller (1995), but it has never posed a problem for production or safety. Minor water weeps are also associated with clay, but are believed to be a result of compaction, especially where thick clay seams exist.

Fracture and re-compaction of less competent strata including anhydrite, polyhalite, and silt members within the salt, and salt creep, are believed to contribute to the time delay measured between mine closure and surface subsidence. At the US Potash Mine⁴, the major movement at the surface took place within 175 to 200 days after pillar extraction, and after 500 days lapsed time, the movement was minimal (Cummings, 1962).

The first visible evidence of subsidence on the surface is small hairline cracks following secondary mining which rapidly develop into openings measuring 1 inch wide and a hundred feet long. Such cracks develop around the boundary of mined areas and become larger with time, measuring from 6 to 24 inches wide. Slump holes also develop and measure 8 to 15 ft across and 15 ft deep. The development of these features is associated with horizontal ground tension.

The US Potash mine is 1000 ft deep and the seam thickness ranged from 5 to 15 ft in height. Figure 17 shows a typical subsidence profile over the edge of the mine. The surface strains are shown along with two angles commonly used to characterize subsidence. The angle of draw is used to define the extent of measurable subsidence. Measurable subsidence is about 0.01 ft. The angle of break is used to define the location on the surface most vulnerable to tensile cracks. Figure 17 shows a an angle of draw of about 40 degrees and an angle of break of 20 degrees. The maximum tensile and compressive strains are 0.5 and 0.8 percent, respectively. These are associated with about 6.4 ft of subsidence over area where the potash seam is about 9 ft thick.

⁴ Ref to as US Borax mine

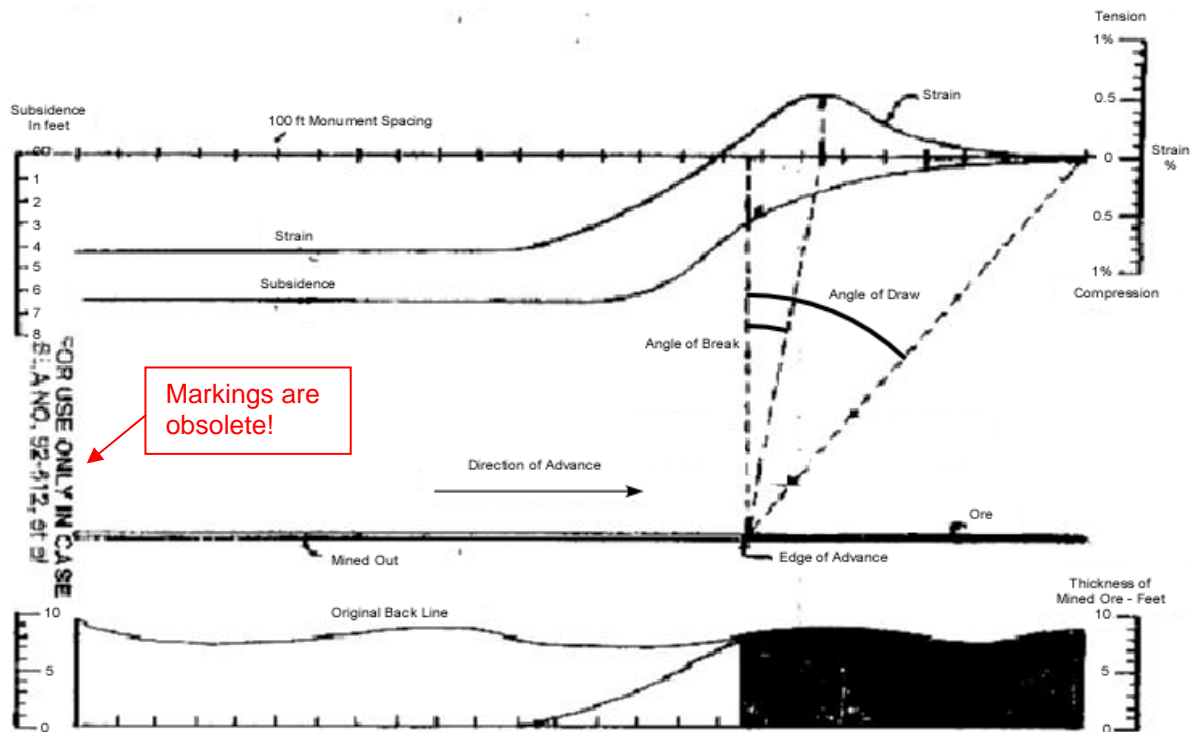


Figure 17. Subsidence Measurements over US Potash Mine (after Miller and Pierson, 1958).

Deere (1961) measured the horizontal and compressive strains on the surface over various seam heights at the US Potash mine⁵. The measured surface strains are presented in Table 10. Greater subsidence magnitudes generally result in higher strains, although the type of mining may have an impact.

Table 10. Max Surface Strains and Subsidence at US Potash Mine (Deere, 1961)

Baseline	Max. Compressive Strain %	Max. Elongation %	Max. Subsidence ft
75 E	0.6	0.9	10.2
69 N	0.3	.25	7.0
130 E	.5	.4	6.3
79 N	.3	.2	3.8

Pierson (1965) found that longwall mining produced smaller strains in the US Potash mine. In areas where 5 ft of subsidence was measured, the maximum tensile strain was 0.23 % measured at 150 ft from the panel edge or an angle of break of about 10 degrees. The maximum compressive strain was 0.06 % measured over the mine workings. One factor that was attributed to the lower surface strains was the presence of primary mining

⁵ US Potash merged and became US Borax and Chemical in 1956. They were then sold to US Potash and Chemical Co, in 1968, to Teledyne in 1972, and MS Chemical Co. in 1974.

beyond the edge of the longwall panel. Pierson compared these to areas that were conventionally mined up to the edge of the panel. Tensile strains of 0.67 % and compressive strains of 0.75 % were associated with 9 ft of subsidence. Adverse ground conditions were encountered in the mine. As a result, an experience based rule of thumb was developed from the subsidence measurements and observations underground, whereby the differential strain (difference between the maximum compressive and tensile strains) is limited to 1 % to prevent adverse mining conditions. The measurements over both conventional and longwall sections supported a rule of thumb that subsidence is approximately two-thirds the mining height. Pierson's measurements are shown in Figures 18 through 20.

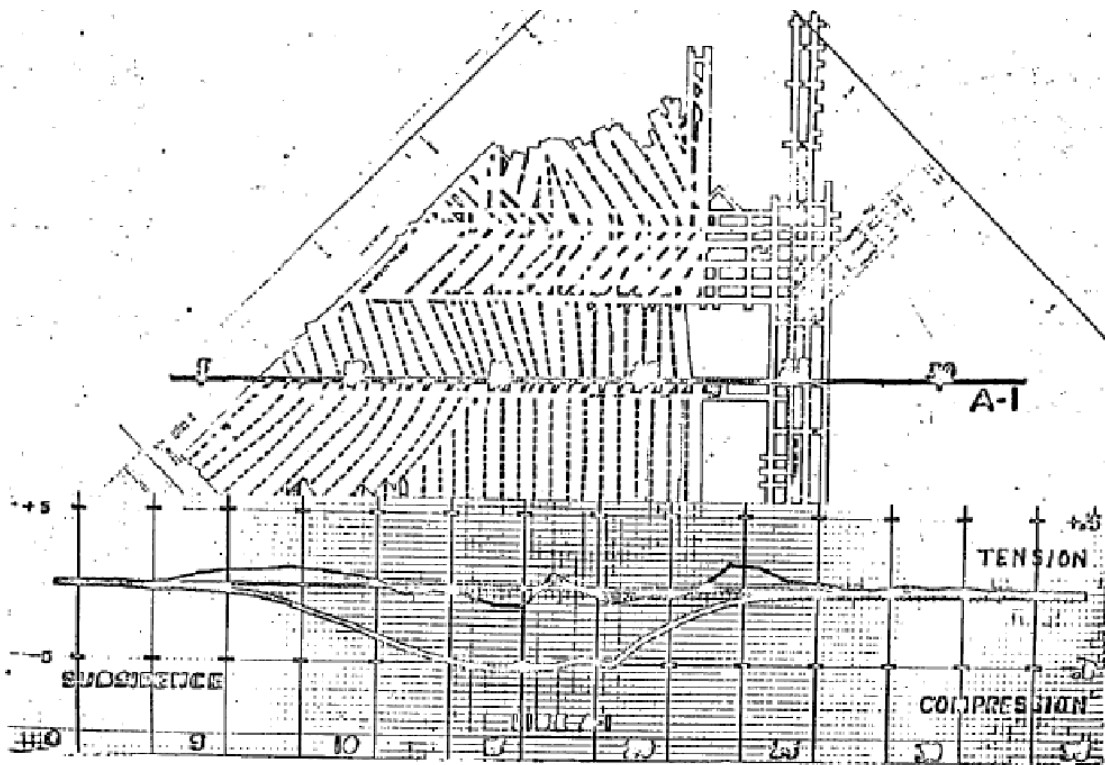


Figure 18. Subsidence and Strain over the Modified Longwall Operation (line A-1). Pierson (1965). Subsidence is in ft (left scale) and strain in units of percent (right scale).

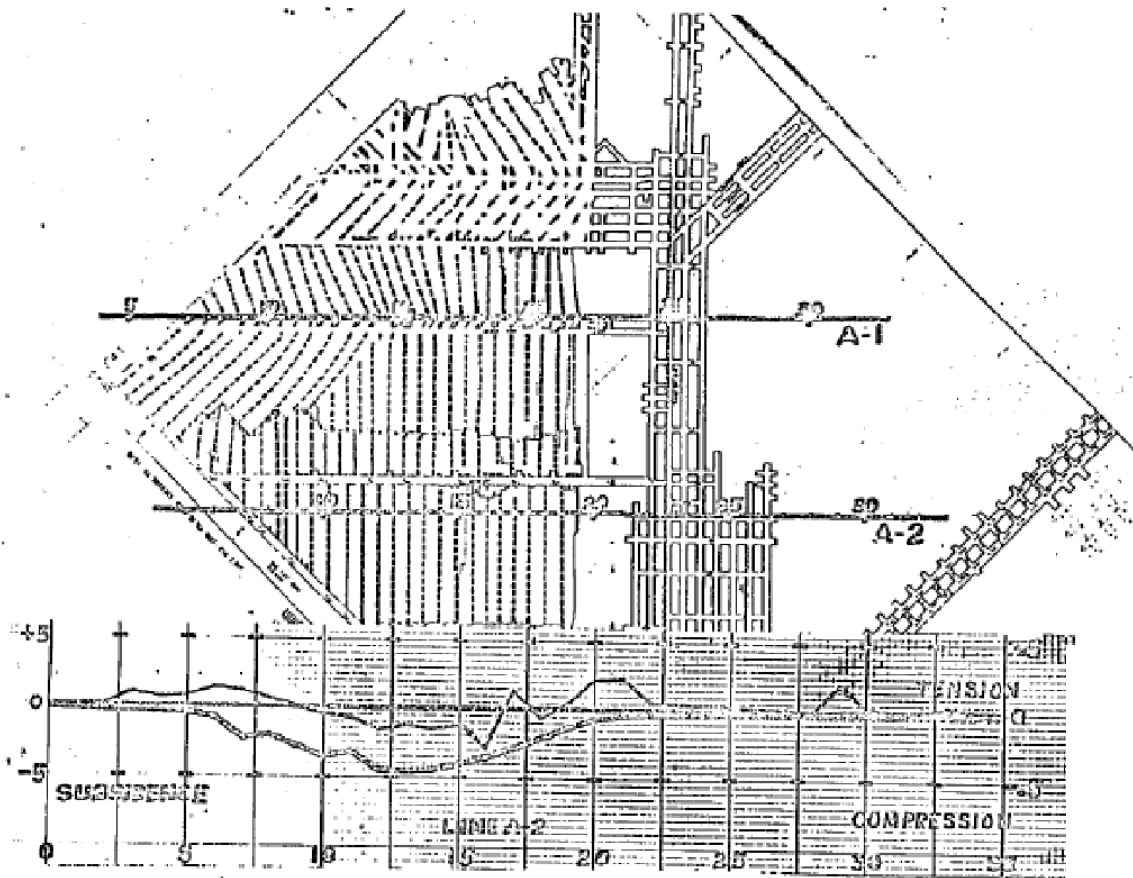


Figure 19. Subsidence and Strain over the Longwall Operation (Line A-2). Pierson (1965). Subsidence is in ft (left scale) and strain in units of percent (right scale).

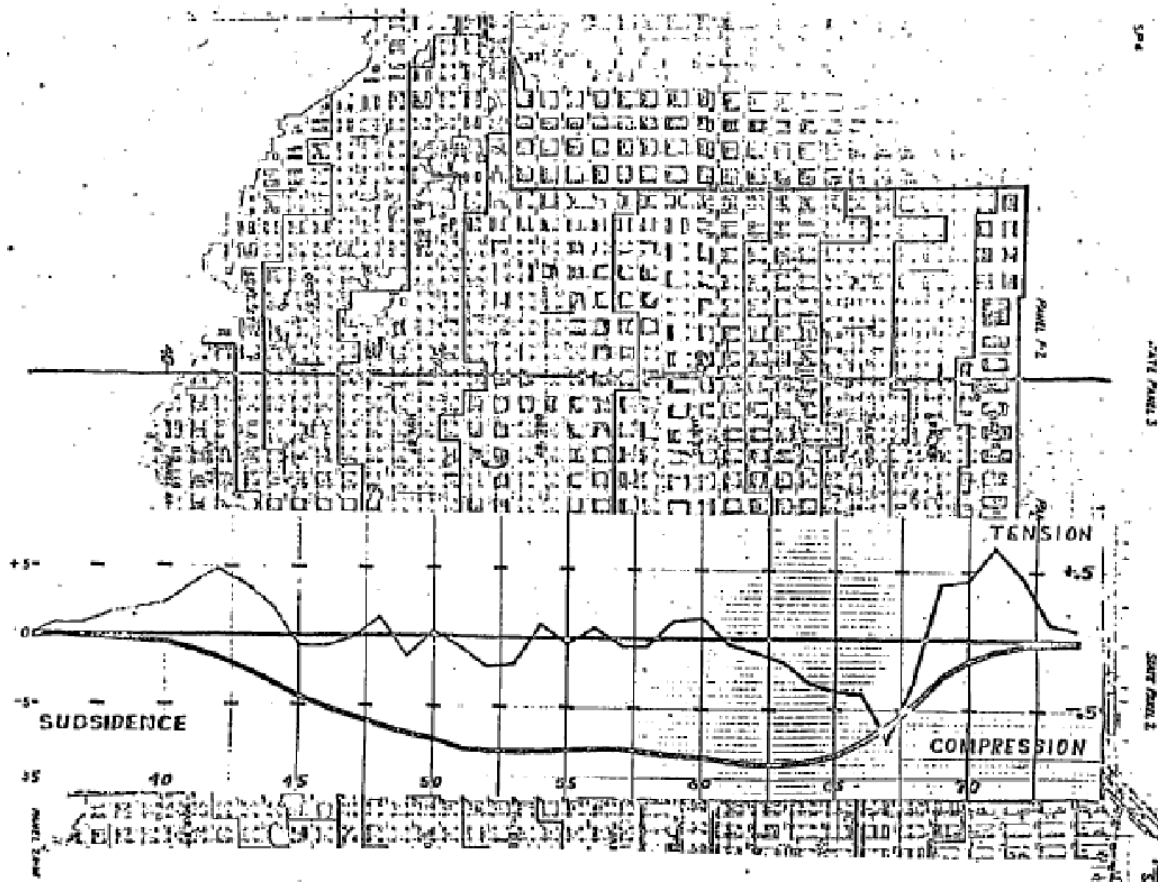


Figure 20. Subsidence and Strain over the Conventional Operation. Pierson (1965). Subsidence is in ft (left scale) and strain in units of percent (right scale).

Horizontal ground motions over time were recorded by Deere (1957) at the US Potash mine. Station 65N 125E recorded a horizontal movement of 4 ft, but the net movement was only 1.52 ft because of reversal in direction of the movement (Figure 21). This was in an area of approximately 6.75 ft of subsidence. Other stations produced net horizontal movements ranging from 0.59 to 1.73 ft, which occurred near the edge or directly over the mined out areas.

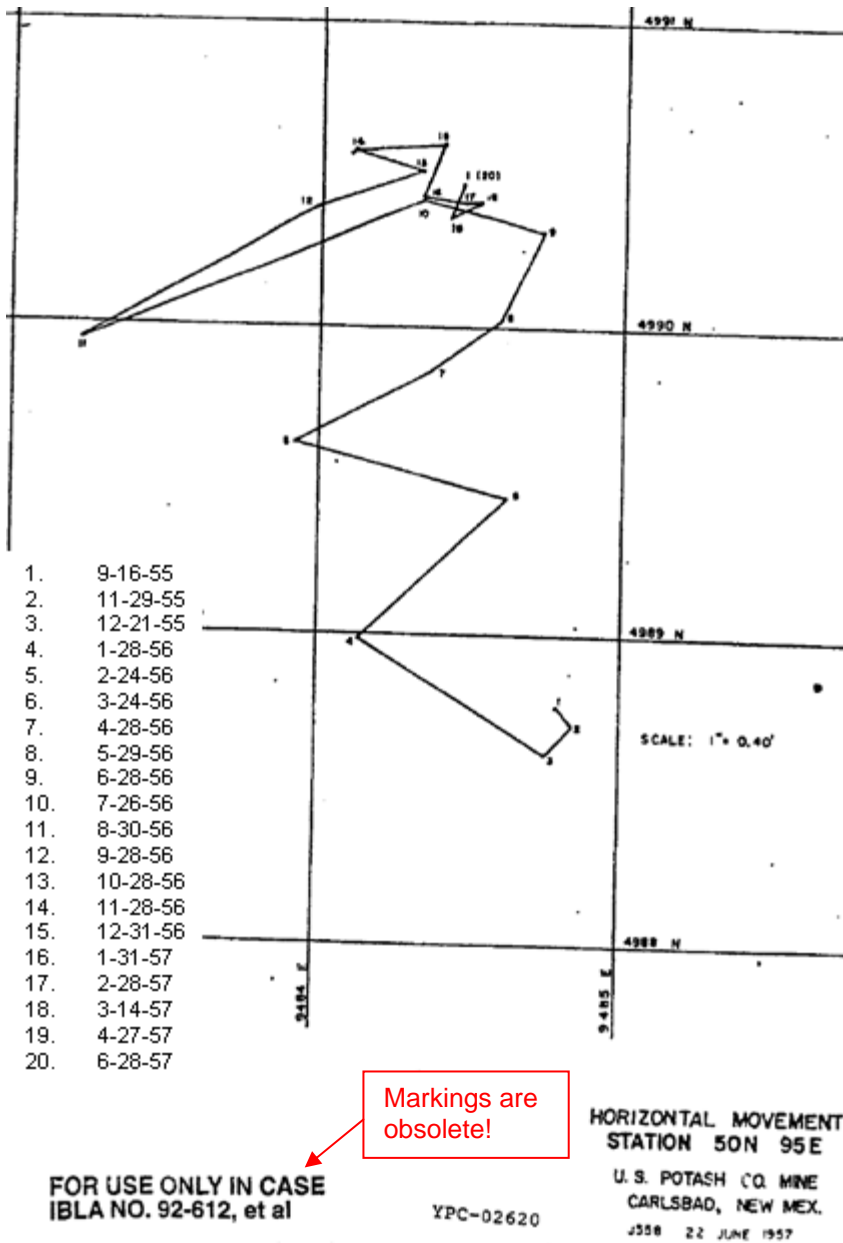


Figure 21. Horizontal ground movement at US Potash Mine.

Subsidence over the US Potash mine was measured 700 ft from the edge of the secondary workings. In areas where secondary mining was halted in a first mined area, the measured distance increased to 1200 ft (from the edge of the secondary workings). The measurements defined a limiting angle, or angle of draw which varied from 30 to 51 deg per Miller and Pierson (1958). It was believed to increase with weaker strata.

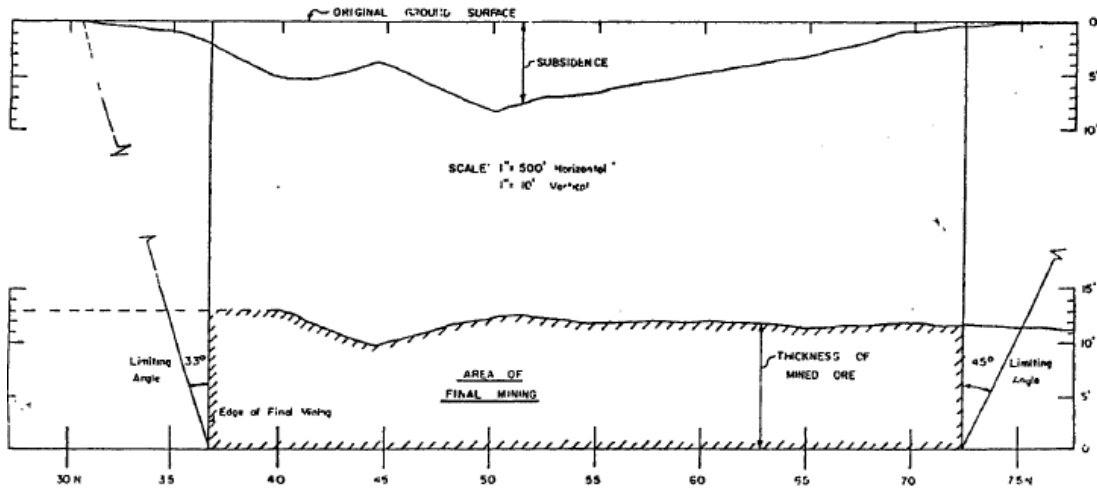
Deere (1961) compared the angles of draw and break over areas that were bounded on one side by primary mining and on the opposite side were secondarily mined to the edge of the panel. A comparison is provided in Table 11. A greater influence is noted in the

areas where primary mining is present beyond the secondary mining limits. The angles are measured from the edge of the secondary workings from vertical. Angles of break are reported elsewhere relative to horizontal.

Table 11. Angle of Draw and Break (Deere, 1961)

Baseline	Bounded by Unmined Area		Bounded by Room and Pillars	
	Draw	Break	Draw	Break
75E	>49	-3	56	10
130E	53	0	55	9
69 N	>47	4	-	-
79N	-	-	58	20

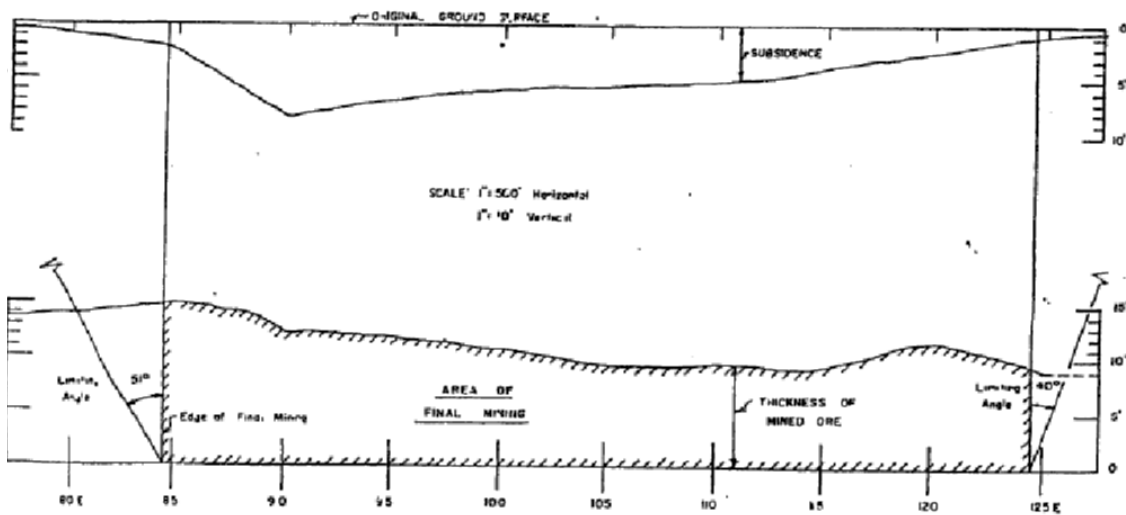
Subsidence profiles suggest that seam thickness and other factors may influence the shape of the subsidence trough. Two cross-sections are provided above the US Potash Mine in Figure 22.



Markings are obsolete!

FOR USE ONLY IN CASE

SECTION A-A
U.S. POTASH CO. MINE



Markings are obsolete!

FOR USE ONLY IN CASE

SECTION B-E

Figure 22. Subsidence Profiles above US Potash Mine (Deere, 1957).

Subsidence versus time over the US Potash mine is plotted in Figure 23. The plot shows that subsidence is nearly finished at 6.8 ft after 240 days when the face has passed 1250 ft past the measurement station. The distance required for maximum subsidence is not known, but it appears from the data that 1500 to 2000 ft may be required (Deere, 1957).

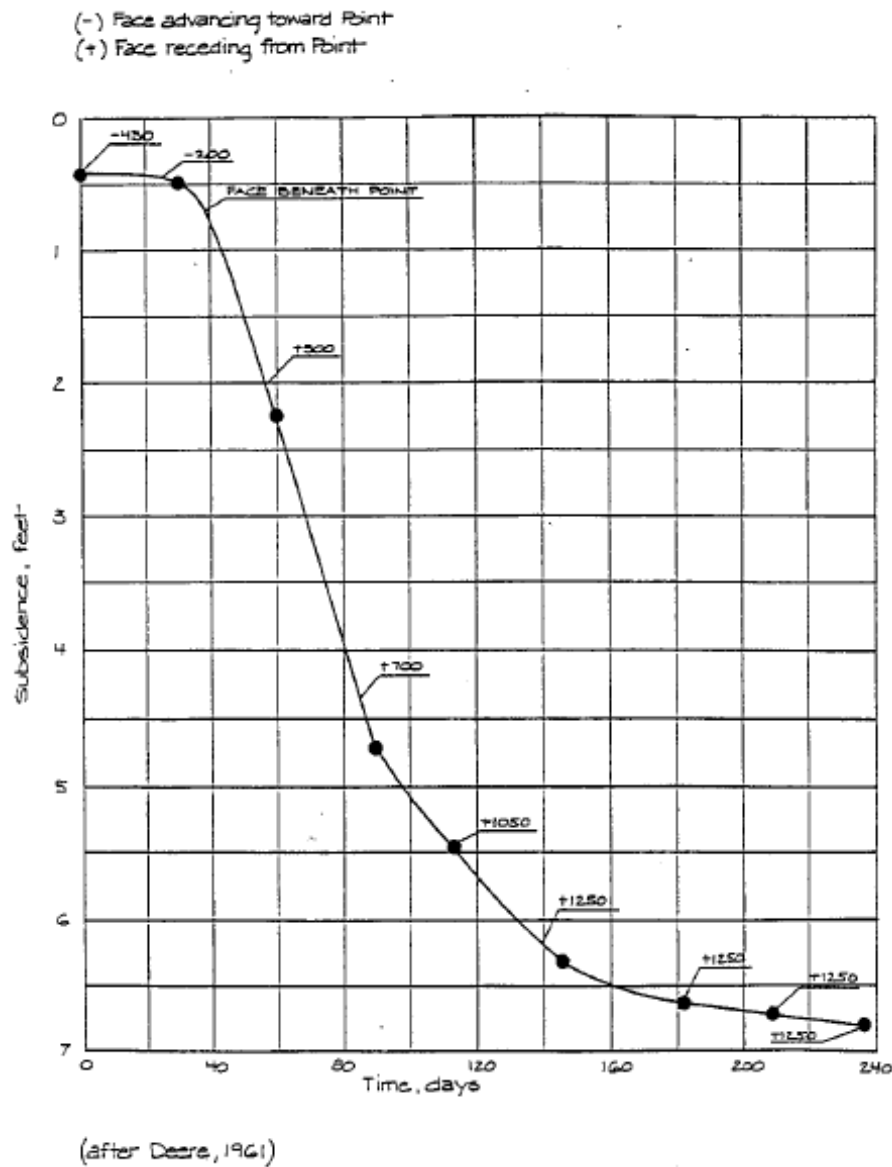


Figure 23. Subsidence over the US Potash Mine.

Table 12 shows that the ratio of subsidence to closure measured underground. The ratio increases with time and final subsidence is approximately two-thirds the underground room closure (underground subsidence) to approach the measured surface subsidence. In cases where the subsiding strata experiences limited disturbance and the lateral extent of the mined area is large enough, final subsidence may be on the order of the extracted seam height (Golder, 1979).

Table 12. Relationship between Subsidence and Closure at US Potash Mine (Miller and Pierson, 1958).

Time days	Room ht ft	Subsidence ft	Ratio of Subsidence to Closure
0	12.75	0	
60	9.5	0.75	0.23
140	5.25	3.5	0.47
200	-	6	
1000	-	7.5	
Final	-	8.5	0.67

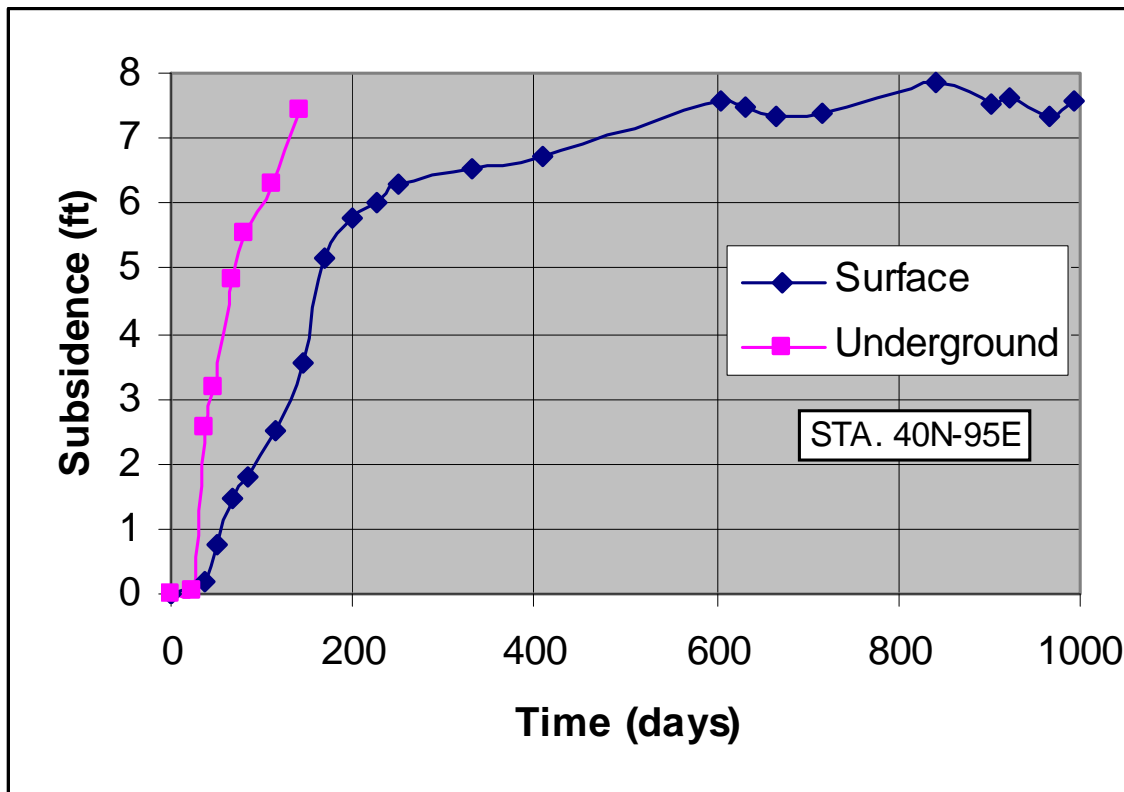


Figure 24. Subsidence and Closure at US Potash Mine.

Subsidence measurements were also performed at other mines. Golder (1979) performed a limited amount of subsidence measurements above the Wills-Weaver mine.

Approximately 1.8 ft of subsidence had occurred over 2 years in a seam height of 4.3 ft where the extraction ratio averaged 80 to 85 percent and the mine depth was 990 ft. The locations and measurements over the two subsidence arrays are shown in Figures 25 through 27. Retreat mining of the 1st North panel occurred from 9/20/1963 to 1/31/1964 and retreat mining of the 2nd North panel from 7/20/1964 to 1/25/1965. The earlier measurements occurred during mining of the panels which proceeded in a southerly direction (higher numbered stations were mined first).

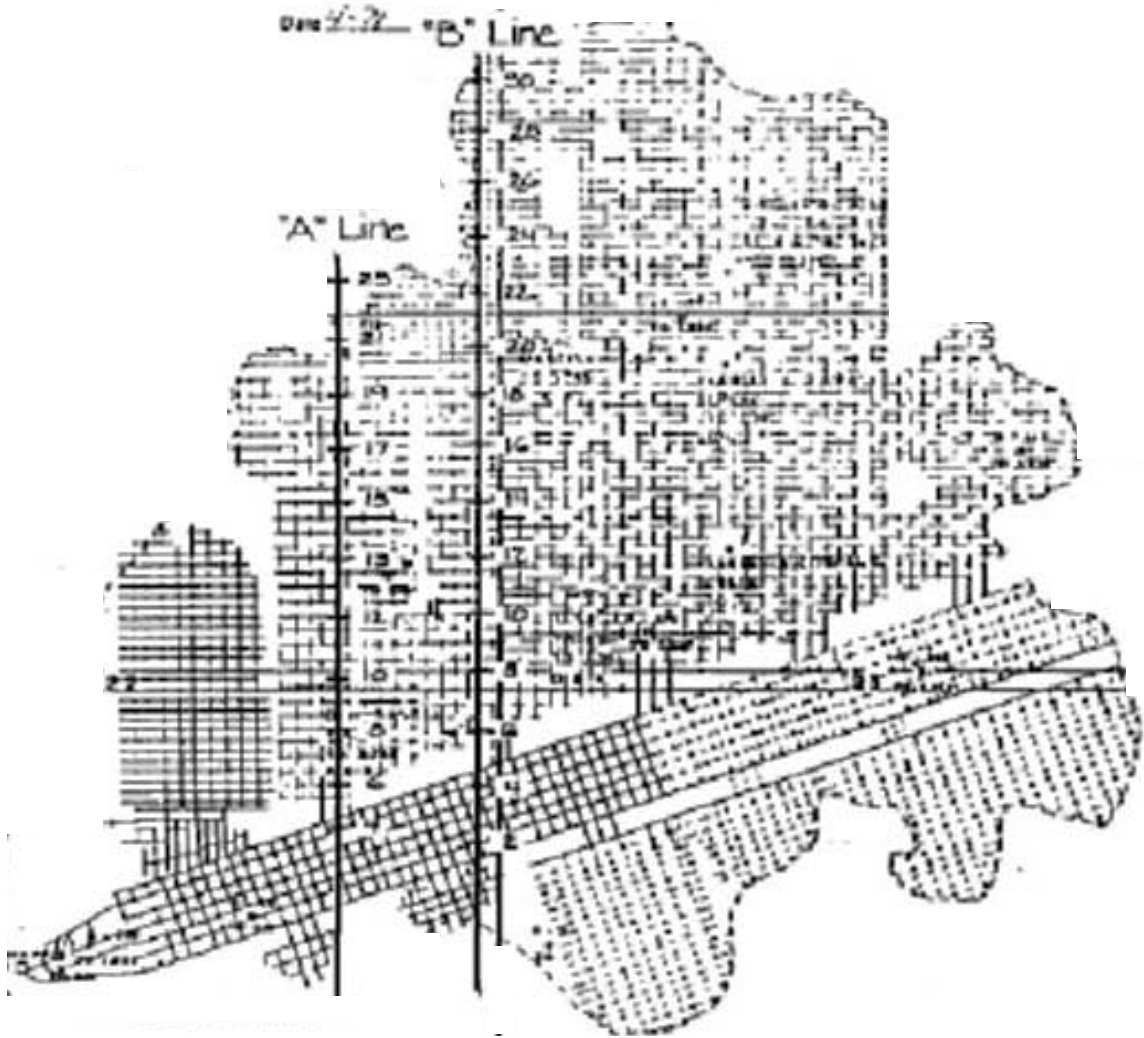


Figure 25. Subsidence Stations over Wills Weaver Mine

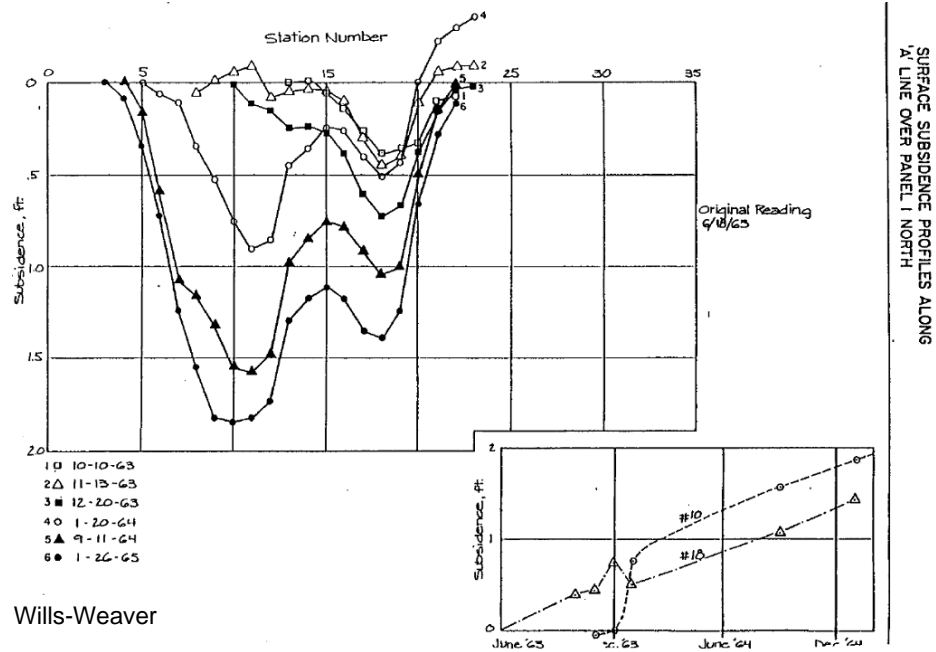


Figure 26. Subsidence Measurements over 1st North Panel

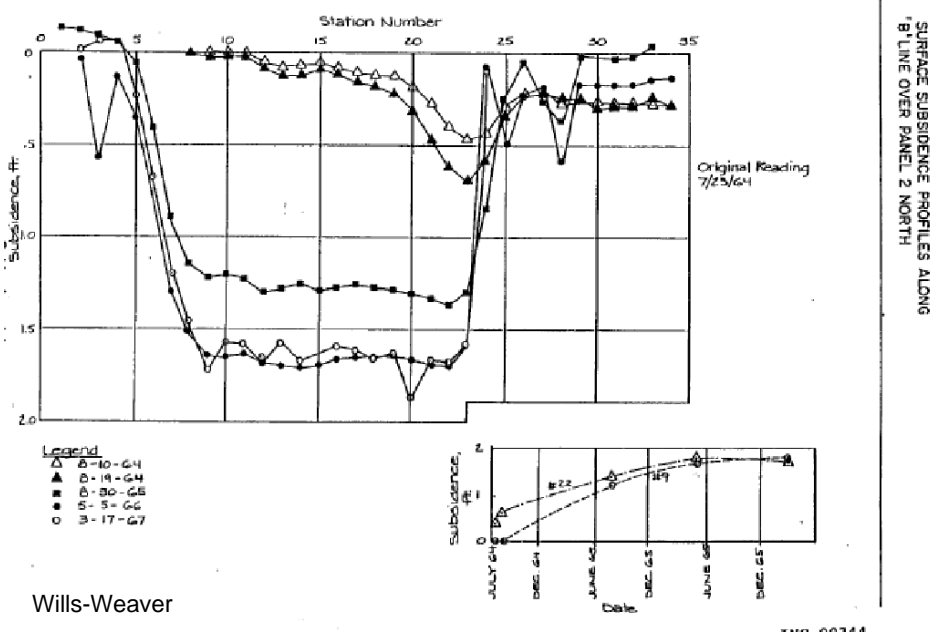


Figure 27. Subsidence Measurements over 2nd North Panel

Subsidence measurements (1959) were also presented (Figure 28) over a secondary mined area of the Southwest Potash (AMAX) that showed a maximum angle of draw of 36 deg. (Kirby, 1973). Details are very limited in this case.

According to Warnock (1995) other subsidence measurements have also been taken, but not published. A memo by Walter Burlson (1968) provides information on the NMP Kermac mine. At a depth of 1700 ft, it had 3 ft of subsidence over 5 ft openings. The MS Chemical Lea mine had 4 ft of subsidence over 5 ft openings. No angles of draw were reported, and both mines are on the east side of the district which is considerably deeper.

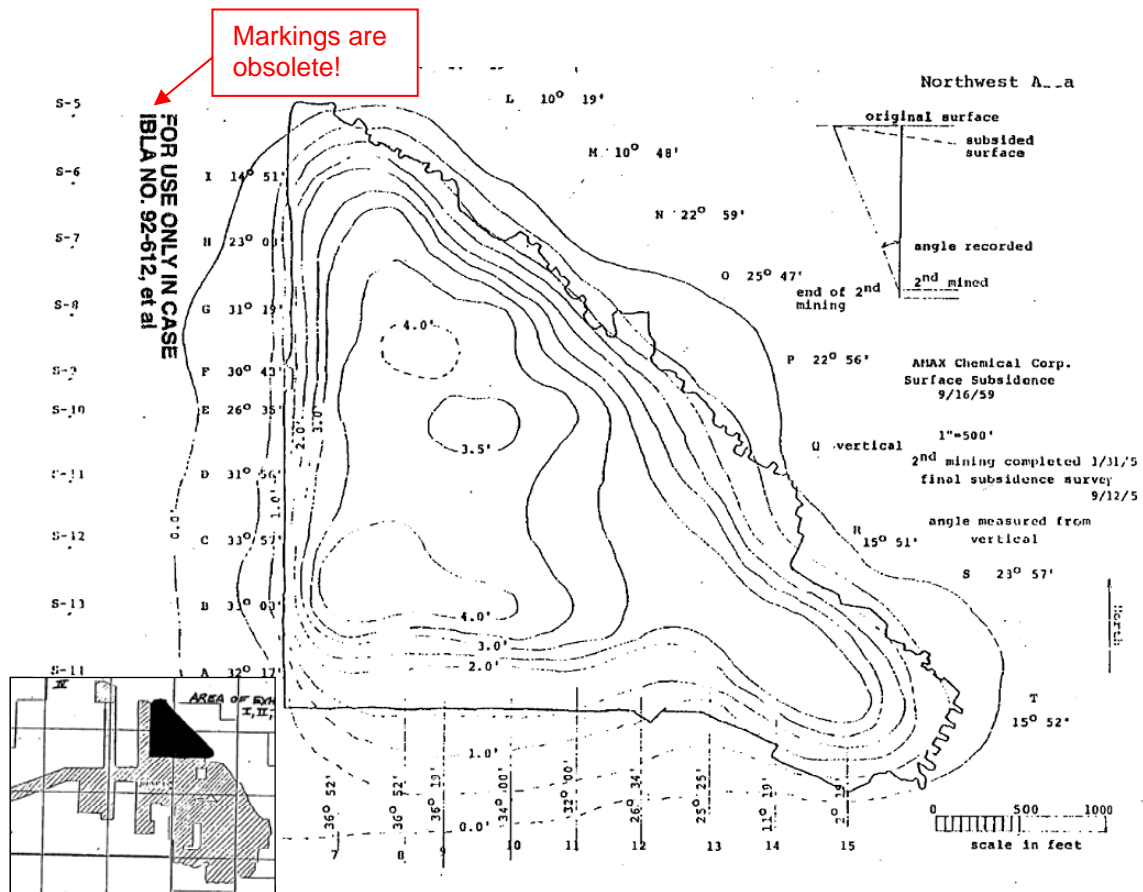


Figure 28. Subsidence Measurements over AMAX Mine (Kirby, 1973)

In addition to the underground closure measurements presented above in conjunction with subsidence studies, additional closure information is available. Abel (1996) compiles a list of salt and potash mine closures. The closure data for MS Potash and the Kerr-McGee (NM Potash) mines and calculated rates are presented in Table 13.

Table 13. Mine Closure Data

Mine	Depth	Extraction Ratio %	Height (ft)	Closure (ft)	Time yrs	Rate %/yr
MS Potash	1060	92	6	3	0.17	290
Kerr-McGee	1900	20	5	0.17	10	0.34
		25	5	0.42	3	2.8
		25	5	1	5	4.0
		25	5	1.5	5	6.0
		30	5	1.1	5	4.4
		32	5	1	3	6.7
		32	5	2	10	4.0
		80	5	1.75	1.25	28.0

Closure rates were also monitored at the Wills-Weaver mine by Golder (1979). The locations of the stations are shown in Figure 29. In areas where no secondary mining occurred, the rates were only 0.1 to 0.2 inches per year in the main entries of the East Panel and in the north panel (60 to 75 % extraction). In the 1st and 2nd north panels, where pillar retreat was occurring (85 % extraction rate), convergence stations showed rapid increases in rates up to 12 to 18 inches per month as the mining progressed southward. Some of this was attributed to roof sag and floor heave, so the closure may not be representative of pillar shortening. The measured closures are presented in Figures 30 and 31 in weekly intervals. Mining height was 4.3 ft.

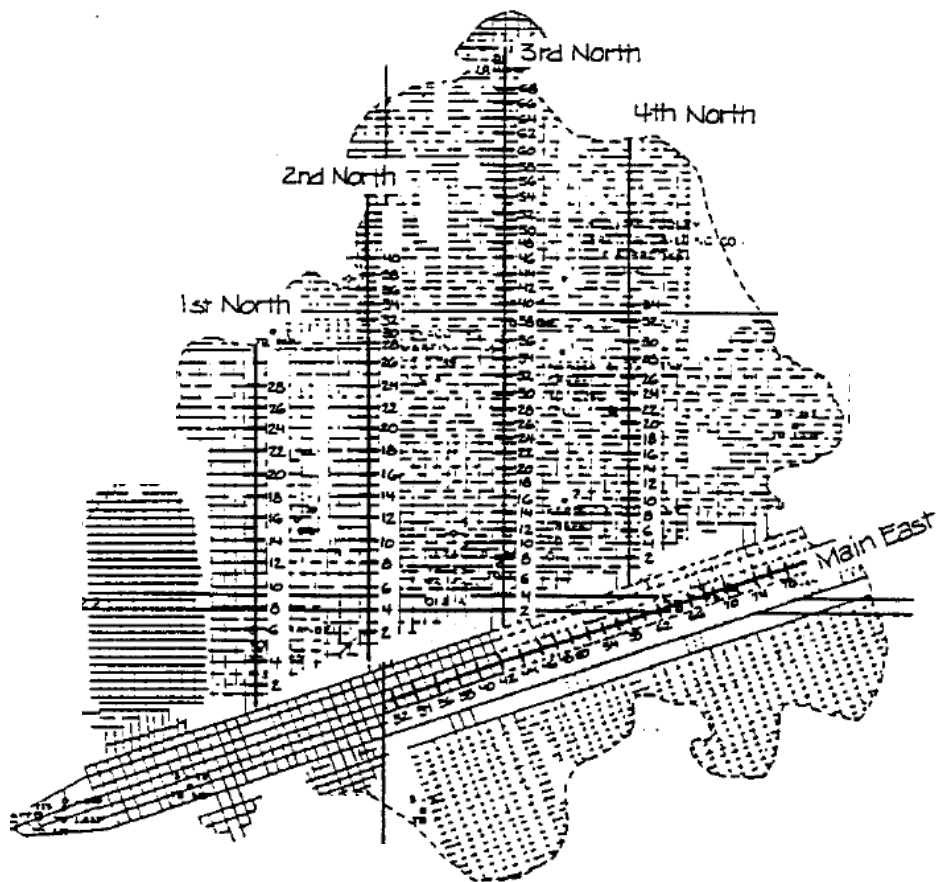


Figure 29. Location of Closure Measurements at Wills-Weaver (Golder, 1979)

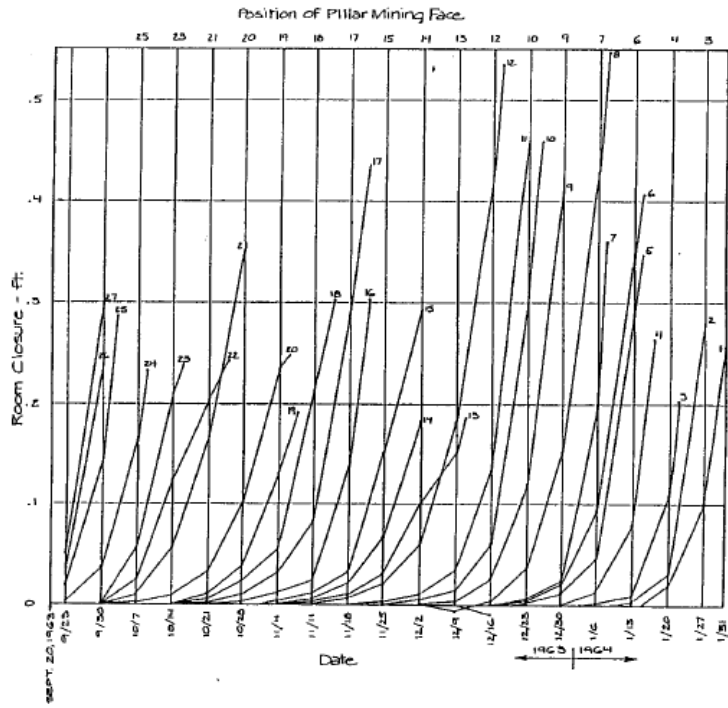


Figure 30. Measured Convergences in Wills Weaver Mine- 1st North (Golder, 1979).

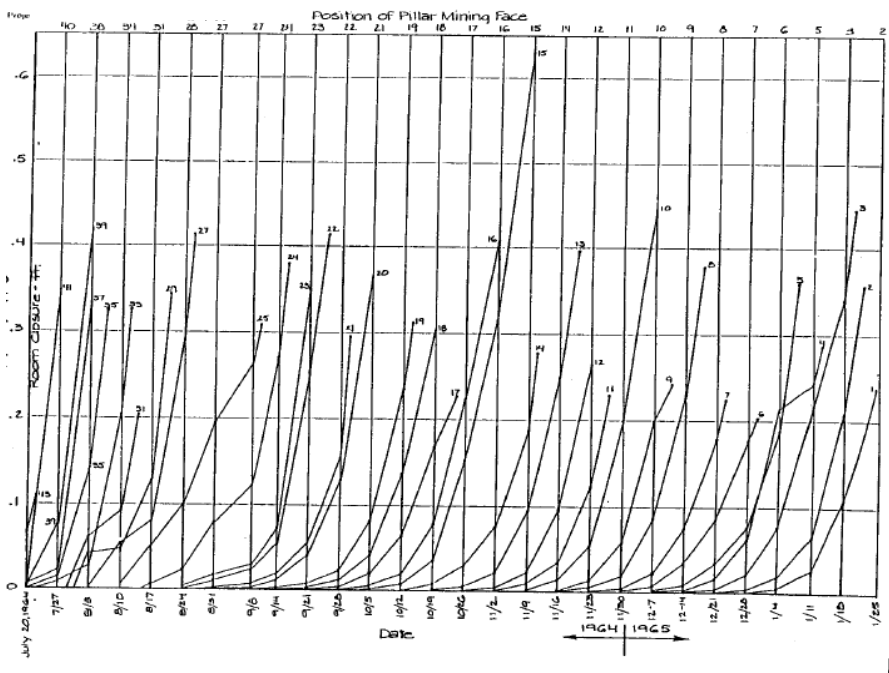


Figure 31. Measured Convergences in Wills Weaver Mine- 2nd North (Golder, 1979).

In addition to subsidence and closure measurements, observations have also been recorded. At the US Potash mine, room closure is sensitive to the presence of clay seams. Normally, failure of pillars is not sudden, but gradual and allows for sufficient time for pillar-robbing operations to progress beyond the area before the roof is let down too far (Deere, 1957). However, in areas where a thin clay seam is present within 3 ft of the roof, it is impossible to enter the final mined areas after a few weeks because the collapsed roof and floor are in contact. In other areas, where there are no serious roof falls, it is possible to enter the final mined area for as long as several months after final mining, although the distance between the roof and floor may be reduced from the original 12 ft to about 4 ft.

From the above measurements and observations, a list of metrics can be derived for potential comparison to modeling predictions, especially for the 1000 ft deep mine. They all apply to final (secondary) mining conditions, except for the last item. The conclusions of the field measurements and observations are:

1. most of the surface subsidence occurs over 1 to 3 years
2. final subsidence magnitude ranges from two-thirds to approaching full underground closure
3. angle of draw ranges from 30 to 55 degrees from vertical
4. angle of break ranges from -10 to 20 degrees from vertical
5. maximum tensile strain ranges from 0.04 to 0.09 % per ft of subsidence
6. a differential surface strain above 1% results in adverse ground conditions
7. tensile stresses and hence cracks can occur on the ground surface over mined boundaries
8. maximum compressive strain ranges from 0.01 to 0.13% per ft of subsidence
9. net horizontal ground motions range from 0.1 to 0.25 ft per ft of subsidence over mined boundaries
10. underground closure ranges from 30 days (poor ground conditions) to 150 days
11. rates of subsidence and closure decrease with time after mining
12. primary mining results in a few inches of subsidence and closure rates ranging from 0.2 to 7 % per year.

Because of the various simplifications and assumptions inherent in any model, no single mathematical idealization of the underground can be expected to capture all the salient features found in mining. On the field measurement and observations side, without knowing the pedigree of the data, it is difficult to ascertain the degree of uncertainty that may exist in it. Thus, the model used herein is formulated to, at least in a qualitative sense, capture many of the observations noted above. The model will be compared to the above behaviors in an effort to validate its field performance. Where major deviations are predicted, an attempt will be made to explain them and point out potential impacts on results and the conclusions reached.

Well Completions

New Mexico Oil Conservation Division (OCD) of the Energy, Minerals, and Resources Dept. issued Order R-111 in 1951, and more recently R-111-P (1988), that defines the oil and gas casing program for the Potash area. The regulations call for:

1. Surface casing set in the “Red Bed” section of the basal Rustler formation immediately above the salt section, or in the anhydrite at the top of salt. The cement shall be circulated to the surface.
2. Salt protection string set not less than 100 ft or more than 600 ft below the base of the salt section cemented to the surface. The string may be pulled in shallow wells if the production string is cemented to the surface.
3. Optional intermediate string cemented to surface for wells drilled into the deep zone.
4. Production string set on top or through the oil or gas pay zone. The well shall be cemented with a volume adequate to protect the pay zone and casing above the pay zone.
5. Production strings in shallow wells shall be cemented to the surface if the salt protection string was pulled.
6. Production strings in deep wells shall be cemented to the surface is required if no intermediate string was run and cemented to the surface.

The distinction between a shallow or deep well is the depth to the base of the Delaware Mountain Group or a depth of 5,000 ft whichever is less. Therefore in the salt section, shallow wells will have one cemented casing through the salt and deep wells require two cemented casings. In addition, the surface casing is cemented above the salt. These requirements, along with pressure tests at the casing seat, have been in effect since 1951. Without centralizers (R-111 does not require them), casings can contact the formation or each other (DOI, 1962) and result in asymmetric geometries, which are not modeled.

A summary of wells located within the mines and their status is provided in Table 14 (Appellants IBLA92-612, 1997). At least one of the active wells at the Eddy mine is a high pressure gas well which produced approximately 0.5 BCF and 2 wells at the Horizon mine are high pressure gas wells drilled after 1975, one of which produced 1 BCF.

Table 14. Well Status in Mines (1997)

Mine	Prior to 1951			After 1951			Year not Specified
	Active	P & A	Inactive	Active	P & A	Inactive	P & A
Eddy	10	43	2	3	6	0	
Horizon/Amax/SW Potash	1	12	0	3	3	2	
NM Potash							3
IMC							2
MS Chemical							1

The number of wells located within the mines is small in comparison to the 2800 wells currently drilled into the potash area. Of these about 600 wells were completed prior to 1951, and many are still producing. The older well completions did not have to adhere to order R-111.

An investigation into an oil seep at the Eddy mine (Hager, 1965) refers to a Getty well log that showed an 8 inch casing through the salt that was mudded in and a 6 inch production string that was mudded in at the pay zone. No cement was shown, except for the surface casing. The well was producing 4 bbls of oil per day and located approximately 600 ft from the mine workings. Another example is the Hargraves No. 2 well which was inadvertently mined into. It had a 8 in surface casing to 451 ft (top of salt) and a 7 in production casing to 1568 ft, both of which were cemented with 50 sacks in 1942 (DOI, 1942). Earlier examples of investigated wells, included two 1929 wells. In some cases, such as in the No. 1 Cunningham well, no cement was used on the 8-3/4 production casing set at 1600 ft (NM, 1929). On the Chase No. 1 well a limited amount of cement was used (75 to 150 sacks). The cementing practice was sporadic prior to 1951, but it appears that little to no cement may have been used in some of those wells.

Present day well completions vary, but a typical Delaware deep well is described in YP-411, General Chronology of a Delaware Well.

1. 40 ft of 20 in conductor pipe set at surface
2. 17.5 in hole drilled to 850 ft
3. 13-3/8 in casing emplaced and cemented to surface (Class C cement)
4. Hole extended with 11 or 12-1/4 bit 100 ft past last salt or about 4200 ft
5. 8-5/8 in casing emplaced and cemented to surface (Lite followed by Class C)
6. Hole extended with 7-7/8 in bit through bottom of Castile to Bone Springs (8700 ft)
7. Decide on whether to produce hole (run production casing) or plug and abandon
8. 5-1/2 in production casing cemented (Class H, Lite, and C cements) to surface in several stages.

For plugging and abandonment, the procedure describes at least 35 ft of cement above top perforation and a 25 sack minimum plug across the 8-5/8 shoe. A plug is set across the McNutt and a minimum 25 sack plug is placed across the 13-5/8 shoe. Additional plugs may be required by OCD and BLM. Order R-111 (OCD, 1951), requires plugging in a manner that will provide a solid cement plug through the salt section.

A typical Delaware completion is listed in Table 15.

Table 15. Typical Casing Specs.

Size	Weight lb/ft	Grade	Wall Thickness in
13-3/8	48	H-40	0.330

	54.5	J-55	0.380
8-5/8	24	K-55	0.264
	28	S-80	0.304
	32	J-55 or M-80	0.352
5-1/2	15.5	J-55 or K-55	0.275
	17	J-55 or N-80	0.304

A casing program by Pan American (Croft, 1964) specified surface casing at 94 lb, a 1st intermediate string of 13-3/8 in 54.5 lb to 1400 ft, a 2nd intermediate of 9-5/8 in 40 lb to 4000 ft, and a 5.5 in 20 lb production casing to 13,000 ft. The surface and intermediate casings would be cemented through salt.

Broadhead, Luo, and Speer (1995) compiled typical well completions near the WIPP Site. The geologic column (Figure 32) shows that gas is more commonly encountered in deeper formations. Two completions are shown in Figure 33.

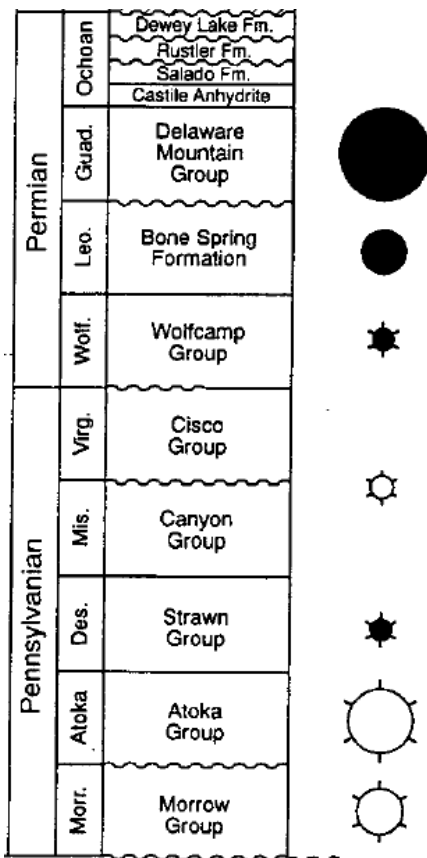


Figure 32. Geologic Column Near WIPP showing Production Zones (Broadhead, 1995)

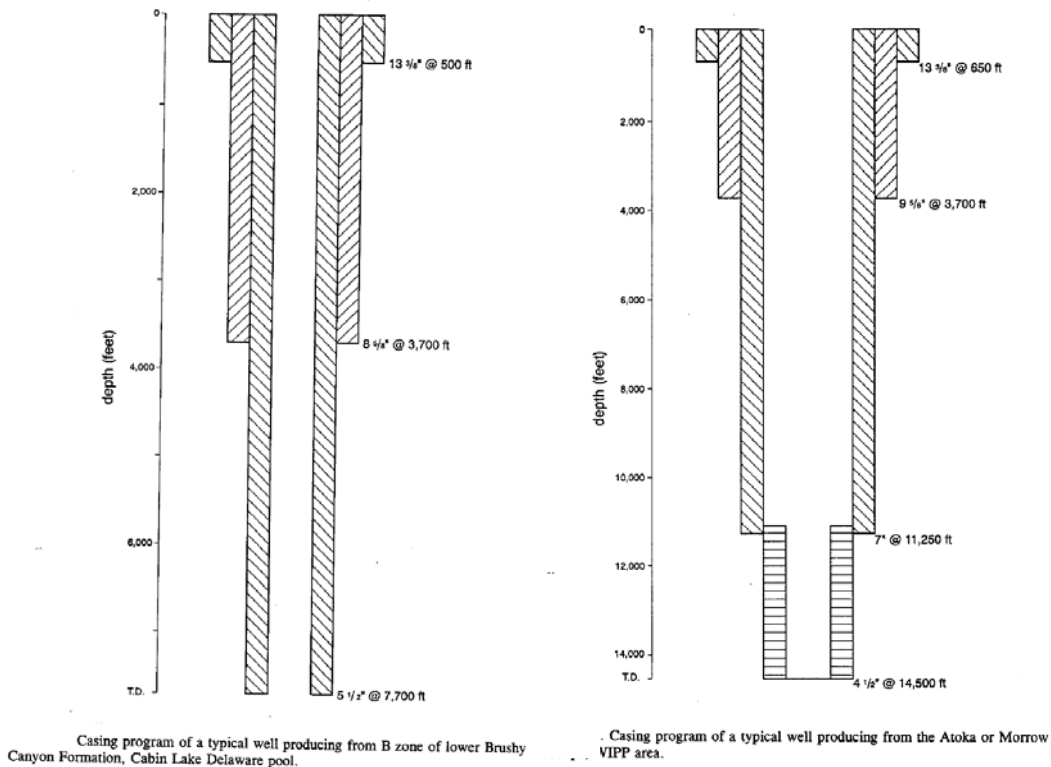


Figure 33. Well Completions in Lower Brushy Canyon and Atoka and Morrow Formations (Broadhead, 1995)

Pressure data is routinely collected downhole at the time the wells are completed. Numerous records exist, and they appear to be consistent in the pressure gradient calculated, regardless of depth. Initial formation pressures average 0.43 psi per ft of depth (Table 16). This is equivalent to a hydrostatic head. Formation pressures in the Salado and Castile are believed to be higher, but these are non-producing formations above the Delaware. A deep gas well (14,000 ft) would have a bottom-hole pressure of 6000 psi. At mine depth (1000 to 2000 ft), the pressure would be less due to the density of the fluid in the wellbore. Assuming a gas column in the well, the pressure at mine depth would be about 4000 psi. Delaware pressures would be less, in part due to depth (8000 ft), and measured pressures are about 3000 psi (Teufel and Hazlett, 2000). These wells commonly produce oil, associated gas, and water. Therefore the slightly higher fluid density in these wellbore may reduce the pressure exerted on the casings at mine depth. Discovery pressures also deplete with time, and depending on completion technique, may not be directly applied to the cemented casings in the McNutt. They represent an upper bound. A lower bound pressure for purposes of the analysis is atmospheric pressure. While one may argue that gas migration may not occur under very low pressure conditions, the impact of gas pressure on well mechanics and integrity will be investigated at both high and low fluid pressures, in part because pressure histories in

the well can vary over the life of the well depending on the production horizon being tapped, workovers, and stimulations.

Table 16. Initial Pressure Gradients in Wells

depth	pressure	psi/ft	Location	ref pg
6050	2425	0.40	Cherry Canyon well	1386
5500	2256	0.41	Cherokee fm 49er well	1403
5500	2425	0.44	Cherokee fm 49er well	1403
6700	2800	0.42	Delaware	1875
2690	1100	0.41	Yates	1919
14633	6400	0.44	Morrow sand	1979
14524	6750	0.46	Morrow sand	1981
4550	1843	0.41	Yates	5119
6550	2738	0.42		5119
10519	4600	0.44		5987
10845	5175	0.48	Morrow	6547
10845	4955	0.46	Morrow	6547
12210	4988	0.41	Morrow	6547
12293	5253	0.43	Morrow	6547
13219	5651	0.43	Morrow	6547
7500	3150	0.42	Delaware	6558
12144	4887	0.40	Fed. Dooley No. 1	16100
		0.43	average	

Well Model and Properties

For modeling the wells, steel and cement properties are needed in addition to the rock and interface (bedding plane) properties mentioned earlier. Table 17 lists the elastic properties for steel.

Table 17. Well Properties

	Steel
Elastic Modulus (psi)	29×10^6
Poisson's Ratio	0.3

The Sandia Geomodel will be used to simulate the cement behavior. Plastic behavior and strain hardening are captured in the model. A complete description of the model and data set for a 23 MPa (3350 psi) sand-quartz aggregate concrete are provided by Fossum and Brannon (2004) and Warren (2002). Table 18 lists the parameters for the cement model. B_0 and G_0 represent the initial elastic bulk and shear moduli of the cement. Other parameters control the inelastic deformation associated with growth and coalescence of microcracks and pores as the material hardens and yields under load. Under larger

confining pressures, the material could behave in a plastic manner. The limit surface for the cement model is shown in Figure 34.

Yielding of the steel casing will be assumed to follow the von Mises criterion when it reaches the specified API yield limit. Yielding will be evaluated not only in direct shear, but also due to bending and axial deformations from the mine model that will be imposed on a well casing to calculate stresses and strains. Couplings in the casing will not be modeled or individually evaluated. Threaded couplings add a complexity to the calculation that is difficult to simulate, especially under axial and bending loads where leakage can occur. In evaluating the integrity of the well casing, a reasonable safety factor must be used to offset the lack of modeling complexity and uncertainties that occur in the field.

Table 18. Properties for Geomodel Cement

```

B0 = 5.5e9          $Pa
B1 = 28.78e9       $Pa
B2 = 0.623e9       $Pa
B3 = 0.0           $Pa
B4 = 0.0           $Dimensionless
G0 = 1.9026e9      $Pa
G1 = 0.890513      $Dimensionless
G2 = 3.55e-9       $1/Pa
G3 = 0.0           $Pa
G4 = 0.0           $Dimensionless
RJS = 0.0          $Meters
RKS = 0.0          $Pa/m
RKN = 0.0          $Pa/m
A1 = 1255.7e6      $Pa
A2 = 1.93e-10      $1/Pa
A3 = 1248.2e6      $Pa
A4 = 0.0           $Radians
P0 = -1.067e8      $Pa
P1 = 7.66e-10      $1/Pa
P2 = 3.88e-20      $1/Pa^2
P3 = 0.1538        $Dimensionless (strain)
CR = 10.0          $Dimensionless
RK = 1.            $Dimensionless
RN = 3.0e6         $Pa
HC = 1.0e11        $Pa
CTI1 = 3e6         $Pa
CTPS = 1.e6        $Pa
T1 = 0.0           $Sec
T2 = 0.0           $1/Sec
T3 = 0.0           $Dimensionless
T4 = 0.0           $1/Sec
T5 = 0.0           $Pa
T6 = 0.0           $Sec
T7 = 0.0           $1/Pa
J3TYPE=3
A2PF = 0.0 $zero defaults to A2 (associative)
A4PF = 0.0 $zero defaults to A4 (associative)
CRPF = 0.0 $zero defaults to CR (associative)
RKPF = 0.0 $zero defaults to RK (associative)
SUBX = 0.0

$model 2 generic eos
$ rho ref = 2030.          $ kg/m^3
$ tref = 298.             $ K
$ ref sound speed = 4500.0 $ m/s
$end

```

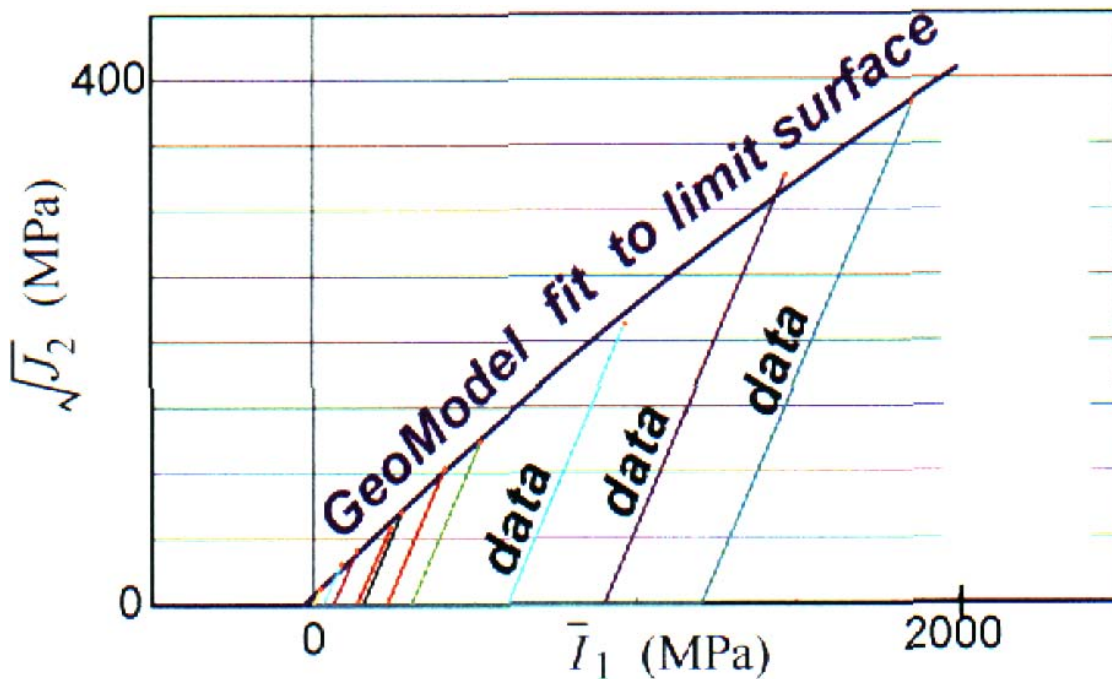


Figure 34. Yield Surface of Geomodel Cement (from Fossum and Brannon, 2004)

Based on the variation in well completions, 3 casing models will be considered. The first model will represent old practice, whereby a single cemented casing may exist. For this purpose, an 8-5/8 in casing cemented into an 11 in hole and 40 ksi yield strength steel will be assumed. The second model will consider two (8-5/8 in and 13-3/8 in) cemented 55 ksi steel casings. The third model will add a 5-1/2 in cemented casing to the second model and assume that all 3 casings are 55 ksi steel. The specific casing and hole dimensions are provided in Table 19.

Table 19. Well Model

Casing Number	Outside Diameter (in)	Thickness (in)	Hole Diameter (in)
1	8-5/8	.264	11
2	13-3/8	.33	17-1/2
3	5-1/2	.275	

No pre-loading will be assigned to the casings as a result of emplacement and cementing. In practice such loads exist due to the weight of the mud, density of the steel, and cementation pressures. After the cement sets, the degree of loading is difficult to estimate. In many cases, a micro-annuli surrounding a well casing is not uncommon which suggests a relatively low loading.

Model Variations

The mechanical properties of the rock overlying the salt can vary and test data is apparently not available. Table 8 provided some values assumed in a previous study by Teufel (1996). In that study, the Dewey lake Beds and Rustler formations were assigned an elastic modulus of 15 and 20 GPa, respectively. However, these formations contain different types of rocks. Table 20 shows a range reported in literature.

Table 20 Young's Moduli of Rocks from Handbooks (unit: GPa)

Rocks	Carmichael (1984)	Toulukian and Ho (1981)
Anhydrite	-	1 to 20
Dolomite	10 to 80	2 to 71
Gypsum	-	2
Limestone	3 to 100	2 to 81
Sandstone	0.4 to 70	4 to 52
Shale	0.4 to 70	2 to 52

Properties of rock are also influenced by large scale features not necessarily represented in laboratory size specimens, such as fractures. Therefore, the rock properties in the subsidence model will be adjusted within reason, based in part on the above ranges, to best represent the field measurements and observations previously summarized. Mine subsidence and closure data will be compared to model predictions. A calibration of the material used to simulate room and pillar behavior may also be required to better approximate mining conditions.

A crushed salt or similar model may be used to simulate the response of the mined out room and pillar panels (Hansen, et al., 1998; Callahan and Hansen, 1999). The model is intended to capture time dependent deformations of a panel based on the extraction ratio of the panel. Individual pillars and rooms will not be explicitly modeled. The initial fraction density of the material will be set to 0.1 to represent a 90 percent extraction ratio when simulating secondary mining. When the fractional density of the salt reaches one due to closure and consolidation of material, the model produces intact salt (potash) behavior. The model parameters were originally developed to simulate consolidation of crushed salt at WIPP which has an initial fractional density of 0.6 ($\rho_o=1300 \text{ kg/m}^3$). In our case, the WIPP reference model parameters (Table 21) may need to be adjusted to better simulate actual room closure rates.

Table 21. WIPP Crushed Salt Parameters (Butcher, 1997)

Parameter	Units	Value
ρ_0	kg/m ³	1300.
ρ_f	kg/m ³	2140.
K_0	MPa	0.0176
G_0	MPa	0.0106
K_1	m ³ /kg	0.00653
G_1	m ³ /kg	0.00653
K_f	MPa	20667.
G_f	MPa	12400.
B_0	kg/m ³ ·s	1.3E8
	kg/m ³ ·yr	4.102E15
B_1	MPa ⁻¹	0.82
A	m ³ /kg	-0.0173

A plastic model may be used to capture the behavior of anhydrite in the casing model if casing damage is predicted along an anhydrite interface. Anhydrite is found in the Rustler and bands occur within the Salado, often on top of the clay and mudstones. Yielding may occur in the anhydrite if significant casing resistance to slip induces large stresses in the anhydrite. The anhydrite layer can be considered isotropic and elastic until yield occurs (Butcher, 1997). The behavior of the anhydrite will be assumed to be the same as the WIPP anhydrite. Once the yield stress is reached, plastic strain begins to accumulate. Yield is assumed to be governed by the Drucker-Prager criterion:

$$\sqrt{J_2} = C - aI_1$$

where J_2 = the second deviatoric stress invariant

I_1 = the first stress invariant (σ_{kk})

A non-associative flow rule is used to determine the plastic strain components. Drucker-Prager constants, C and a, for the anhydrite are given in Table 22.

Table 22. Drucker-Prager constants for anhydrite (Butcher, 1997)

Parameters	Units	Values
C	MPa	1.35
a		0.45

The input to the model (soil and crushable foam) in the JAS3D code requires the analyst to provide TWO MU, 2μ , and the BULK MODULUS, K . The conversion from Young's modulus, E , and Poisson's ratio, ν , to the JAS3D input parameters is given by the following relationships taken from Fung (1965):

$$2\mu = \frac{E}{(1 + \nu)}$$

$$K = \frac{E}{3(1 - 2\nu)}$$

The JAS3D code requires the input to the material model which describes the anhydrite's nonlinear response to be given in terms of effective stress, $\bar{\sigma} = \sqrt{3J_2}$, and pressure, $p = \frac{I_1}{3}$. Rewriting the above equation in terms of $\bar{\sigma}$ and p the following relationship is obtained:

$$\bar{\sigma} = \sqrt{3}C - 3\sqrt{3}ap$$

The JAS3D input parameters A_0 and A_1 are $\sqrt{3}C$ and $3\sqrt{3}a$, respectively. The JAS3D input parameters for the anhydrite are given in Table 23.

Table 23. Material properties of anhydrite (Butcher, 1997)

Parameters	Units	Values	
Density (ρ)	kg/m ³	2300	
Young's Modulus (E)	GPa	75.1	
Poisson's Ratio (ν)	-	0.35	
Bulk Modulus (K)	GPa	83.4	
Shear Modulus (μ)	GPa	27.8	
Constants	A0	MPa	2338
	A1	-	2.338
	A2	-	0

The finite element code JAS3D (Blandford, 1998) will likely be used in the calculations. It uses an eight-node hexahedral Lagrangian uniform strain element with hourglass stiffness to control zero energy modes. A nonlinear conjugate gradient method is used to solve the nonlinear system of equations. This efficient solution scheme is considerably faster than the direct solvers which are used in most commercial codes and is a product of decades of research and development into nonlinear large strain finite element analyses.

Evaluation of Results

Yielding of steel in a well casing will be considered as unacceptable. It is common engineering practice to design steel structures so that the members do not yield under the design loads. The structure in this case is the well. The integrity of the well will be compromised if yielding occurs in any of its casings. In addition a safety factor will be used depending on the uncertainties in the analyses and consequences at stake. The uncertainties are related to the naturally occurring geologic variations in the field, and unknowns in modeling their behavior, primarily rock properties and constitutive models. Additional uncertainties arise due to the generic and idealistic assumptions used in the models and the limited number of conditions evaluated. The consequences of being wrong in establishing the standoff distances can be enormous. In this case, life and significant economics are at risk. Therefore, while the study will present findings at the yield limit for steel, it will recommend standoff distances greater than those calculated at the yield limit.

The risk tolerance of individuals or for that matter the two industries involved, varies along with what it has at stake. The oil and gas industries may be willing to take greater risks as long as the consequences are largely upon the mining industry. It is also possible for the mining industry, in their desire to protect their valuable assets and considerable investment, to try and prohibit any hydrocarbon development regardless of what may be reasonable from a technical point of view. Thus, the extensive litigation and lack of resolution on this issue. The potash and oil and gas industries will likely remain divergent in establishing what is acceptable. In this study, the project team will propose a reasonable safety margin, but will not establish it for purposes of our report until after review and consensus (see Foreword).

Damage to casing cement is not necessarily unacceptable, unless it is predicted to extend vertically along the casing from the oil to potash production zones. We don't anticipate any such response in the modeling, but will verify through examination the analysis results. It should be noted that in the field, leakage along the cemented annulus is common in wells, and could be problematic if not during production, possibly after the well is plugged and abandoned. Modeling of flow along a microannulus is challenging as the characteristics of the flow channel are largely unknown and dependent upon the cement job and other factors beyond the scope of this investigation.

The yield model used for cement is intended to produce realistic load transfers to the casing, however, yielding of the cement does not imply loss of well integrity. The steel serves to contain the well fluids. However, a practical consideration to cement damage is the possibility of enhanced corrosion of the casing. We will therefore note it in discussing the results, but predictions of corrosion are outside the scope of the analyses.

Damage of rock or separation of strata can also be important, as it impacts the hydrological properties, facilitating flow, either of gas or oil from the well into the mine or inflow of water into the mine from overlying water bearing formations. Therefore these results will be evaluated and weighed accordingly. In the case of gas migration, it is desirable to maintain integrity of the salt between the well and mine. Damage across this region is considered unacceptable regardless of the state of the well. This will help ensure that microannular or gas from thread leaks do not readily migrate into the mine.

Position on Gas Migration

Hydrologic or frac analyses are not included in this analysis plan. It is assumed that if well integrity is compromised, gas pressures can be sufficiently high enough to either fracture the formation or permit flow into the mine through the natural flow system. These two flow systems (hydrofracture and natural flow) are addressed below.

Wellbore fluid pressures, exerted against the rock, in excess of lithostatic pressure can fracture the formation. Theory holds that the overpressure must be greater than the tensile strength or cohesion of the rock for the formation to fracture. In the case of a fractured anhydrite or clay marker bed, the cohesive strength is insignificant. The lithostatic pressure at mine depth is about 1000 and 2000 psi for the typical and deep mines, respectively. Since initial gas pressures in the wells are much greater (up to 4000 psi) than the lithostatic stress state, fracturing or separation of existing fractures will occur. The fractures will propagate as the reservoir can supply and maintain pressure on the system. No analysis needs to be done to arrive at this conclusion. The practice of fracturing a formation by over-pressurizing it is routinely exercised in the oil and gas industry to stimulate production from wells.

As discussed above (see Well Completions), high reservoir gas pressures rapidly deplete during production of a zone, and frac pressures may not exist for long periods of time after production commences. However, wells are typically completed at various horizons or pay zones over time, and wells can be reworked to even greater depths. Such stages throughout the life of a well periodically restore high pressures conditions. Shut-in wells, that are not producing nor plugged and abandoned, may also repressurize with time.

When examining the natural flow system, the anhydrite marker beds and associated clay seams are considered as likely flow conduits. In order for flow to occur into the mine, the well pressures have to be greater than the formation fluid pressures. Formation pressures in the McNutt are not known, measurements in pressure relief boreholes suggest low pressures (60 psi). These pressures may have been reduced due to the

presence of the mine. However, in a similar manner, the pore pressure in the well pillar may also be depleted with time due to the presence of the mine. Therefore, the formation pressures in the rock between a well and a mine may be quite low and easily allow for migration of oil or gas into the mine, even when well fluid pressures are low.

The Salado formation can not be relied upon to isolate gas pressures from the mine. Further evidence of this can be found in the field. Pressures less than lithostatic are sufficient to open fluid pathways in the anhydrite marker beds at WIPP (Wawersik et al, 1997). The WIPP project is not relying on the integrity of the Marker Beds in the Salado to isolate itself from potential gas flow. On the contrary, the project assumes that the Marker Beds will accommodate gas generated by the waste in the repository and thereby reduce the potential to fracture the repository horizon (Wawersik, et al, 1997). The amount of gas generated by the WIPP will be limited and produced over a long period of time. The wells outside the WIPP boundaries are not considered a threat to the repository because of the low probability of a well breach (Rechard, 1999). This is justifiable as the subsidence associated with the repository (Pfeifle, 2004) is small to negligible in comparison to that experienced by the potash mining.

Other field observations are from the nearby waterflooding operations (Vacuum, Monument, and Rhodes-Yates fields) that contaminated vast sections of the Salado (Silva, 1995), in some cases over miles in lateral extent and reportedly along 48 distinct horizons or interbeds within the Salado (Bailey, 1990); and also from the potash mines themselves where oil seeps have been observed in the mine near wells (PCA, 1973). These items have been argued in extensive litigation and it is not our intent to reproduce the materials presented there. It is sufficient to say that the above field observations support the position that flow can occur through the Salado.

Conclusion

This document constitutes a plan. It represents our best estimate at how we will proceed, what we will base our analyses upon, and the criteria to be used in evaluating the results. However, some latitude may be required in order for the analysis team to investigate analysis results and understand the underlying mechanics, and also to make recommendations relevant to the mine-well mechanics and gas migration issue.

The study aims to understand and characterize mine-well interactions for the conditions encountered in the potash area, and finally suggest a standoff criteria between the wells and mines. In practice, one must consider the uniqueness of each situation and considerable judgment will still be needed to make appropriate calls on standoff distances. Additional analyses for specific or unique cases may be required.

References

Abel, J.F. Jr. Potential for Potash Mining Subsidence Impact on a Pressurized Cased Gas Well. Letter Report to Bill Lane, American Mine Services, August 24, 1992.

Abel, J.F. Jr. Wellbore Subsidence. Letter Report to C. High, Kemp, Smith, Duncan, and Hammond PC, Golden Co. August 14, 1996.

Appellants to IBLA 92-612, et al. Proposed Findings of Fact and Conclusions of Law. Council for Appellant Yates Petroleum Corp, E. Carroll, M. Bogle, and G. Nibert, October 29, 1997.

Austin, G.S. Potash in New Mexico: New Mexico Geology, v. 2., 1980

Bailey, J. New Mexico State and Office memorandum to Marsh LaVenue, Interra Consulting Company, August 13, 1990. Ref to in EEG-62, June 1995.

Blandford, M.L., 1988. JAS3D- A Multi-Strategy Iterative Code for Solid Mechanics Analysis: User's Instructions, Release 1.6, Sandia National Laboratories, Albuquerque, New Mexico.

Boyd, J. T. Findings on the Effects of Oil and Gas Wells Drilled in Potash Reserve Areas. Report prepared for the Potash Committee, NM Mining Association, July 27, 1973.

Broadhead, R., F. Luo, and S. Speer. Oil and Gas Resource Estimates. Westinghouse Electric Corp. Waste isolation Division, by NM Bureau of Mines and Mineral Resources, Socorro, NM, March 31, 1995.

Bureau of Mines. U.S. Dept. of Interior. Develop Data For Review of Metal and Non-Metal Mine methane Hazard Classification. Report prepared by A. Lumsden and R. Talbot, Golder. Bellevue, Washington, January 1983.

Bureau of Mines. Valuation of Potash Occurrences within the Waste Isolation Pilot Plant Site in Southeastern New Mexico. Prepared by System Operation Group, Domestic Evaluation Group, Minerals Availability System, Intermountain Field Operations Center for Minerals Availability System Special Project, Energy, Research, and Development Administration. November 1977.

Butcher, B.M. A Summary of the Sources of Input Parameter Values for the WIPP Final Porosity Surface Calculations, SAND97-0796, Albuquerque, NM: Sandia National Laboratories, 1997.

Callahan, G.D. and Hansen, F.D. Crushed-Salt Constitutive Model. SAND99-3003c, 1999.

- Carmichael, R.S. CRC handbook of Physical Properties of Rocks, CRC (Chemical Rubber Company) Press, Inc. Boca Raton, Fl. 1984.
- Colorado School of Mines, Lab Test Results, Direct Shear, Compressive, Elastic, and Density Tests (1982, 1991)
- Croft, B.H. Conflicts Between Potash and Oil and Gas Developments. Mineral Law Institute. Boyden, Tibbals, Staten, & Croft, Salt Lake City, Utah, 1964.
- Cummings, J.B. Affidavit before USGS, Appeal of PCA to Dir . of USGS, January 30, 1962.
- Department of Interior. Geologic Survey. Log of Oil or Gas Well. Hargraves No. 2. January 30, 1942.
- Department of Interior. Geologic Survey. Duvall Operations, Oil-Potash Area, Eddy and Lea Counties, New Mexico, Letter to file from Regional mining Supervisor, R.S. Fulton, March 16, 1962.
- Deere, D.U. Subsidence and Rock Pressure Conditions. United States Potash Company Mine, Carlsbad, NM Interim Report No. 1 for US Borax and Chemical, LA, California, June 30, 1957.
- Deere, D.U. Influence of Surface Movements Associated with Final Mining on the Proposed Plant at Carlsbad, NM, Mine. Report for US Borax and Chemical Co., June 1, 1961.
- Fossum, A.F. and R.M. Brannon. The SANDIA GEOMODEL- Theory and User's Guide. SAND2004-3226, Sandia National Laboratories, Albuquerque, New Mexico, August 2004.
- Fung, Y.C. Foundations of Solid Mechanics, Englewood Cliffs: NJ. Prentice Hall Inc., 1965.
- Golder and Assoc. Recommendations for Abandonment of the Wills-Weaver Mine and Mine Shafts, Carlsbad, NM. Report to USGS, November 1979.
- Griswold, G.B. Final Report on Talisman Proposal. NM Institute of Mining and Technology Report to Don Roberts, PCA, May 14, 1984.
- Griswold, G.B. Geology of the Carlsbad Potash Mining District. Report to C. High, March 9, 1982.
- Gunn, R. and J. Hills. Geology of the Tenth Potash Ore Zone: Permian Salado Formation, Carlsbad District, New Mexico. NM MMR Open File Report 146, 1975.

Hager, J.W. Oil Stain Occurrence in National's Eddy Mine. Letter to File, US Dept. of Interior, Geologic Survey, Carlsbad, NM May 18, 1965.

Hansen, F.D., G.D. Callahan, M.C. Loken, and K.D. Mellegard. Crushed-Salt Constitutive Model Update. SAND97-2601, January 1998.

Hazlett, G.H. and L.W. Teufel. Concurrent Development of Delaware Oil Reservoirs and Potash Mineral Deposits in Southeastern New Mexico- Fluid Flow, Rock Mechanics and Safety Considerations. May 2000.

Kirby, R.E. Letter to R. Blackman. AMAX to PCA, Subsidence Measurements, May 18, 1973.

Jones, C.L. Potash Resources in Part of Los Medanso Area of Eddy and Lea Counties, N. Mex., U.S. Geol. Survey Open File Rept. 75-407, 1975.

Jones, C.L. Permian Basin Deposits, South-Western United States; Geology of Saline Deposits, UNESCO, Earth Sci. Ser 7, Proceedings, Hanover Symposium, 1968 (reprinted in A.L. Brokaw et al., 1972, Geology and hydrology of the Carlsbad potash Area, Eddy and Lea Counties, NM: U.S. Geologic Survey Open File Report 4339-1, Appendix A).

Munson, D.E. Mechanical Parameters for Update of Reference Data Report. Letter Report to M. Tierny, Sandia National laboratories, 9/26/1995 as published in SAND97-0796, A Summary of the Source of Input Parameter Values for the WIPP Final Porosity Surface Calculations, B. Butcher, August 1997

Miller, E.M. and F.L. Pierson. Underground Movement and Subsidence Over United States Potash Company Mine. Society of Mining Engineers of A.I.M.E. Feb. 16-20, 1958.

New Mexico School of Mines, State Bureau of Mines and Mineral Resources. NM Well Log Division, No. 1 Cummingham Permit, June 22, 1929.

Obert, L.A. Creep in Model Pillars. US Bureau of Mines. RI6703, 1965.

Olsen, J.A. Federal Management of the Potash Area in Southeastern New Mexico. New Mexico Geological Society Guidebook, 44th Field Conference, Carlsbad Region, New Mexico and West Texas, October 6-9, 1993.

PCA. Multiple Use - Waste of Potash from Drilling through Known Potash Deposits. Report to S. Wakefield, Asst. Sec. Energy and Minerals, Potash Committee of the New Mexico Mining Association. Carlsbad, NM, August 7, 1973.

Pfeifle, T.W. and F.D. Hansen. Database of Mechanical and Hydrological Properties of WIPP Anhydrite Derived from Laboratory-Scale Experiments. SAND98-1714, October 1998.

Pfeifle, T., L. Pyeatt, and S. Patchet. Subsidence Monitoring at the Waste Isolation Pilot Plant. Solution Mining Research Institute; Spring 2004 Technical Meeting, Wichita, Kansas, USA, 18-21 April, 2004.

Pierson, F.L. Application of Subsidence Observations to Development of Modified Longwall Mining System for Potash. Society of Mining Engineers of A.I.M.E. Feb. 14-18, 1965.

Powers, D.W., S.J. Lambert, S.E. Shaffer, L.R. Hill, and W.D. Weart, eds. Geological Characterization Report, Waste Isolation Pilot Plant (WIPP) Site, Southeastern New Mexico. SAND78-1596, 1978.

Rechard, R. Historical Background on Assessing the Performance of the Waste Isolation Pilot Plant. SAND98-2708, Sandia National Laboratories, June 1999.

Rutledge, P.A. E. Morgan, J. Kennedy. Investigation Into the Occurrence of Gas Pressure Above the First and Tenth Ore Zones in the Potash District, Carlsbad, New Mexico. U.S. Dept of Interior, Bureau of Mines, Health and Safety Activity Report, December 3, 1963 through March 15, 1964.

Silva, M. Fluid Injections for Salt Water Disposal and Enhanced Oil Recovery as a Problem for the WIPP. Proceedings, NM Environmental Evaluation Group, Technical Workshop August 1996.

Stoller, S.M. Investigation of Borehole Brine Migration in Potash Mines. RFP No. 63789. Prepared for Westinghouse Waste Isolation Division by the Stoller and Merrick Companies. 1995. YP 575.

Teufel, L.W. Model Properties for Yates Exhibit YP674, pg 16965, 1996.

Traywick, C.C. and R.S. Fulton. Review of Oil Industry and Potash Industry Papers Presented to Secretary Wakefield on May 8 and August 7, 1973. USGS Memorandum to Conservation Division Chief, August 24, 1973.

Tavares, M.P. Dilatancy and Failure Criteria for SPR Rock Salt, Internal Report to J.K. Linn, Sandia National Laboratories, Albuquerque, NM, August 9, 1994.

Thorton, C.H. and I.P. Lew. Concrete and Design Construction, Standard Hand-book for Civil Engineers, Chapter 8, 3rd ed., F.S. Merritt, editor, McGraw-Hill, NY. 1983.

Traywick, C.C. Meeting with Oil-Potash Liaison subcommittee of NMOCA on proposed expansion of the Secretary's Potash Area, Southeastern NM, Geological Survey Letter to files, May 15, 1963.

Touloukian, Y.S. and C.Y. Ho. Physical Properties of Rocks and Minerals. McGraw Hill, Vol 2. 1981.

OCD. Order R-111-P, Oil conservation Commission, Energy, Minerals, and Natural Resources Dept., State of New Mexico, Case No. 9316, April 21, 1988.

US Dept. of Interior, Bureau of Land Management. Potash Enclave Mineral Report, 2005.

US Dept. of Interior, Bureau of Land Management. Report to Potash Committee Concerning Prospecting for Oil and Gas in the Potash Area. July 1973. Exhibit K BLMC042164. 25996

US Dept. of Interior, Bureau of Land Management. Memorandum from District Mining Engineer to the District Manager. March 26, 1987. BLMC006895 ref to Statement of Reasons and Brief, IBLA 2003-335 and 2003-336, APD Denials, Yates Appellants, US Dept of Interior Office of Hearings and Appeals, Washington DC, Sept 10, 2004.

Warren, T.L., A.F. Fossum, and D.J. Frew. Penetration into Low Strength (23 Mpa) Concrete: Target Characterization and Simulations. SAND2002-2584, 2002.

Warnock, G. Economic Analysis Carlsbad Potash District Eddy and Lea Counties, NM. April 30, 1973 ref to Brokaw, A.L. et al. Geology and Hydrology of the Carlsbad Potash Area, Eddy and Lea Counties, New Mexico, USGS-4339-1, Open File Report, 1972.

Warnock, G. Response to Decision Denial of Application for Permit to Drill in the Secretaries Potash Area, Sept 16, 1992.

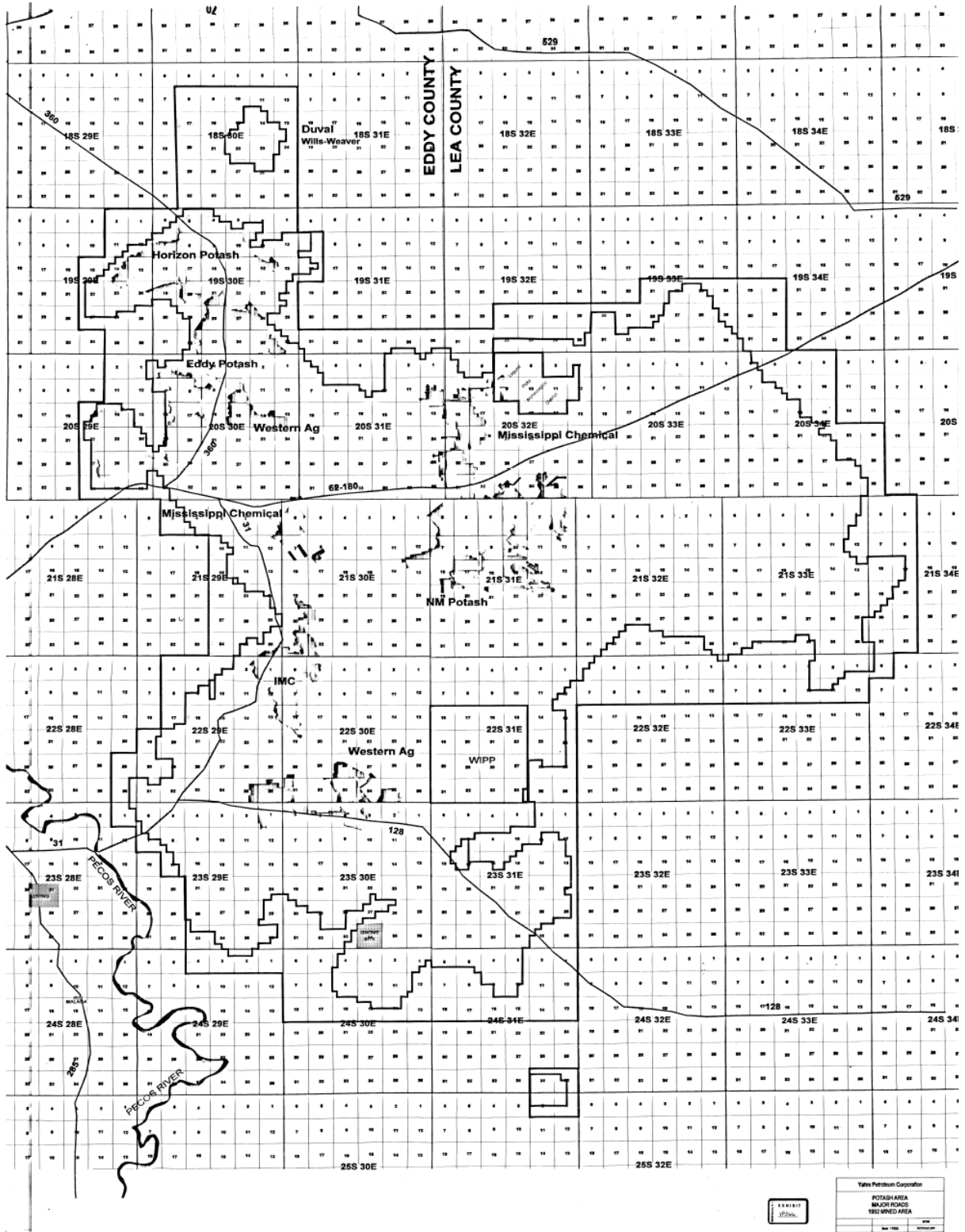
Wawersik, W., L. Carlson, J. Henfling, D. Borns, R. Beauheim, C. Howarth, and R. Roberts. Hydraulic Fracturing Tests in Anhydrite Interbeds in the WIPP, Marker Beds 139 and 140, SAND95-0596, Sandia National Laboratories, May 1997.

YP-411. General Chronology of a Delaware Well.

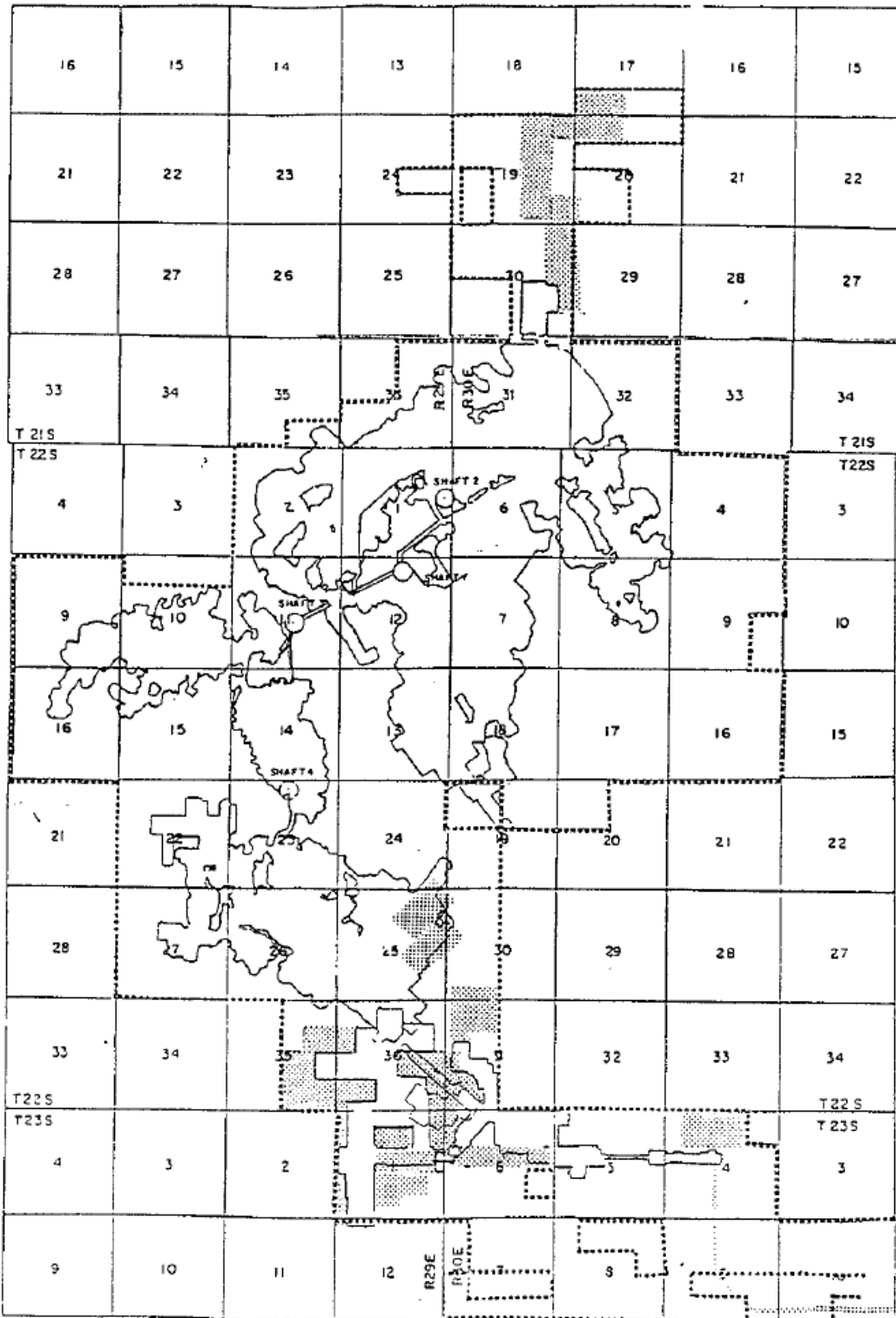
YP-409. Properties of Casing and Tubing Typically Run in Delaware Completions.

APPENDIX A. Maps of Potash Area and Mines

Mine Locations in Potash Lease Area



IMC Mine

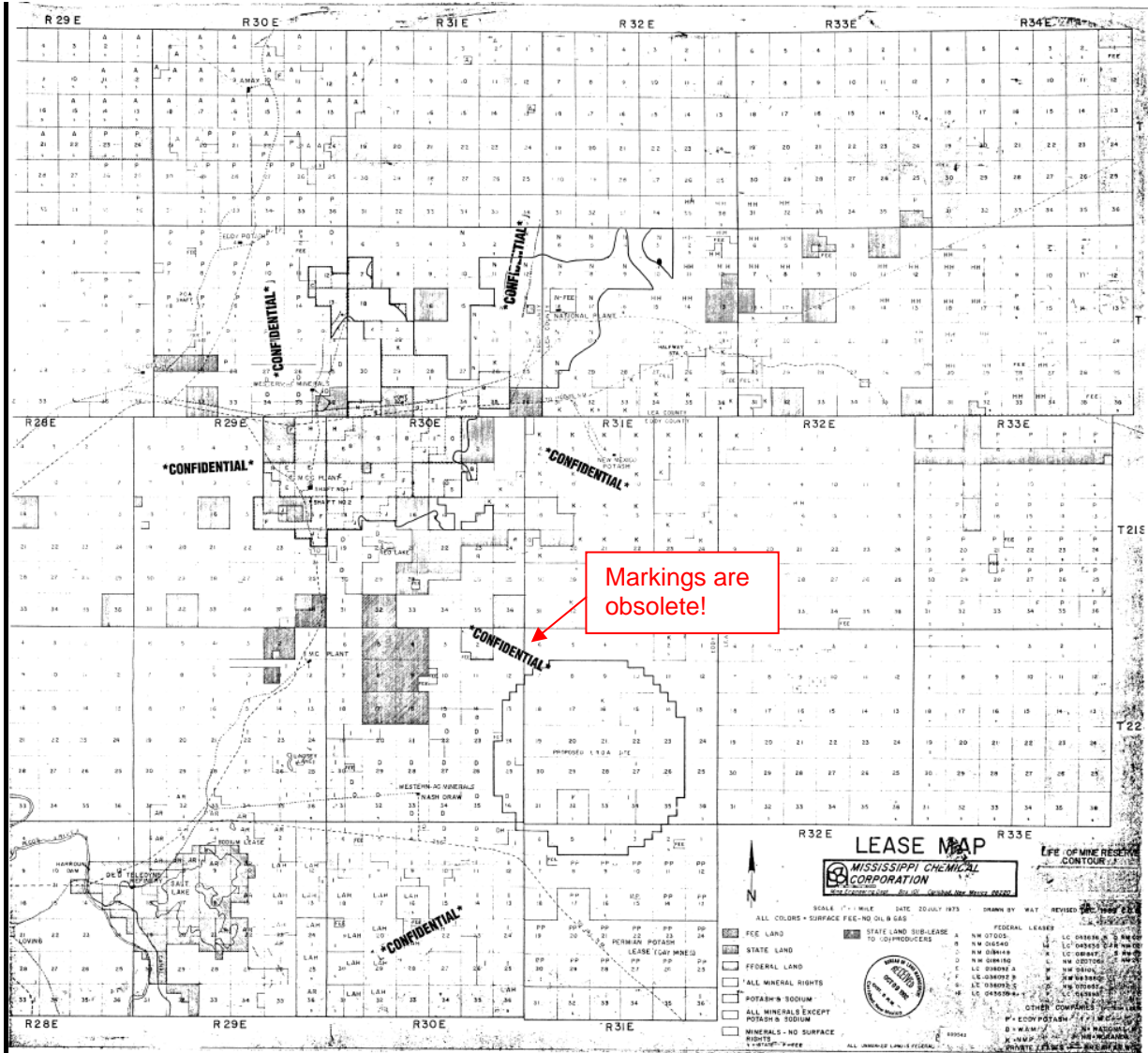


-  OPEN MINE WORKINGS
-  LEASE BOUNDARY
-  PLANNED DEVELOPMENT

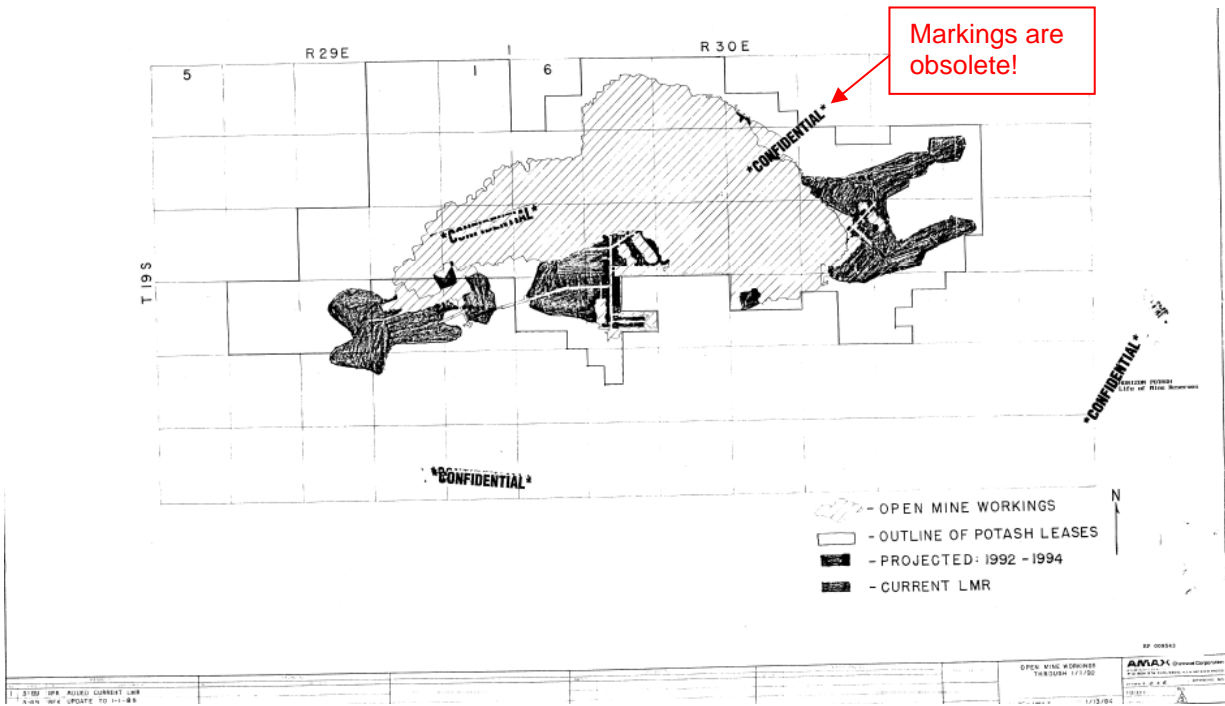
INTERNATIONAL MINERALS & CHEMICAL CORP.
 900', 850', 800', 700' LEVEL PERIMETER
 SCALE 1" = 6000' JANUARY 1, 1989

BI

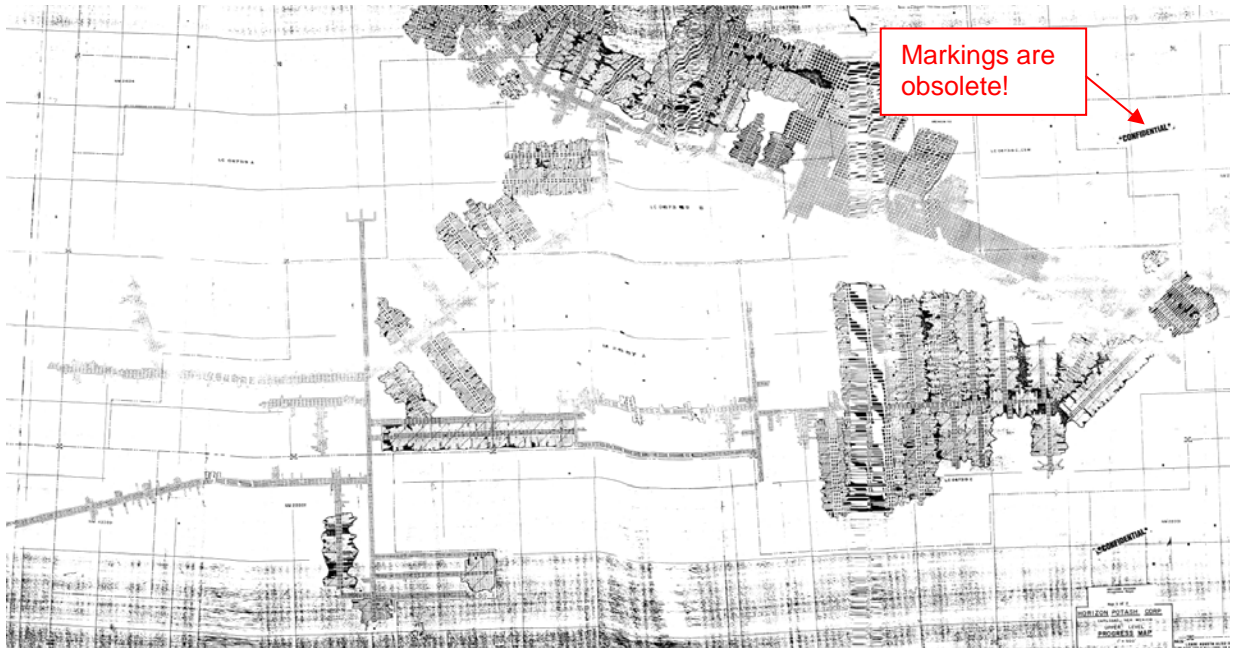
Interpids Lease (MS Chemical)



AMAX Mine



Horizon Mine

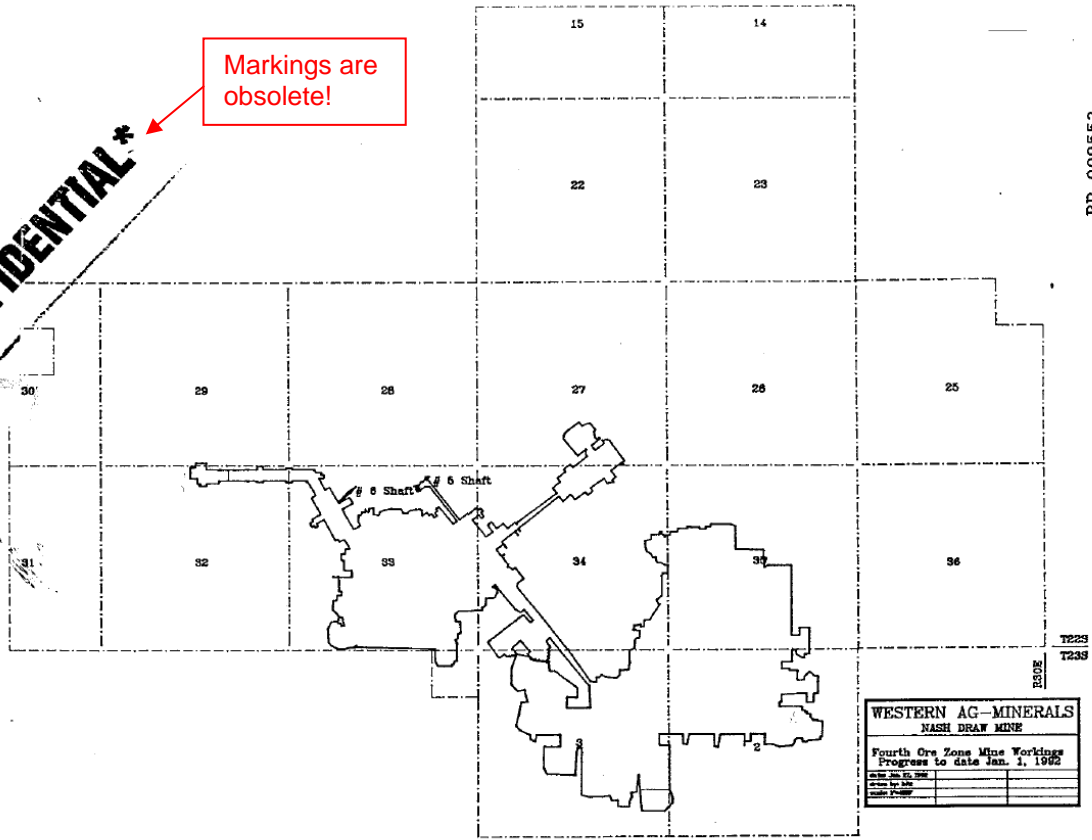


Western Ag Mine

WESTERN AG MINERALS COMPANY
PRESS MAP (1991)

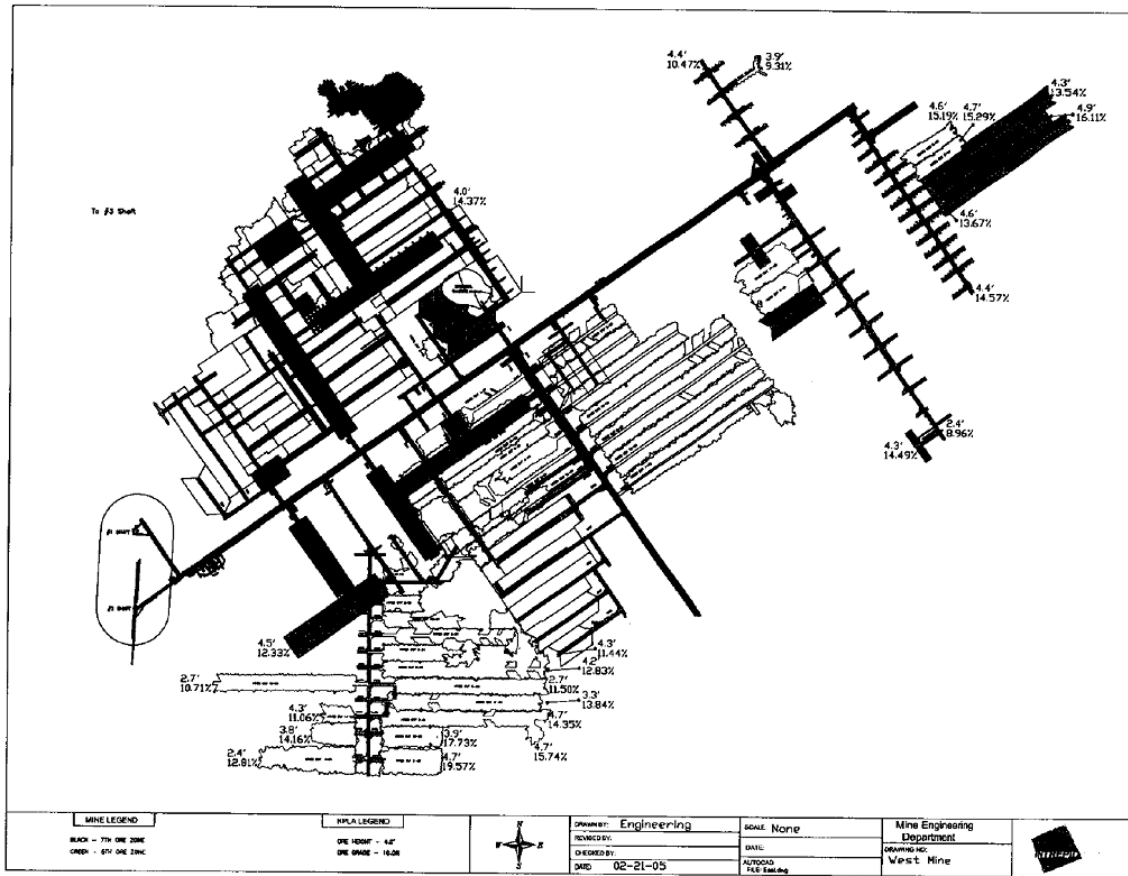
CONFIDENTIAL*

Markings are
obsolete!



RP 009552
020784

Intrepid West Mine (US potash, US borax, Teledyne, CARGO, MS Potash Mine)

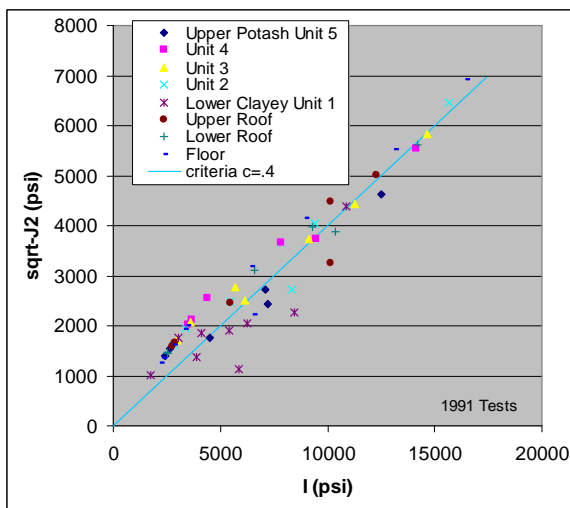
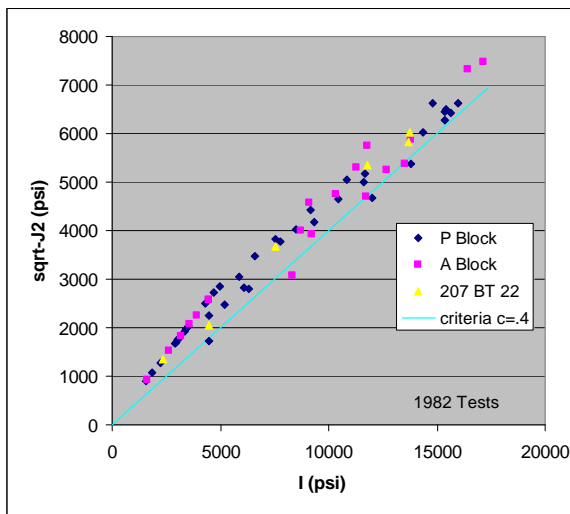


APPENDIX B. Strength Data (Colorado School of Mines)

1982 Data				1991 Data	
Confinement (psi)	Strength (psi)	Confinement (psi)	Strength (psi)	Confinement (psi)	Strength (psi)
Block P		Block A		Upper Potash Unit 1	
0	2890	1000	6330	800	5500
1400	12570	0	4450	1000	5210
800	8860	700	8940	0	2430
1000	9640	1400	14340	0	2670
500	5330	0	2640	1500	9500
0	2230	1200	10280	500	3530
500	3490	0	3160	Unit 4	
1500	12370	800	7590	1000	7480
0	3040	1200	9340	0	3690
200	4090	1200	11380	0	4410
1300	11740	0	3900	1500	11120
0	3410	600	7540	500	6830
500	8160	1400	10700	0	3510
0	4310	0	1610	Unit 3	
400	5290	700	9880	1500	11620
200	5490	0	4460	1200	8890
0	2940	0	3580	900	7350
300	4600	600	10560	600	4940
1300	9390	400	8320	300	5100
0	1540	1250	13920	0	2960
700	9440	Blocks 207, BT, and 22		0	3610
300	6920	1200	11310	Unit 2	
0	3520	850	10100	0	3370
0	1870	300	3850	0	2810
1500	12630	1100	11540	1500	12680
500	7470	400	6750	1200	5910
0	3340	0	2350	800	7830
700	7920			400	4690
1400	12640			Lower Clayey Unit 1	
0	4720			0	1760
400	6950			300	3500
900	9880			500	2870
0	3090			0	3040
1500	10820			700	3990
200	6200			900	4430
1500	12980			1100	8680
1100	12580			1500	5440
0	4950			1300	3280

1991 Data					
Roof		Floor			
0	2740	0	2180		
0	2880	0	3340		
400	4650	0	2320		
800	8550	0	3450		
1200	9880	300	5820		
1500	7120	600	7780		
0	2520	900	4730		
0	2550	1200	10750		
400	5790	0	2800		
800	7700	1500	13460		
1200	7940				
1500	11220				

Additional plots of data in terms of stress invariants:



Appendix II: Sandia Response to Stakeholder Comments on Analysis Plan

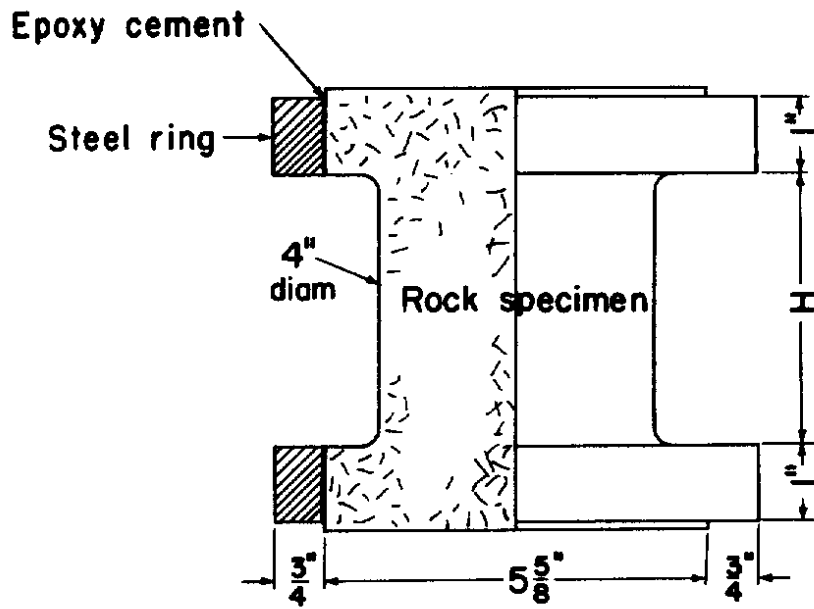
Sandia Response to Stakeholder Comments

Issues Addressed

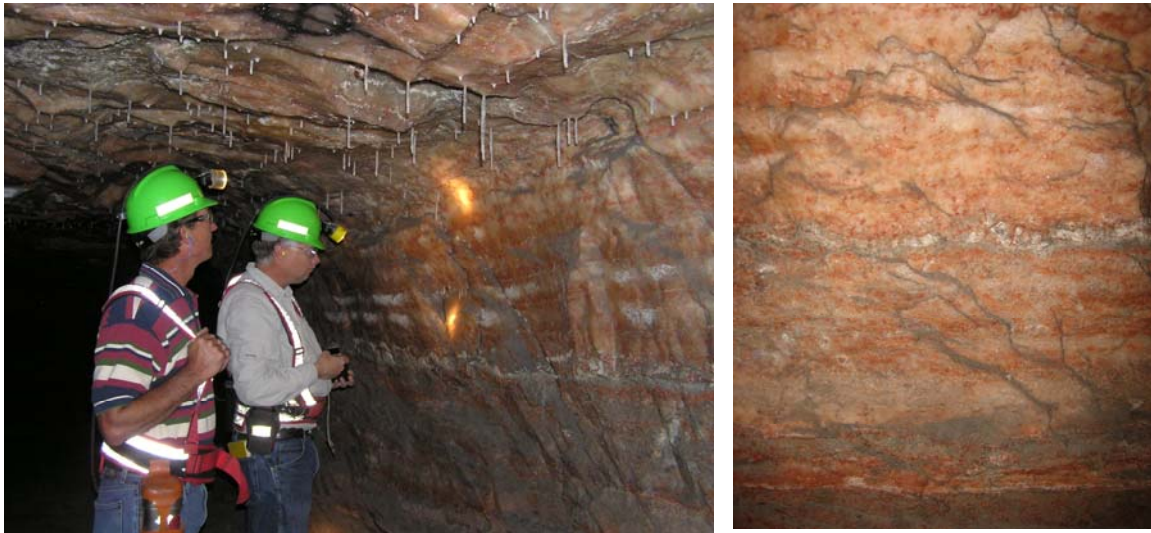
- Creep Testing
- Elastic Properties from Logs
- Thickness of Shear Plane
- Friction
- Cement Modulus
- Role of modeling
- Well Design
- Field Experiment
- Integrity Testing of Existing Wells
- Non-Technical

Creep Testing

Initially we desired to obtain potash core and perform creep tests. Our attempts to obtain core were unsuccessful. We therefore decided to simulate some of the potash core tests published by Obert (1965) on specimens extracted from a local mine. The laboratory scaled pillars that Obert tested did not maintain a constant deviatoric stress, either spatially or temporally. Therefore, we were not able to derive constitutive properties from the test results. Testing procedures have changed since Obert's tests. Today we would use cylindrical core, not pillar mockups, and we would maintain control over the deviatoric stress state while measuring deformation with time. We were pleased that Intrepid recently offered to take core for testing. Unfortunately creep testing would delay the project and it would cost a considerable amount. A test matrix would have to be comprised of different potash types and grades, with various impurity types and levels. A single creep determination requires three to six tests. To test all the variations found in the field, numerous tests would be required. This would likely result in a wide range of creep rates that would spatially vary within and among the various potash seams. Using this information in a model may not be feasible since the spatial variations would be difficult to map over the entire basin. The information may not be significant to the modeling since the maximum predicted shear displacements occur well above the potash mine, and the amount of potash in the Salado is small compared to salt. Creep tests performed on New Mexico potash and other potash (Obert, 1965; Jeremic, 1994) show the rates can be either higher or lower than salt. Therefore salt properties are used for the unmined portions of the mine horizon. The mined potash areas will be simulated using a model that represents the large deformations associated with secondary mining. It will be calibrated using mine closure and subsidence information.



Obert's Model Pillar for Creep Testing (1965)



Pictures of Mosaic Mine Potash showing localized variations in mineralogy.

Elastic Properties from Logs

Logs can be used to derive rock properties. In this case, Intrepid provided density and sonic logs for 5 coreholes. Both normal and shear velocities are needed along with the density to determine the modulus of elasticity and Poisson's ratio. The compensated sonic tool did not measure the transverse velocity, therefore properties were not derived from the logs.

Thickness of Shear Plane

A 3 ft thick shear plane was used in a Trona study and suggested for the potash study. Geologists (Gunn and Hills, NMBMMR Open File Report 146) state that clay seams vary in thickness from thin film to 5 inches. Core wells and logs substantiate this. If resources permit, we will develop a casing model that evaluates a finite size slip layer, say 5 inches. However, the possibility of a thin layer as simulated is realistic.



Pictures of clay strings and bedding planes in Mosaic Mine (pillar and close-up)

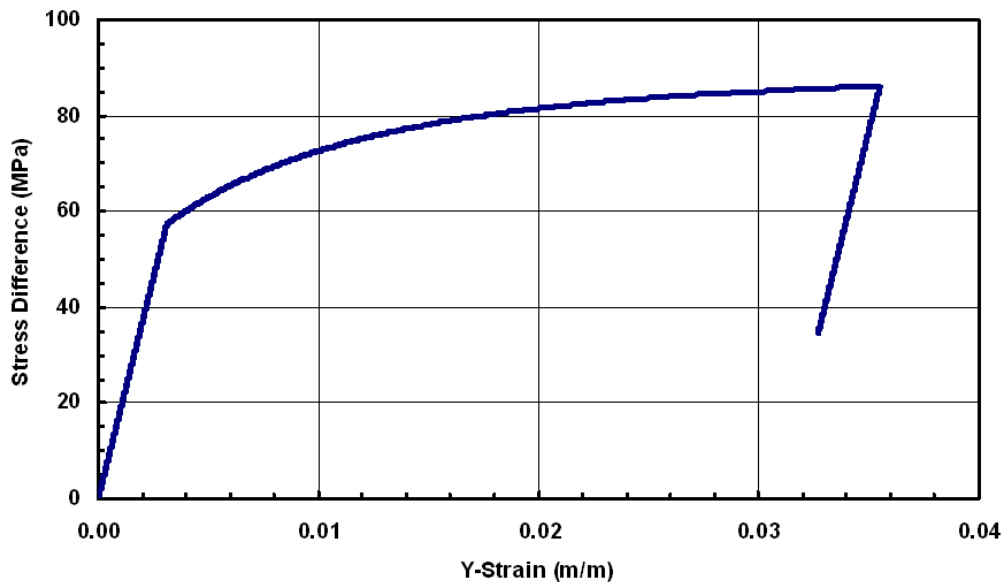
Friction

The value used for WIPP and in our analyses is a friction coefficient of 0.2. Calculations using that value compare well to measured room deformations at WIPP. A similar value was used for the Trona analyses (Marl, 0.26), and measured frictions in shear tests of potash samples suggest 0.2 as appropriate. In studies of slip in oil fields, Hamilton found that at Wilmington, a frictional coefficient of 0.18 best matched the measured subsidences. A study on Belridge used 0.1 to match field measurements of shear displacement across failed casings and subsidence (Hilbert, Fredrich, Bruno, Deitrick, and Rouffignac, 1996)

The reference to gouge tests by Price (1980) may reflect the material found in faults. It is difficult to say as the thesis is unpublished and the referenced author states that he performed tests on the effect of anhydrite on the intact mechanical properties of salt. Tests by Bowles (1978) on clay show the internal friction angle of vary from 3 to 20 degrees for consolidated undrained conditions. The average of this range results in a friction coefficient of 0.2

Cement Modulus

The modulus of Portland cement varies from $3-8 \times 10^6$ psi (Lea 1971) or $2-6 \times 10^6$ psi Merritt 1981. The initial modulus of Geomodel cement is 2.7×10^6 , which is at the low end of the ranges found in the literature. Sandia has previously used a value of 3.8×10^6 psi in its modeling of SPR wells (Sobolik and Ehgartner, 2005), which use a Class-C cement similar to those found in the potash basin. Softer values 0.7 to 1.5×10^6 psi are recommended by oil and gas reviewers (no reference provided). We note that the cement behavior in the model softens upon loading (slope of stress-strain curve decreases). The unconfined compressive strength of the cement used in the Geomodel is approximately 4000 psi, which is less than the typical 5000 psi compressive strength reportedly used in oil and gas wells in the potash area (O'Brien, 2008).

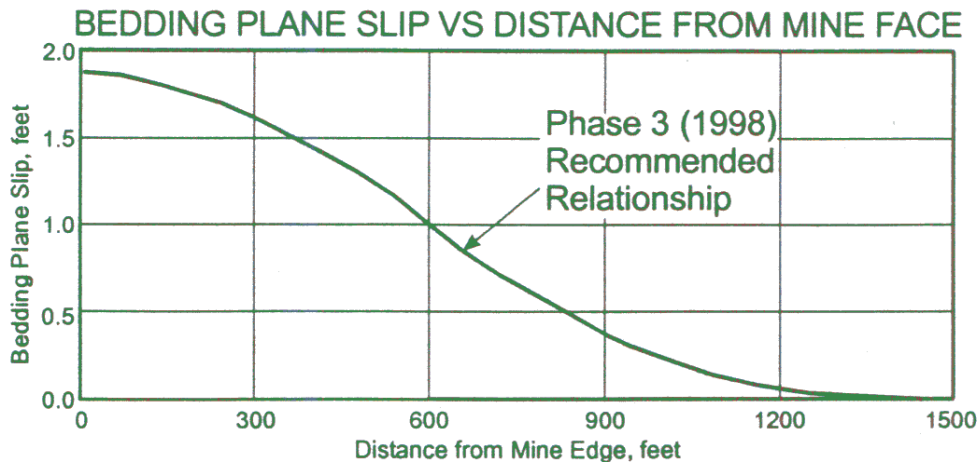


Stress Strain Behavior of Geomodel Conventional Strength Portland Cement- 5000 psi confinement (Arguello, 2008)

Role of modeling

Modeling allows us to examine the possibilities. A model that uses the best available information and data, as presented in the analysis plan, and matches the underground closure and surface subsidence deformations also captures the deformations in the strata between the mine and surface. Thus, our comparison to field observations. The structural behavior of steel and cement are well known, therefore the modeling of the well is also credible. It is argued that there are any number of input variations to the model that could produce similar matches to the field measurements, but could effect the slippages predicted. We don't know whether that speculation is true or not, but there is no reason to pursue it. In our analyses we did not have to arbitrarily vary parameters to match the field data. To do so would result in less credible predictions.

We conclude that the model results are very realistic possibilities. Given this, we intend on providing 1) a slip envelope curve such as the one from the Trona studies and 2) the maximum slip allowable for the wellbore models, such that one may quantitatively define a standoff criterion.



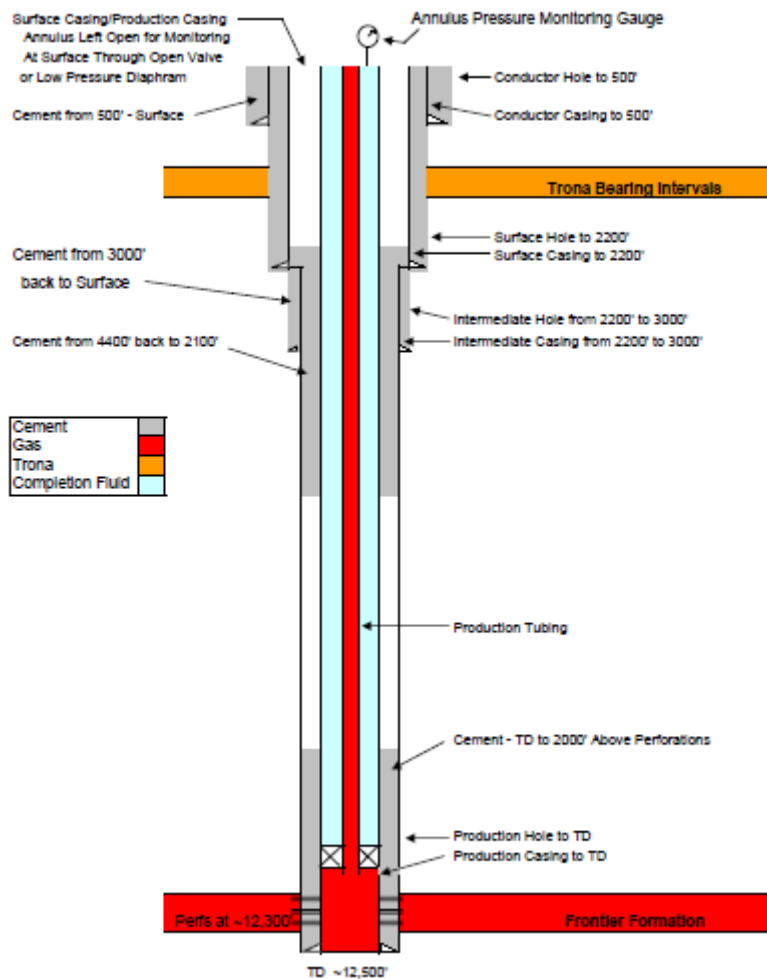
Slip Envelope from Trona Study

Well Design

A suggestion to design a well to accommodate slippage perhaps by under reaming or using specialized cements at interface locations is an interesting consideration, but outside the scope of work for this project. We do note that there are numerous potential slip planes in the geology, and locating them using logging tools may not be possible as

the clay interfaces are very thin. Therefore while a theoretical design may be possible, it may be very difficult to implement in the field due to the preponderance of thin beds.

Thus far, only conventional well designs have been proposed for use in the potash area. A well could be designed to accommodate slippage. One such idea is to have uncemented annuli between the salt string and production string. The annuli could be pressure limited by a blow out diaphragm at the well head, thus preventing pressure buildup at the salt string in the event of leakage of the production string. Annular pressure could be monitored in real time if necessary. This approach allows for yielding of the salt string to the point where it contacts the closest inner string and compromises its integrity. A large annulus would permit significant deformation. This design by definition requires yield and loss of integrity of the salt string. An idea that may be hard to adjust to as the practice of a salt protection string commenced in the early 1950's. In a similar manner, novel design concepts may be considered unproven and unconventional, and as such not suitable for applications where life is at stake.



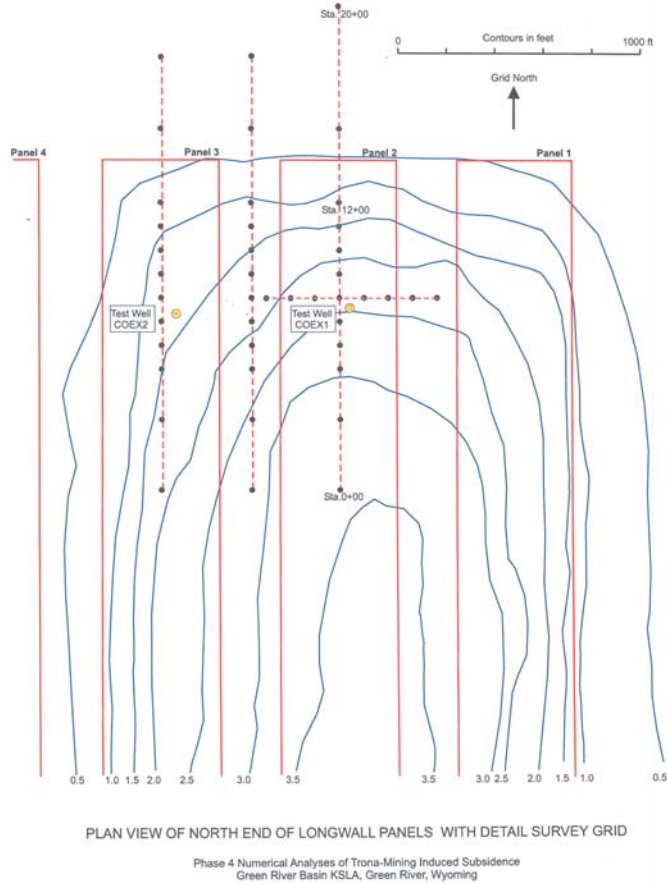
Concept Well Proposed for Protection of Wyoming Trona Mines (Yates)

In any of the designs that have been or may be proposed, one must keep in mind that wells are not always build as-is, that is constructed as planned. This is also true in how they are operated. An argument was exerted that Sandia should have performed a risk assessment. That is not within our SOW, however to do so would address the failures of wells and the imperfect record of the oil and gas industry. A number of such studies have already been done to address that, one of which focused specifically in the potash area as part of litigation records using NMOCD incident reports. The challenge with such evaluations is determining what an acceptable risk is to human life. That is difficult to answer and it is therefore difficult to use the results of risk studies. In the current study performed by Sandia, we can provide answers to and define what an acceptable standoff distance is for a conventional well design. That information will be of value to BLM.

Field Experiment

A well test similar to that conducted in the Trona formation was suggested as a means to validate the model and provide final resolution. The concept is to install a test well, mine the area around it, while logging the well and measuring subsidence. This would provide a case study, but may require years to complete depending on mining schedules. It would represent a single data point in a very large field, where the geology is known to vary and the mines differ considerably in depth, mining rates and extraction ratios, and horizons. Undoubtedly a model could be developed to match the measurements as was done for the Trona study, but the question will remain as to its ability to predict behavior in other areas of the field. We do not view a single test as being conclusive. A number of tests may be required.

Despite the inconclusive nature of any field test, a test will provide additional information, and close agreement between the measurements in the field and the modeling would result in additional confidence in analysis predictions.



Fugro Plate 4.6 Report No. 0201-4296, 2002.

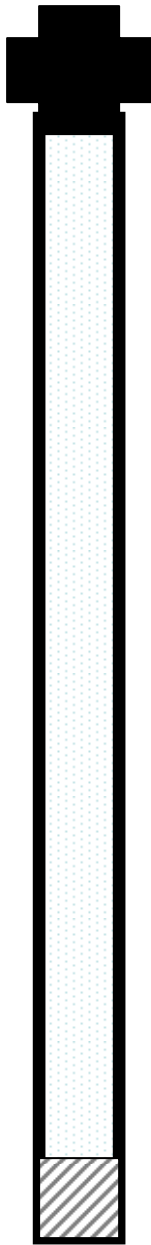
Another possibility is to use core holes to be drilled by the mining industry. The current practice is to cement the holes after coring potash. Plugging is necessary to protect the mine from water inflow. However, the wells do not need to be cemented for this purpose until the mine approaches them. During that time, measurements of well deformations (including slippage) due to mining could be collected. The condition of the holes would have to be adequate for logging or casing would be required. If the mines were uncomfortable with leaving the coreholes open, the holes could be partially plugged near the mine level, and logging and measurements could be performed in the upper reaches of the Salado and McNutt. The wells could be fully cemented upon completion of data collection. This would require cooperation with the mining companies.

It was argued that Sandia must insist upon a field experiment conducted by BLM similar to the Trona study. There are alternatives to this using the existing and planned wells owned by industry. This would put the burden of proof back on industry. Whether a field test is conducted or not, does not remove the fact that the analysis will represent and provide BLM the best available information to date. It will be their decision as to whether it is adequate enough for their purposes.

Integrity Testing of Existing Wells

A field test could utilize existing oil and gas wells within or nearby the mine workings. It has been argued by the oil & gas stakeholders that the existing wells within the mined areas demonstrate that they are safe. Others argue that the sometimes present oil seeps near wells suggest the opposite. Integrity testing of existing wells could resolve this argument and provide a quantitative assessment of the impacts of mining on the nearby wells. The information could also be used to validate modeling and it could be used empirically to quantify well mine interactions.

The tools are available for integrity testing and it is an industry standard for storage and disposal wells. A typical integrity test injects nitrogen at the maximum gas pressures that is possible in a well. The test pressure is maintained by injecting additional nitrogen if required. The leak rate is calculated by the amount injected due to loss over the test period. Such tests are routinely performed in hydrocarbon storage wells. Wells would have to be located within or nearby mine workings and be open for testing. A number of wells fall within this category and probably experience large deformations due to mining. The degree of deformation experienced could be quantified through logging the hole. This information alone could be used to compare to modeling results. If the wells were tested and proven to have integrity, the confidence gained in the ability of casings to protect the mines could result in a breakthrough and resolve the issue. This would require cooperation with the oil and gas companies.



Pressurize existing well with N₂
 Max gas pressure applied
 Maintain pressure
 Measure any N₂ loss with time

Could add tracer and examine mine workings

Investigate leak (optional)
 Use a nitrogen/fluid interface or logs- casing, cement bond, caliper, visual, sonic, deformation (gyro&caliper)

Packer or plug set in well
 Slightly below mine horizon



Images of Joint 82 Casing Damage at a Depth of 3,250 Feet.

Illustration of Integrity Test for Existing Wells (left) and Example of Breached Well (Osnes, et al. SMRI 2007)

Non-Technical

There were a number of comments on the analysis plan that were of a non-technical nature, some of which were provided well-after the comment period closed on the analyses plan, as part of the review of this SAND report; in particular, the use of wording and interpretation of regulations, such as R-111-P. These comments have come from attorneys, on different sides of the issue, and they would like to clarify and correct the statements in Appendix I that relate to regulations based on the various rulings, opinions, and judgments made. Anything we could add or discuss on this matter would probably not satisfy everyone. It's clearly outside the expertise of the team, and we have no intent of arguing or judging the matter one way or another. What has been stated in the analysis plan may very well be incorrect, but it was presented as background information and has no impact on the analyses that were performed. Consequently, we will not alter the analysis plan after the analyses were done. The plan provided in Appendix I is viewed as a historical document that was part of the process used to solicit input and involvement from the stakeholders prior to performing the analyses. In our view, stakeholders should consider the analyses and results, as described in the main body of this report, and jointly work on a path forward, that may include revision or writing of new rules and regulations for both industries.

References

Arguello, J. Computational geomechanics & applications at Sandia National Laboratories, SAND2008-6647, Sandia National Laboratories, NM, 2008.

Bowles, J.E. Foundation Analysis and Design. Mc-Graw-Hill, NY, 1982.

Fossum, A and R. Brannon, The Sandia GeoModel : theory and user's guide. SAND2004-3226, Sandia National Laboratories, NM, 2004.

Fugro-McClelland Marine Geosciences. Phase 4 Numerical Analyses of Trona-Mining Induced Subsidence Green River Basin Known Sodium Lease Area Green River , Wyoming. Plate 4.6 Report No. 0201-4296, 2002.

Gunn, R. and J. Hills. Geology of the Tenth Potash Ore Zone: Permian Salado Formation, Carlsbad District, New Mexico. NM MMR Open File Report 146, 1975.

Hilbert, L., Fredrich, J., Bruno, M., Deitrick, G. and Arguello, J. Geomechanics analysis of reservoir compaction and well failures in the Belridge Diatomite. Society of Petroleum engineers 71st Annual Technical Conference and Exhibition held October 6-9, 1996 in Denver, CO, 1996.

Jeremic, M.L. Rock Mechanics in Salt Mining. Balkema , Rotterdam, and Brookfield, Netherlands, 1994.

Obert, L.A. Creep in Model Pillars. US Bureau of Mines. RI6703, 1965.

O'Brien, T. Potash Gas Migration Project: Comments of Oil and Gas Stakeholder to Analysis Plan for BLM Potash Gas Migration Study. September 26, 2008.

Osnes, J., J. Ratigan, M. Meece, M. Thompson, and G. Spencer. A Case History of the Threaded Coupling Production Casing Failure in Gas Caverns— Part 1: Detection and Geomechanical Analysis. Solution Mining Research Institute, Fall Meeting, Halifax, Nova Scotia, October 2007.

Sobolik, S. and B. Ehgartner, Analysis of salt and casing fracture mechanisms during cavern integrity testing for SPR salt caverns. SAND2006-1974. Sandia National Laboratories, NM, 2005.

Distribution:

U.S. Department of the Interior
Bureau of Land Management
New Mexico State Office
1474 Rodeo Road
P.O. Box 27115
Santa Fe, NM 87502-0115

Tony Herrell, Tony_Herrell@blm.gov
Bill Auby, Bill_Auby@blm.gov

University of Colorado
Department of Civil, Environmental, and Architectural Engineering
1111 Engineering Dr.
428 UCB, ECOT 441
Boulder, CO 80309-0428

Richard Regueiro, Richard.Regueiro@Colorado.edu

Sandia Internal:

Sandia National Laboratories
P.O. Box 5800
Albuquerque, NM 87185

Geoscience Research and Applications
MS 0735
John A. Merson, jamerso@sandia.gov

Geotechnology and Engineering
MS 0706
David J. Borns, djborns@sandia.gov
Brian L. Ehgartner, blehgar@sandia.gov
Darrell E. Munson, demunso@sandia.gov

Geophysics
MS 0750
Gregory J. Elbring, gjelbri@sandia.gov
Carolyn L. Kirby, clkirby@sandia.gov

National Security Applications
MS 0751
Barry L. Roberts, blrober@sandia.gov

Geomechanics

MS 0751

Tom W. Pfeifle, twpfeif@sandia.gov

Strategic Initiatives

MS 0372

James M. Redmond, jmredmo@sandia.gov

Jose G. Arguello, jgargue@sandia.gov

Charles M. Stone, cmstone@sandia.gov

Joseph E. Bishop, jebisho@sandia.gov

Solid Mechanics

MS 0376

James E. Bean, jebean@sandia.gov

John F. Holland, jfholla@sandia.gov

Geothermal Research

MS 1033

Charles E. Hickox, cehicko@sandia.gov

Central Tech. Files, 8945-1

MS 9018

Technical Library, 9616 (2)

MS0899

